A thesis entitled

An investigation into the efficiency of strained and strain-balanced quantum well solar cells

by

Nicholas J. Ekins-Daukes,
M.Sci. (University of St Andrews) 1995
M.Sc. Imperial College, Univ. London 1996

Submitted for the degree of
Doctor of Philosophy
of the
University of London

Imperial College
1999

BIBL
LONDON
UNIV.

Abstract

The optical absorption of a p-i-n solar cell may be increased by incorporating quantum well layers in the intrinsic region, resulting in a larger short-circuit-current. Further, the additional quantum well absorption may be achieved without incurring a comparable loss in open-circuit-voltage; offering potential for enhanced solar power conversion efficiencies. The work reported in this thesis is concerned with the application of quantum well techniques to the GaAs cell, currently the highest efficiency single band-gap cell. In the absence of lattice matched lower band-gap materials, strained InGaAs was used as the quantum well material. An optical study of the carrier dynamics at the solar cell operating point indicates suppressed quasi-Fermi levels in the QW with respect to the bulk material, with advantageous implications for the open-circuit-voltage. However the strained quantum wells introduce misfit dislocations into the structure that dominate the recombination of the cell. The associated loss in open-circuit-voltage is shown to be too large to allow strained GaAs/InGaAs cells to realistically match GaAs in terms of power conversion efficiency. A strain-balance technique is presented, surmounting the limitations imposed by strain and is applied to a 5% InGaAs virtual substrate GaAs/InGaAs structure and a GaAs substrate GaAsP/InGaAs structure. An equivalent power conversion efficiency to GaAs is demonstrated for the GaAsP/InGaAs cell. The scope for further improvement of the GaAsP/InGaAs cell is discussed, with particular reference to light trapping.

Contents

List of Figures 6

List of Tables 11

1 Introduction to Photovoltaics 2
1.1 Solar Irradiance 2
1.2 Photovoltaic Cells and Device Physics 4
1.2.1 Photocurrent 6
1.2.2 Dark Current 6
1.2.3 Power output and fill factor 8
1.2.4 Bulk GaAs cells 10
1.2.5 Limits to efficiency and InGaP/GaAs Tandem cells 14
1.2.6 MQW solar cells 16

2 Survey of GaAs/InGaAs QWSC 19
2.1 GaAs/InGaAs p-i-n structures 19
2.1.1 Strain in p-i-n diodes 20
2.1.2 Strained GaAs/InGaAs p-i-n diodes as solar cells 24
2.2 Potential for enhancing the GaAs efficiency 28

3 Growth and Characterisation 30
3.1 Growth 31
3.1.1 MBE Growth 31
3.1.2 MOVPE Growth 32
3.2 Processing 33
3.2.1 Processing device type a) Doped substrate 34
3.2.2 Processing device type b) Top contacting 34
3.2.3 Processing device type c) Substrate removal 35
3.3 Characterisation 35
3.3.1 Dark and Light IV 36
3.3.2 Quantum Efficiency; experiment and model 37
3.3.3 Reflectivity and Transmission 38
3.3.4 Monochromatic-IV 38
3.3.5 Low Temperature Photocurrent 41
3.3.6 X-ray diffraction 42

4 Carrier dynamics & quasi-Fermi level measurements **43**
4.1 Models for quantum well solar cell efficiency 43
4.2 Determining the quasi-Fermi level separation 45
4.2.1 Absolute measurement of photon flux 46
4.3 Samples for experiment 49
4.4 Modeling EL emission 50
4.5 Results from EL measurements and modelling 51
4.5.1 Results for QT458 and NU972 52
4.5.2 Results for shifted-well samples: RM1368, RM1369, RM1370 52
4.6 Discussion of suppressed quasi-Fermi levels 56
4.7 Probing bias dependencies in GaAs/InGaAs QW photocurrent 58
4.8 Conclusions and further work 65

5 Light trapping **66**
5.1 Light trapping techniques 66
5.2 Planar cells, undoped substrates and rear reflectors 68
5.2.1 Doped and undoped substrates 72
5.2.2 Epoxy-Gold mirrors 75
5.3 Achieving textured GaAs surfaces 78
5.4 Photon recycling and cavity cells 79
5.4.1 A photon recycling theory for optically thin cells 81
5.4.2 Samples for investigating photon recycling 84
5.4.3 Effects of substrate removal 89
5.4.4 MQW photon recycling - alternative explanations 97
5.5 Light-trapping conclusions 98

6 Strain Balance Techniques **99**
6.1 GaAs/InGaAs Strain-Balance 100
6.1.1 Virtual Substrates 101
6.1.2 Growth specification 102
6.1.3 Experimental results 103
6.1.4 Discussion of the results 111
6.1.5 5% InGaAs Conclusions 114
6.2 GaAsP/InGaAs Strain-Balance 115
6.2.1 GaAsP/InGaAs Dark-IV 116
6.2.2 GaAsP/InGaAs Quantum Efficiency 117
6.2.3 GaAsP/InGaAs Light-IV 119
6.2.4 Optimisation of GaAsP/InGaAs cell 120
6.3 Tandem cells using strain-balance MQW cells 123
6.4 Conclusion 125

7 Summary and further work **126**

A Record Cell Efficiencies **128**

B Background Doping **131**

C Sample Descriptions **134**
C.1 GaAs/InGaAs Single Quantum Well (SQW) Samples 134
C.1.1 QT458 (MOVPE) 134
C.1.2 RM1368 (MBE) 135
C.1.3 RM1369 (MBE) 135
C.1.4 RM1370 (MBE) 136
C.2 AlGaAs/GaAs Single Quantum Well (SQW) Samples 136
C.2.1 NU972 (MBE) 136
C.2.2 QT902B (MOVPE) 137
C.3 GaAs/InGaAs MQW Samples 137
C.3.1 QT957A (MOVPE) 137
C.3.2 QT957B (MOVPE) 138
C.3.3 QT957C (MOVPE) 138
C.3.4 QT957D control (MOVPE) 139
C.4 GaAs/InGaAs Strain Balance Samples 139
C.4.1 RM1271 & RM1386 139
C.4.2 RM1276 & RM1391 140
C.4.3 RM1277 & RM1389 & RM1390 140
C.5 GaAsP/InGaAs Strain-Balance Samples 141
C.5.1 QT1227 (MOVPE) 141
C.5.2 QT1228 control (MOVPE) 141

D Matthews-Blakeslee formalism **142**
D.0.3 Strain balance calculation 142

E EBIC Images **144**

Bibliography **148**

List of Figures

1.1 Standard spectra for AM 0 and AM 1.5 illumination 3
1.2 Band diagram for a p-i-n diode, indicating the electron and hole quasi-Fermi levels (ϕ_n, ϕ_p) and intrinsic potential (ψ). 7
1.3 Light-IV characteristic. The maximum power rectangle indicates the current density (J_{op}) and voltage (V_{op}) for optimum power output. 9
1.4 Schematic band-structure diagrams for a typical high-efficiency p/n GaAs cell(after ref. [1]) and the IC p-i-n GaAs cell. 11
1.5 Quantum efficiency for a typical high-efficiency p/n GaAs cell (after ref. [1], this data has been corrected for a 4.9% shading loss) and the IC p-i-n GaAs cell (QT1228). 12
1.6 Dark-IV for typical MBE and MOVPE high-efficiency p/n GaAs cells (after ref. [2]) and the IC p-i-n GaAs cell (QT1228). The mesa areas are indicated, together with estimates of the V_{oc} assuming $J_{sc} = 280A.m^{-2}$ 13
1.7 Limiting efficiency for single-band gap solar cells as a function of band-gap. 15
1.8 1 sun, AM0 isoefficiency contours for a monolithic tandem cell (after reference [3]). 16
1.9 Band diagram indicating absorption and recombination in the bulk and QW regions of the cell. 17
1.10 a) Quantum efficiency for an AlGaAs/GaAs MQW cell and a homogenous AlGaAs p-i-n control cell. b) Dark-IV densities for several AlGaAs/GaAs cells, together with a line indicating the dark-IV level for a homogenous bulk of equivalent effective band-gap 17

2.1 Graph showing the relationship between band-gap and lattice constant for various semiconductors 20
2.2 External quantum efficiency and dark current density profiles for: 10 MQW strained cell (QT957C), 23 MQW relaxed cell (QT510B) and GaAs control (QT957D). 20
2.3 Typical structure for a p-i-n MQW diode, indicating the barrier thickness t_b, QW thickness t_{qw} and InGaAs fraction x. 21
2.4 Variation in dark current density at 0.5V with excess strain. Experimental points for strained cells are indicated by open circles and relaxed cells by filled circles. The GaAs baseline corresponds to the dark current density at 0.5V for a GaAs p-i-n control. 23

2.5 Contour curves showing the relationship between average strain and quantum well number for a 80/300Å QW/barrier combination as a function of indium fraction. 24
2.6 Quantity of 80Å QW layers that may be incorporated into a p-i-n cell before exceeding the critical thickness of Drigo, et al. [4]. The graph is plotted as a function of indium fraction and barrier width. 25
2.7 AM0 and AM 1.5 J_{sc} curves for strained GaAs/InGaAs 80Å MQW cells with varying barrier width (120-780Å) and QW indium fraction. 27
2.8 Variation in J_{sc} for an 'optimised barrier' structure as a function of well width. This calculation has been performed under AM0 illumination, but the same result holds under AM1.5 illumination. 28

3.1 Schematic device diagrams; a) typical cell structure, b) typical cell structure with AlGaAs etch-stop layers. 31
3.2 Three types of device: a) Contacting through n^+ substrate, b) Top contacting for samples with an undoped (UD) substrate, c) Substrate removal requiring an AlGaAs etch-stop. 33
3.3 Typical IV profiles, showing the effects of shunt and series resistance. 36
3.4 Schematic diagram to show the apparatus used for the quantum efficiency measurement. 38
3.5 Quantum efficiency data and fit using the 'Sol' model. The p, i and n components to the modelled QE are also shown. 39
3.6 Apparatus used for the non-normal incidence reflectivity measurement from pieces of unprocessed but AR coated wafer. 39
3.7 Mono-IV profiles for a good sample with low background doping and a poor sample with high p-type background doping. The inset shows probable field distributions for each sample at 0V. 40
3.8 Mono-IV profile for QT902B at 300K, exciting carriers into the QW. Note the signal falls-off around -0.7V, corresponding to the loss of field across the QW depicted in the insert. 41

4.1 Schematic diagram showing the apparatus used for measuring PL and EL. . 47
4.2 Bias dependence for the PC, PL and non-radiative efficiencies (NR=1-PC-PL); GaAs/InGaAs sample (QT458) at 10K. 47
4.3 Temperature dependent PC, PL and non-radiative efficiencies (NR=1-PC-PL); GaAs/InGaAs sample (QT458) at $V_{\text{app}} = 1.2V$. 48
4.4 Diagram indicating the optical paths for a_{front} in equation 4.7 and a_{back} under the two regimes ($\theta \geq \theta_c$) and ($\theta \leq \theta_c$) in equation 4.8 51
4.5 Data from QT458: a) EL spectra at 300K for biases between 0.88-1.00V. b) Current-voltage characteristics for radiative currents (filled circles), dark currents (open squares) and theoretical line J_{rad} with $\Delta\phi_{\text{f}} = V_{\text{app}}$ 53
4.6 EL spectrum for QT458 at 300K; experimental data for $V_{\text{app}} = 1.000V$ denoted by solid dots, theory with $\Delta\phi_{\text{f}} = 1.000V$ denoted by a chained line and theory with $\Delta\phi_{\text{f}} = 0.977V$ denoted by a solid line. 54
4.7 EL spectrum for the NU972 (AlGaAs/GaAs sample) at 300K; experimental data for $V_{\text{app}} = 1.040V$ denoted by solid dots, theory with $\Delta\phi_{\text{f}} = 1.040V$ denoted by a chained line and theory with $\Delta\phi_{\text{f}} = 1.026V$ denoted by a solid line. 55

4.8 EL spectra for RM1369(c) at 200K and 300K 56
4.9 Quasi-Fermi levels for a forward biased p-i-n bulk diode in the ideal limit and under the influence of strong non-radiative recombination. 57
4.10 Photocurrent curves for RM1369 at 300K, showing the quantum confined stark effect and related stationary points 59
4.11 Experimental setup for room temperature photocurrent measurement: a) photogenerating with the Ti:Sapphire laser only, b) photogenerating with the Ti:Sapphire laser under continous background illumination. 60
4.12 Monochromatic IV curves for QT458 taken with different strengths of ND filter. A typical dark-IV curve is also shown. 61
4.13 Monochromatic IV curves for RM1368 taken at different laser intensities. The red curves indicate data taken with 3000K background illumination and the blue curve indicates the dark-IV profile. The AM 1.5 line shows the approximate level of QW photocurrent under AM 1.5 illumination 62
4.14 Monochromatic IV curves for RM1368 taken at different laser intensities. The red curves indicate data taken with 3000K background illumination and the blue curve indicates the dark-IV profile. The AM 1.5 line shows the approximate level of QW photocurrent under AM 1.5 illumination 63
4.15 Monochromatic IV curves for RM1368 taken at different laser intensities. The red curves indicate data taken with 3000K background illumination and the blue curve indicates the dark-IV profile. The AM 1.5 line shows the approximate level of QW photocurrent under AM 1.5 illumination 64

5.1 Four types of light trapping structure. In each case the rear has a mirror deposited upon it. 67
5.2 Diagram to show the general geometry and terms used in the normal incidence model. 69
5.3 Two possible reflectivity scattering functions and the definition of Δ (inset). 69
5.4 Optical paths for the diffuse reflected light 71
5.5 Measured transmission and reflectivity data for doped and undoped substrates 73
5.6 Calculated values for r_f and a from the doped and undoped substrate data shown in figure 5.5 74
5.7 Reflectivity for an AR coated undoped substrate with a smooth gold mirror and a gold-epoxy mirror. 76
5.8 Diagram to show the extent of the gold-epoxy mirror and the black paint . 77
5.9 Quantum efficiency for QT957C, processed with black paint. 77
5.10 Two geometries representing the limits; 1) radiation into free space with no photon recycling and 2) radiation into a mirrored cavity with total photon recycling 80
5.11 a) Ray diagram and emission geometry for a planar cell with substrate. b) Ray diagram and emission geometry for a planar cavity cell with rear mirror. c) Geometry used to calculate the emission cone surface area. 82
5.12 Quantum efficiency curves for the QT957 series of samples when processed with substrate. The insert represents an enlargement of the MQW region. . 86
5.13 Dark current curves for the QT957 series of samples when processed with substrate. 88

5.14 Mono IV curves for the QT957 series of samples when processed with substrate. 89
5.15 Dark current curves for QT957B and QT957C with and without substrate. 90
5.16 Cavity quantum efficiency for QT957B and QT957C 91
5.17 Possible Fabry-Perot behaviour for QT957B. The upper graph shows the optical intensity as a function of distance along the cavity, the vertical lines from $0.8\mu m$-$1.4\mu m$ indicating the position of the QWs, the dotted lines indicating the extent of the p, i and n region. The lower graph shows the fit to the cavity minima, obtained by varying the phase at the rear (semiconductor/gold mirror) surface. The vertical lines indicate the cavity minima observed in the QE data (see figure 5.16. 93
5.18 Theoretical EL calculation from QE data; QT957B with cavity+mirror and with substrate. 94
5.19 Integrated EL data for the constant current and constant voltage regimes. Note sample names with substrate are QTxxxx and cavity samples are followed by the suffix B='black paint' and c='gold mirror'. 95
5.20 Images from a device on QT957BB, white light illumination and spatial EL. 96

6.1 A modulated structure composed of materials 1 and 2, grown on an arbitrary substrate of lattice parameter a_s 100
6.2 Schematic diagram and band-structure for the GaAs/InGaAs strain balanced cell, with $In_{0.05}GaAs$ virtual substrate. 102
6.3 Dark IV curves for both series of strain-balance samples. (Nominally identical structures are grouped by line colour) 104
6.4 External quantum efficiency for samples RM1270, RM1271, RM1276 and RM1277 in the upper graph, and samples RM1386, RM1389, RM1390 and RM1391 in the lower graph. 106
6.5 Mono-IV curves for both series of strain-balance samples. (Nominally identical structures are grouped by line colour) 107
6.6 XRD rocking curves for samples grouped by type. 108
6.7 Composite TEM image of RM1277, showing strain relaxation between InGaAs/AlGaAs layers and the MQW region in the top left hand corner . . . 109
6.8 TEM image of RM1276, showing strain relaxation between GaAs/InGaAs layers and the MQW region in the top right hand corner. A threading dislocation is noted at the the lower MQW interface. 110
6.9 Plot showing the general trend between dark-current density at 0.5V and average strain. The modulus of the average strain is plotted, so compressively strained samples are shown by filled circles and tensile samples shown by open circles. 112
6.10 Critical thickness limits for variations of a strain-balanced cell (balanced with $t_b = 30$, $x_w = 24\%$) 113
6.11 Schematic diagram of the GaAsP/InGaAs strain-balance structure and 3-period band structure. 115
6.12 XRD rocking curve showing the measured data and the simulation with $GaAs_{0.939}P_{0.061}$ barrier half-width $t_b = 215$Å and 75Å wide $In_{0.17}Ga_{0.83}As$ quantum wells. 117

6.13 Dark IV curves for GaAsP/InGaAs strain-balance MQW cell (QT1227), a relaxed GaAs/InGaAs MQW cell (QT510B), a strained GaAs/InGaAs MQW cell (QT459B) and a GaAs control (QT1228) 118
6.14 External Quantum Efficiency for the GaAsP/InGaAs strain-balanced sample 119
6.15 3000K Light-IV for GaAsP/InGaAs strain-balanced sample and GaAs control. 120
6.16 Projected AM0 and AM1.5 short-circuit current density curves showing the effect of indium and phosphorous composition on the GaAsP/InGaAs strain balanced cell. 122
6.17 Matthews-Blakslee calculation for the critical thickness of GaAsP on GaAs as a function of phosphorous composition. The symbols indicate $GaAsP_x$ total barrier thickness required to balance an 80Å QW composed of $In_{0.1}GaAs$ (circles), $In_{0.2}GaAs$ (triangles) and $In_{0.25}GaAs$ (squares). The existing $GaAsP_{0.06}/InGaAs_{0.17}$ sample is indicated by a plus (+). 123
6.18 AM0 tandem isoefficiency contours (after ref [3]). The dashed curve indicates the monolithic tandem efficiencies accessible using lattice bulk GaInP/InGaAs based tandems. The grey bars indicate the efficiencies available by replacing the lower cell by a strain-balanced MQW cell. 124

B.1 Electric field distribution across p,i and n regions for a cell with p-type background doping 132
B.2 InGaAs/GaAs MQW limiting purity level required to maintain the indicated depleted i-region width. Calculation assumes $V_{bi} = 1.1V$, $V_{app} = 1.0V$ and $N_D = 1 \times 10^{18}/cm^3$ 133

D.1 Critical thicknesses for defect introduction for $In_xGa_{1-x}As$ on GaAs 143

E.1 RM1271, RM1276 and RM1277 EBIC Images 145
E.2 RM1390 and RM1391 EBIC Images 146
E.3 Lecce001 and RM1391 EBIC Images, both taken at 30kV 146
E.4 EBIC image for QT1184, taken at 10kV indicating excellent growth quality 147

List of Tables

1.1 Power densities for various appliances and minimum solar cell efficiency, assuming one side of the appliance is covered with solar cells. 5
1.2 Solar cell parameters calculated from the QE and dark-IV data of figures 1.5 and 1.6. These parameters are calculated under 1 sun AM 1.5 illumination and do not take shading losses into account. 14

2.1 Projected solar cell parameters and efficiencies for 10 MQW strained cell (QT957C), 23 MQW relaxed cell (QT510B) and GaAs control (QT957D). . 21
2.2 Modelling parameters used to generate figures 2.7 and 2.8 26
2.3 Cell parameters for: MQW device corresponding to the optimised structures of figures 2.7, 2.8 and a typical strained MQW dark-IV profile (QT459B). GaAs A corresponds to a bulk GaAs cell (x=0 in figure 2.7) but possessing the MQW dark-IV profile. GaAs B corresponds to a bulk GaAs cell with a dark-IV profile equivalent to the 'GaAs control baseline' shown on figure 2.4. 29

4.1 Characterisation data for single QW samples for which EL measurements were performed. The well position column indicates the location of the QW, with reference to the figure above. 49
4.2 Summary of EL modelling, showing the values of $\Delta\phi_f$ required to fit the QW emission for samples QT458 54
4.3 Temperature dependence of the Quasi-Fermi level suppression required to fit the QW signal from the bias deduced from the barrier signal 57

5.1 Values for r_f, calculated using the normal incidence model with the parameters shown. 75
5.2 Summary of photon recycling expressions in the constant current and constant voltage regimes. Optically thin cells correspond to $\alpha W \ll 1$ while optically thick cells correspond to $\alpha W \gg 1$ 84
5.3 QT957 sample series: brief description and characterisation data 85
5.4 EL_{cavity}/EL_{sub} ratios for QT957B and QT957C, together with the value expected from the radiative theory of section 5.4.1. 96

6.1 Sample summary for GaAs/InGaAs strain-balance series. 103
6.2 Dimensions for RM1276 and RM1277 derived from TEM images together with the width specified on the growth sheet 109
6.3 Barrier dimensions obtained from XRD and TEM measurements. The nominal barrier width was 300Å 110

6.4 Summary of QW indium fraction x, QW thickness t_{qw}, XRD barrier thickness t_b and extracted values for MQW thickness t_{mqw}, average indium fraction $\langle x \rangle$, average strain $\langle f \rangle$. The parameters for a hypothetical 'balanced' cell are also shown 111
6.5 AM 1.5 Projected Efficiency for Strain-Balanced and GaAs Control cells . . 120
6.6 AM 0 Projected Efficiency for Strain-Balanced and GaAs Control cells . . . 121

A.1 Single junction AM 1.5 and AM 0 cell efficiencies 129
A.2 Multi-junction AM 1.5 and AM 0 cell efficiencies 130

Acknowledgements

First I must thank Keith Barnham for offering me the opportunity to work in his group and for guidance, advice and enthusiasm over the last three years. I must also thank Jenny Barnes for being my mentor during my first year, introducing me to the world of spectroscopy, Ti:Sapphire lasers, PCPL and solar cells. Jenny Nelson's work on the models was as invaluable as her theoretical advice, without which I would have remained in a state of dizzy confusion. All three have had the dubious pleasure of proof reading this thesis, for which I am extremely grateful.

Were it not for the samples grown at the EPSRC III-V central facility, this thesis would have been so short as to question its existence. Incalculable thanks are extended to John Roberts and Bob Grey at Sheffield for growing the wafers, Malcolm Pate, Jan Clark and Geoff Hill for processing them and also to John David for help with characterisation. Max Mazzer not only provided extremely useful EBIC images and expert materials advice, but also extremely generous hospitality in Italy. Everything from fine Italian wine to a car for visiting Otranto became possible with Max's assistance. I am also very grateful to Professor Masafumi Yamaguchi for arranging an excellent visit to the Toyota Technical Institute, Japan.

Antonio Martí is gratefully acknowledged for writing a comprehensible paper on photon recycling and assistance with the MQW limit. In the lab, Ian, Paul, James, Ben, Carsten, Laila, Markus and Ruth all have provided advice and assistance as well as coffee and lunch-time banter. James wins the unusual accolade for understanding both Fabry-Perot cavities and Japanese ticket machines. The XRD measurements could not have been performed without the help of Jing Zhang. His tireless assistance often extended into unsociable hours, rewarded only by a pint of Guinness in the Holland Club. Of Guinness, there are many who have assisted but shall remain nameless for risk of libel. Eng-Soon Tok deserves a special mention as a trusty companion on several mountaineering expeditions and subsequent pints of Dark Ale in Grasmere. On the domestic front, Rob van Dalen is accredited for achieving the impossible, finding a decent yet affordable flat within cycling distance of Imperial College (and also for writing up early). Greg O'Sullivan as a fellow cyclist and Sarah Craig for organising parties.

Space does not permit the scores of others who deserve mention, the late John Tyne of Whitley, the congregation at St Peters, Walthamstow (especially Nick, James B. and Nicole). Last, but on no account least, there are my parents and Helena, who have put up with my thesis blues for so long.

Chapter 1

Introduction to Photovoltaics

The conversion of sunlight into other forms of energy forms the basis of life on Earth, penetrating everything from climate to the food-chain. Indeed, modern society retains its ancient reliance upon the discovery of fire for its survival and it is inevitable that the need for energy will increase as a larger population aspires towards ever increasing living standards.

The ecological impact of a greatly increased combustion of fossil fuels is predicted to be catastrophic. If one chooses to neglect such apocalyptic prophesies, estimates of reserves are placed at 50 years for oil and 200 years for coal. Thereafter, the age of abundant energy will be over and the sun will have to be harnessed in a more direct and immediate manner.

1.1 Solar Irradiance

The sun produces a power density of $5.961 \times 10^7 \mathrm{W.m^{-2}}$ at its surface at a temperature of about 6000K. In Earth orbit, a distance of 150×10^6km, the power density reduces to $1353 \pm 21 \mathrm{W.m^{-2}}$ [5] and drops to below $1000 \mathrm{W.m^{-2}}$ at the Earth's surface. The exact figure for the solar power density depends on latitude, season, climatic conditions and albedo of the surroundings. Variations in latitude are accounted for through the air mass (AM) factor, defined as the secant of the angle from the sun to the zenith. Therefore AM0 is appropriate for space, AM1 appropriate at midday on the equator and rising to AM2 at other latitudes and times of day. The scientific standard [6], agreed for terrestrial solar cell calibration is AM 1.5 at $1000 \mathrm{W.m^{-2}}$ at 25°C, an artificial quantity but convenient as an accurate basis for comparison. More realistic values for AM1.5 irradiance are $768 \mathrm{W.m^{-2}}$ direct (no secondary reflection from the ground) and $963 \mathrm{W.m^{-2}}$ global (37° tilt,

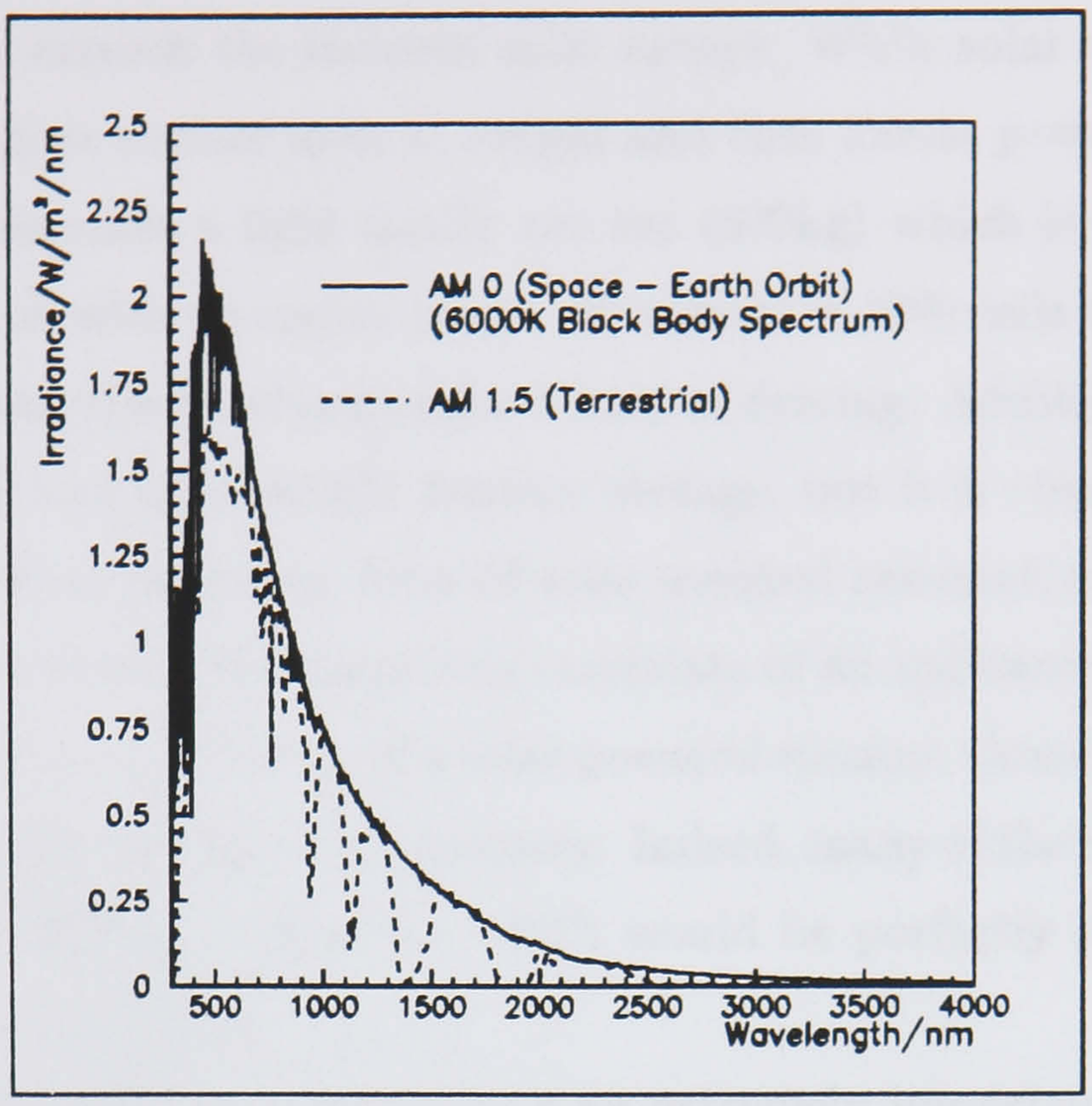

Figure 1.1: Standard spectra for AM 0 and AM 1.5 illumination

incorporating an average ground albedo) [6].

The differences in power density stem from transmission losses in the atmosphere and the spectral content of the solar radiation depends strongly on the AM factor. The graph shown in figure 1.1 shows two standard solar spectra. The AM0 curve corresponds to a black-body temperature of roughly 6000K. The AM 1.5 spectrum follows the same form, but is strongly attenuated over certain bands, corresponding to atmospheric absorption lines.

Whatever air mass condition one considers, the power density of the sun can be considerable on a clear day. To provide a means of comparison, table 1.1 lists the power output of various appliances together with an estimate of the surface area available for photovoltaic cells. A minimum cell efficiency required to satisfy the power consumption over the available area is calculated. It is interesting to see that a modern laptop computer could be sustained using the slightly more efficient (18%) solar cells commercially available today. As the minimum efficiency rises above that attainable using today's most efficient cells (30%) it is necessary to consider battery storage and the final column gives an estimate of the capacity for a 12V battery required to power the appliance for one hour. Battery capacities of 80Ah are attainable without undue bulk making all devices up to the electric car viable for solar power.

The electric car is presented as an example of an application where the required

power output greatly exceeds the incident solar energy. While solar cars do exist, they are optimised for the highest surface area to weight and thus lowest power density. The power output quoted here assumes a light family car car (800kg) which is capable of climbing a 15% gradient at 30mph with no engine losses. If covered in 20% cells the charge/usage ratio falls to 17, i.e. 17 hours of solar charging for 1 hour of driving. Additional problems remain, such as vehicle range and light-weight battery storage, but it is clear that highly efficient solar cells are required to make any form of solar assisted automotive transport viable.

The vacuum cleaner is a surprising candidate of an appliance requiring the highest power density. While the application of a solar powered vacuum cleaner is somewhat absurd, it could operate from a battery basis if necessary. Indeed, many of the household items would be powered from a roof-top installation which would be perfectly capable of powering a vacuum cleaner on a bright day.

The power analysis of households is an extremely important issue, but is limited by economic rather than physical issues. Currently solar modules can be purchased from £2.5/W, which over a 20 year life time span with $100W/m^{-2}$ average irradiance[1] gives 14p per KWh, compared to 10p per KWh from the grid. The situation is complicated by installation costs, long financial payback time and potential economies of scale. A detailed discussion of these issues is not relevant to this thesis and is documented by existing literature [7].

Space applications currently represent the only commercially viable application for high-efficiency solar cells; modules costing around £65/W. The launch cost of a satellite is determined by its weight, so the power density of the solar cells become more important than their component price.

1.2 Photovoltaic Cells and Device Physics

The operation of photovoltaic cells is well described in many general texts [8, 9, 10, 11] and only a brief outline of the principles will be discussed here.

The sun may be considered as a back-body emitter at a temperature of 6000K. If a solar cell was constructed that could behave as a 300K black-body absorber, then the power conversion efficiency would approach that of the Carnot efficiency at 95%. However, photovoltaic devices employ semiconductors as absorbing media and absorption usually takes place by exciting carriers across a band-gap. As a consequence the semiconductor does not behave as a black body absorber, resulting in a lower limiting efficiency.

[1] Climatic average over day and night and all seasons

Appliance	Area/m^2	Power/W	P. Density/$W.m^{-2}$	Eff. /%	Battery/Ah
Palm top	0.015	700×10^{-6}	0.46	0.1	50×10^{-3}
Mobile phone (standby)	0.0088	42×10^{-3}	4.7	0.6	3.5×10^{-3}
Walkman	0.009	0.23	26.7	3.2	20×10^{-3}
Radio & speaker	0.024	1.0	42.7	5.1	83×10^{-3}
Mobile phone (talk)	0.0088	0.63	71.6	8.5	53×10^{-3}
Fridge/Freezer	0.88	68	77.5	9.2	5.6
Laptop Computer	0.10	11	111	13.2	0.94
TV	0.18	55	305	36.1	4.6
Lawn Mower	0.45	350	780	92.5	29
Electric Car	3.5	10×10^3	2900	341	833
Washing Machine	0.49	3300	6700	789	270
Hoover	0.13	1000	7500	885	83

Table 1.1: Power densities for various appliances and minimum solar cell efficiency, assuming one side of the appliance is covered with solar cells.

- Area is taken as the largest single exposed face.
- Power corresponds to the power consumption. In many cases this is an average quantity, for example the fridge/freezer.
- Power density is simply power consumption/area.
- Eff. corresponds to the minimum solar cell efficiency under $844W.m^{-2}$ solar illumination required to satisfy the power consumption over the stated area.
- Battery corresponds to the battery storage capacity required to run the appliance from a 12V battery for one hour. The charge/usage ratio may be computed for a particular solar module by dividing the minimum solar efficiency by the solar module efficiency.

1.2.1 Photocurrent

The photocurrent of a solar cell is determined by the overlap of the absorption characteristics of the solar cell with that of the incident spectrum. Defining $QE(E)$ as the quantum efficiency, $F(E)$ as the incident spectral flux for photon energy E and q the electronic charge, the short-circuit current of a solar cell is given by:

$$J_{sc} = |q| \int_0^\infty QE(E)F(E)dE \tag{1.1}$$

In an ideal solar cell, QE=1 for all photon energies in excess of the band-gap E_g. In reality the QE depends upon the absorption characteristics of the semiconductor and the transport processes within it and is used as a powerful characterisation tool described in section 3.3.2.

1.2.2 Dark Current

The dark current of a solar cell represents the recombination inherent to a semiconductor diode. At zero bias in the dark, the only generation and recombination processes are thermal and balance to yield no net current flow.

Once a forward bias is applied, carriers are injected into the diode junction and the excess carrier concentrations are characterised by two potentials or quasi-Fermi levels ϕ_n and ϕ_p for electrons and holes respectively. Under ideal conditions, the separation of the quasi-Fermi levels is constant and equals the applied bias V_{app}.

The quasi-Fermi levels are shown in figure 1.2 and defined by the electron and hole carrier densities, n and p and the intrinsic level ψ.

$$n = n_i e^{q(\psi-\phi_n)/kT} \tag{1.2}$$

$$p = n_i e^{q(\phi_p-\psi)/kT} \tag{1.3}$$

The potential V_{app} induces radiative recombination, described by the Planck laws of radiation and in ideal conditions, the electrical current drawn into the cell equates to the radiative loss from the cell.

The rate of radiative recombination is given by U_{rad} where B is the radiative recombination coefficient:

$$U_{rad} = Bnp \tag{1.4}$$

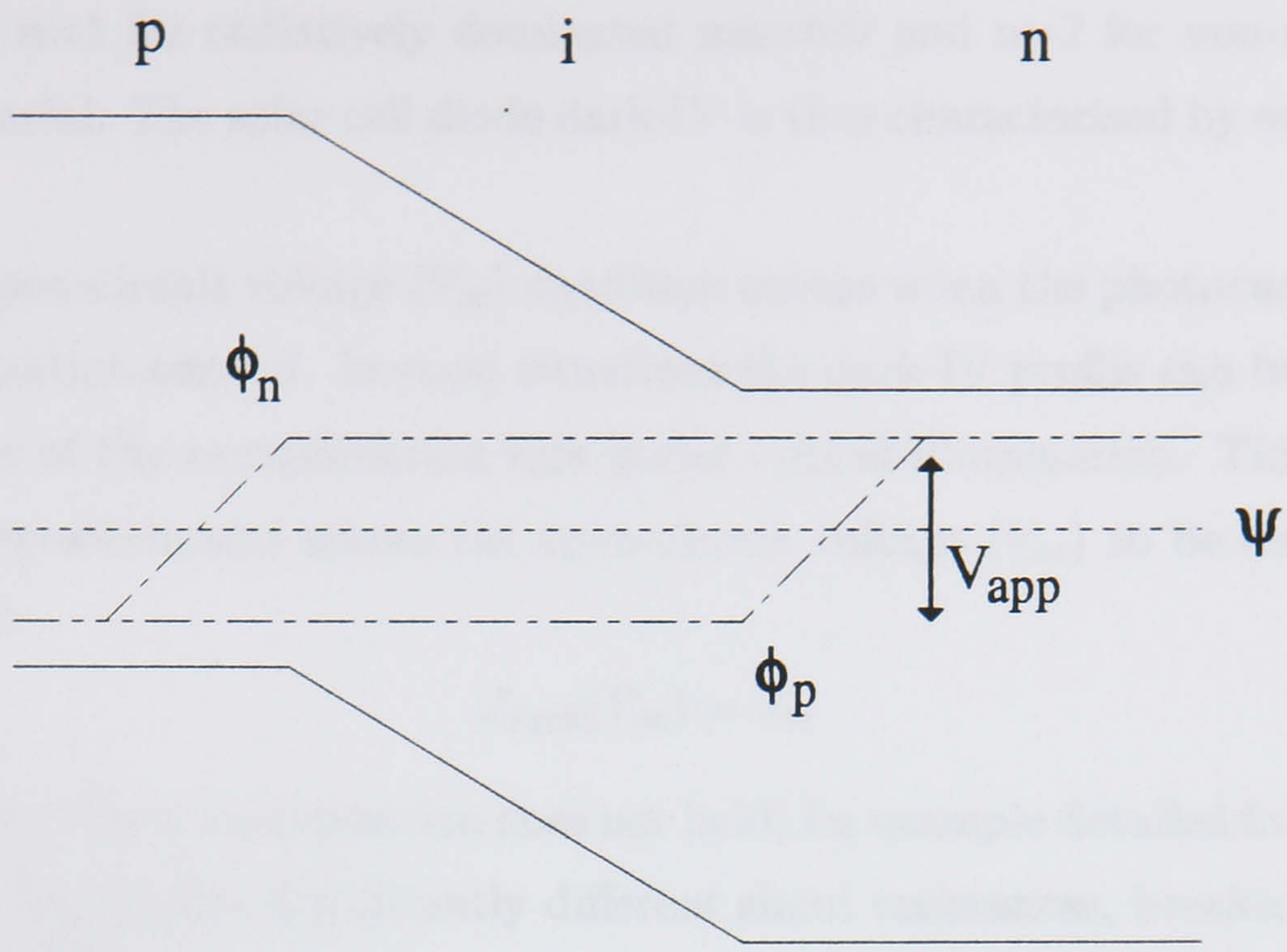

Figure 1.2: Band diagram for a p-i-n diode, indicating the electron and hole quasi-Fermi levels (ϕ_n, ϕ_p) and intrinsic potential (ψ).

which gives rise to the Shockley equation for radiative processes [12];

$$J_{rad}(V) = J_0(e^{qV/kT} - 1) \tag{1.5}$$

The presence of impurity states in the band-gap gives rise to further modes of non-radiative recombination. The recombination processes are described by Shockley-Hall-Read statistics and the recombination rate is given by a more complex function U_{SHR} in equation 1.6, where τ_n and τ_p are the electron and hole lifetimes and n_t and p_t are the equilibrium population of occupied electron and hole trap states,

$$U_{SHR} = \frac{np - n_i^2}{\tau_n(p + p_t) + \tau_p(n + n_t)} \tag{1.6}$$

The SHR recombination statistics gives the following current voltage relationship [13]:

$$J_{SHR}(V) = \frac{qn_iW}{\sqrt{\tau_n\tau_p}}(e^{qV/2kT} - 1) \tag{1.7}$$

The equations 1.5 and 1.7 may be summarised by the empirical current voltage relationship:

$$J_{dark}(V) = J_0e^{qV/nkT} \tag{1.8}$$

where n=1 for radiatively dominated material and n=2 for non-radiative (SHR) dominated material. The solar cell diode dark-IV is thus characterised by equation 1.8 with $1 < n < 2$.

The open-circuit voltage (V_{oc}) condition occurs when the photocurrent is matched by the recombination current. In most situations the dark-IV profile can be assumed to be a good estimate of the recombination rate under optical illumination. This assumption is known as superposition and allows the open-circuit voltage (V_{oc}) to be deduced from the J_{sc} by virtue of:

$$J_{dark}(V_{oc}) = J_{sc} \tag{1.9}$$

Instances do arise where superposition does not hold; for example detailed fitting of dark and light-IV curves has yielded significantly different shunt resistances, breaking the condition of superposition [14].

Throughout this thesis, superposition is assumed to hold and section 4.7 describes an experiment confirming superposition for QW photocurrent to beyond V_{oc}. Superposition provides a convenient means of estimating the V_{oc} of a solar cell simply from its quantum efficiency and dark-IV profile. J_{sc} may be calculated for any illumination spectra by virtue of equation 1.1 and an experimental dark-IV may then be used to compute the V_{oc} through the superposition equation 1.9.

1.2.3 Power output and fill factor

The condition for maximum power output occurs at some voltage and current below that of the V_{oc} and J_{sc}. Consulting figure 1.3, it is convenient to define the optimum operating voltage V_{op} and current J_{op}, by

$$P_{max} = V_{op} J_{op} \tag{1.10}$$

With knowledge of the dark-IV profile and J_{sc}, P_{max} may be deduced under the assumption of superposition.

The fill-factor (FF) is defined by equation 1.11 and gives a measure of the matching between the maximum power rectangle and light-IV curve. The FF represents important parameters, hidden by the J_{sc} and V_{oc}. For example series resistance will not become apparent from figures of the J_{sc} and V_{oc}, but the FF will show a marked loss. Diode ideality plays a role in the FF, essentially determining the gradient of the upwards rise to V_{oc}.

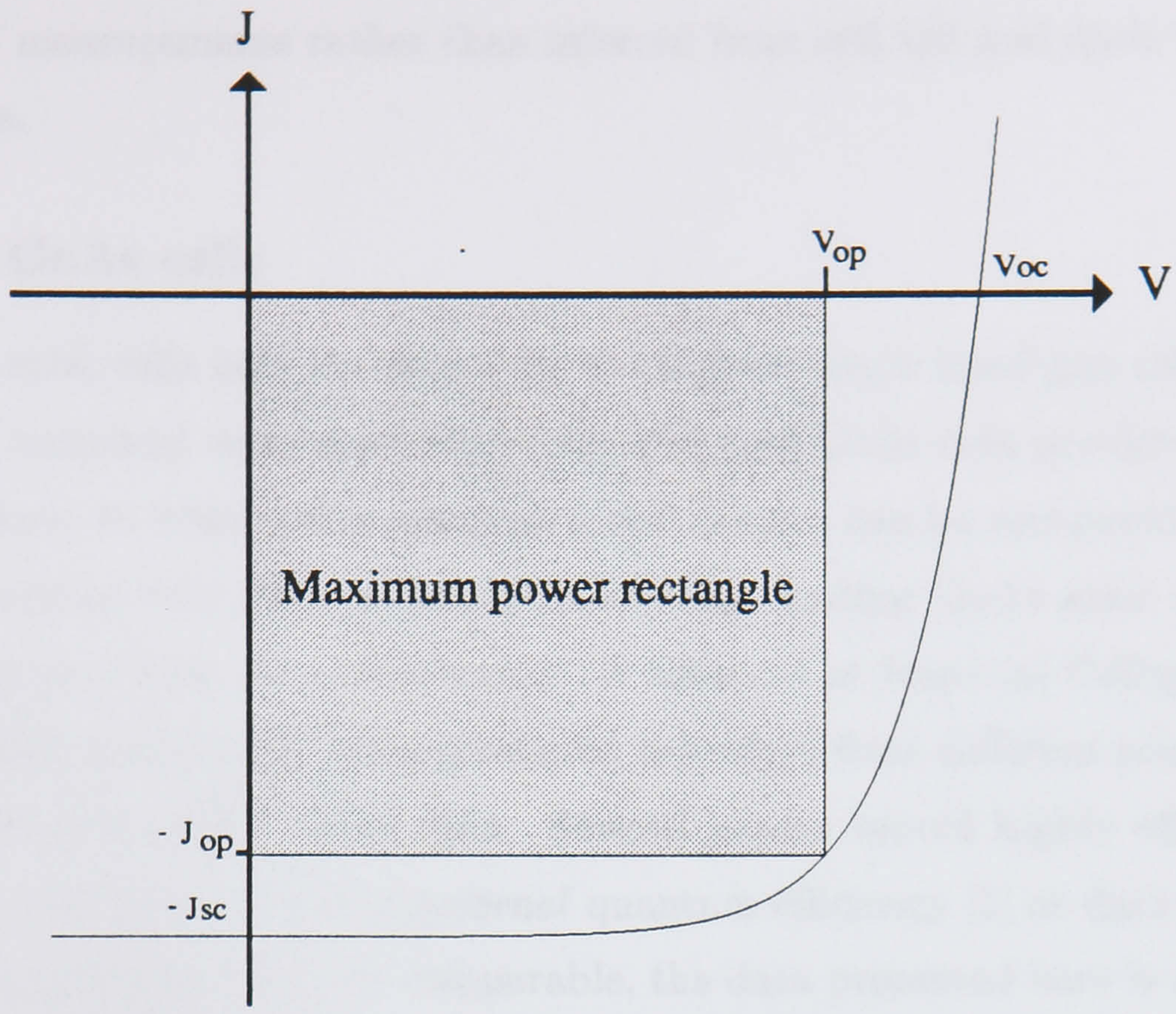

Figure 1.3: Light-IV characteristic. The maximum power rectangle indicates the current density (J_{op}) and voltage (V_{op}) for optimum power output.

$$FF = \frac{V_{op} J_{op}}{V_{oc} J_{sc}} \tag{1.11}$$

Finally the cell efficiency (ρ) may be determined from the J_{sc}, V_{oc}, FF and incident power density P_{in}:

$$\eta = \frac{V_{oc} J_{sc} FF}{P_{in}} \tag{1.12}$$

Using this formalism, a computer program was written to estimate the efficiency of solar cells, simply from experimental measurements of the quantum efficiency and dark-IV profile. The limitations of this approach have been discussed with respect to the validity of superposition, but to date no serious discrepancy has emerged from comparison with cells whose efficiency have been measured experimentally at the NREL[2] calibration facility. The efficiency projecting model used throughout this thesis performs a trapezium integration upon the QE data, interpolates the dark-IV data and solves the FF numerically. Overall, the fractional error of this technique is 5%.

The efficiencies and solar cell parameters for various III-V cells are listed in appendix A and provide a useful source for comparison. The data stems directly from cali-

[2]National Renewable Energy Laboratory, Cole Boulevard, Golden, Colorado, USA

brated light-IV measurements rather than inferred from cell QE and dark-IV properties as described above.

1.2.4 Bulk GaAs cells

GaAs solar cells hold the record for the highest single band-gap cell efficiency [15]. The record has remained unchanged since 1990 and such GaAs cells provide a useful benchmark of excellence, to which other competing cell designs can be compared.

This section will discuss data published by leading GaAs solar cell groups and compare it with the GaAs p-i-n characteristics achieved at Imperial College. It should be noted that the QE and dark-IV data presented here stem from different sources on account of the incompleteness of published data. Several papers report highly efficient (24-25%) p/n GaAs cells, but either omit the *external* quantum efficiency [2] or dark-IV [1] data. As the efficiencies of all these cells are comparable, the data presented here is a representative selection of what can be achieved and provides a testing ground for the cell efficiency model described in the previous section.

Cell design

The GaAs cell design is depicted by the band-structure diagrams of figure 1.4, together with the equivalent diagram for the Imperial College (IC) p-i-n GaAs control cell. Both cells possess a minority electron reflector but only the p/n cell possesses a minority hole reflector and the significance of this is discussed later. The composition of these minority carrier reflector layers is usually AlGaAs, although InGaP is reported to have a lower surface recombination velocity [16] and yields comparable n/p GaAs cell performance [17]

The p/n cells were processed into 0.5 × 0.5cm mesas, described in reference [2] and the IC p-i-n cells processed into 1mm diameter mesas using the processing described in section 3.2.

Quantum Efficiency

The external QE is shown in figure 1.5 and shows how the IC p-i-n cell compares with a 24.8% efficient p/n cell [1]. The p/n cell possesses superior QE for wavelengths under 550nm, resulting in the p-i-n cell generating 90% of the p/n current. The short wavelength degradation is likely to be due to a superior AR coating and transport in the p-region. The p-i-n cell could be optimised in this respect, the double layer ZnS/MgF_2 AR coating is

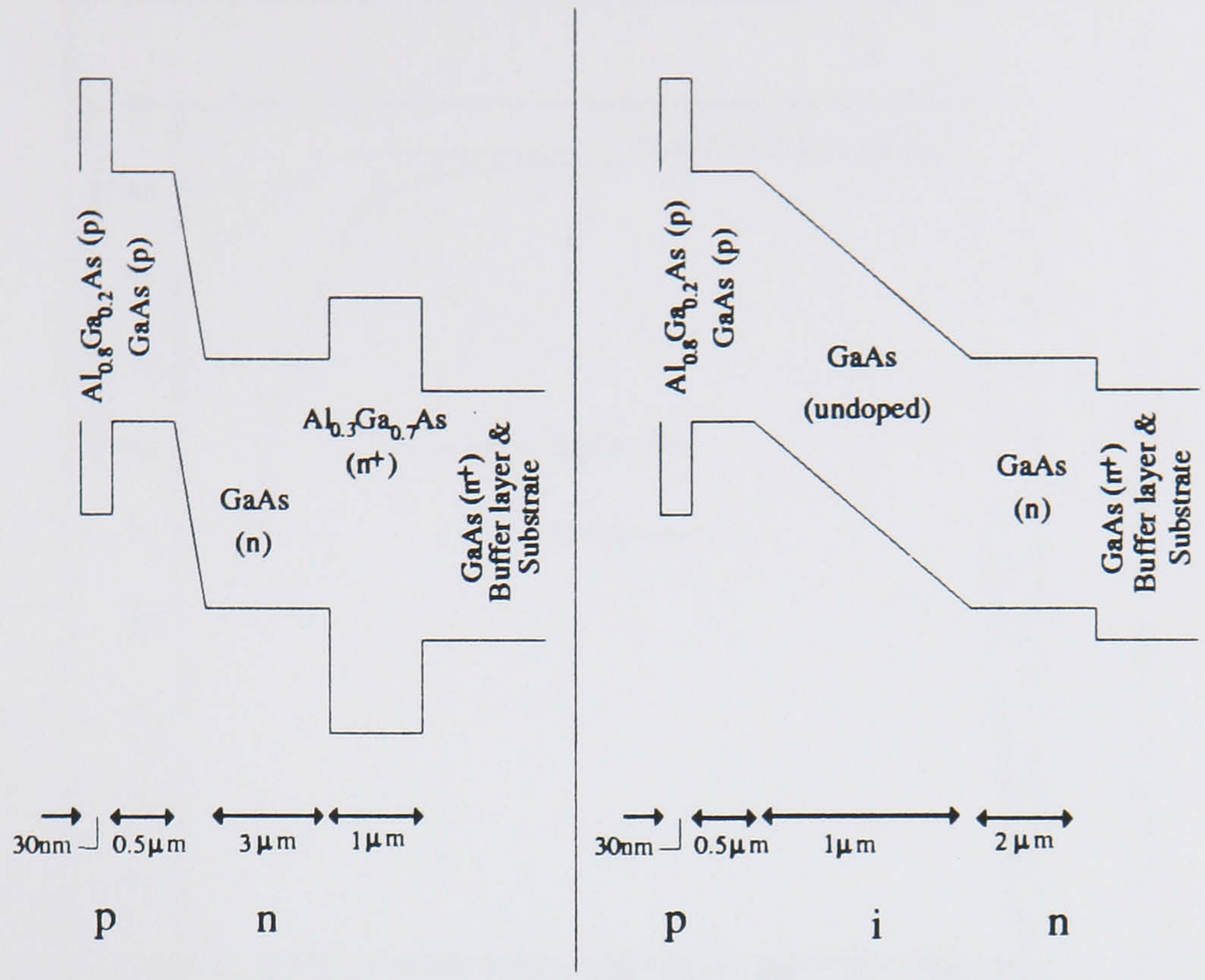

Figure 1.4: Schematic band-structure diagrams for a typical high-efficiency p/n GaAs cell(after ref. [1]) and the IC p-i-n GaAs cell.

likely to perform better than the single SiN AR coat employed for the p-i-n cell. Further, the p-i-n cell would benefit from passivation schemes discussed in the dark-IV section.

Dark-IV

The dark current densities are shown in figure 1.6, showing data from a MOVPE Spire corporation cell and a MBE Purdue University cell [1], together with the MOVPE IC p-i-n GaAs cell. The growth processes have been specified because the dark-IV profile has been noted to be lower and more consistent under MOVPE conditions [2]; an issue which is discussed briefly in section 3.1. The Spire MOVPE and Purdue MBE p/n dark-IV indicate exceptional growth quality, showing a clear transition between SHR dominated recombination (n=2) and radiative recombination (n=1). The IC MOVPE p-i-n is typical of cells grown as bulk GaAs controls. Such p-i-n control cells have shown little variation with i-region width, and are used as the baseline for comparison throughout this thesis.

The dark-IV level is considerably higher for the p-i-n cell and it does not show such a marked transition from n=2 to n=1 behaviour. The reasons for this is likely to be linked to the short wavelength degradation in the QE and is worthy of some discussion.

Referring to equation 1.7, the SHR (n=2) current is directly proportional to W, the width of the depletion region. For the p-i-n cell, the depletion region is approximated by the width of the i-region at $\approx 1\mu$m. The width of the p/n depletion region is determined

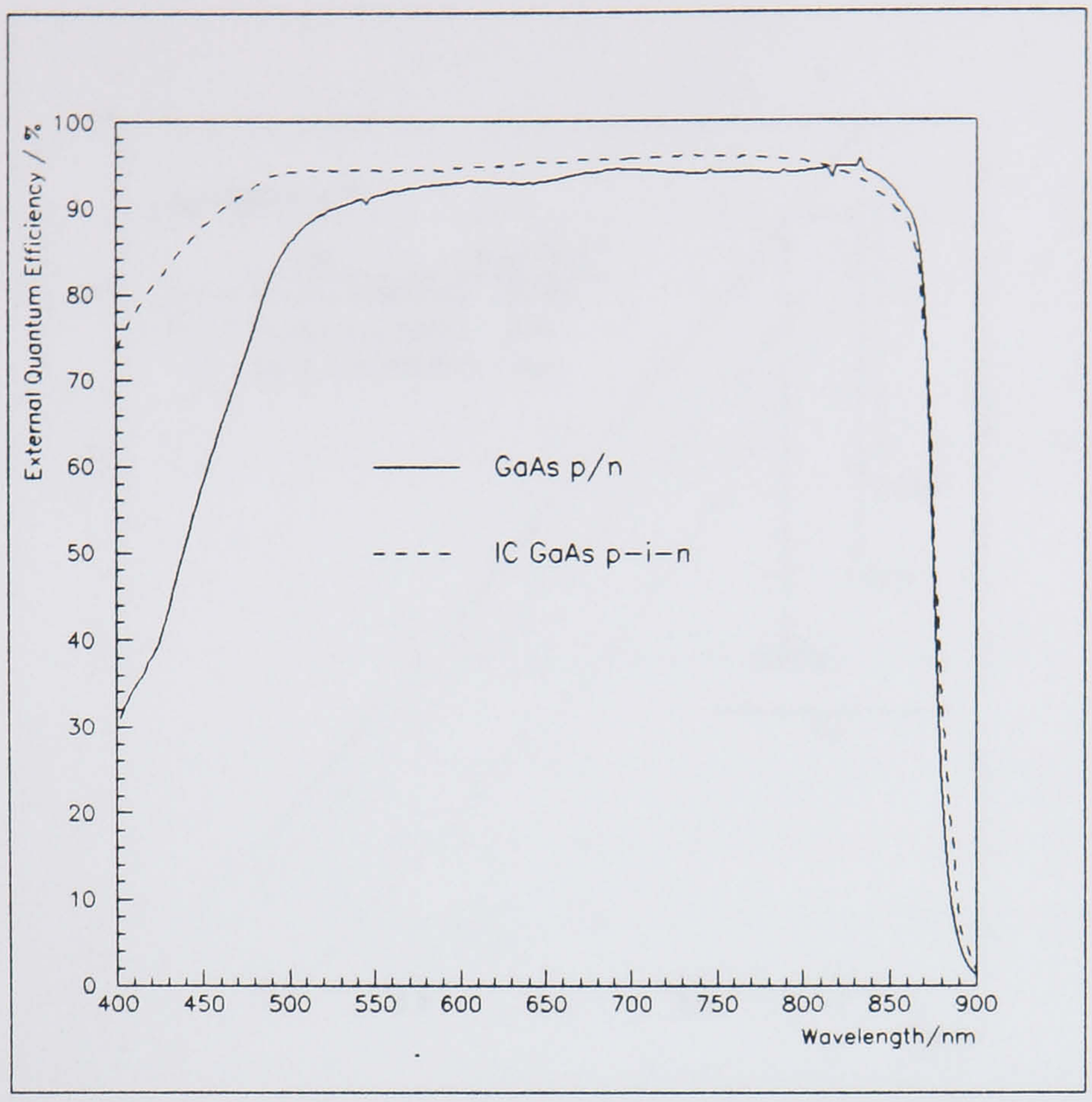

Figure 1.5: Quantum efficiency for a typical high-efficiency p/n GaAs cell (after ref. [1], this data has been corrected for a 4.9% shading loss) and the IC p-i-n GaAs cell (QT1228).

largely by the p and n doping densities [8], giving a depletion width of ≈100nm. Thus an increase in n=2 recombination for the p-i-n cell over the p/n cell is expected, simply from standard SHR recombination theory.

Perimeter recombination will also influence the n=2 contribution. Unlike the p/n cells reported here, the p-i-n cell is processed as a 1mm mesa test diode, which although convenient for optical characterisation, is not an optimal design for minimising recombination due to perimeter effects. The influence of perimeter recombination has been correlated to the current contribution, concluding that the n=1 current scales with cell area while the n=2 current scales with cell perimeter [18]. Indeed, the effects of perimeter recombination are so great that even 'large-area' $4 \times 4\text{cm}^2$ cells are expected to show strong perimeter recombination.

It is likely that perimeter recombination dominates the effects due to differences in i-region width, explaining the unexpected reproducibility of the p-i-n dark-IV profile. The cell areas are quoted in figure 1.6 and the perimeter to area ratio P/A is 4cm^{-1} for the p-i-n cell and 0.8cm^{-1} for the p/n cells.

To conclude, the p-i-n bulk GaAs cells provide a reproducible baseline for comparing new designs, although they do not exhibit the exceptional performance of 24% cells.

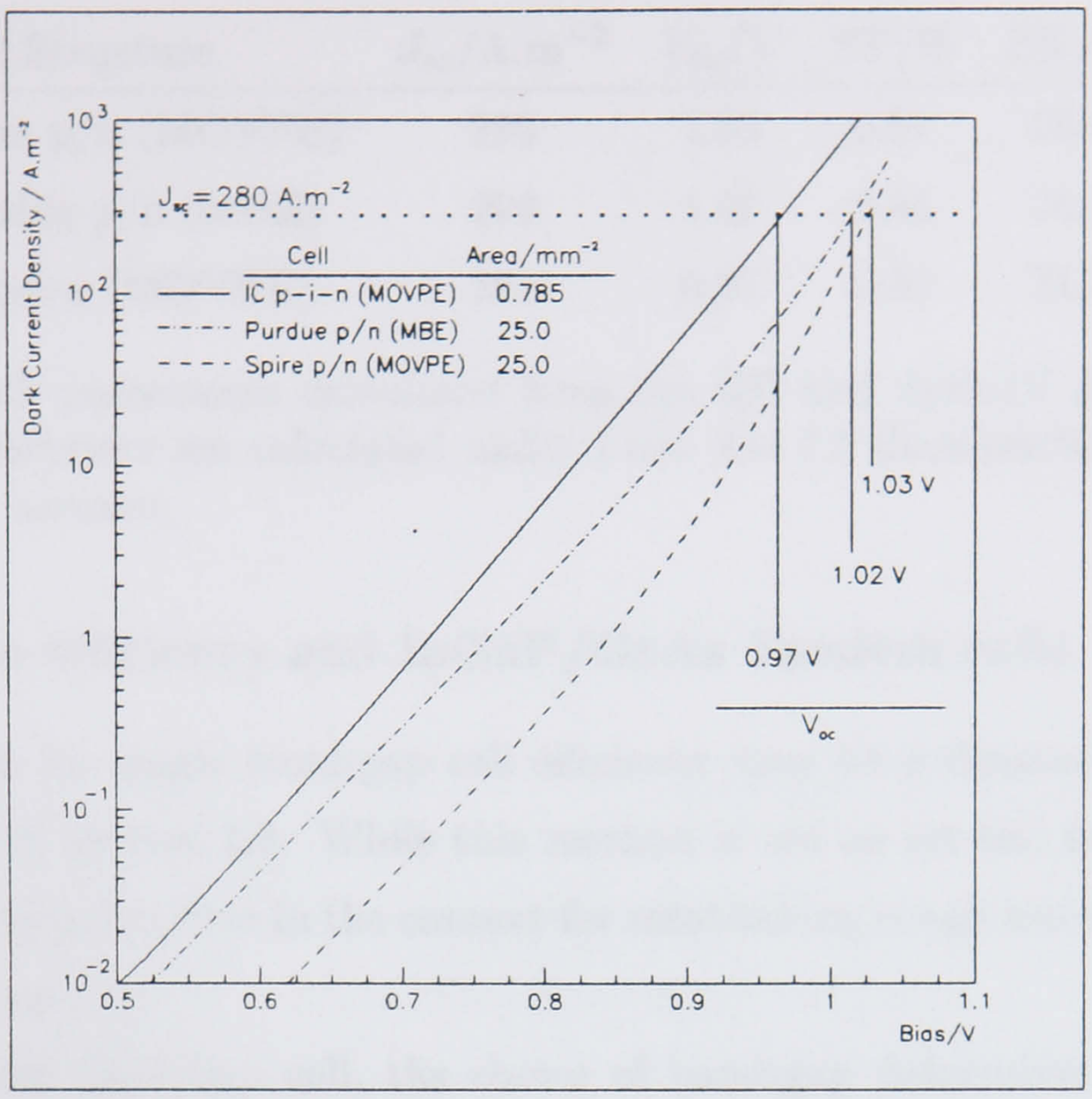

Figure 1.6: Dark-IV for typical MBE and MOVPE high-efficiency p/n GaAs cells (after ref. [2]) and the IC p-i-n GaAs cell (QT1228). The mesa areas are indicated, together with estimates of the V_{oc} assuming $J_{sc} = 280 A.m^{-2}$

The p-i-n cells are likely to benefit from a better perimeter/area ratio and passivating techniques described by [18, 19] and references therein. Further improvement in the recombination profile may be possible by employing a minority hole reflector as in the p/n cell.

Cell Performance

The QE and dark-IV data of figures 1.5 and 1.6 were integrated and interpolated by the efficiency projecting model described in section 1.2.3 and the results are shown in table 1.2.

The IC p-i-n cell is clearly not as efficient as the world's best GaAs p/n cells and the reasons for this have already been discussed in the quantum efficiency and dark-IV sections. As the p-i-n result has been found to be entirely reproducible, it will be used as a benchmark for the other cells discussed in this thesis. Once an alternative (MQW) design is shown to surpass the p-i-n cell in terms of efficiency, then efforts should be made to improve the overall efficiency, through the techniques discussed above.

Cell Structure	J_{sc}/A.m^{-2}	V_{oc}/V	FF/%	Eff./%
Spire p/n (MOVPE)	296	1.03	0.87	26.8
Purdue p/n (MBE)	296	1.02	0.84	25.2
IC p-i-n (MOVPE)	268	0.97	0.82	21.3

Table 1.2: Solar cell parameters calculated from the QE and dark-IV data of figures 1.5 and 1.6. These parameters are calculated under 1 sun AM 1.5 illumination and do not take shading losses into account.

1.2.5 Limits to efficiency and InGaP/GaAs Tandem cells

The limits for single band-gap cell efficiency may be estimated using the device analysis presented in section 1.2. While this method is not as general as detailed-balance approaches [20], it is instructive in the context for establishing rough estimates to the limits of solar cell efficiency.

For a single band-gap cell, the choice of band-gap determines the J_{sc} but also influences the V_{oc} via equations 1.9 and 1.5, in ideal (radiatively dominated) material. The interplay between the J_{sc} and V_{oc} determines the optimum band-gap for a solar cell.

The graph shown in figure 1.7 depicts a limiting efficiency curve for single band-gap cells. The calculation was performed using the efficiency projecting methodology, described in section 1.2.3. The quantum efficiency was assumed to be unity for all wavelengths less than the band-gap ($QE(\lambda) = 1, \lambda < 1240/Eg$ and $QE(\lambda) = 0, \lambda > 1240/Eg$. Realistic diode parameters [9] were used to estimate the ideal (n=1) dark-current characteristic from equation 1.5.

The experimental efficiencies for several cells are shown and with the exception of the dye sensitised cell [21], it may be concluded that most single band-gap cells are close to their efficiency limit. Concentrator cells for solar illumination greater than 1 sun, afford higher conversion efficiencies and possess lower optimum band-gaps [22]. Extremely good concentrator cells exist and are limited by series resistance and heat dissipation, rather than semiconductor deficiencies.

To achieve experimental conversion efficiencies in excess of 30%, it is necessary to employ multijunction cell designs. The advantage of a multijunction cell is that the solar spectrum is collected by two or more semiconductor band-gaps, reducing the losses due to carriers thermalising to the band-edge.

Tandem cells contain two band-gaps and may can be configured in slightly different ways. Currently the leading tandem cells are monolithic GaInP/GaAs two terminal

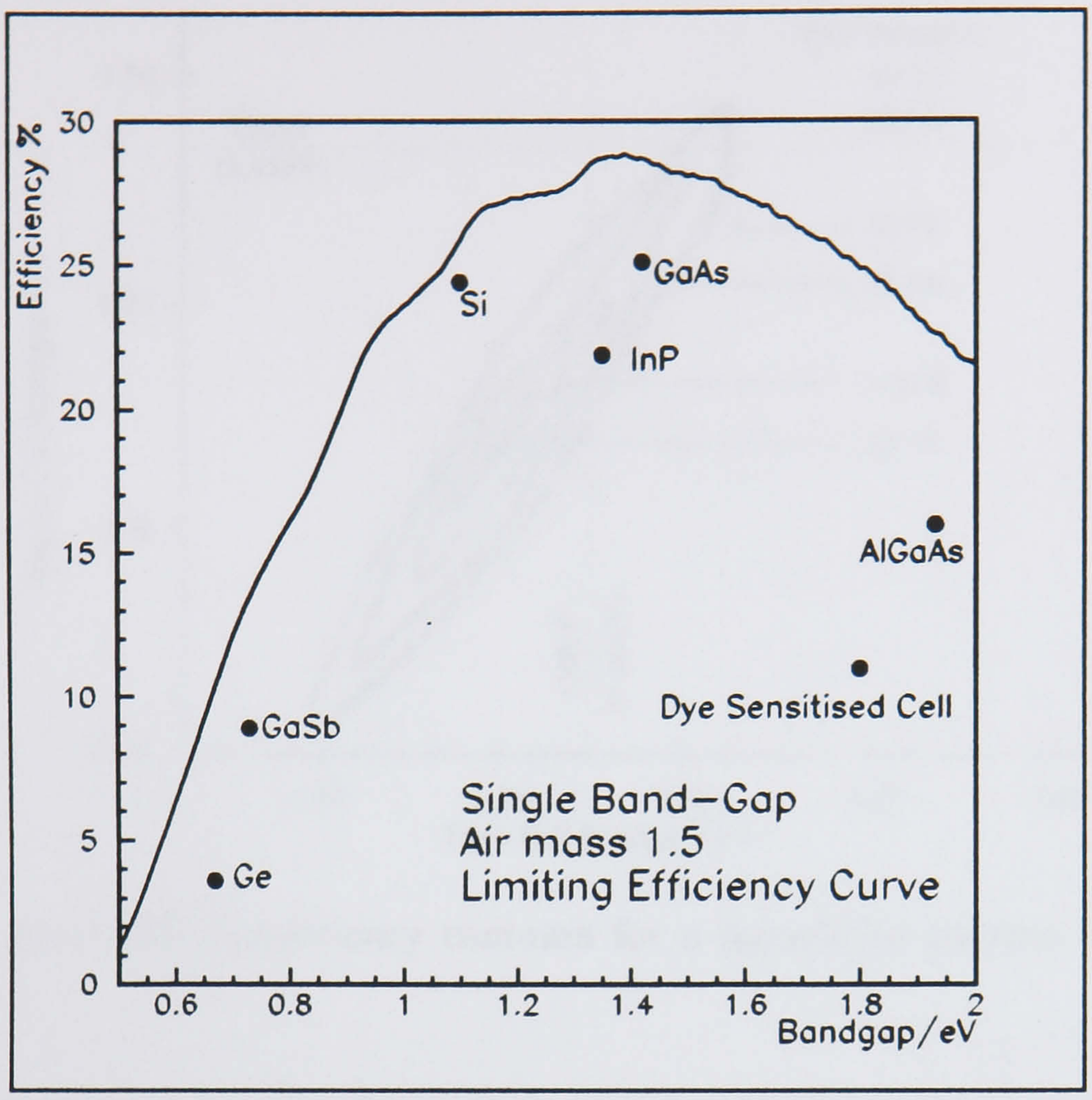

Figure 1.7: Limiting efficiency for single-band gap solar cells as a function of band-gap.

devices [23, 24]. The upper and lower cells are connected in series via a tunnel junction and require that the currents be matched in the upper and lower cells. The current matching condition places a strict tolerance upon the optimum band-gap combinations [3]. Figure 1.8 shows AM 0 isoefficiency curves for various upper and lower band-gap combinations, together with the GaInP/GaAs band-gap combination.

It is clear from the isoefficiency curves of figure 1.8 that the GaInP/GaAs tandem cell is far from optimum in terms of its conversion efficiency. The solar cell parameters for the leading tandem cells are reproduced in appendix A, but briefly the best experimental AM0 and AM1.5 conversion efficiencies are 26.9% and 30.3% respectively [24].

The GaInP/GaAs tandem cells are also close to their limiting conversion efficiencies and research is now being directed towards making a third junction around 1eV and a fourth in Ge at 0.66eV. The 1eV junction is being attempted in a quaternary alloy of InGaAsN but with limited success [25]. Other approaches include using materials which are not lattice matched to GaAs, and good 1eV cells have been achieved with ternary InGaAs alloys [26].

The pursuit of an optimised tandem cell has largely been abandoned, there being no lattice-matched, bulk material with the required band-gap. However, it has been pointed

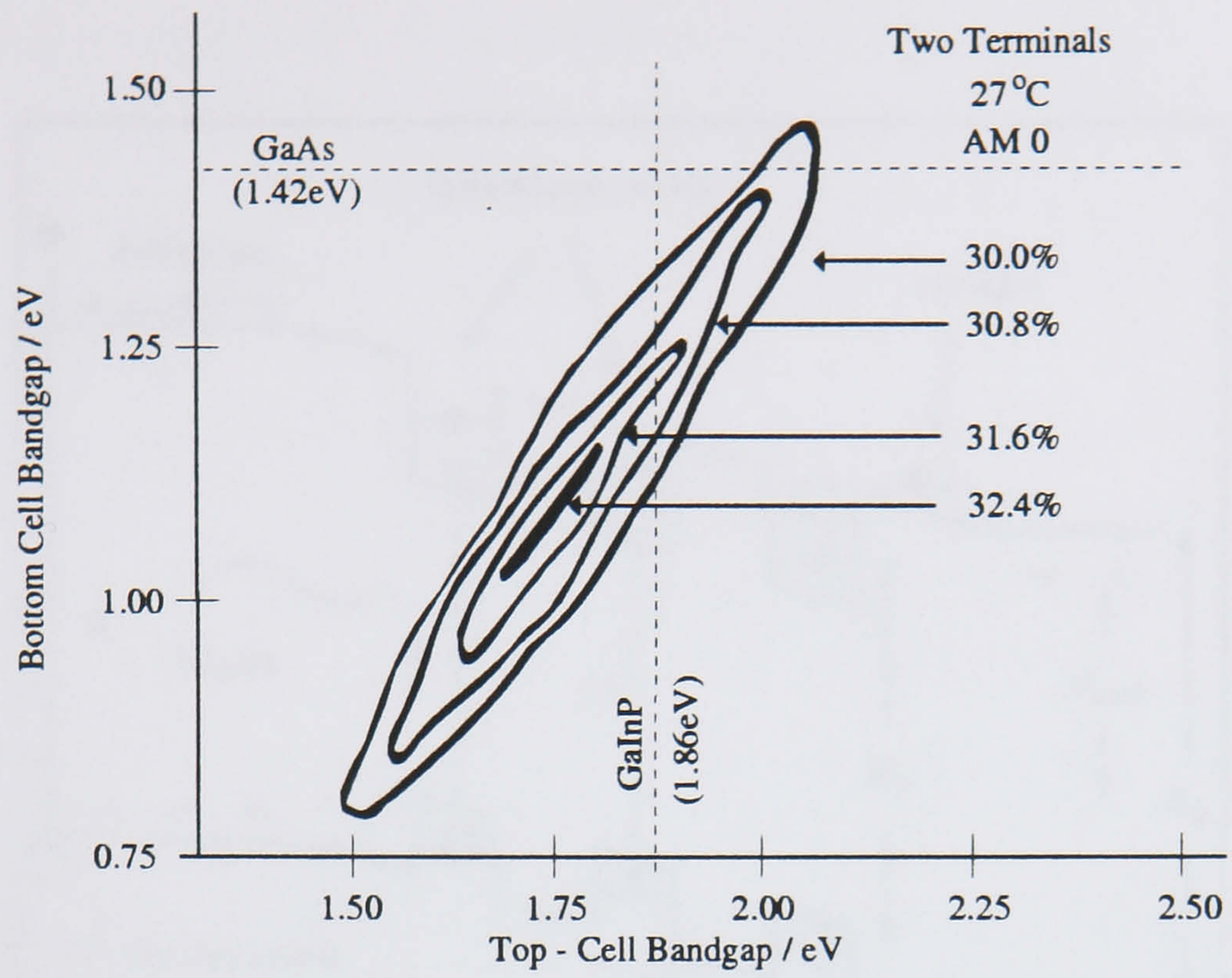

Figure 1.8: 1 sun, AM0 isoefficiency contours for a monolithic tandem cell (after reference [3]).

out that the InGaP/GaAs tandem cell could be improved by lowering the GaAs band-gap via MQW techniques [27]. Further, the strain-balance techniques of chapter 6 and specifically section 6.3, outline a scheme by which both the upper and lower band-gap cells may be freed from some of the restrictions inherent to bulk material. Using these techniques it may be possible to access the optimum AM 0 efficiency depicted in figure 1.8.

1.2.6 MQW solar cells

The quantum well solar cell (QWSC) was proposed as a novel structure for high efficiency solar power conversion [28]. The design is shown in the schematic band structure of figure 1.9 The QW layers provide discrete energy levels in the band-gap, by which the absorption of the cell may be extended. Extensive reviews of QWSCs may be found in existing literature [29, 30], so a brief survey of existing work will be presented here, concentrating on the aspects most relevant to this thesis.

The primary function of the QW layers is to extend the absorption of the host p-i-n cell. Figure 1.10 shows a typical quantum efficiency profile for a homogenous AlGaAs p-i-n cell together with the profile for an AlGaAs/GaAs MQW cell. While neither cell indicates as good quality current collection as the GaAs cells of figure 1.5, the MQW principle of extended absorption is evident [31].

The recombination processes in a MQW cell are somewhat more complicated than

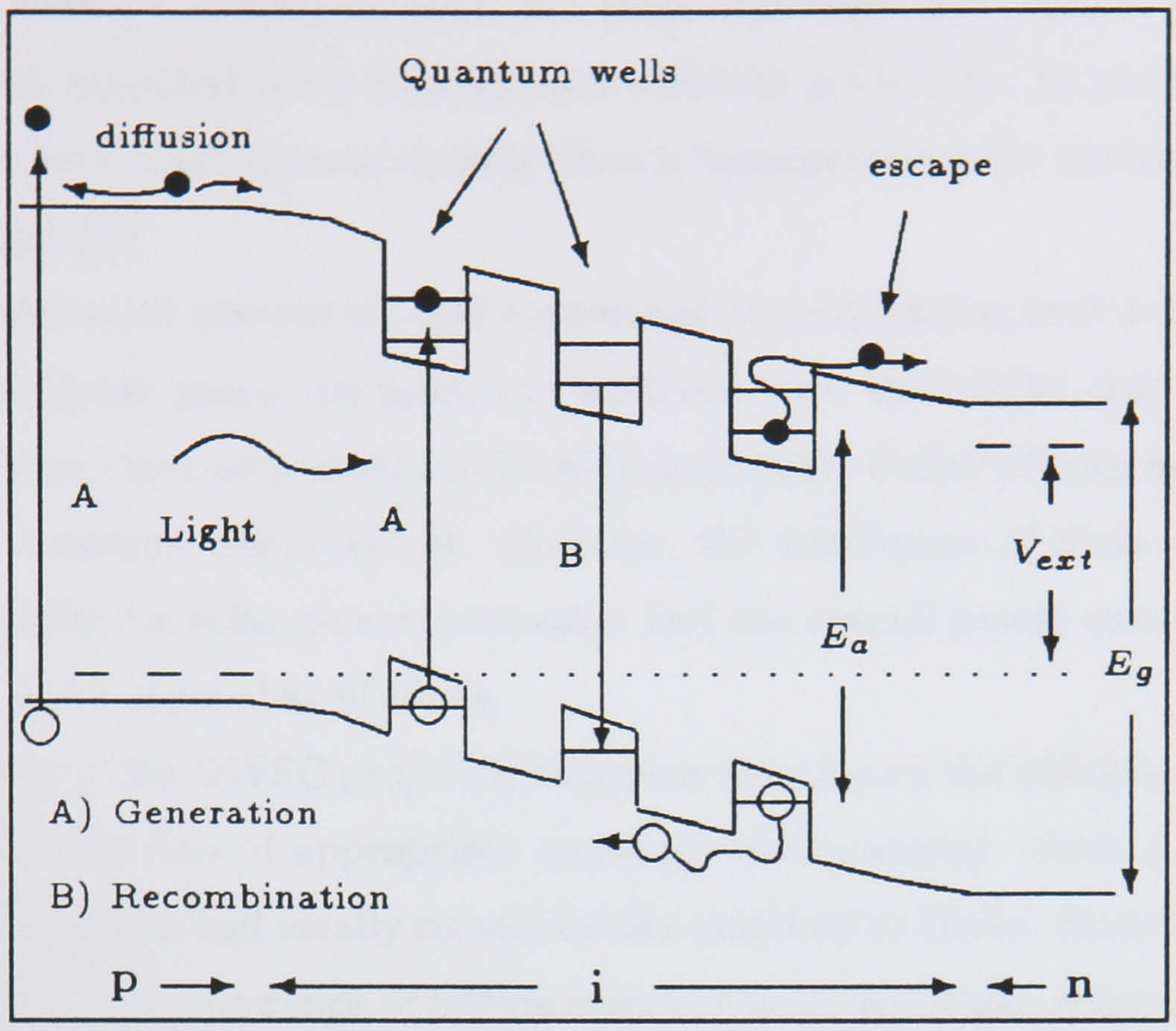

Figure 1.9: Band diagram indicating absorption and recombination in the bulk and QW regions of the cell.

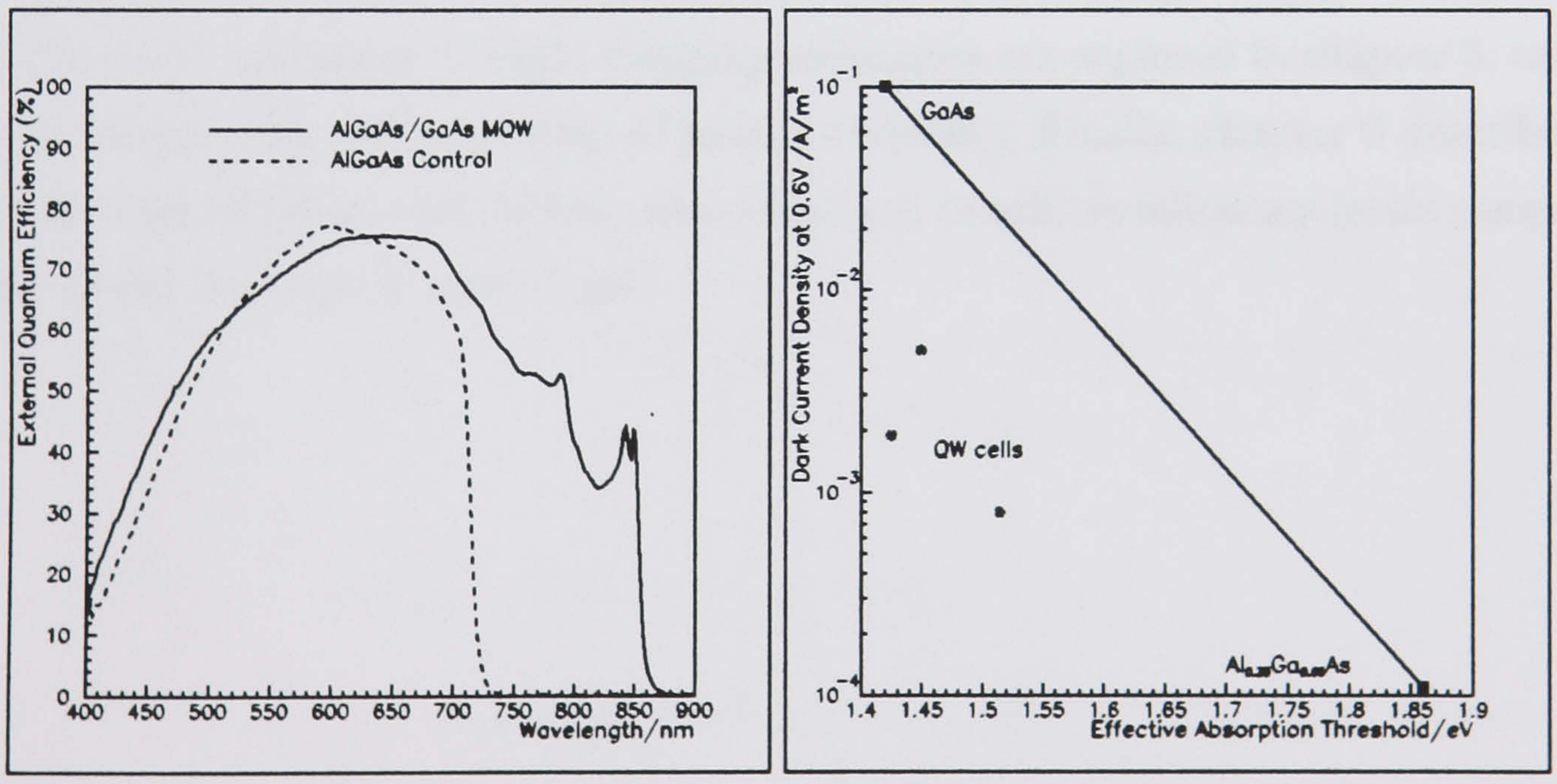

Figure 1.10: a) Quantum efficiency for an AlGaAs/GaAs MQW cell and a homogenous AlGaAs p-i-n control cell. b) Dark-IV densities for several AlGaAs/GaAs cells, together with a line indicating the dark-IV level for a homogenous bulk of equivalent effective band-gap

in a p-i-n cell and a detailed discussion of this matter is left to chapter 4. However, figure 1.10 shows the dark-IV density at 0.6V for three AlGaAs/GaAs MQW cells and a line showing the level expected for a homogenous AlGaAs p-i-n cell. In each case, the QW cells possessed a lower dark current density than a homogenous p-i-n control with the same effective band-gap [32].

With increased absorption and suppressed recombination over a homogenous p-i-n control cell, a higher power conversion is achieved with the MQW cell. To date, these characteristics have been demonstrated in AlGaAs/GaAs, GaInP/GaAs and InP/InGaAs lattice matched material combinations. However, the band-gaps of these material combinations are ill suited for solar power conversion and the overall power conversion efficiency for such cells is lower than that of GaAs.

The goal of the QWSC project is therefore to enhance the efficiency of a GaAs cell through the incorporation of appropriate quantum well material. Such a material would possess a lower band-gap and ideally remain lattice matched to GaAs. However, as discussed in the following chapter, the range of lattice-matched lower band-gap materials is extremely limited, requiring strained layer techniques to be employed.

The work presented in this thesis describes how a GaAs/InGaAs based MQW solar cell could be engineered to outperform a GaAs p-i-n solar cell. Chapter 2 discusses the extent to which the dark-IV allows for an efficiency enhancement in GaAs/InGaAs MQW structures. Evidence for a fundamental efficiency advantage in MQW cells over bulk cells is discussed in chapter 4. Light trapping techniques are explored in chapter 5, together with a discussion over the possibility of photon-recycling. Finally, chapter 6 describes how strain-balanced MQW structures have been employed to achieve efficiency levels comparable to those of the GaAs p-i-n control cell.

Chapter 2

Survey of GaAs/InGaAs QWSC

A property of GaAs is that while it may be grown lattice matched to higher band-gap materials, such as AlGaAs and InGaP there are no lattice matched ternary alloys with lower band-gaps. Figure 2.1 depicts the relationship between the lattice constant and band-gap for various elements and semiconductor alloys. Notably Ge is almost lattice matched to GaAs with a band-gap of 0.66eV at 300K, providing a rigid and economic substrate material that can be exploited as the lowest band-gap component in multi-junction cells [33, 34].

Recently a quaternary alloy of GaInNAs has been grown lattice matched to GaAs with a band-gap of 1eV, but as yet, the diffusion lengths of this material make it unsuitable for photovoltaic cells [25]. GaInNAs has been grown in a quantum well structure [35], but the type-II band-offsets lead to unbound hole states and the material is thus ill suited for QWSC applications. The only lower band-gap alternatives are strained materials and in particular strained InGaAs forming the well material in a GaAs MQW structure. The technology for GaAs/InGaAs diode lasers is well established and good, optical quality InGaAs may be grown using standard MBE and MOVPE techniques [36]. It is therefore appropriate to consider strained InGaAs for a GaAs based QWSC structure.

2.1 GaAs/InGaAs p-i-n structures

The conventional p-i-n MQW structure, successfully applied in the AlGaAs/GaAs material system was employed. The diagram shown in figure 3.1 depicts a p-layer consisting of a capping layer, AlGaAs window and 500nm p-layer. The i-region was typically composed of 80Å $In_xGa_{1-x}As$ quantum wells where $0.1 < x < 0.24$ and separated by 30nm GaAs barriers. The n region was typically $2\mu m$ wide and the device grown on a n^+ GaAs substrate. Full details of the growth and processing of these devices may be found in chapter 3.

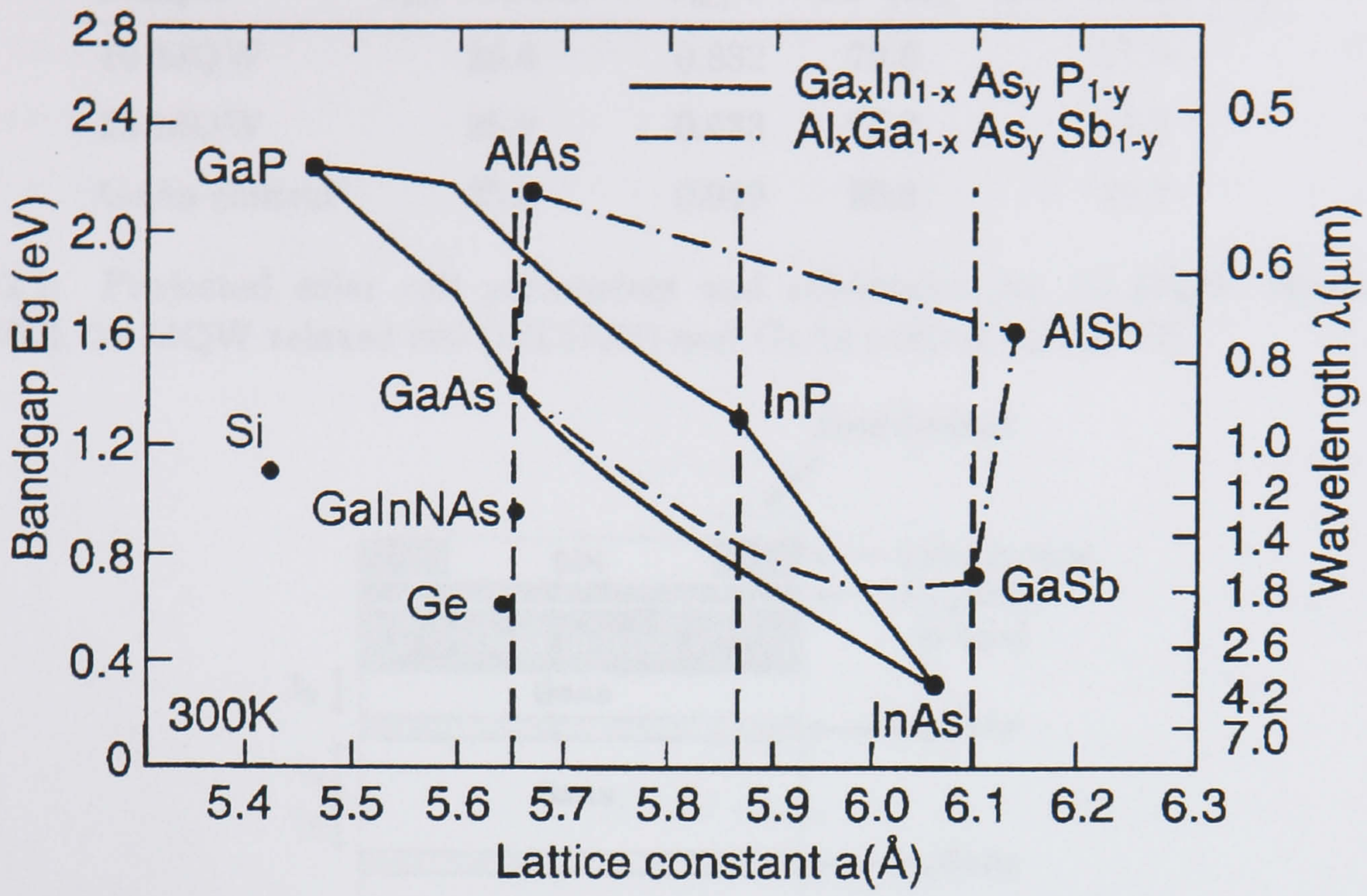

Figure 2.1: Graph showing the relationship between band-gap and lattice constant for various semiconductors

Figure 2.2: External quantum efficiency and dark current density profiles for: 10 MQW strained cell (QT957C), 23 MQW relaxed cell (QT510B) and GaAs control (QT957D).

Typical quantum efficiency and dark-IV data for 10 and 23 strained GaAs/InGaAs MQW p-i-n cells are presented in figure 2.2, together with data for a GaAs control. From the quantum efficiency, the InGaAs QWs clearly extend the cell's absorption to longer wavelengths without degrading the bulk quantum efficiency [37, 38]; leading to larger J_{sc} for the QW cells. Similarly the dark-IV characteristics of the same cells are shown, indicating much higher levels of recombination in the QW cells and thus a lower V_{oc}. Table 2.1 provides estimates for the solar cell parameters, extracted from the QE and dark-IV profiles, as described in section 1.2.3.

From the table, it is clear that the incorporation of QWs into a p-i-n structure degrades the electrical performance of the cell. The dark-IV behaviour may be understood in terms of strain induced dislocations and a summary is presented in the next section.

2.1.1 Strain in p-i-n diodes

The lattice constant for a given composition x of $In_xGa_{1-x}As$ is given by Vegard's law, expressed in equation 2.1 as a linear expression in indium composition x. The lattice mismatch is defined as $(a_x - a_0)/a_x$ where a_0 and a_x are the respective GaAs and $In_xGa_{1-x}As$

Sample	$J_{sc}/mA.cm^{-2}$	V_{oc}/V	FF (%)	AM 1.5 Eff.(%)
10 MQW	25.6	0.832	79.6	17.0
23 MQW	25.9	0.633	75.2	12.3
GaAs control	25.0	0.949	80.9	19.2

Table 2.1: Projected solar cell parameters and efficiencies for 10 MQW strained cell (QT957C), 23 MQW relaxed cell (QT510B) and GaAs control (QT957D).

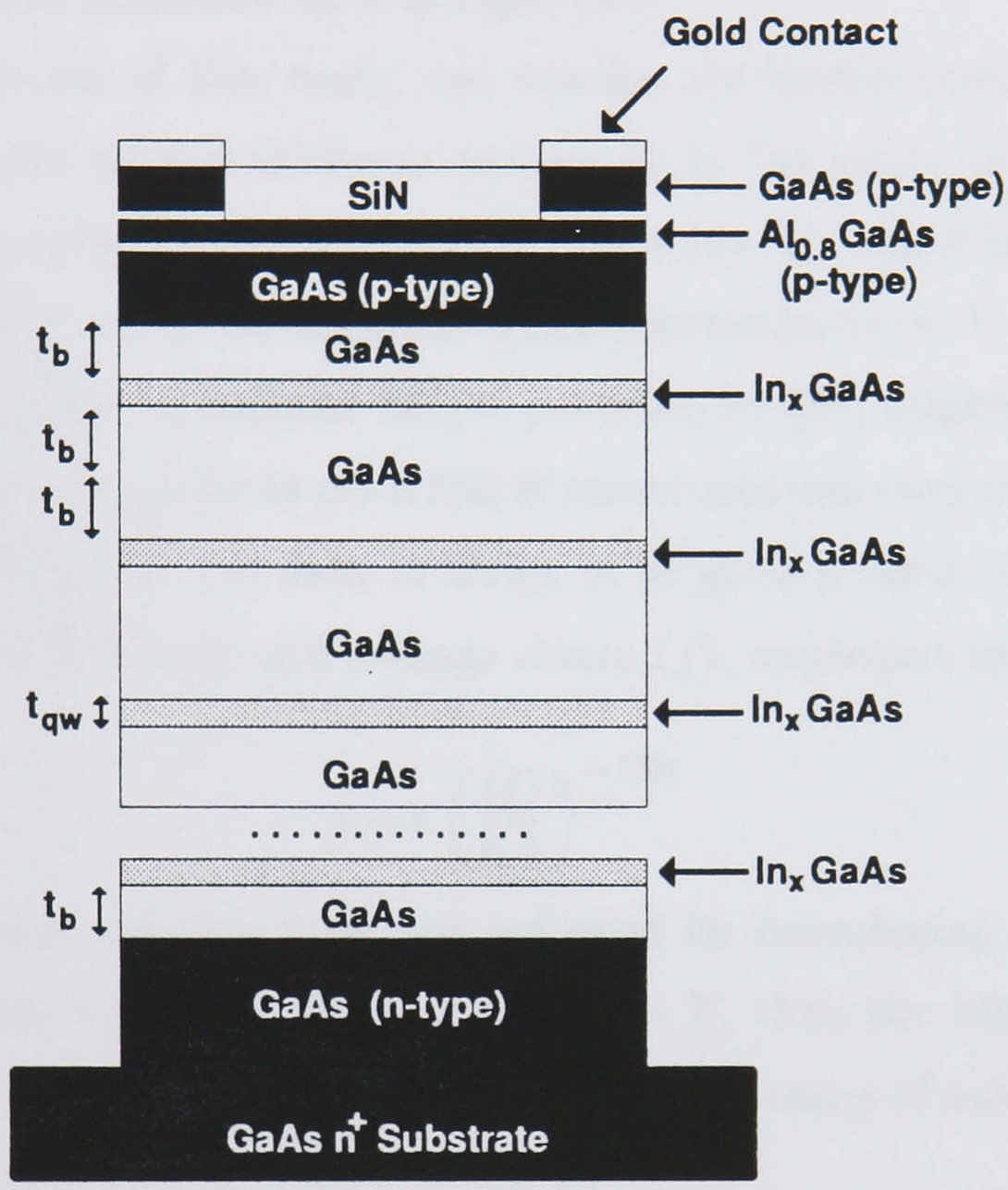

Figure 2.3: Typical structure for a p-i-n MQW diode, indicating the barrier thickness t_b, QW thickness t_{qw} and InGaAs fraction x.

lattice parameters. The MQW is composed of alternating compressively strained InGaAs and GaAs layers, overall the structure is described by an average $\langle f \rangle$. While the mismatch depends only on material parameters, the average strain takes into account the thicknesses of the strained layers and is dependent on the device geometry. For the MQW device depicted in figure 2.3, the average strain is given by equation 2.2, assuming that no relaxation takes place between the modulated layers.

$$a_x = 5.6533 + 0.4050x \tag{2.1}$$

$$\langle f \rangle = \frac{(a_x - a_0)Nt_{qw}}{a_0(Nt_{qw} + (N-1)t_b)} \tag{2.2}$$

The onset of strain-relaxation, via the formation of misfit dislocations, depends on the strain and thickness of the strained layer. A critical thickness h_c is defined as the thickness of strained material that may be grown before the onset of strain-relaxation. Relationships exist relating the strain f to the critical thickness h_c, as do experimental studies whereby the onset of strain-relaxation is measured. At the time of writing, there is still much discussion over the relative merit of one model over another and the reader is referred to the extensive literature on this topic [39].

For the purposes of this work, two studies are drawn upon. For determining a relationship between the critical thickness and strain in the layer, the Matthews-Blakeslee formalism is employed [40] and is reviewed in appendix D. As a basis for experimental study, the work of Drigo, et al. on InGaAs/GaAs heterostructures is used [4].

Early work on GaAs/InGaAs MQW p-i-n diodes [41] established that the critical thickness for strained GaAs/InGaAs p-i-n MQW structures was very similar to that of Drigo, et al. A numerical fit [42] to the data in Drigo et al gives a useful empirical relationship between the critical thickness h_c and average strain $\langle f \rangle$, expressed by equation 2.3.

$$h_c = \left(\frac{\langle f \rangle}{6.5}\right)^{-1.94} \tag{2.3}$$

A neat summary of this work was achieved by introducing the concept of excess strain. If one considers a strained layer of thickness T, then the Matthews-Blakeslee formalism gives an estimate of the strain required f_{eq} for the onset of misfit dislocations, while $\langle f \rangle$ represents the overall average strain in the layer[1].

The term excess strain is only meaningful when $\langle f \rangle > f_{eq}$, allowing the excess strain to be defined as in equation 2.4. The excess strain thus represents the degree by which the limiting strain for the onset of misfit dislocations f_{eq} is exceeded.

$$f_{excess} = \langle f \rangle - f_{eq} \tag{2.4}$$

The graph shown in figure 2.4 indicates how the dark-current density increases with increasing strain. As the excess strain is increased, the dark-current density remains constant, corresponding to a constant dislocation density (threading + misfit). However, once the excess strain reaches about 0.13% the dark-current rises rapidly, indicating an increase in the dislocation density. Further increase in strain leaves the dark-IV and dislocation density unchanged until the excess strain reaches about 0.23%.

[1]The notation f_{eq} is chosen to be consistent with earlier literature, in which the Matthews-Blakeslee approach is called the equilibrium theory, leading to terms such as equilibrium strain f_{eq}.

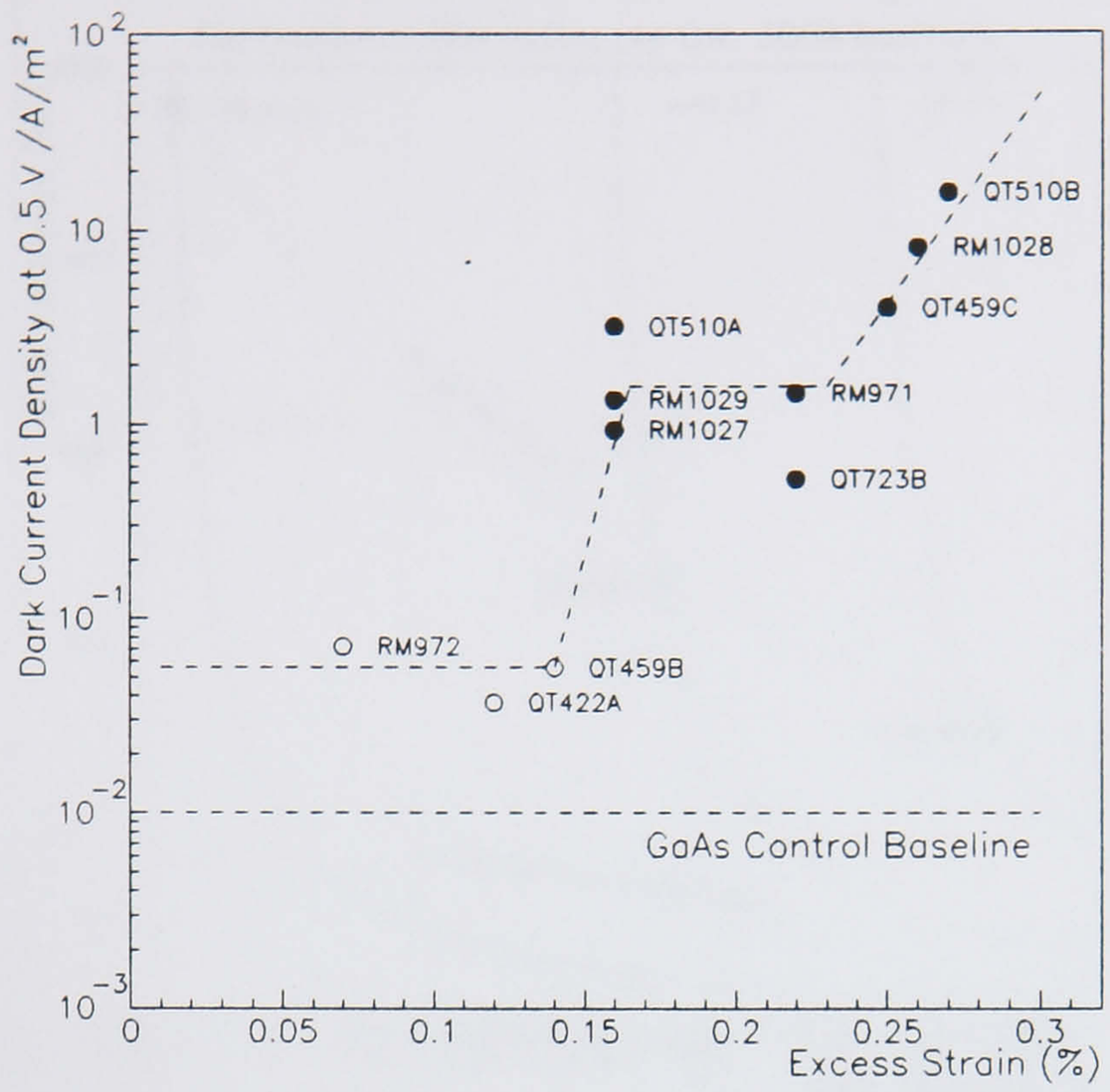

Figure 2.4: Variation in dark current density at 0.5V with excess strain. Experimental points for strained cells are indicated by open circles and relaxed cells by filled circles. The GaAs baseline corresponds to the dark current density at 0.5V for a GaAs p-i-n control.

The interpretation of this behaviour was achieved using EBIC microscopy [43], in which it was shown that the dark-current density at fixed voltage was proportional to the EBIC dark-line density. Three regimes were identified:

1. $0 < f_{ex} < 0.13\%$ Strain is accommodated by the bending of threading dislocations into misfit dislocations. When no more threading dislocations are available, the strain energy increases elastically.

2. $0.13\% < f_{ex} < 0.23\%$ Once the excess strain reaches 0.13%, there is sufficient elastic energy to induce strain relaxation at the lower MQW interface, leading to the generation of many misfit dislocations and an overall increase in the dislocation density. At this point, the MQW becomes strained at the upper MQW interface and strain is accommodated elastically once more.

3. $f_{ex} > 0.23\%$ The strain at the upper MQW interface relaxes, leading to a further increase of the dislocation density. This time, the dislocations are formed at the upper MQW interface. Further increase in strain, leads to further dislocations being generated at the lower and upper interfaces.

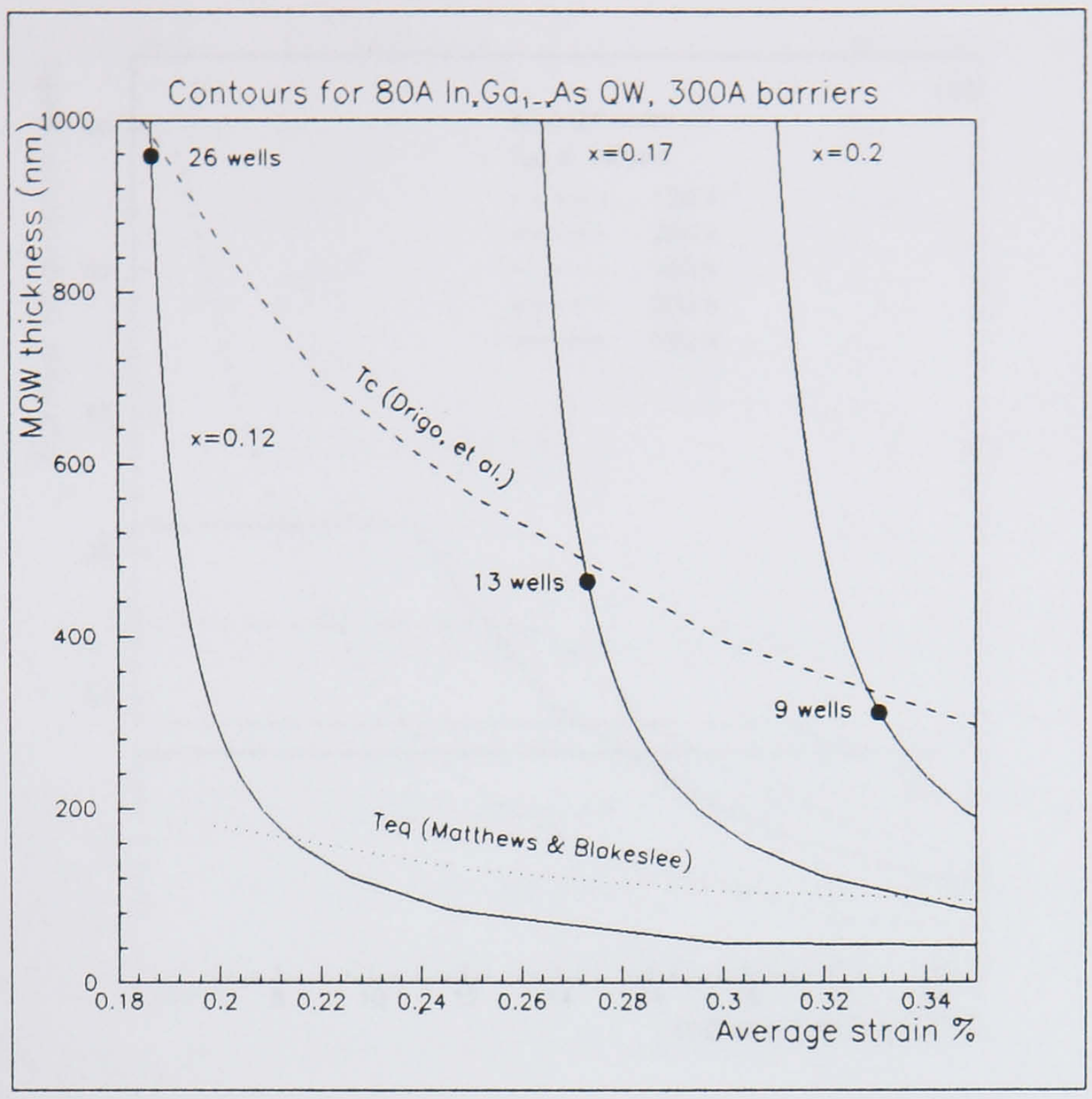

Figure 2.5: Contour curves showing the relationship between average strain and quantum well number for a 80/300Å QW/barrier combination as a function of indium fraction.

2.1.2 Strained GaAs/InGaAs p-i-n diodes as solar cells

The consequences of the critical thickness for solar cell operation are quite severe. Essentially a limit is placed upon the overall number of quantum wells which may be successfully accommodated in a p-i-n structure. The graph depicted in figure 2.5 shows contour curves of MQW thickness vs average strain for cells of fixed composition; 12%, 17% and 20% InGaAs.

The strain/thickness behaviour is counter intuitive at low compositions, where the number of QWs is low and the average strain is high. Considering equation 2.3, when N=1, $\langle f \rangle = (a_x - a_0)/a_0$ and is dominated by the QW mismatch. However when N is large, $\langle f \rangle \rightarrow t_w(a_x - a_0)/a_0(t_w + t_b)$ and becomes independent of well number.

The empirical strain-thickness relationship expressed by equation 2.3 provides a limit to the number of quantum wells that may successfully accommodated. Any cell lying above the 'Drigo' curve will undergo strain-relaxation, leading to a high dark current. Any cell substantially below the Drigo curve will not possess the optimum absorption and could accommodate further QWs with no penalty. Evidently there is a strong tradeoff between the spectral and optical extent of the QW absorption in a successful (low dark-IV) solar cell.

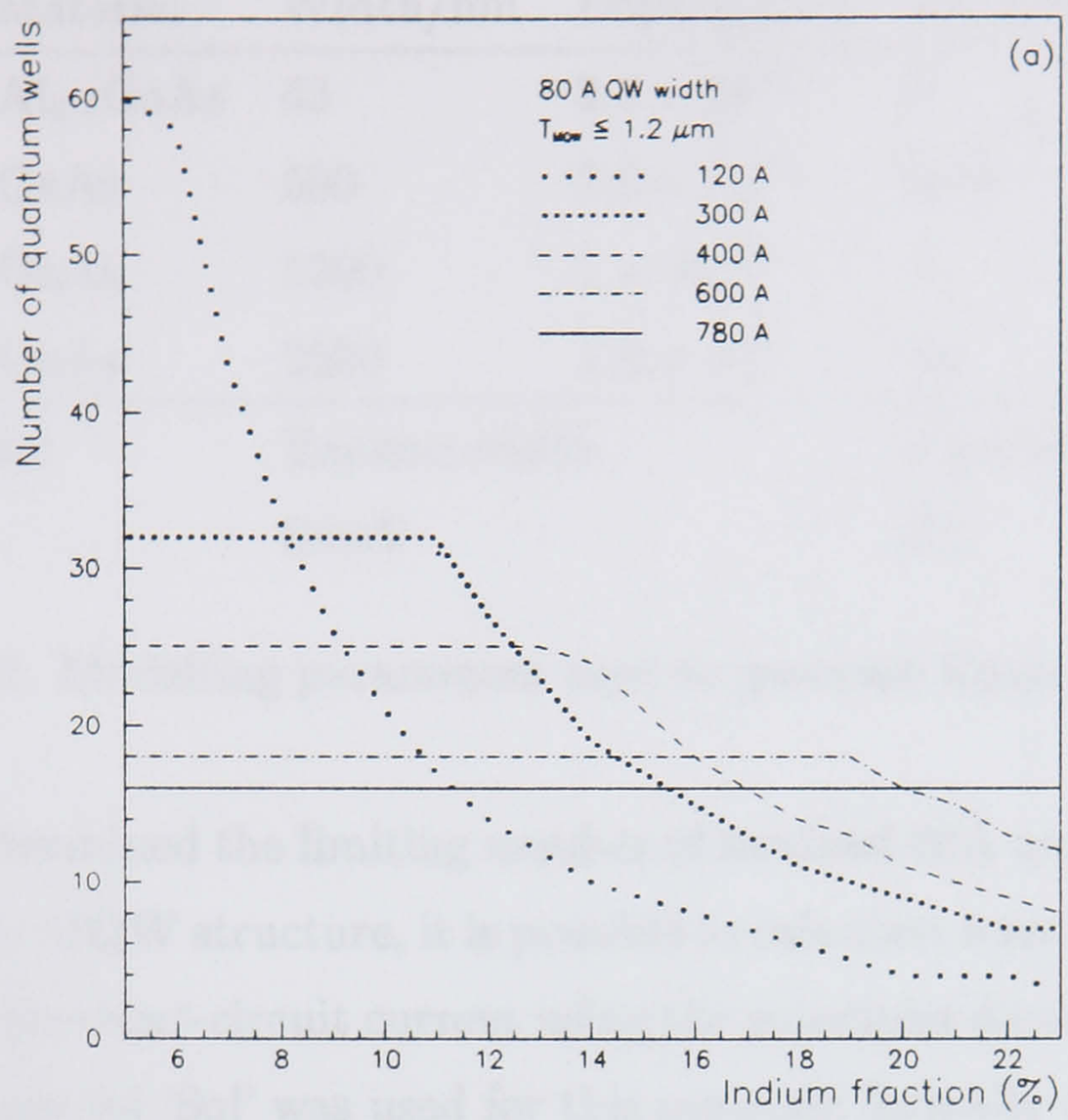

Figure 2.6: Quantity of 80Å QW layers that may be incorporated into a p-i-n cell before exceeding the critical thickness of Drigo, et al. [4]. The graph is plotted as a function of indium fraction and barrier width.

The width of the i-region enforces another physical limitation upon the cell design. A large i-region could accommodate many QWs, but would have to be composed of extremely pure quality material in order to remain depleted at the operating point. A realistic limit to the background doping is $10^{14} cm^3$ which, by solving Poission's equation as described in appendix B, gives a limit of 1.2μm.

Within these boundary conditions, sets of optimum well/barrier combinations were calculated for which the number of QWs was maximised for a particular combination of t_b and t_{qw}. The results for an 80Å MQW structure is shown in figure 2.6.

At low indium fractions, the critical thickness is large and in the regime where $h_c > 1.2\mu m$ the QW number is pinned by the condition that the i-region may not exceed $1.2\mu m$. Therefore the number of QWs which may be accommodated depends not on strain, but on the barrier thickness.

At higher indium fractions, the critical thickness becomes significant ($h_c < 1.2\mu m$) and the QW number is strongly influenced by the degree of strain in the structure. A special case occurs with barriers of 780Å in width, whereby $h_c \geq 1.2\mu m = T_{qw}$ for all indium fractions. From the graph it is evident that the barrier width is an important quantity, if one is interested in a maximising the number of QWs for a certain indium fraction.

Layer	Material	Width/nm	Doping/cm^3	Recomb. Vel. /cm.s^{-1}
Window	$Al_{0.7}GaAs$	43	2.3×10^{18}	0
p	GaAs	500	2.3×10^{18}	3000
i	GaAs	1200	1×10^{14}	0
n	GaAs	2000	1.8×10^{17}	10
QW material		Exciton width		ν parameter
In_xGaAs		5meV		0.3

Table 2.2: Modelling parameters used to generate figures 2.7 and 2.8

Having determined the limiting number of strained 80Å quantum wells that can be accommodated in an MQW structure, it is possible to calculate a series of quantum efficiency curves and project the short-circuit current using the principles described in section 1.2.3. A quantum efficiency model 'Sol' was used for this purpose; formally developed by Dr. Jenny Nelson to model AlGaAs/GaAs QW cells [44] and later modified by Dr. Jenny Barnes to account for the strained GaAs/InGaAs material system [45]. A wide i-region cell design was employed with fixed bulk dimensions, so to eliminate any variation in the bulk behaviour. The cell parameters are typical of strained GaAs/InGaAs cells and are listed in table 2.2. The top surface reflectivity was taken from a measured 100nm SiN anti-reflection coating.

The short-circuit current density computed under AM0 and AM1.5 illumination is shown in figure 2.7 as a function of indium fraction and barrier width for an 80Å QW. First one notes that the AM0 J_{sc} maxima rise steadily with indium fraction and increasing barrier width, corresponding simply to a greater absorption of available photon flux. In contrast, the AM1.5 curve shows a dead region, where the J_{sc} maxima drops for $In_{0.14}GaAs$/400Å, corresponding to the absorption dip in the AM1.5 spectrum at 930nm. The rise in J_{sc} around 16% InGaAs is due to the second electron level becoming bound. In the AM1.5 spectrum, the additional absorption due to the second level is sufficient to further raise the J_{sc}, despite the modest incident photon density at 930nm.

In both AM0 and AM1.5 cases, each J_{sc} curve peaks when the critical thickness equals the maximum i-region width ($h_c = 1.2\mu m$). In terms of QW number, this is the largest permitted indium fraction that maintains the maximum QW number. The maximum overall J_{sc} is achieved when this condition is met with 23% InGaAs QWs, the highest indium composition achievable using 2D epitaxial growth techniques.

By employing the maximum J_{sc} condition above, it was possible to calculate the variation in 'maximum J_{sc}' as a function of quantum well width, shown in figure 2.8.

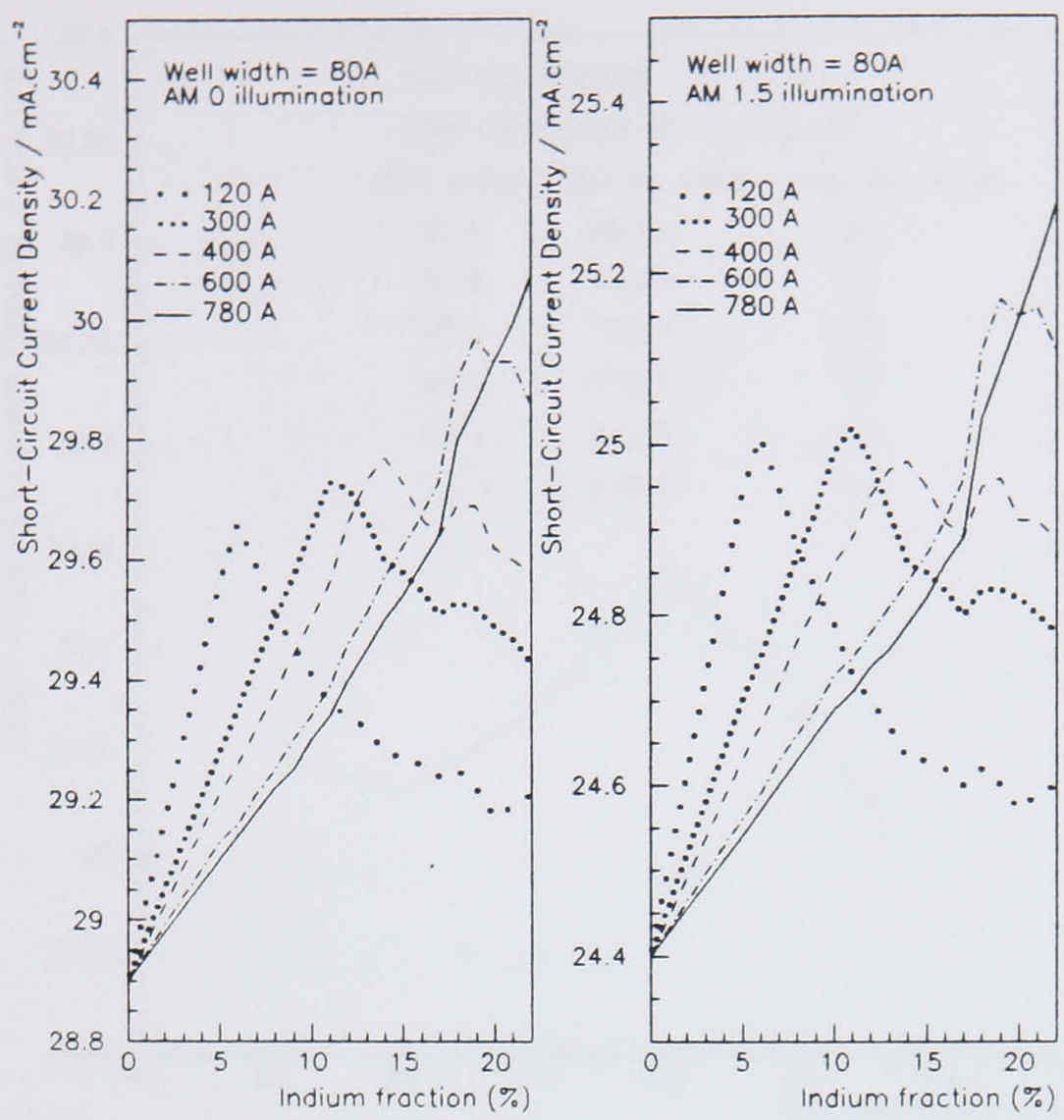

Figure 2.7: AM0 and AM 1.5 J_{sc} curves for strained GaAs/InGaAs 80Å MQW cells with varying barrier width (120-780Å) and QW indium fraction.

Studies of the well width vs oscillator strength [46] have shown 50Å QWs to be optimum for photoconversion but the results in figure 2.8 suggest a modest improvement using 80Å QWs. The oscillator strength study of reference [46], was concerned with the weakening of the oscillator strength under an electric field, and showed that 50Å QWs were most robust in this respect. While this is a valid concern for the design of optical modulators, where the absorption must remain strong under a range of electric fields (0-100kV/cm), this is not so relevant for QW solar cells where the absorption will take place at the operating point and the field will be no more than a few kV/cm.

Finally table 2.3 compares calculated efficiencies for an optimised GaAs/InGaAs MQW cell against two bulk GaAs cells. The MQW cell parameters are derived from the optimum well/barrier combination of figures 2.7 and 2.8, maximising J_{sc}. The V_{oc} is calculated from a typical strained MQW dark-IV profile, such as QT459B in figure 2.4. The bulk GaAs cells correspond to J_{sc} at $x = 0$ in figure 2.7, but with different dark-IV profiles. GaAs A indicates the cell performance with the MQW dark-IV of QT459B, whereas GaAs B demonstrates the performance achieved with a dark-IV corresponding to the 'GaAs control baseline' of figure 2.4. The modeling parameters remain identical to those of table 2.2. The effect of a strained GaAs/InGaAs MQW cell can be observed by comparison with the

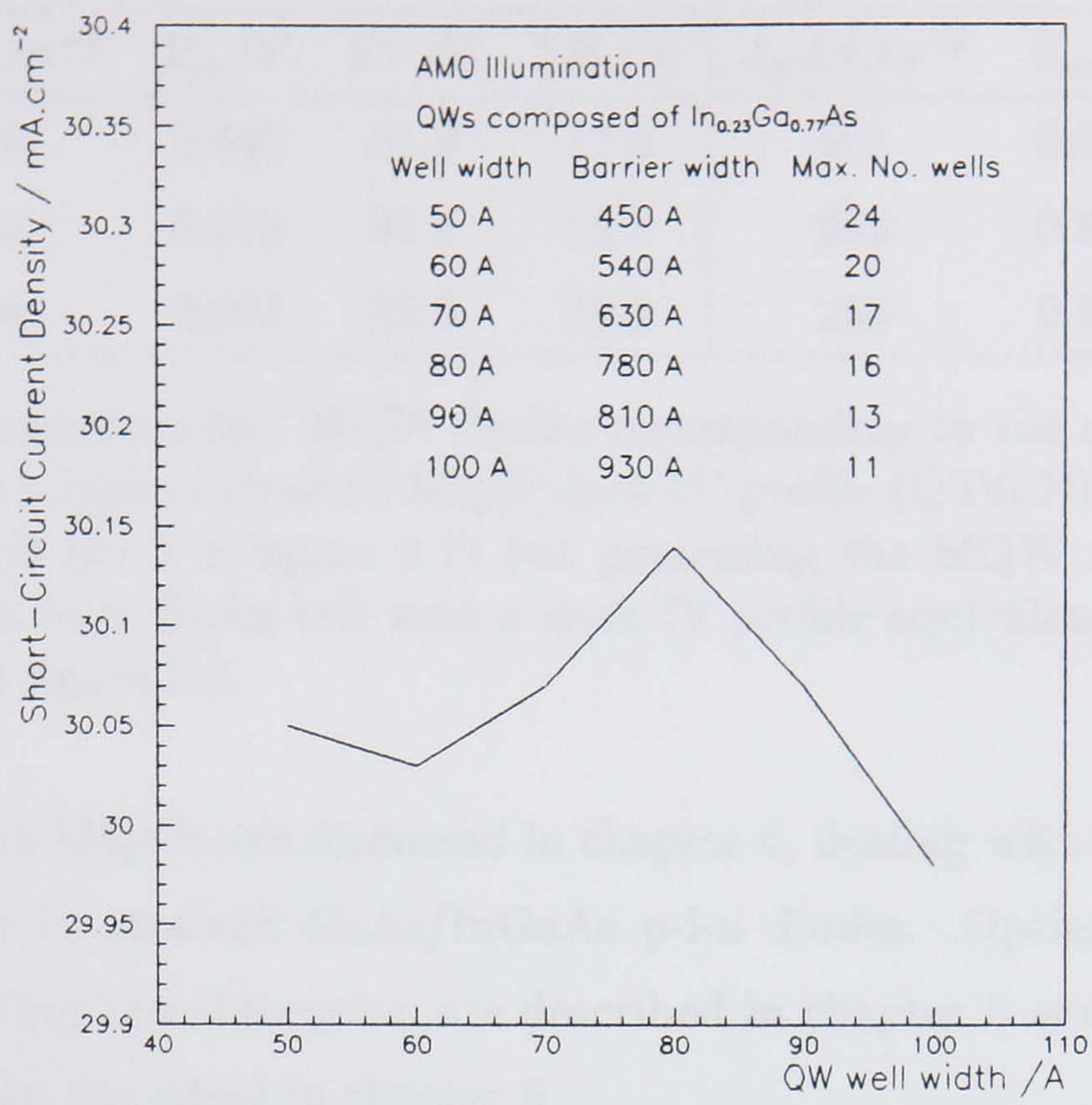

Figure 2.8: Variation in J_{sc} for an 'optimised barrier' structure as a function of well width. This calculation has been performed under AM0 illumination, but the same result holds under AM1.5 illumination.

bulk cell GaAs A. However, the realistic comparison must be made against bulk cell GaAs B, its dark-IV profile being typical of a GaAs cell. Under these circumstances, it is clear that an optimised strained GaAs/InGaAs MQW can never possess sufficient absorption[2] to overcome the loss in dark-current and will never surpass a good GaAs cell in terms of solar power conversion efficiency.

2.2 Potential for enhancing the GaAs efficiency

Earlier sections in this chapter have described the limitations inherent to strained GaAs/InGaAs cells. It is now evident that the standard p-i-n strained structure is unable to enhance a GaAs cell efficiency, on account of the large dark-current associated with strain induced dislocations. Any possibility for enhancing a GaAs cell efficiency requires the dark current to be comparable to that of a GaAs cell and strong absorption across the QW wavelengths.

The remainder of this thesis is concerned with schemes for overcoming the limitations described in this chapter. Evidence for a fundamental efficiency enhancement in

[2]Without substantial light trapping.

	AM 1.5				AM 0			
Cell	$J_{sc}/A.m^{-2}$	V_{oc}/V	FF/%	Eff./%	$J_{sc}/A.m^{-2}$	V_{oc}/V	FF/%	Eff./%
MQW	254	0.840	81.9	17.4	301	0.849	81.9	15.35
GaAs A	244	0.838	81.8	16.7	289	0.846	81.9	14.7
GaAs B	244	0.963	82.3	19.3	289	0.973	82.1	16.9

Table 2.3: Cell parameters for: MQW device corresponding to the optimised structures of figures 2.7, 2.8 and a typical strained MQW dark-IV profile (QT459B). GaAs A corresponds to a bulk GaAs cell (x=0 in figure 2.7) but possessing the MQW dark-IV profile. GaAs B corresponds to a bulk GaAs cell with a dark-IV profile equivalent to the 'GaAs control baseline' shown on figure 2.4.

GaAs using InGaAs MQWs are discussed in chapter 4, dealing with the radiative and non-radiative processes in strained GaAs/InGaAs p-i-n diodes. Optical trapping techniques suitable for extending the absorption are described in chapter 5 and schemes for reducing the dark-current are described in chapter 6.

Chapter 3

Growth and Characterisation

All the cells reported in this thesis were grown by epitaxial techniques, either by molecular beam epitaxy (MBE) or metal organic vapour phase epitaxy (MOVPE); the differences between these techniques is discussed in section 3.1. The wafers were subsequently processed into 1mm diameter mesa test diodes at the University of Sheffield. An outline of the processing steps is described in section 3.2.

The characterisation was performed at Imperial College and routinely involved measurements of the diode dark-IV profile, the quantum efficiency and monochromatic-IV. These measurements are described in section 3.3 together with some more specialist techniques for determining MQW properties.

Two typical QWSC solar cell structures are depicted schematically in figure 3.1. The devices were all of a p/n configuration and grown upon either n^+ or undoped substrates. The first epitaxial layer to be grown was typically a 300nm thick n^+ buffer layer, followed by a more lightly doped 2μm thick n-type layer. The i-region was typically between 400-1200nm thick and its nature varied from sample to sample. The precise growth parameters may be found in appendix C. The p-region was typically 500nm thick and was followed by a thin (430Å) p-type AlGaAs layer, serving as a minority electron reflector. Finally a 220nm GaAs cap layer was grown to prevent the AlGaAs from oxidising. The cap layer was subsequently etched off for AR coated samples.

When a sample was designed to have its substrate removed, a thin AlAs layer was grown followed by a thicker (1μm) $Al_{0.3}GaAs$ layer, shown in figure 3.1b. These layers served as an etch-stop, allowing the substrate to be wet-etched, leaving an extremely thin 'cavity' cell. The properties of these cavity cells are discussed in section 5.4.3. The substrate removal processing steps are summarised in section 3.2.3.

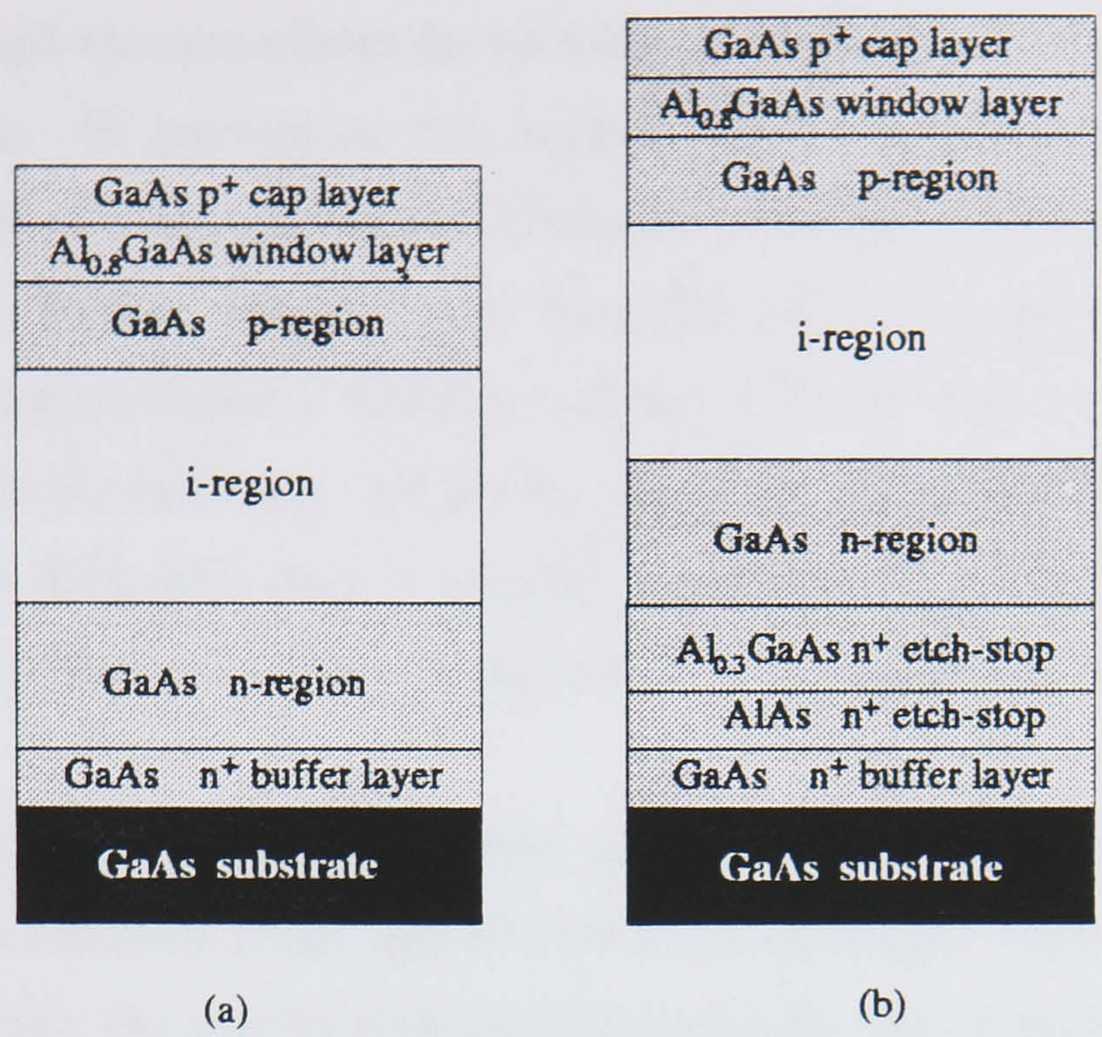

Figure 3.1: Schematic device diagrams; a) typical cell structure, b) typical cell structure with AlGaAs etch-stop layers.

3.1 Growth

The samples were grown exclusively by epitaxial methods, either MOVPE or MBE. The two techniques are quite different in their approach. MOVPE remains the industrial method of choice, on account of high throughput and yield. MBE is better suited to research applications, allowing a high degree of control over the growth surface and a wealth of in-situ probes.

For solar cell applications, MOVPE has proved to yield consistently higher efficiencies; mainly on account of a more reliable dark-IV characteristics [2]. The differences in growth conditions will be discussed briefly in order to clarify the limitations of each technique.

3.1.1 MBE Growth

MBE growth takes place under ultra high vacuum (UHV), requiring base pressures of 1×10^{-10}torr. Deposition is achieved by evaporating elemental sources into a molecular beam which is directed towards a wafer heated to around (490 – 600°C). The growth and incorporation rates depend upon the flux density and substrate temperature, controlling the mobility of the atomic species on the surface and the associated desorption rate. While several growth modes are possible, step-flow growth allows monolayer by monolayer growth across the wafer and is the mode used for growing high-quality QW structures.

The ultra high vacuum allows for an array of surface analysis tools to be integrated into an MBE system. In particular, the surface state may be inspected, in-situ, using reflection high energy electron diffraction (RHEED) and the growth rate monitored from RHEED oscillations. Further analysis may be performed using in-situ mass spectrometry and scanning tunneling microscopy (STM), making MBE an ideal technique for research.

All III-V compounds may be grown by MBE, including reactive elements such as aluminium. While AlGaAs purity is usually limited by the purity of the Al source, the UHV environment prevents excessive contamination from oxygen or carbon; a problem with MOVPE growth.

Certain drawbacks exist with MBE growth, in particular the existence of oval defects. Comparisons between MBE and MOVPE material have shown that the oval defect density is responsible for the poorer yield of GaAs cells [2]. However high efficiency (23.8%) GaAs p/n cells have been grown by MBE [47]. From the industrial viewpoint, the surface analysis offered by MBE is less useful and the UHV conditions place a restriction on wafer throughput. As a result MBE is best suited for low volume research work, although there are instances of MBE growth for mass production of laser diodes and other such miniature devices.

3.1.2 MOVPE Growth

MOVPE growth usually takes place under atmospheric conditions. A H_2 carrier gas transports the group III elements as a metal-organic vapour and the group V elements in hydrogenated form into the growth chamber. The vapour is passed over a heated substrate, above which the metal-organic compound disassociates depositing the metal on the substrate surface. Growth and incorporation rates depend upon the metal-organic flow rate, substrate temperature and surface reaction.

MOVPE can produce exceptional growth quality, routinely producing high yield, 25% efficient GaAs p/n cells [2] and also 30% efficient GaInP/GaAs tandem cells [24, 48]. Further, the growth takes place at higher substrate temperatures ($600-700^\circ$C) than MBE, which is found to reduce surface roughness [49].

The limitations of MOVPE are that relatively few in-situ growth probes may be used to assess the surface during growth. There are also problems when growing compounds of aluminium, on account of its reactivity. Exceptionally pure Al sources are required, with low oxygen content [50]. Also, the reactivity of Al brings an unavoidable incorporation of carbon from the carrier gas, resulting in a higher AlGaAs background doping for nominally

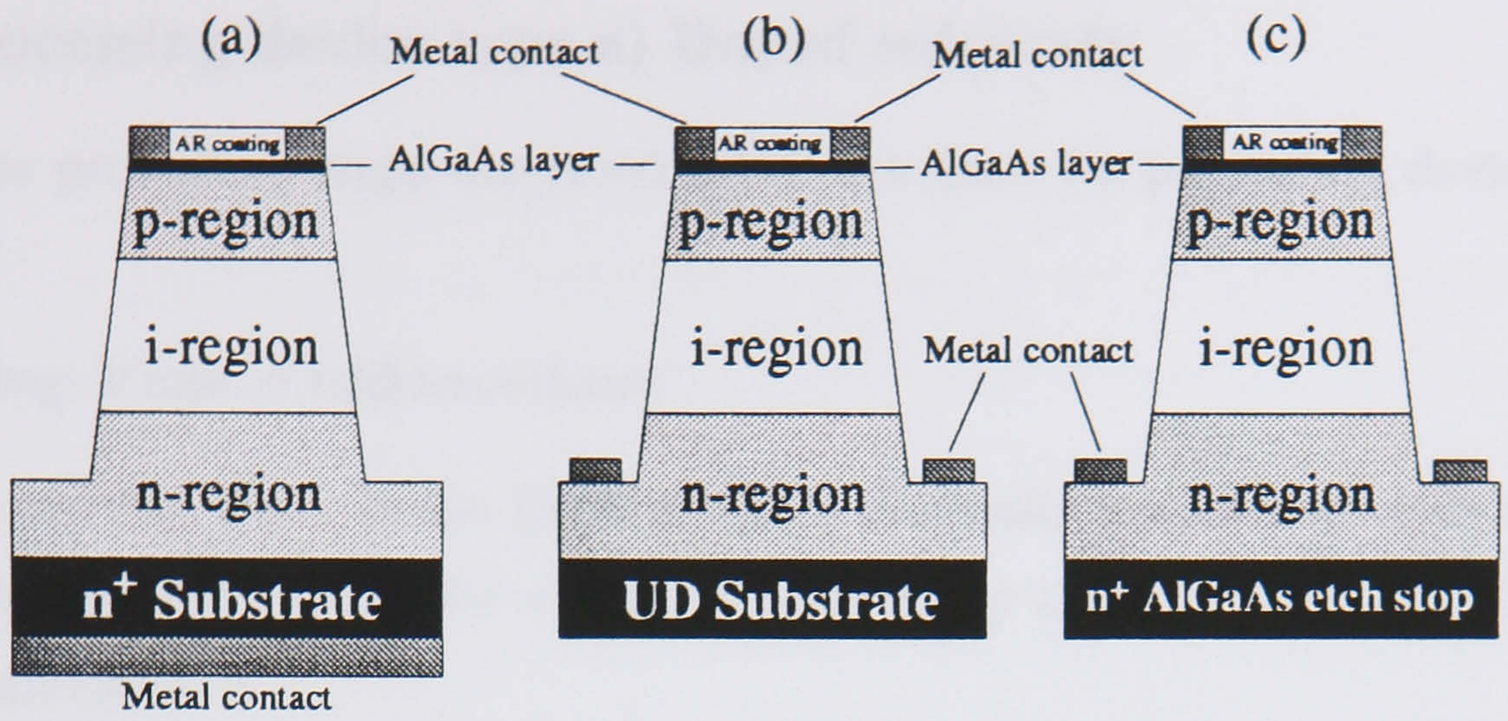

Figure 3.2: Three types of device: a) Contacting through n^+ substrate, b) Top contacting for samples with an undoped (UD) substrate, c) Substrate removal requiring an AlGaAs etch-stop.

undoped AlGaAs for MOVPE than MBE. The incorporation of Al into a solar cell structure by MOVPE, usually introduces a higher level of impurities.

The growth of low P content (6%) GaAsP alloys has recently been achieved in a GaAs MOVPE reactor, using a sufficiently low phosphene flow-rate not to require special precautions for collecting phosphorus residues [51]. Using this technique, extremely high purity $GaAs_{0.94}P_{0.06}$ has been grown and successfully employed in the GaAsP/InGaAs strain-balance cells reported in chapter 6, section 6.2.

3.2 Processing

All the samples were processed by Drs. Malcolm Pate, Jan Clark and Geoff Hill at the EPSRC III-V semiconductor facility[1]. The capped structures grown as shown in figure 3.1 were processed into circular mesas of 1mm diameter with a top ring contact of 600μm inner diameter. Samples were processed both with and without an anti-reflection (AR) coating. The samples with no AR coating were processed with the GaAs cap intact whereas for the AR coated samples, the cap was wet etched to the AlGaAs layer and a 74nm SiN AR coating deposited upon the AlGaAs surface.

Figure 3.2 depicts the three types of device which were processed. Device a is suitable for samples with n^+ doped substrates, device b is suitable for top contacting devices with undoped substrates and device c is the result after substrate removal. The following subsections describe the processing stages for each of these types of device.

[1]University of Sheffield, U.K.

3.2.1 Processing device type a) Doped substrate

The processing steps described below are used for processing devices on doped substrates.

1. Cleaning: Rinse in trichloroethane.

2. Back contact: 200Å In-Ge (50% alloy) is thermally evaporated onto the substrate followed by 2000Å Au. The contact is annealed by ramping up to 420°C and cooling in N atmosphere.

3. Front contact: Photoresist spun onto wafer and contact ring defined by mask. Thermal evaporation of 50Å Au followed by 100Å Zn followed by 2000Å Au. Excess metalisation is removed, followed by anneal: ramp to 360°C, followed by cooling in N atmosphere.

4. AR coating (if required): GaAs cap removed using wet etch. 740Å SiN deposited via plasma deposition at 300°C. Photoresist spun onto wafer and optical window defined by mask. Excess AR coating removed using Freon-oxygen etch.

5. Mesa definition: Photoresist spun on and mesa defined by mask. Etch using 1 part hydrogen bromide, 1 part acetic acid, 1 part potassium dichromate in water. Etch terminated in the n-region, the depth is gauged by etching time; 30s of etching removes 2μm of material.

6. Devices are cleaved, mounted onto TO5 headers using gold-epoxy resin and bonded.

3.2.2 Processing device type b) Top contacting

The processing steps for samples with undoped (semi-insulating) substrates, differed from (a) in that the n-type contact was made to the upper surface as shown in figure 3.2b. This was achieved by following steps 2,3,4,5 described above and then making the n-type GaAs contact using an In dot.

The top contacting was first applied to samples QT957B, QT957C and QT957D. The top-contacting technique was assessed using QT957B as a test device, it possessing a doped substrate, allowing it to be processed by both techniques (a) and (b). Comparable device performance was observed under both processing techniques, establishing the top contacting technique as a reliable process. Samples QT957C and QT957D which both possessed undoped substrates, showed good device performance under the top-contacting process.

MIM structures

A practical application of the top-contacting technique has been developed to overcome heating problems under high photon densities such as concentrated sunlight [52] and thermophotovoltaics [53]. The Monolithic interconnect modules (MIM) structures are essentially an elaborate form of top-contacting, incorporating bus-bar and finger grids on the top surface for both the top and bottom contact. The cells are arranged in series, adding to the cell voltage and reducing series resistance problems under high levels of concentration. While such an arrangement leads to a high shading loss, MIM cell designs exploit the optical transparency of undoped semi-insulating substrates, avoiding free-carrier absorption of sub-band gap radiation which would otherwise serve to heat the cell.

While no specific work on MIM structures has been performed for this thesis, it represents a viable technology for processing cells grown on undoped substrates, whose desirable light-trapping properties are reported in chapter 5.

3.2.3 Processing device type c) Substrate removal

The process for substrate removal followed all the steps for top-contacting, described above. However, before bonding, the wafer was mounted onto a glass slide using wax. The glass slide provided a rigid fixture during the etching process and a freon etch was used to remove the substrate to the thick AlGaAs n^+ etch-stop. The resulting thin sample was then mounted on a TO5 header and the wax removed.

3.3 Characterisation

The routine for characterising layers was to first measure the dark-IV profile, it being a rapid measurement and indicating defective devices. The quantum efficiency (QE) measurement was then performed on devices from at least two headers and repeated until three identical profiles were obtained. Background doping and field dependencies in the QE were probed qualitatively using monochromatic-IV measurement. In the instance of a diode possessing exceptional characteristics, light-IV measurements were taken to determine the fill-factor (FF). These measurements constitute the standard characterisation which was performed for every layer grown. The details of the experiments are presented in the relevant sections below.

A series of more specialist techniques were available for determining MQW properties. Low temperature photocurrent measurements allowed the MQW width and com-

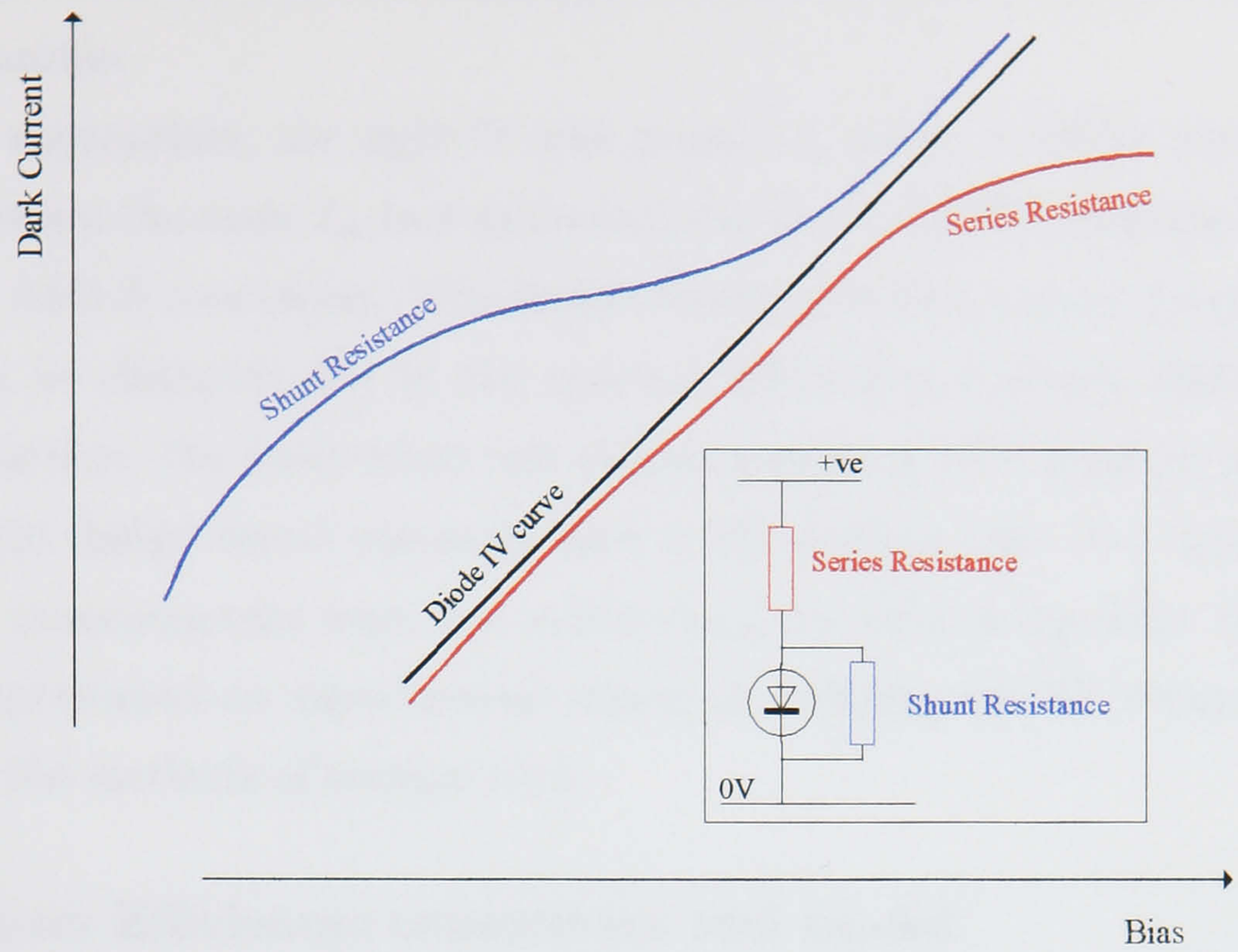

Figure 3.3: Typical IV profiles, showing the effects of shunt and series resistance.

position to be determined, while X-ray diffraction together with transmission electron microscopy, provided a means for determining the barrier thickness. Electron beam induced current microscopy proved an invaluable tool for determining the structural quality of the MQW regions. Each is briefly discussed in the sections below, indicating the accuracy and scope of the measurement.

3.3.1 Dark and Light IV

The dark-IV was measured at room temperature using a Keithley source-measure unit (SMU) controlled by computer via an IEEE interface. Typically IV data points were taken at forward bias to currents of 1mA; a current sufficiently large to determine the electrical characteristics, but sufficiently small not to damage the bond wires. Reverse bias data points were taken to -2V to verify diode behaviour. The SMU was able to source and measure to 5dp accuracy, making external factors, such as temperature fluctuations the greatest uncertainty in the measurement.

While the criteria for 'good' diode behaviour varies, generally a good diode will possess negligible reverse bias leakage current, small series resistance and a large shunt resistance. The graph shown in figure 3.3 depicts three IV profiles, together with the definitions of series and shunt resistances. In general it was found that most diodes on most headers were good, although there were instances where a systematic processing fault gave entire batches of samples a high series resistance. Numerical values for the series

resistance, shunt resistance and diode parameters were obtained though numerical fitting of the dark-IV profile.

When appropriate, the light-IV was measured under a 3000K tungsten filament lamp, set to generate the same I_{sc} in a calibrated cell under 3000K illumination as achieved under standard AM1.5 conditions. This measurement provides a good measure of the FF, but the J_{sc} will be distorted due to the spectral differences between 3000K and AM1.5 illumination. Further, the 1mm mesa test diodes possess a 70% shading loss, whereas a good bus-bar grid design would normally have a 5% shading loss. For these reasons, the 3000K light-IV measurements were not relied upon for estimating solar cell efficiencies. Instead, they represented an experimental means of verifying the FF when projecting the efficiency using the methods of section 1.2.3.

3.3.2 Quantum Efficiency; experiment and model

The quantum efficiency was measured using the optical setup illustrated in figure 3.4. A 100W quartz halogen bulb served as an illuminator and was coupled through a chopper, into a 30cm, 1200 line/mm Bentham monochromator. The beam emerged through a pinhole aperture, was collimated by one 45mm focal length lens and focussed by another 45mm focal length lens onto the optical window of the 1mm mesa diode. The photocurrent was measured using a Stanford lock-in amplifier (LIA) and the experiment controlled by a computer through an IEEE interface. As the photocurrent is measured from the voltage appearing across a precision 100kΩ resistor, the QE setup was only suitable under bias conditions where the diode resistance was much greater than 100kΩ. Typically this allowed QE measurements to be performed up to 0.5V, before the resistance of the device became comparable to the 100kΩ resistor.

Photocurrent measurements were made from 400nm up to 1100nm at 2nm intervals for the cell in question. The same measurement was then performed with a calibrated silicon photodiode, allowing the quantum efficiency to be deduced with a fractional error of 5%.

A model 'Sol'[2] was used to fit the quantum efficiency profile of MQW and bulk p-i-n diodes, allowing quantitative information to be deduced [44, 45]. The relative p and n contributions to the photocurrent are controlled by varying the appropriate minority carrier diffusion length and/or the surface recombination velocity. In many cases it is difficult to isolate the effects due to diffusion or surface recombination precisely, but the model does identify the role of the p, i and n layers. For example, the data depicted in figure 3.5

[2]Developed by Dr. Jenny Nelson to model AlGaAs/GaAs QW cells and later modified by Dr. Jenny Barnes

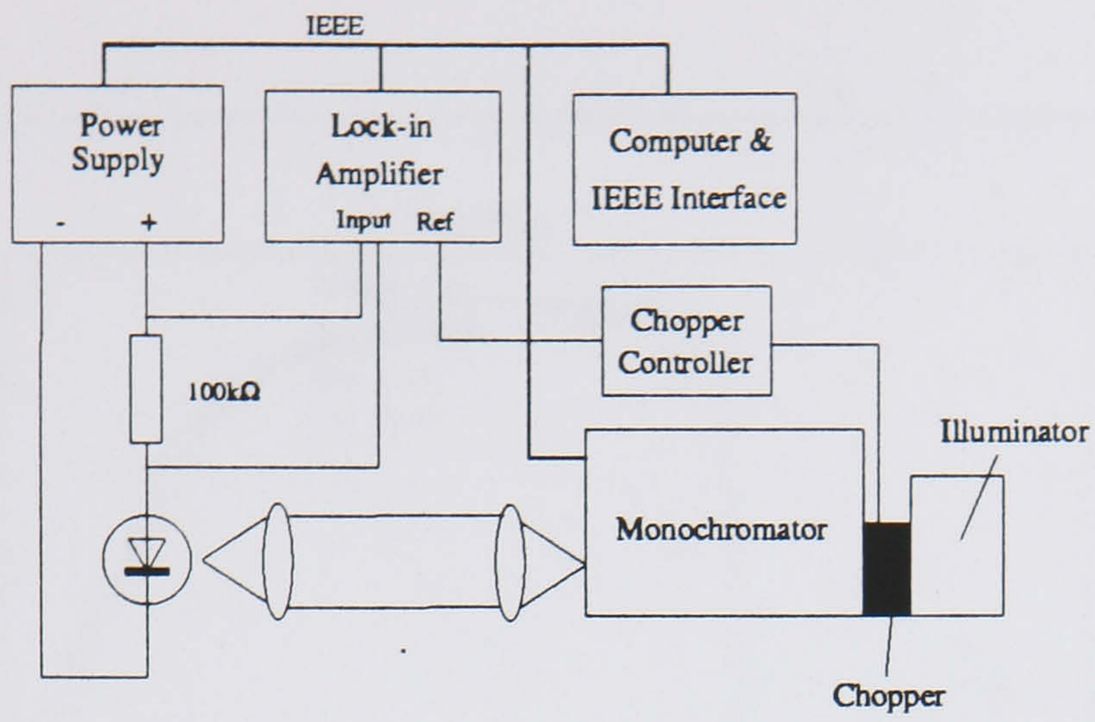

Figure 3.4: Schematic diagram to show the apparatus used for the quantum efficiency measurement.

shows that the p region dominates the short wavelength response. The mid-wavelengths (500-700nm) are a combination of p and i region and only the long wavelengths (700nm+) involve the n region.

3.3.3 Reflectivity and Transmission

The sample reflectivity and transmission were measured from AR coated but otherwise unprocessed chips of the wafer. The experiment was performed using the same experimental setup as for the quantum efficiency, but replacing the second focusing lens with a longer focal length lens.

The optical arrangement for a reflectivity measurement is shown in figure 3.6 and was optimised such that the reflected beam was focused on the detector. While this measurement served as a good estimate for the reflectivity, its accuracy was limited to $\approx 10\%$ due to the incident and reflected beams being non-normal. A normal incidence technique was developed for more accurate reflectivity measurements [54, 55] required for light-trapping work, but all reflectivity measurements reported in this thesis were performed using the non-normal method described here.

Transmission experiments could be performed at normal incidence. The beam incident on the wafer remained defocused on sample but focused on the silicon detector, located behind the sample.

3.3.4 Monochromatic-IV

The mono-IV is measured using the same apparatus as the QE, shown in figure 3.4. For this measurement, the wavelength remains fixed but the bias is varied, changing the

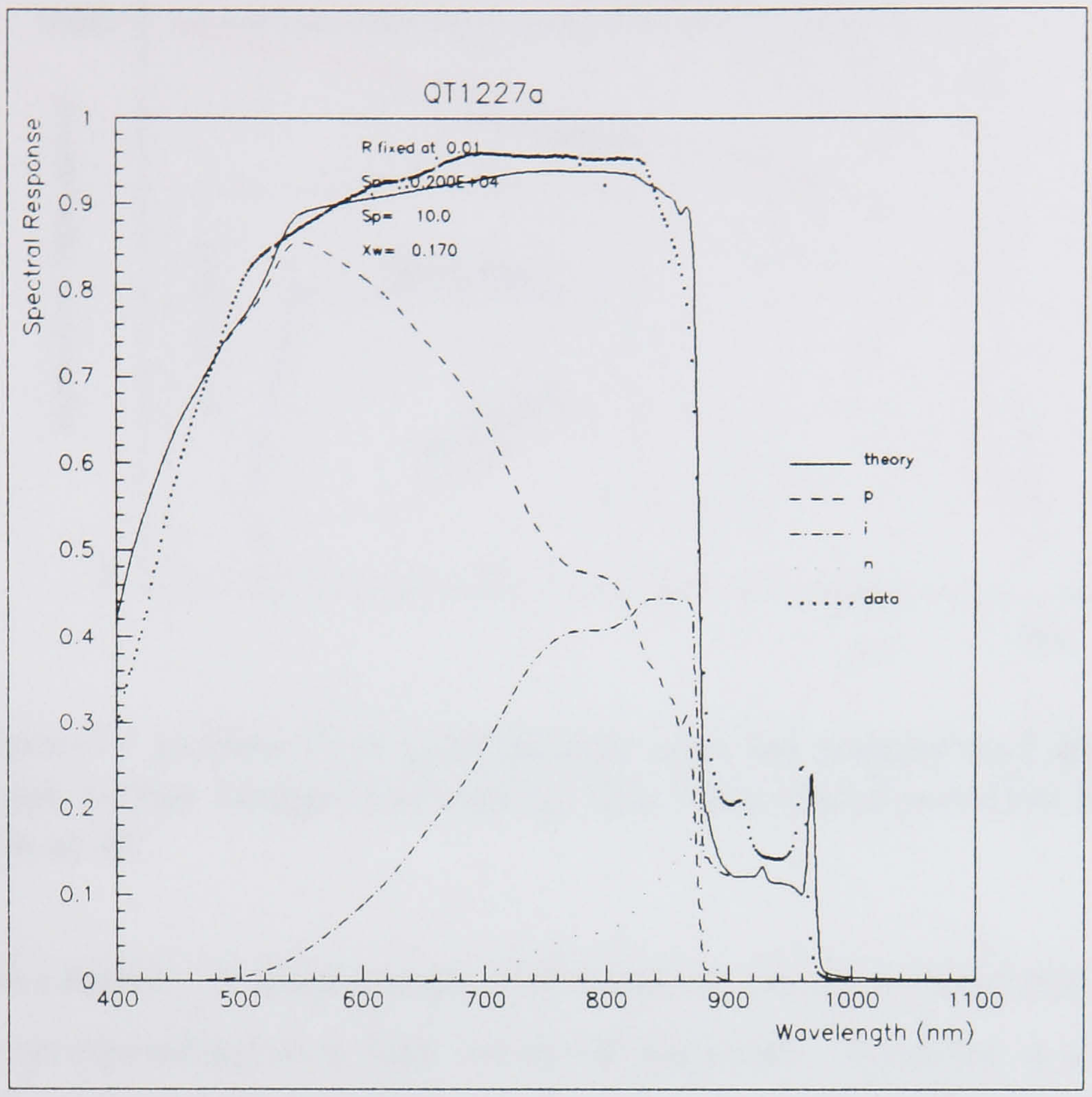

Figure 3.5: Quantum efficiency data and fit using the 'Sol' model. The p, i and n components to the modelled QE are also shown.

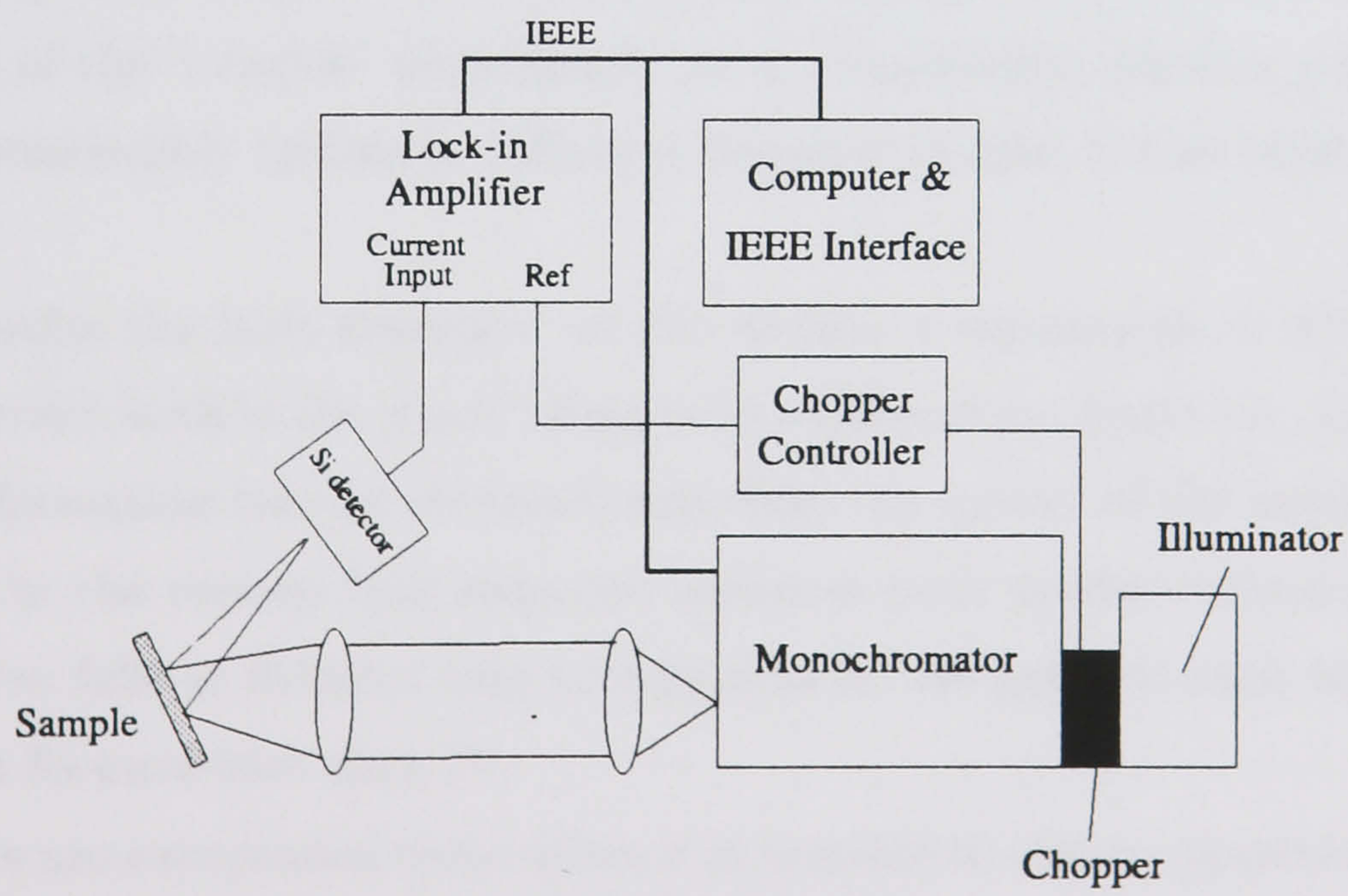

Figure 3.6: Apparatus used for the non-normal incidence reflectivity measurement from pieces of unprocessed but AR coated wafer.

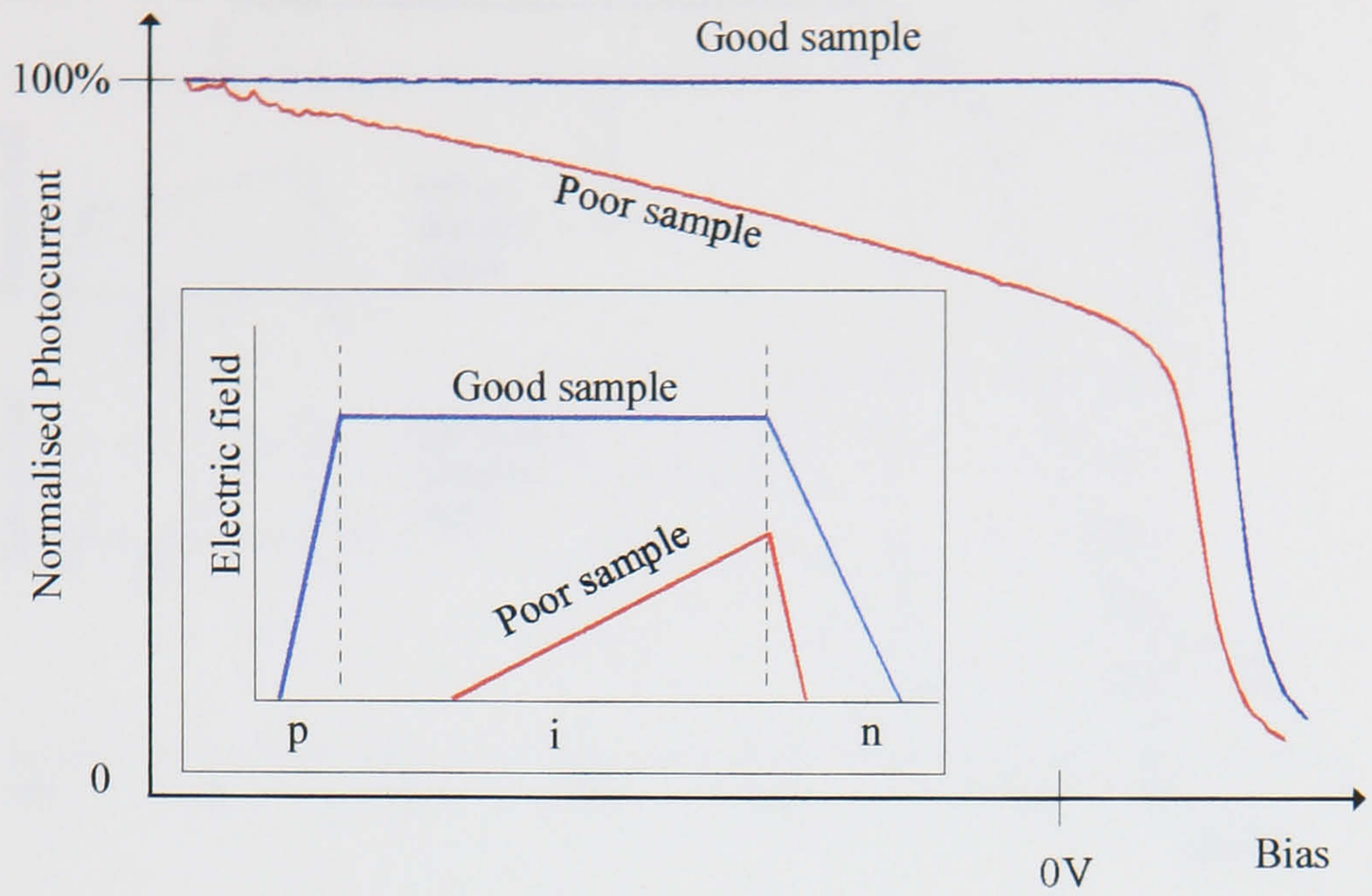

Figure 3.7: Mono-IV profiles for a good sample with low background doping and a poor sample with high p-type background doping. The inset shows probable field distributions for each sample at 0V.

field across the i-region. A good sample will maintain the same collection efficiency across the i-region, corresponding to a 'flat' mono-IV response. However, a poor sample with high background doping will lose some of the field across the i-region with increasing bias, resulting in a gradual loss in collection efficiency.

This behaviour is depicted in figure 3.7, showing both a good sample and a poor sample, together with illustrations of the field distribution in each case. The good sample maintains a depleted i-region, whereas the p-type background doping for the poor sample has left much of the 'i region' undepleted. As a consequence, carriers generated in the p-region have considerably further to diffuse in the poor sample, before reaching the depletion region.

To probe the bulk transport of the device, a wavelength of 600nm is chosen, it generating carriers both in the p and i regions as evident from figure 3.5. In most cases, only qualitative information can be obtained regarding the extent of the depletion region [56]. Any gradient in the reverse bias response indicates poor carrier collection. The point at which the curve falls at forward bias corresponds to the measurement breaking down, on account of the forward-bias dark-IV.

There are exceptional cases when it is possible to obtain quantitative information. For example, figure 3.8 shows the mono-IV profile for a single QW AlGaAs/GaAs sample with a high background doping and illuminating at a wavelength such that carriers are only generated in the QW. In this particular sample, the QW is located 227nm from the p region. The marked drop in collection efficiency, evident at -0.7V, is due to the QW

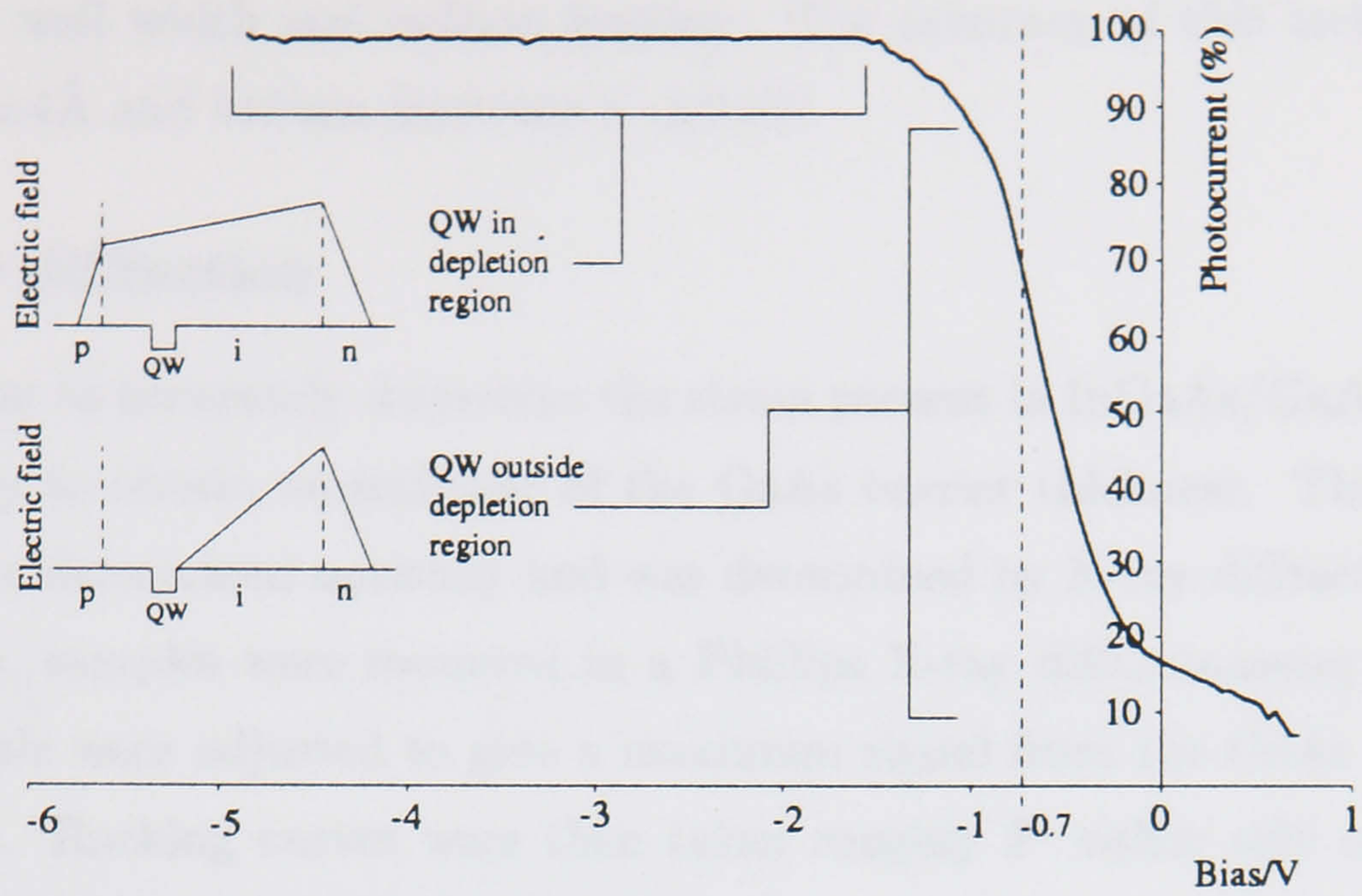

Figure 3.8: Mono-IV profile for QT902B at 300K, exciting carriers into the QW. Note the signal falls-off around -0.7V, corresponding to the loss of field across the QW depicted in the insert.

becoming undepleted as the electric field recedes towards the n-region. With knowledge of the bias and width of the depletion region, and assuming $V_{bi} = 1.4V$ (after ref [45]), it is possible to employ Poisson's equation to deduce the background doping. In this example, the background doping is found to be $5 \times 10^{15}\text{cm}^{-3}$, giving good agreement with alternative estimates [57]. A derivation of the equations involved for this calculation is given in appendix B.

The mono-IV experiment has been extended to low temperature, where the relative photocurrent (PC) and photoluminescence (PL) contributions may be measured at forward bias, allowing the extent of non-radiative recombination to be estimated [58]. This PCPL technique is applied in chapter 4 and discussed in some detail in section 4.2.1.

3.3.5 Low Temperature Photocurrent

The composition and well width of the InGaAs/GaAs MQW was determined from photocurrent spectra taken at low temperature. The technique is described in detail elsewhere [59, 45]. Briefly, the low temperature photocurrent measurements were taken using the same optical setup as depicted in figure 3.4, but with the sample placed in an Cryophysics closed cycle cryostat. The samples were cooled to 50-100K, reducing the thermal broadening of the exciton peaks and allowing the QW transition energies to be determined to within 4meV. So long as four or more energy levels could be identified, a contour map in QW width and band-offset was plotted for each energy level and their intersection deter-

mined the QW well width and indium fraction. The accuracy of this technique afforded well widths to ±4Å and indium fractions to ±0.5%.

3.3.6 X-ray diffraction

In order to accurately determine the strain present in InGaAs/GaAs MQW layers, it was necessary to obtain an estimate of the GaAs barrier thickness. This is a quantity which cannot be determined optically and was determined by X-ray diffraction (XRD).

Briefly, samples were mounted in a Phillips X-ray diffractometer and the X-ray beam and sample were adjusted to give a maximum signal from the GaAs substrate from the [004] plane. Rocking curves were then taken roughly 2° either side of the substrate signal.

The rocking curves were subsequently analysed using an accompanying simulation program (PC-HRS). The program was able to fit any strained sample to a high degree of accuracy, giving information about the MQW dimensions and composition (see section 6.2). However, the software package was unable to take strain relaxation into account, complicating the analysis of the relaxed 5% virtual substrate InGaAs/GaAs strain-balance samples, discussed in chapter6. Simulations assuming GaAs or $In_{0.05}Ga_{0.95}As$ substrates, were unable to give satisfactory fits to the lattice-parameter peaks. However, the period of the satellite peaks was largely independent of the choice of substrate and allowed the MQW period to be determined. Section 6.1.3 reports good agreement between barrier thicknesses obtained using this XRD technique with values obtained from high-resolution transmission electron microscopy (TEM).

Chapter 4

Carrier dynamics & quasi-Fermi level measurements

The physical principles for a photovoltaic cell were discussed in chapter 1.2 and showed how it is possible to determine limits to the photovoltaic power conversion efficiency for bulk semiconductor solar cells. The issues are more complex for quantum well solar cells and the issue of a fundamental efficiency advantage has yet to be fully resolved.

This chapter briefly reviews existing models for quantum well solar cell efficiency and describes an attempt to determine the validity of certain models via an experimental determination of the quasi-Fermi level separation.

4.1 Models for quantum well solar cell efficiency

Before describing any particular model in detail, it is worth noting that until the proposal of quantum well solar cells, the diode characteristics of quantum well devices had not been extensively studied in the low forward bias regime.

An early analysis by Ross & Nozik [60] showed that extremely high efficiency cells could be achieved using hot-carriers. In an entirely general analysis, they showed that if a material were able to sustain a hot-carrier population over the carrier collection time scale, then efficiencies reaching 65% could be achieved. Subsequent searches for such a material have shown that carrier cooling proceeds about ten times more slowly for superlattice p-i-n structures than equivalent bulk cells [61]. However, the rate of carrier cooling remains orders of magnitude faster than the rate of collection [62] and an improved V_{oc} has yet to be observed experimentally.

The proposal for a quantum well solar cell by Barnham and Duggan [28] high-

lighted the potential advantages which could be gained from the inclusion of quantum well layers. The analysis relied upon decoupling the usual relationship between the absorption and recombination. Under this condition the J_{sc} was determined by QW absorption, yet V_{oc} was determined by the barrier regions, leading to enhanced cell efficiencies of up to 50%.

The analysis was reconsidered by Corkish and Green [63], assuming that an MQW cell behaves as a bulk cell with some number of incremental QW cells placed in parallel with the bulk cell. The results broadly agrees with those of Barnham and Duggan, although the maximum efficiency is somewhat lower at 35%.

A number of critical reviews have been published, mainly contesting the recombination behaviour assumed by Barnham & Duggan and Corkish & Green. A study based on detailed balance theory by Araújo and Martí [64] concluded that a MQW cell possessed no efficiency advantage under assumptions valid for ideal bulk semiconductors at equilibrium. Specifically the assumptions were:

- Electrons and holes remain in thermal equilibrium and their population described by two quasi-Fermi levels ϕ_n and ϕ_p.
- Carriers possess infinite mobility and ohmic losses are neglected, implying that the quasi-Fermi levels remain constant through the device and are separated by the applied bias V_{app} such that $\phi_n - \phi_p = V_{app}$.
- Non-radiative recombination is neglected. The carrier population is only affected through photon absorption and emission.

An accompanying experimental study [65] offered experimental results in *qualitative* agreement with the quasi-thermal equilibrium theory. In particular radiative recombination was demonstrated at the QW wavelengths questioning the dominant role of the barrier as the determinant of the V_{oc}. Further work on entropy production in photovoltaic conversion [66] has shown that the models considered in references [28] and [63] violate the second law of thermodynamics, producing negative entropy in a 2-band model.

However recent theoretical work has predicted large efficiency advantages for multiband cells [67, 66]. Such cells accommodate the usual conduction and valance bands, but also at least one additional band whose carriers are described by a quasi-Fermi level ϕ_i such that $\phi_i \neq \phi_n \neq \phi_p$. Under such circumstances, the limiting efficiency is 64%.

It has been proposed that the quantum well cell is best described by the multiband model [67], rather than the two-band models in which entropy becomes negative. The

remainder of this chapter is concerned with establishing whether the quantum well solar cell corresponds to a double band model or multi-band model.

4.2 Determining the quasi-Fermi level separation

The 2-band detail balance model of Araujo & Marti made the important assumption that the quasi-Fermi level separation was constant throughout the depleted region of the device. Under their analysis, the cell behaves in fashion analogous to a bulk cell with an absorption edge equivalent to the QW cell absorption edge.

The first evidence for suppressed quasi-Fermi levels was obtained from a computer model, which was unable to fit the dark-IV profile of AlGaAs/GaAs MQW cells under the assumptions of Araujo & Marti [68].

The diode current density-voltage characteristic is influenced by a large number of recombination mechanisms, which for the sake of simplicity are separated into radiative J_{rad} and non radiative $J_{non-rad}$ components below.

$$J(V) = J_{rad}(V) + J_{non-rad}(V) \tag{4.1}$$

The dark-IV model was only consistent with experimental data when the QW quasi-Fermi level was reduced with respect to the bulk and applied bias. However the extent of non-radiative recombination is a source of considerable uncertainty for such calculations, the level being strongly dependent on material quality as discussed in chapter 2. It is much more desirable to perform calculations of J_{rad}, for which the material parameters are well known.

From a detailed balance treatment [20], the radiative current for a biased device may be expressed as $|q|$ times the photon flux emitted through the surface of the device. Neglecting thermal generation of photons, the radiative current density is expressed by equation 4.2.

$$J_{rad} = |q| \int_0^\infty \int_S a(E, \theta, \mathbf{s})(b(E, \Delta\phi)) d\omega \cdot \mathbf{dS} dE \tag{4.2}$$

where q is the electronic charge, $a(E, \theta, \mathbf{s})$ is the probability that a photon of energy E is emitted from a point $\mathbf{s}$ on the surface at an angle θ. $b(E, \Delta\phi)$ is the photon flux density from spontaneous emission under a potential $\Delta\phi$. The equation 4.3 is a generalised form of the Planck equation for emission from a non-black body [69].

$$b(E, \Delta\phi)dE = \frac{2n^2}{h^3c^2}\frac{E^2}{e^{(E-\Delta\phi)/kT} - 1}dE \tag{4.3}$$

n and T correspond to the device's refractive index and temperature, h is the Planck constant, k the Boltzmann constant and c the speed of light.

For a two-band semiconductor device, the potential $\Delta\phi$ is given by the difference between the electron and hole quasi-Fermi levels defined in section 1.2.2, such that $\Delta\phi = \phi_p - \phi_n$. In the absence of series resistance, the potential or quasi-Fermi level splitting $\Delta\phi$ is equivalent to the applied bias.

4.2.1 Absolute measurement of photon flux

In order to obtain an absolute value for the quasi-Fermi level experimentally, it is necessary to measure the absolute photon flux emerging from the device. While most spectroscopic instruments are designed to determine peak positions very accurately, the calibration of such instruments for absolute photon flux measurements is more complicated.

Figure 4.1 depicts the apparatus used for the experiment. The sample was mounted in a closed cycle cryostat providing a temperature range from 15K to 300K, stable within ± 0.1K. The luminescence was collected and focussed into a 30cm Bentham monochromator by two lenses. A 300 lines/mm grating dispersed the luminescence and the resulting spectra was imaged onto a Peltier cooled CCD camera. When the sample was illuminated with a laser, a neutral density (ND) 2 filter was placed in front of the monochromator, to reduce the laser line to a level tolerated by the CCD detector. All spectra were corrected for the quantum efficiency of the CCD camera and for spectral fluctuations of the ND filter. A Keithley source measurement unit was used to control the bias and measure the corresponding dark/photocurrent.

The luminescence calibration was performed by exploiting the bias behaviour of SQW diodes at low temperature. With a laser pump exciting carriers only in the quantum well, the photocurrent (PC) is observed to saturate in reverse bias, while the integrated photoluminescence (PL) is observed to saturate at 'flat-band' [1] in forward bias [70]. The graph shown in figure 4.2 illustrates the interplay at low temperature (10K) between carrier escape (tunneling) at reverse bias and luminescence at forward bias; each saturating at the extremes.

In the limit where the non-radiative contribution is small, the generation rate due

[1] At low temperature, the thermal shift in band-gap ensures the biases encountered during the calibration process are well below the point at which EL will occur.

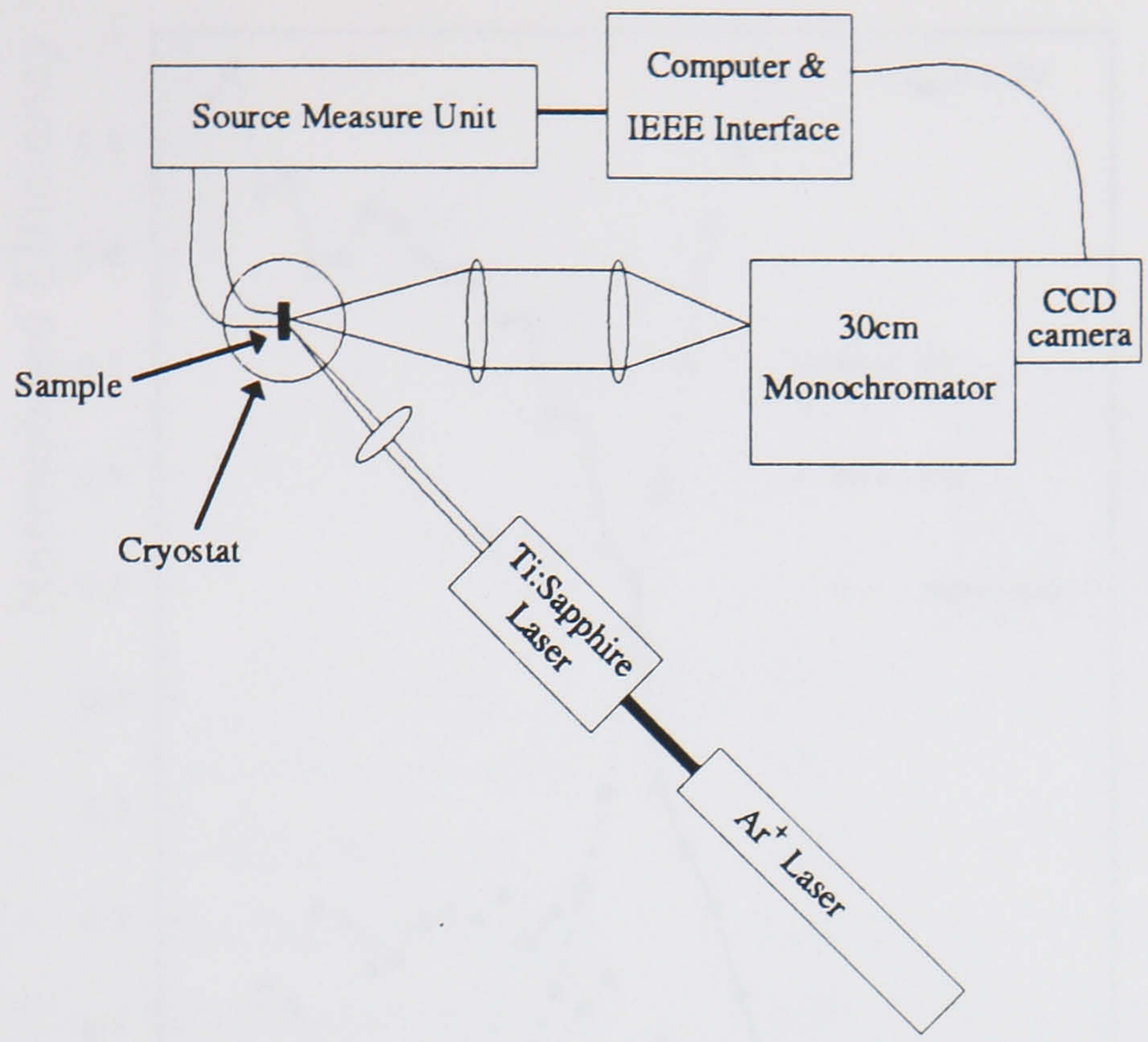

Figure 4.1: Schematic diagram showing the apparatus used for measuring PL and EL.

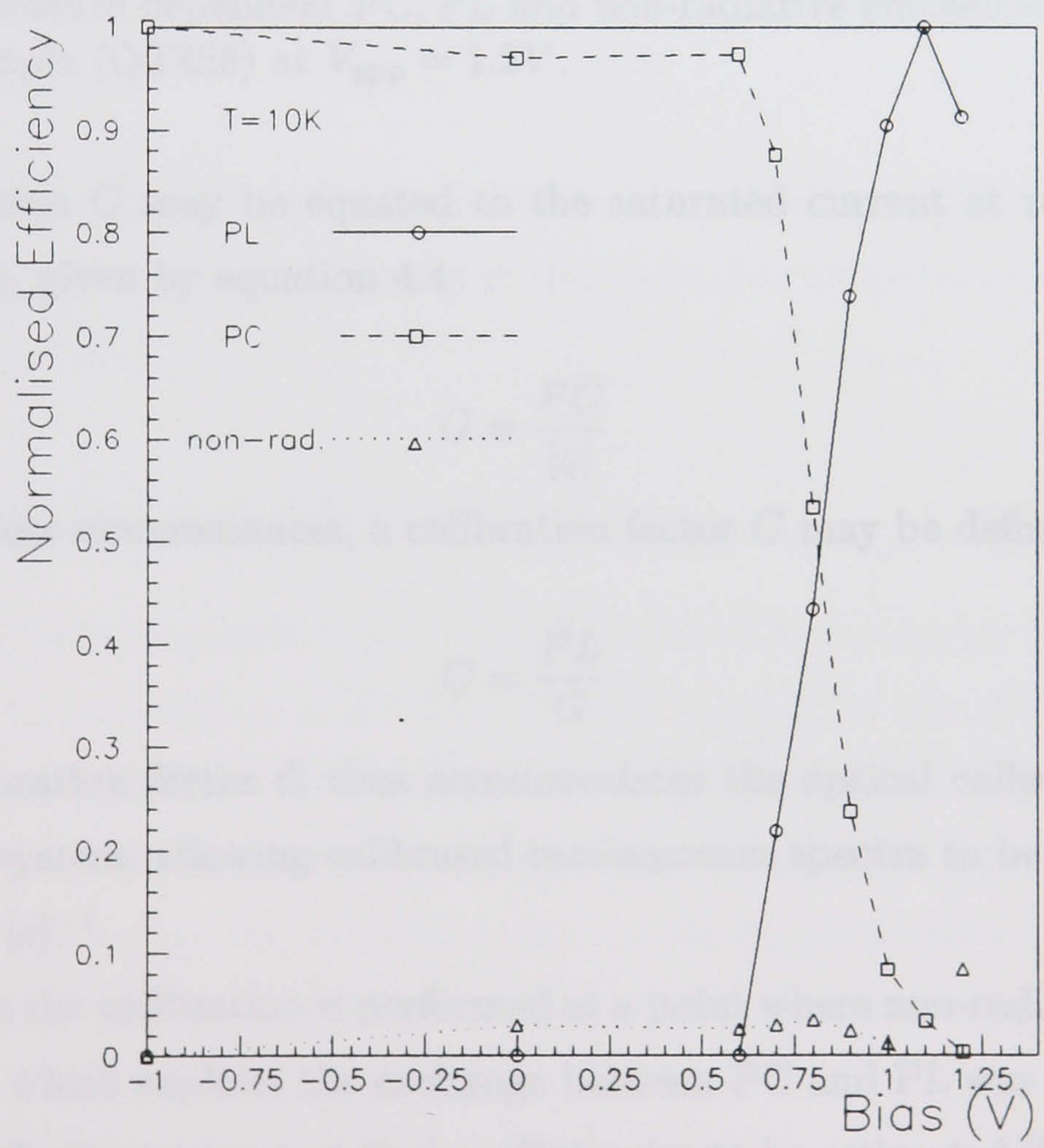

Figure 4.2: Bias dependence for the PC, PL and non-radiative efficiencies (NR=1-PC-PL); GaAs/InGaAs sample (QT458) at 10K.

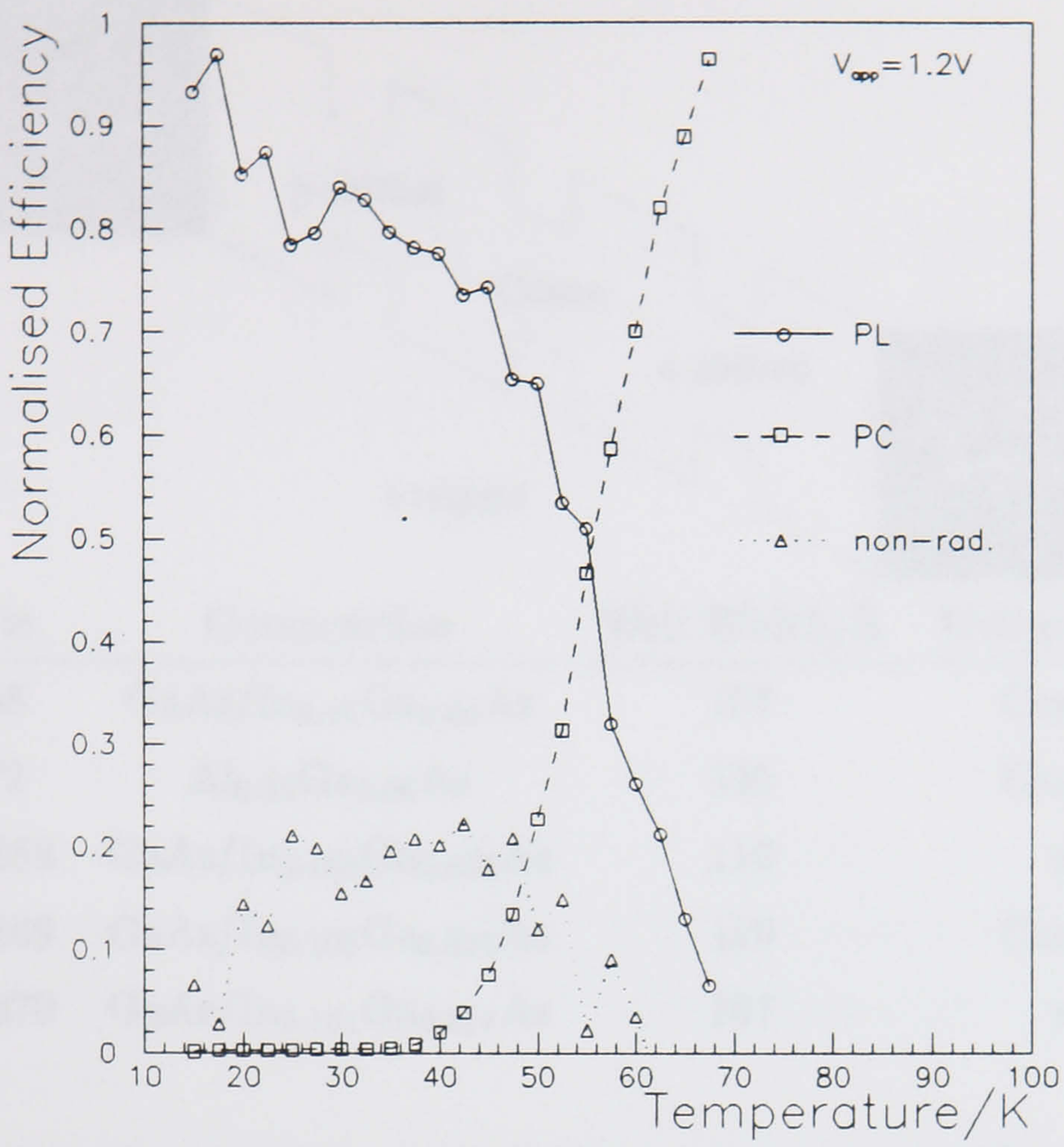

Figure 4.3: Temperature dependent PC, PL and non-radiative efficiencies (NR=1-PC-PL); GaAs/InGaAs sample (QT458) at $V_{\text{app}} = 1.2V$.

to the laser radiation G may be equated to the saturated current at reverse bias by the electronic charge q, given by equation 4.4

$$G = \frac{PC}{|q|} \tag{4.4}$$

Under these circumstances, a calibration factor C may be defined such that

$$C = \frac{PL}{G} \tag{4.5}$$

The calibration factor C thus accommodates the optical collection losses within the measurement system, allowing calibrated luminescence spectra to be measured in units of [photons]$[eV]^{-1}[s]^{-1}$.

To ensure the calibration is performed at a point where non-radiative processes are weak, a technique which exploits the exchange between PC and PL was used, allowing the relative escape, radiative and non-radiative efficiencies to be estimated [58]. The technique relies on simultaneous measurements of PC and PL which are subsequently normalised, taking into account temperature and bias shifts in absorption. Fig. 4.3 shows the PC, PL and non-radiative components for sample QT458, spanning a temperature range from 15

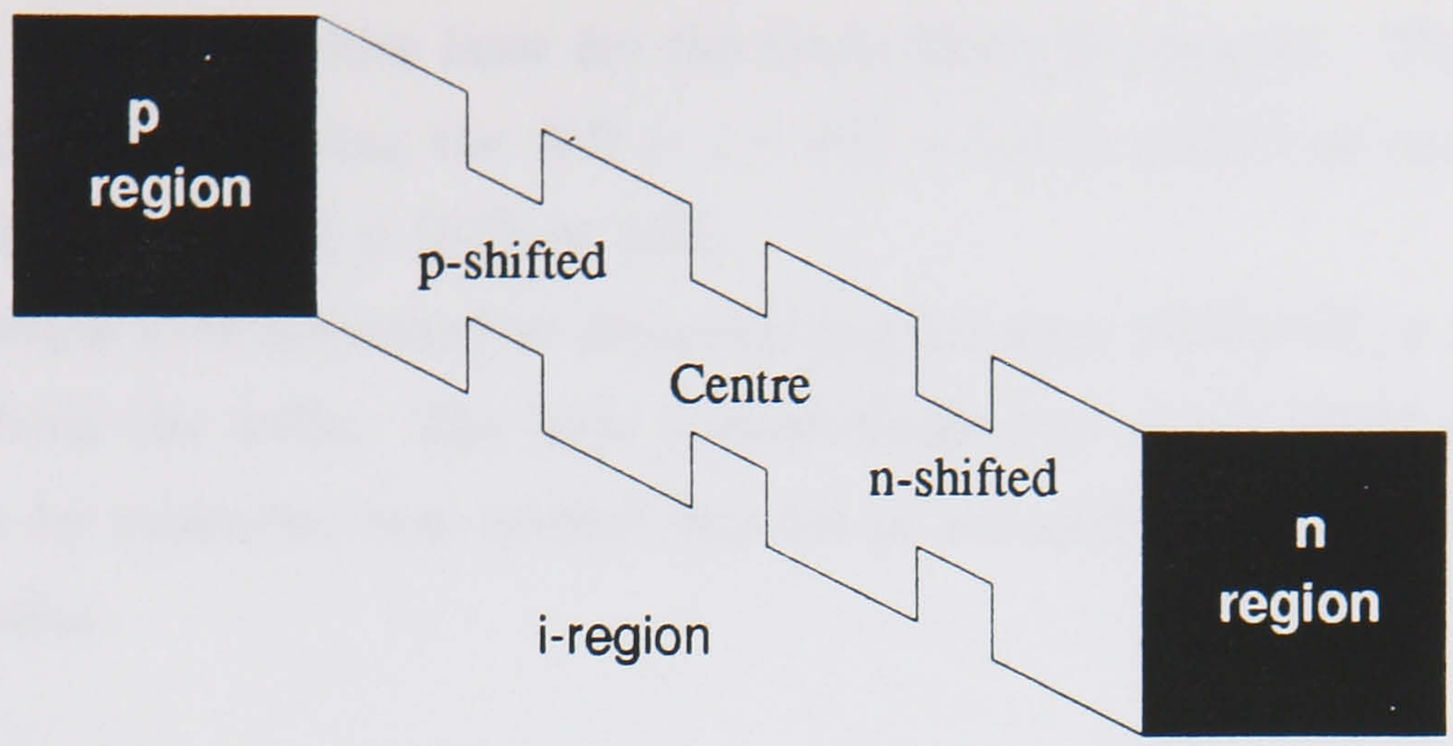

Sample	Composition	Well Width/Å	Well position
QT458	$GaAs/In_{0.16}Ga_{0.84}As$	107	Centre
NU972	$Al_{0.34}Ga_{0.66}As$	145	Centre
RM1368	$GaAs/In_{0.165}Ga_{0.835}As$	110	p
RM1369	$GaAs/In_{0.165}Ga_{0.835}As$	110	Centre
RM1370	$GaAs/In_{0.181}Ga_{0.819}As$	107	n

Table 4.1: Characterisation data for single QW samples for which EL measurements were performed. The well position column indicates the location of the QW, with reference to the figure above.

to 70K. At low temperature impurities are frozen out and carrier lifetimes are long, making radiative processes dominant. The PL is quenched at higher temperatures and carrier escape dominates the system [71].

4.3 Samples for experiment

A GaAs/InGaAs sample (QT458) and AlGaAs/GaAs sample (NU972) were available for the experiment with a single QW (SQW) located at the centre of the i-region. A further three GaAs/InGaAs samples were grown by Bob Grey[2] by MBE, as a nominally homogeneous set for investigating the influence of the QW location in the i-region. Each sample was processed into circular mesas as described in section 3.2 and table 4.1 summarises the samples and their properties deduced from low temperature photocurrent spectroscopy [59]. Full growth descriptions may be found in the appendix.

The calibration was performed at 15K, illuminating with a 752nm, 1.55mW beam from a cw solid state diode laser for the AlGaAs/GaAs sample and a 880nm, 0.9mW

[2]EPSRC III-V Facility, University of Sheffield, U.K.

BIBL
LONDON
UNIV.

beam from the CW Ti:Sapphire laser for the GaAs/InGaAs samples. The non-radiative recombination determined using the $NR = 1 - PC - PL$ as described earlier, yielding a non-radiative efficiency of $(15 \pm 10)\%$ at 15K.

EL spectra were measured at temperatures between 200-300K, a regime of rapid carrier escape from the wells. The high optical sensitivity of the CCD camera allowed luminescence to be measured over several decades of intensity, at biases around the solar cell operating point.

4.4 Modeling EL emission

A computer model was written by Dr. Jenny Nelson and she used it to fit the measured EL data to extract the quasi-Fermi level separation. The model employs the detail-balance theory outlined in section 4.2, applying it specifically to single quantum well devices. A full theoretical treatment has already been published [72, 73], so a review of the model is presented here.

It can be shown from detailed balance theory, that an ideal device in quasi-thermal equilibrium with constant quasi-Fermi level separation, has an emissivity equal to the absorbtivity. Under these conditions and exploiting azimuthal symmetry, equations 4.2 and 4.3 may be expressed as equation 4.6

$$J_{\text{rad}} = q\frac{2n^2}{h^3c^2}\int_0^\infty \frac{E^2}{e^{(E-\Delta\phi)/kT}-1}\int_S\int_0^{\theta_c} a(E,\theta,s)\cos\theta(2\pi\sin\theta d\theta)dsdE \qquad (4.6)$$

Geometrical factors are: θ is the internal polar angle for the emitted flux and θ_c is the critical angle for the relevant surface. The surface integral S refers to both the front and back surfaces and the absorbtivity $a(E,\theta,s)$ depends on the surface in question.

The diagram shown in figure 4.4 shows relevant rays for the absorbtivity. Throughout the analysis, the substrate is assumed to be a perfect photon sink.

The front surface absorbtivity a_{front} is formulated from a single pass through the device where $\alpha(E)$ is the absorption coefficient, z is the thickness of the absorbing layer and $r(E,\theta)$ is the front surface reflectivity.

$$a_{\text{front}}(E,\theta) = (1 - r(E,\theta))[1 - e^{-\alpha z \sec\theta}] \qquad (\theta \leq \theta_c) \qquad (4.7)$$

The calculation for the back surface absorbtivity is separated into two regimes, that of total internal reflection ($\theta \geq \theta_c$) and multiple passes ($\theta \leq \theta_c$). Under total internal

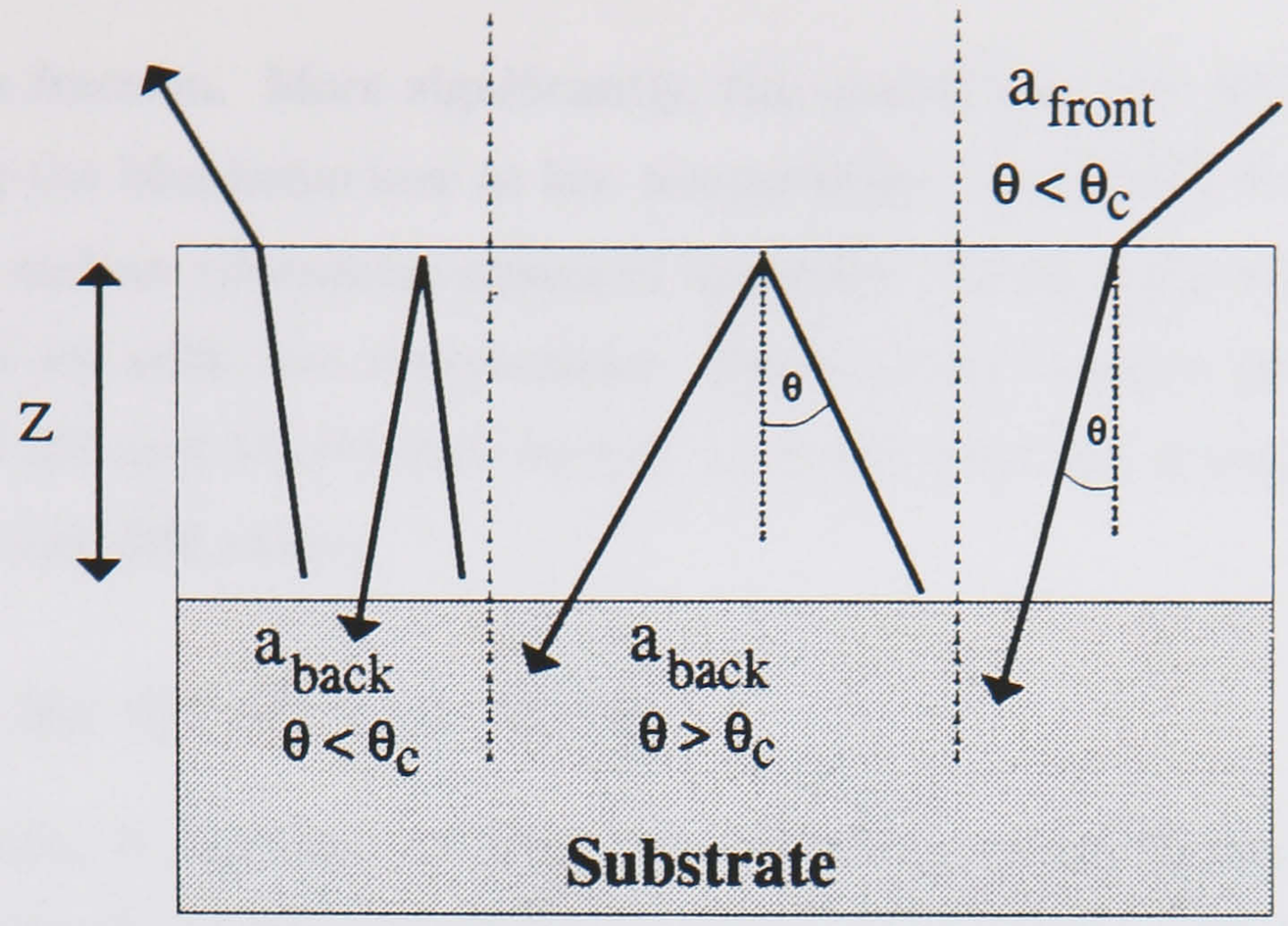

Figure 4.4: Diagram indicating the optical paths for a_{front} in equation 4.7 and a_{back} under the two regimes ($\theta \geq \theta_c$) and ($\theta \leq \theta_c$) in equation 4.8

reflection, the path-length doubles yielding equation 4.8. The multiple pass geometry has two components, one belonging to the single pass yielding the term $(1-r(E,\theta))[1-e^{-\alpha z \sec\theta}]$ and a double pass event adding the term $r(E,\theta)[1-e^{-2\alpha z \sec\theta}]$ term.

$$\begin{aligned} a_{\text{back}}(E,\theta) &= 1 - e^{-2\alpha z \sec\theta} & \theta > \theta_c \\ a_{\text{back}}(E,\theta) &= r(E,\theta)(1 - e^{-2\alpha z \sec\theta}) + (1 - r(E,\theta))[1 - e^{-\alpha z \sec\theta}] & \theta < \theta_c \end{aligned} \tag{4.8}$$

For a planar device, the surface integral reduces to the appropriate surface areas and the angular integrals are evaluated for a_{front} and a_{back}. Published values are used for the refractive index and GaAs absorption coefficient [74, 75]. The QW absorption coefficient is calculated from electron-hole overlap integrals and has been verified by successfully modelling the device quantum efficiencies [44].

The greatest error in determining the quasi-Fermi levels, stem from experimental errors incurred during the calibration. A 10% error in the optical measurement, together with a 4% error due to fluctuations in the laser output, gives an overall error in the quasi-Fermi level of ±3meV.

4.5 Results from EL measurements and modelling

EL data was taken and modelled for all samples listed in table 4.1. Good data was obtained for samples QT458 and NU972, each calibrated at low temperature. The RM series of samples suffered in that contrary to their specification, they did not possess the

same QW indium fraction. More significantly, the contacts to the RM samples were not ohmic, frustrating the bias behaviour at low temperature. As a result the calibration failed for the RM series and an alternative means of analysing the EL data was devised. For this reason the results are split into two sections. Section 4.5.1 reports the rigourous results obtained from QT458 and NU972 and section 4.5.2 describes the relevant data that could be extracted from the RM series.

4.5.1 Results for QT458 and NU972

In Fig. 4.5a, EL spectra are shown for QT458 at biases between 0.88 and 1.00V, while Fig. 4.5b shows the measured radiative currents, obtained by integrating the EL spectra. The measured dark current is also shown together a theoretical line for J_{rad}; calculated from the generalised Planck equation. The measured radiative currents are proportional to $e^{qV/nkT}$ with an ideality factor n of (1.01 ± 0.01), as anticipated for a radiative process and giving confidence in the calibration and measurement techniques. Of particular interest, the $In_{0.16}Ga_{0.84}As$ well is sufficiently shallow for both the well and barrier emission to be measured simultaneously on the same spectrum. In Fig. 4.6 the measured and modelled EL spectra are shown. The model shows that while the barrier emission is well described by $\Delta\phi_{\text{f(barrier)}} = V_{\text{app}}$, the calculated QW emission is an overestimate of the measured QW emission. If one assumes that the same temperature may be applied to the QW and barrier, then the QW emission requires $\Delta\phi_{\text{f(qw)}} < V_{\text{app}}$ and the barrier emission $\Delta\phi_{\text{f(barrier)}} = V_{\text{app}}$.

The equivalent EL spectrum is shown in figure 4.7 for NU972, the AlGaAs/GaAs sample. Very similar QW quasi-Fermi level behaviour is observed, the model indicating that the well emission is described by a quasi-Fermi level separation lower than the applied bias. No signal was obtained from the AlGaAs barriers as the emission wavelength lay beyond the detection limit of the monochromator.

The modelling was performed for EL data taken at 200, 250 and 300K, taking the highest bias which does not show series resistance in each case. The modelling data is summarised in table 4.2.

4.5.2 Results for shifted-well samples: RM1368, RM1369, RM1370

Considerable experimental difficulties were encountered with samples RM1368, RM1369 and RM1370, mainly stemming from a high series resistance. At 300K, the resistance was extracted by fitting the dark-IV curve, values of 54Ω, 76Ω and 84Ω were obtained for samples RM1368, RM1369 and RM1370 respectively. Below 300K it was impossible to

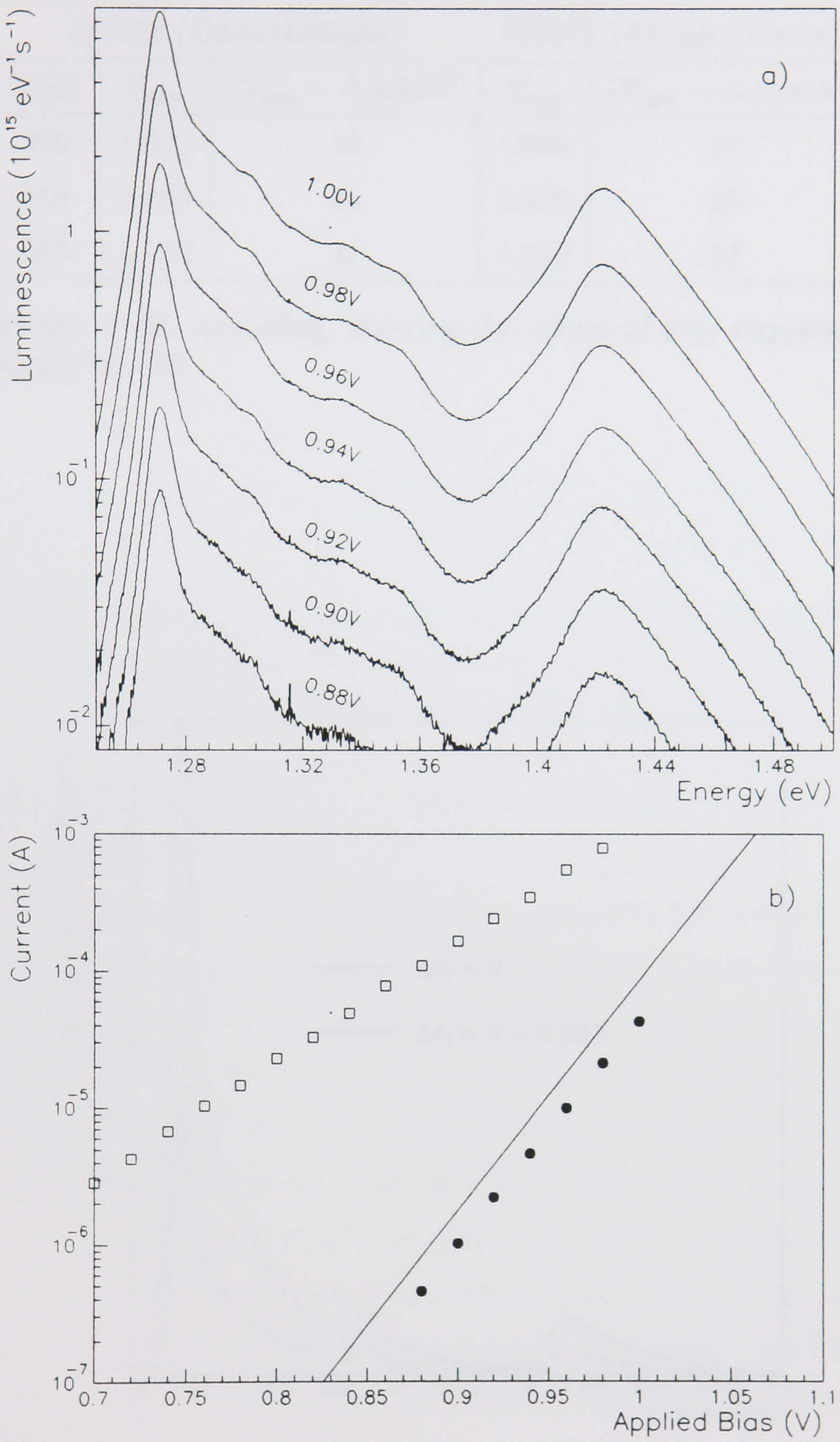

Figure 4.5: Data from QT458: a) EL spectra at 300K for biases between 0.88-1.00V. b) Current-voltage characteristics for radiative currents (filled circles), dark currents (open squares) and theoretical line J_{rad} with $\Delta\phi_{\mathrm{f}} = V_{\mathrm{app}}$

QT458 (GaAs/InGaAs)			NU972 (AlGaAs/GaAs)	
T(K)	V_{app}	$(V_{\text{app}} - \Delta\phi_{\text{f}})mV$	V_{app}	$(V_{\text{app}} - \Delta\phi_{\text{f}})mV$
300	1.000	23	1.040	14
250	1.060	14	1.120	10
200	1.140	6	1.220	23

Table 4.2: Summary of EL modelling, showing the values of $\Delta\phi_{\text{f}}$ required to fit the QW emission for samples QT458

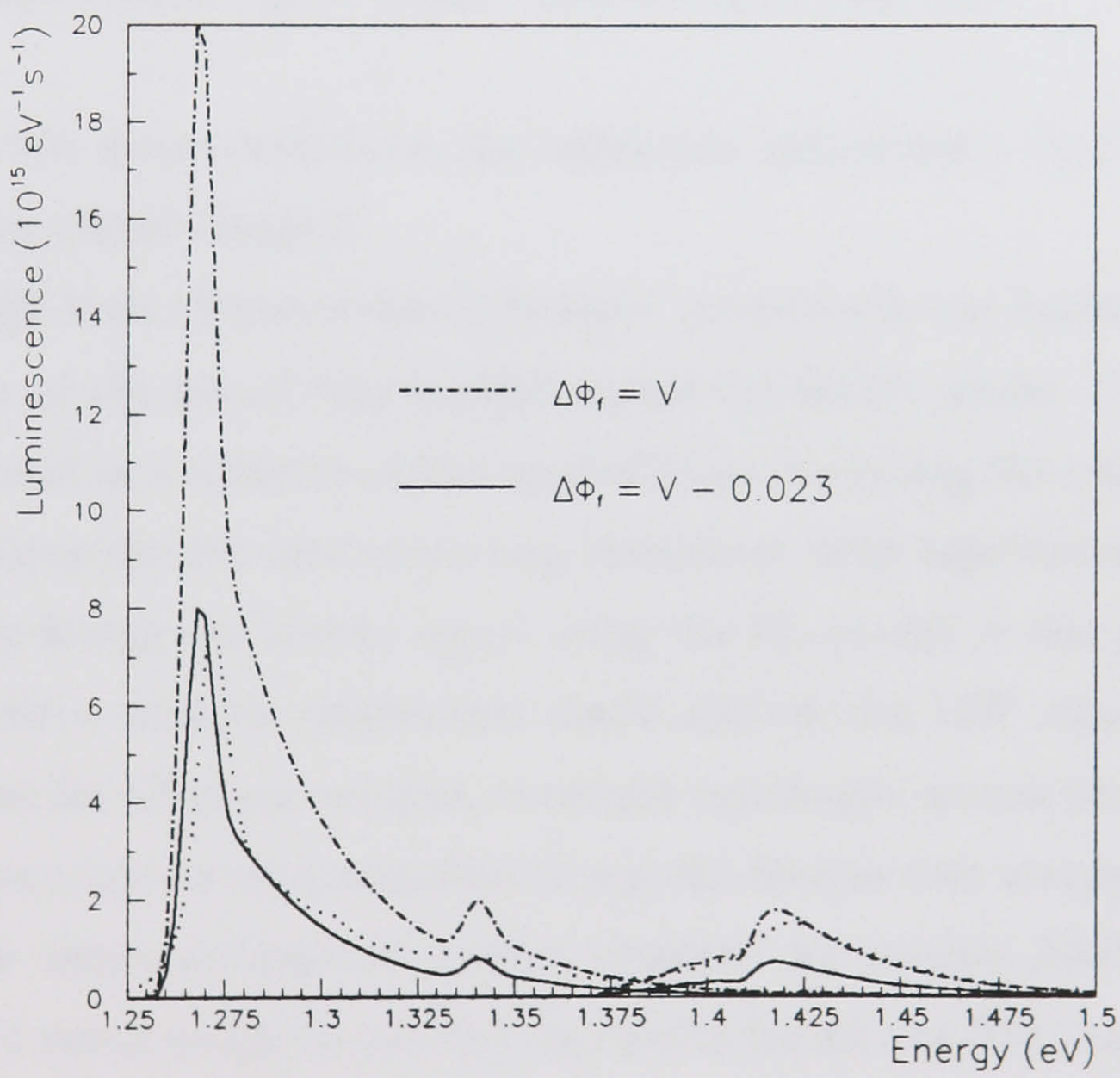

Figure 4.6: EL spectrum for QT458 at 300K; experimental data for $V_{\text{app}} = 1.000V$ denoted by solid dots, theory with $\Delta\phi_{\text{f}} = 1.000V$ denoted by a chained line and theory with $\Delta\phi_{\text{f}} = 0.977V$ denoted by a solid line.

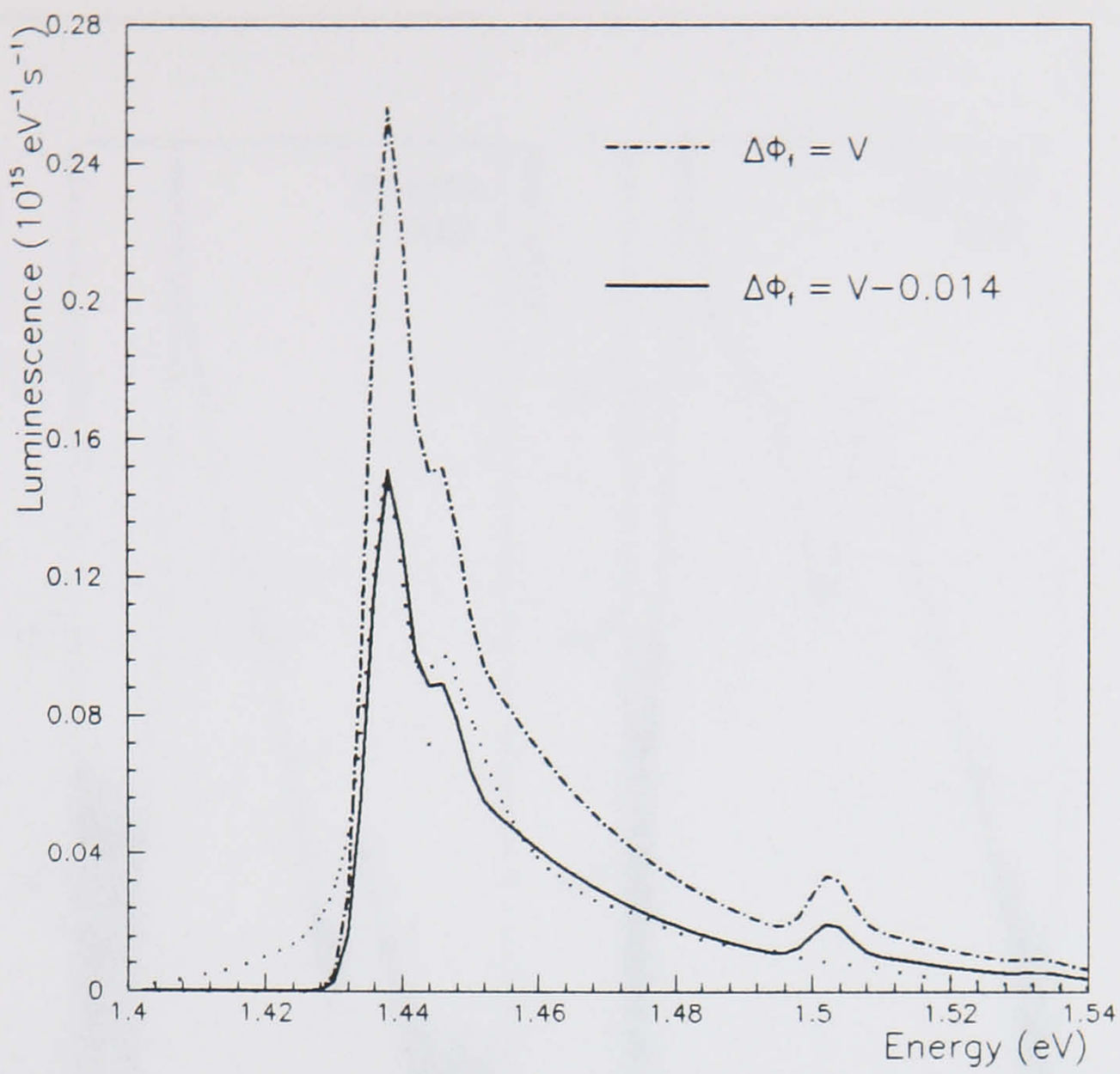

Figure 4.7: EL spectrum for the NU972 (AlGaAs/GaAs sample) at 300K; experimental data for $V_{\text{app}} = 1.040V$ denoted by solid dots, theory with $\Delta\phi_{\text{f}} = 1.040V$ denoted by a chained line and theory with $\Delta\phi_{\text{f}} = 1.026V$ denoted by a solid line.

extract a value for the series resistance, the behaviour indicating a double diode in series, characteristic of non-ohmic contacts.

Such a high level of non-ohmic behaviour complicates the modelling of such cells; one is never certain of the actual bias applied across the MQW diode. For this reason, the barrier signal was used as a measure of the applied bias; exploiting the result established for QT458 in the previous section and remaining consistent with equilibrium theory for bulk semiconductors. By fitting the barrier signal using the EL model, it was possible to deduce the applied bias and a relative comparison made against the QW signal. The shape of the spectra gathered for all three samples remained unchanged across the measured biases, establishing any spectrum as representative of a given sample and temperature.

Figure 4.8 shows normalised spectra obtained for sample RM1369 at 300K and 200K, and table 4.3 summarises the modelling results for all the RM samples. Of primary importance is the extremely good agreement between QT458 and its repeat RM1369, yielding very similar values of quasi-Fermi level suppression at all temperatures. Further, the temperature dependence is consistent with all three samples with a clear loss in QW signal at high temperature with respect to the barrier. A qualitative observation of this is evident from the spectra in figure 4.8, the QW/barrier signal is much greater at 200K than 300K

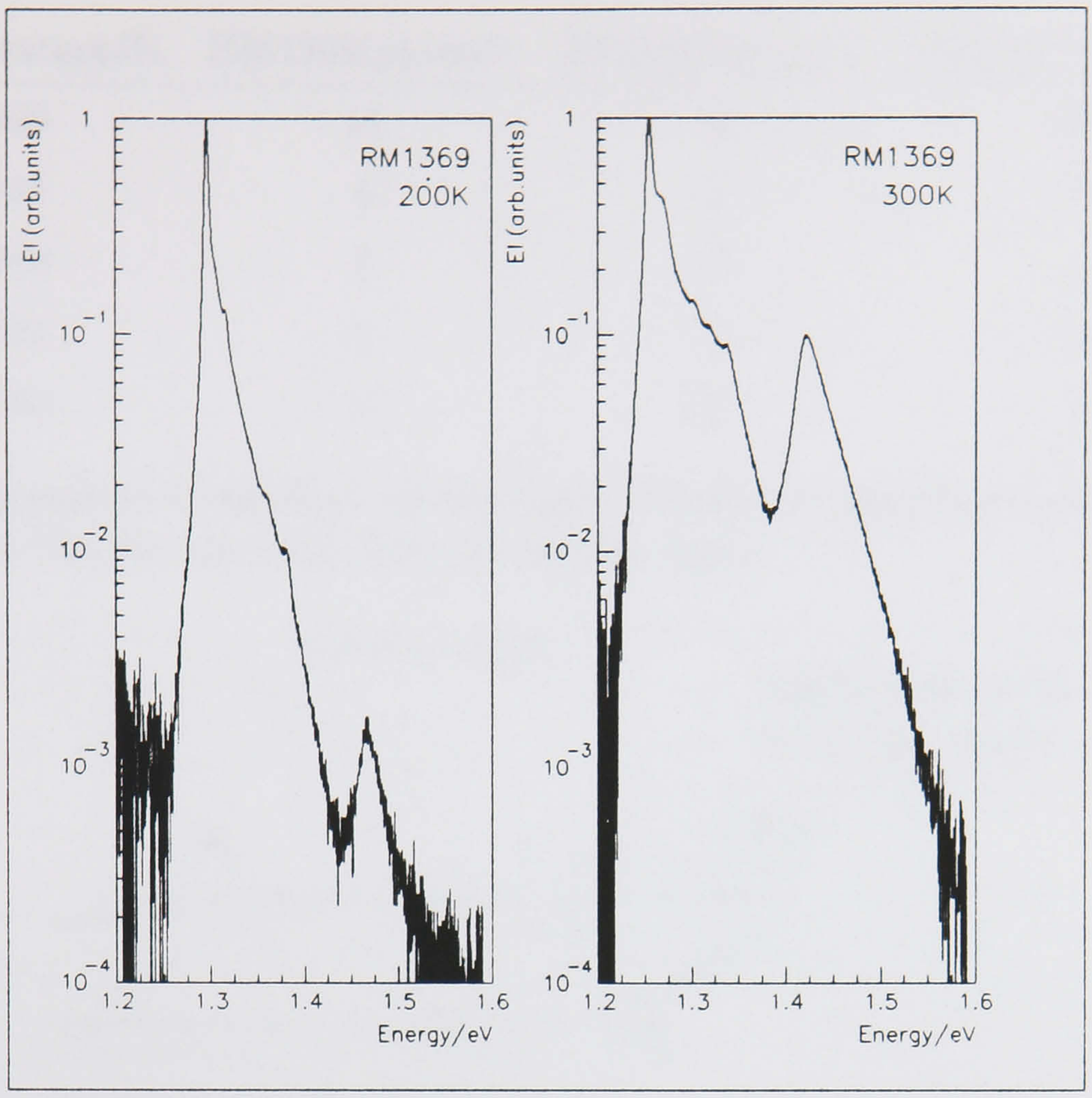

Figure 4.8: EL spectra for RM1369(c) at 200K and 300K

and similar spectra were observed for all other GaAs/InGaAs samples.

4.6 Discussion of suppressed quasi-Fermi levels

The results obtained for QT458 crucially show that the barrier is well described by the equilibrium model assuming $\Delta\phi_{\mathrm{f(barrier)}} = V_{\mathrm{app}}$. The modelling parameters have been tested extensively and are in good agreement with all characterisation performed on the samples [45, 59]. Uncertainties in the well width and alloy composition give J_{rad} to within ±20%,which is too small to explain the suppressed QW emission. Further, the n=1 bias dependence, gives confidence that the experiment is robust and commensurate with radiative theory. Further at 300K the QW emission requires $\Delta\phi_{\mathrm{f(qw)}} < V_{\mathrm{app}}$ and at lower temperatures $\Delta\phi_{\mathrm{f(qw)}} \rightarrow V_{\mathrm{app}}$ as the temperature is reduced.

All the samples showed n=2 dark-IV behaviour, indicating non-radiative processes dominate the recombination in the cell. This has implications over the quasi-Fermi level alignment, as strong levels of non-radiative recombination will lower the quasi-Fermi level separation in the i-region. For example, figure 4.9 depicts two sets of quasi-Fermi levels, relating to the radiative limit and a non-radiative regime. In the radiative limit, the bands

Temperature/K	RM1368(p)/meV	RM1369(c)/meV	RM1370(n)/meV
300	18	20	29
275	6	9	18
250	8	7	9
225	5	4	5
200	0	0	7

Table 4.3: Temperature dependence of the Quasi-Fermi level suppression required to fit the QW signal from the bias deduced from the barrier signal

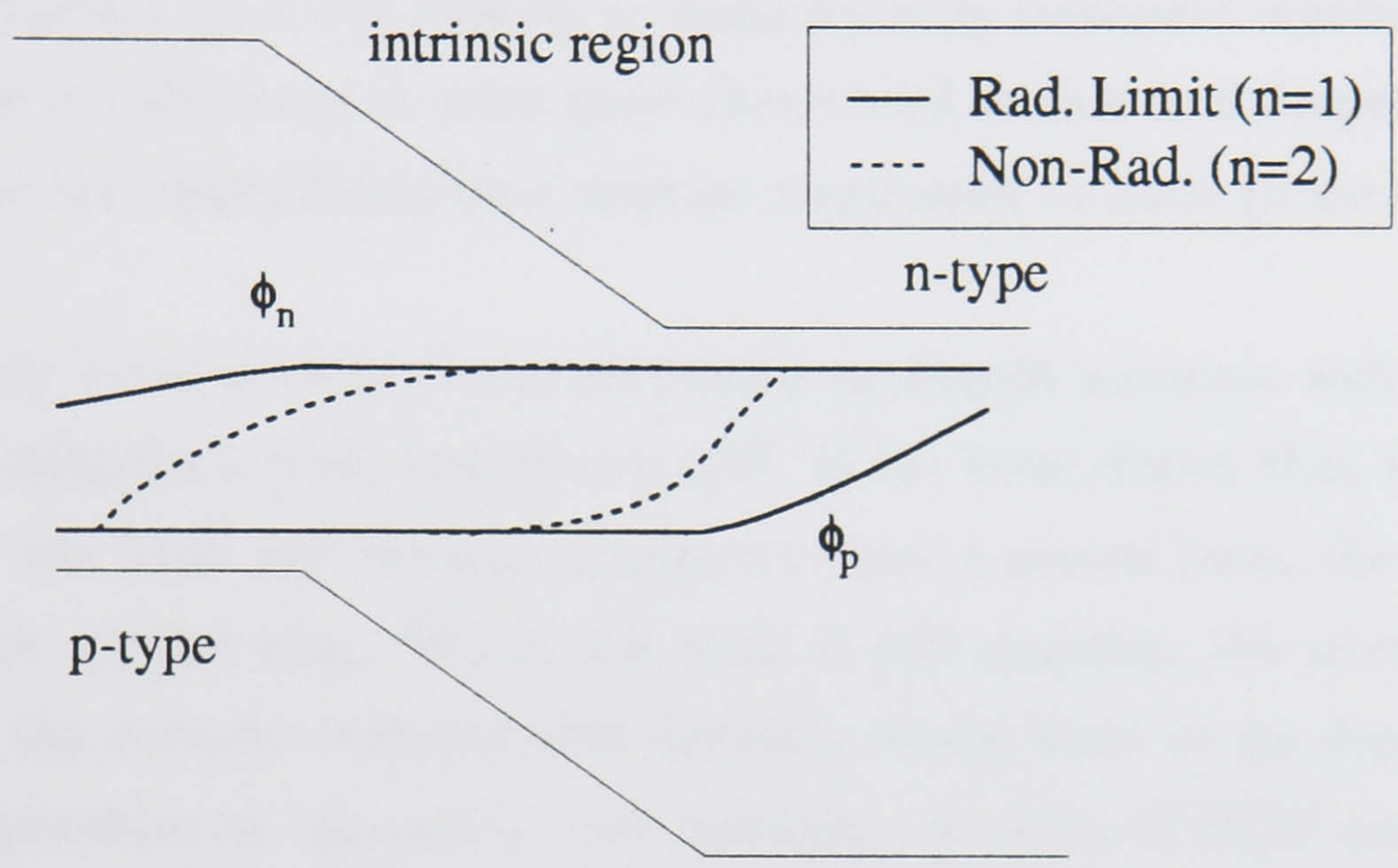

Figure 4.9: Quasi-Fermi levels for a forward biased p-i-n bulk diode in the ideal limit and under the influence of strong non-radiative recombination.

remain at constant separation across the i-region. Under strong non-radiative recombination, the bands bend within the i-region and do not remain at constant separation. Due to the absorption length of GaAs, the barrier emission comes from the first 800nm of material, i.e. all the p and some of the i-region. If non-radiative processes were sufficiently strong to affect the emission levels, then the barrier signal would be suppressed over the QW. It is the reverse that is observed and non-radiative processes are therefore discredited as an explanation for the QW suppression.

These general results support a hypothesis that carriers escape by an irreversible process; the escape time becoming longer at lower temperatures. The situation is likely to be governed by a competition between escape, capture and recombination processes, all taking place in the presence of an electric field and possibly assisted by an entropy driven process stemming from differences in the 2D and 3D density of states [76]. The temperature dependent PCPL illustrated in figure 4.3 shows that thermal escape becomes dominant at

temperatures in excess of 70K at 1.2V. This corresponds to carriers having sufficient thermal energy to escape from the QW, but also to a regime of relatively low current injection. The quasi-Fermi level behaviour reported here, stems from a more complex injected carrier distribution and the balance between capture and escape.

The results from the shifted well samples suggest similar behaviour for the p and centered samples, with a possibility that the n-shifted sample experiences a smaller local quasi-Fermi level separation due to non-radiative processes. However, it is the p and centered samples which are identical in composition and the n-shifted sample which possesses a higher indium fraction. It is not possible to make a strong statement whether the observed difference is due to differences in local quasi-Fermi level or due to a deeper well. What is clear, is that the QW quasi-Fermi level remains suppressed in three probe locations across the i-region.

Recently some work has been performed on double quantum well AlGaAs/GaAs samples [77], possessing a wide and narrow QW. It has been shown that while the quasi-Fermi levels in the wide well remains similar to those reported here, the narrow well is described by the applied bias. While this work is still ongoing, the irreversible process responsible for the reduced radiative QW emission would seem to be dependant on well depth and temperature as opposed to well position. A series of SQW samples could be grown with differing well depths in order to test this hypothesis.

It seems reasonable to conclude that the QW quasi-Fermi level separation is indeed suppressed by an order of kT with respect to the barrier at forward bias. This remains consistent with previous work on the dark currents of similar devices [68] and supports the observation that the open circuit voltage is not fixed at that expected for a device with the same effective band-gap as the QW.

4.7 Probing bias dependencies in GaAs/InGaAs QW photocurrent

The previous section of this chapter was primarily concerned with the QW radiative recombination behaviour over that of the bulk material. The reduced QW quasi-Fermi levels are likely to depend upon an anisotropy related to the electric field; it being responsible for driving charge separation from the QW. As the bias is increased across the diode, the built-in field is reduced and it is interesting to determine to what extent the QW photocurrent is affected by bias. At some point the applied bias is expected to become so great and

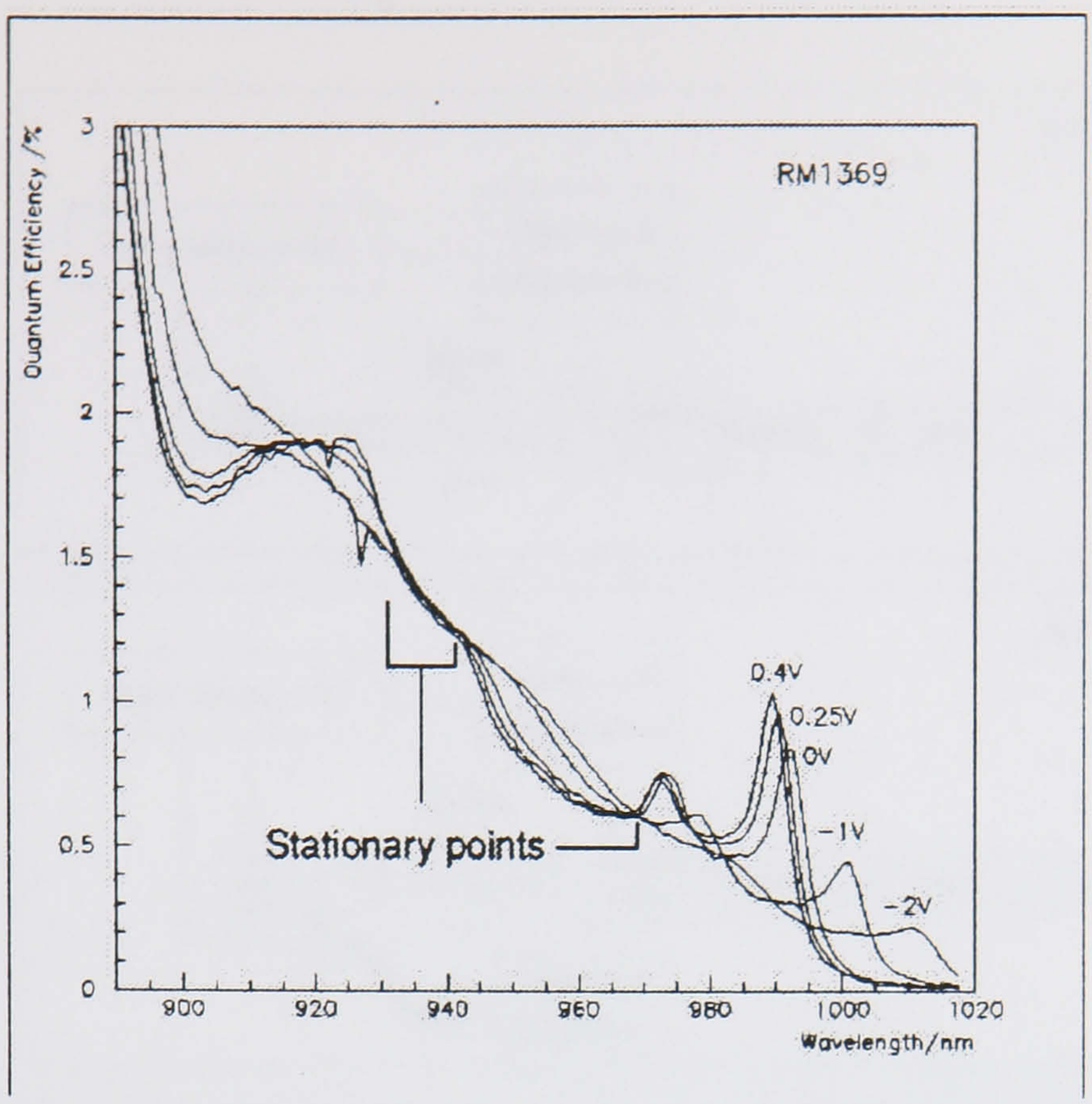

Figure 4.10: Photocurrent curves for RM1369 at 300K, showing the quantum confined stark effect and related stationary points

the internal field so small, to inhibit charge separation and lead to the loss in photocurrent. This having already been observed with the highly 'background doped' SQW reported in figure 3.8.

An experiment similar to the PCPL measurements described in section 4.2.1 was devised in order to probe bias dependencies in the QW photocurrent. The experiment relied upon photogenerating carriers into the quantum well at a range of biases and measuring the resulting photocurrent. To achieve this, it was necessary to ensure that the QW absorption at a particular wavelength is independent of bias; a criterion rarely satisfied, on account of the quantum confined stark effect (QCSE).

The quantum efficiency graphs shown in figure 4.10 indicate the effects of the QCSE from -2V to +0.4V. The exciton peaks follow a quadratic red-shift with electric field [78]. A sum rule has been established both theoretically [79] and experimentally [80], requiring that the sum of all Stark-effect absorption changes are zero. This amounts to saying that the QW absorption integrated over all QW energies, remains independent of local changes in absorption due to the QCSE. The sum rule affords the possibility of stationary points in the absorption profile and the graph shown in figure 4.10 indicates a couple of stationary points, where the QW absorption is independent of bias.

The stationary points were exploited in the non-radiative current measurement by tuning the wavelength of a CW Ti:Sapphire laser to the energy of a stationary point,

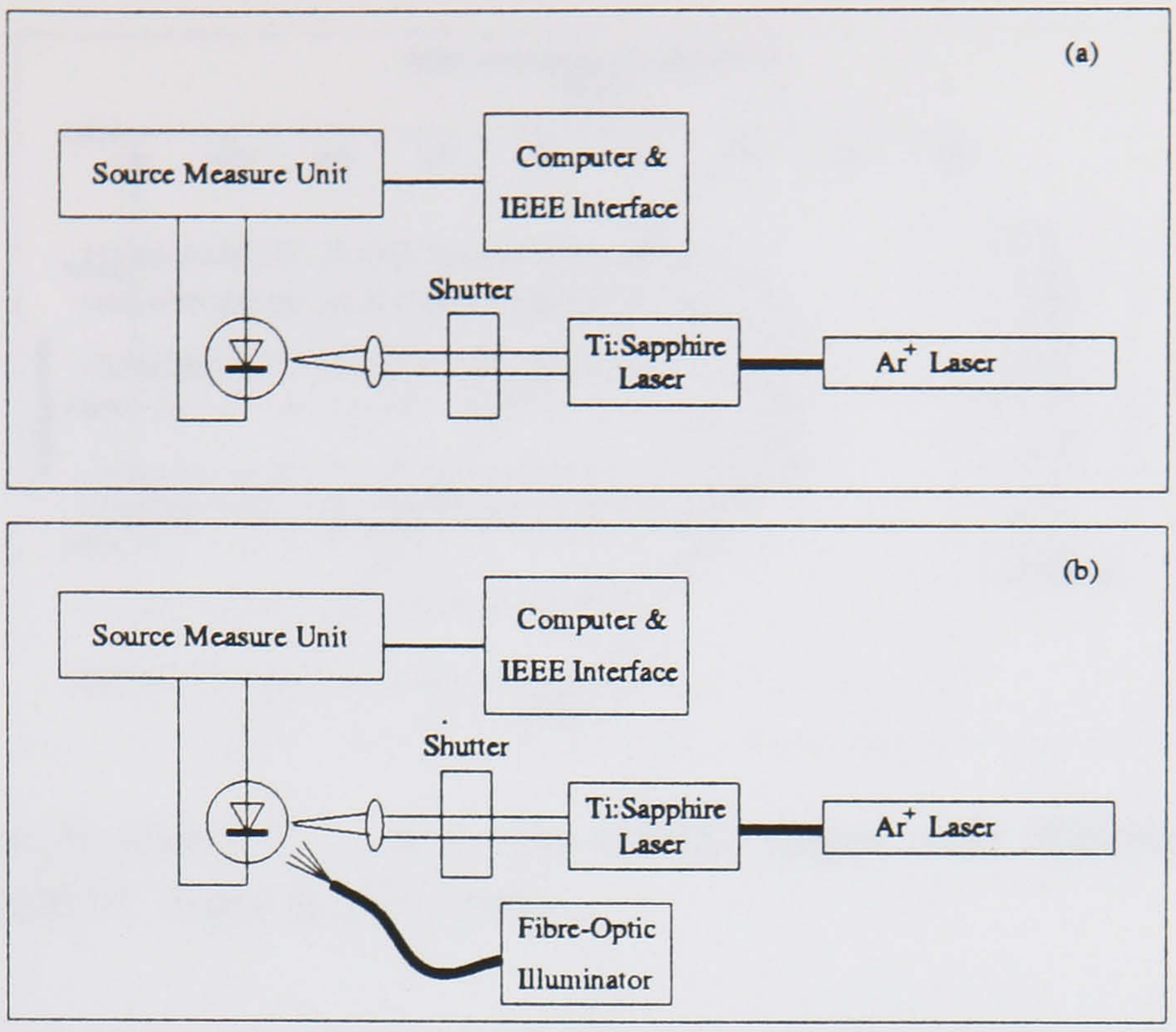

Figure 4.11: Experimental setup for room temperature photocurrent measurement: a) photogenerating with the Ti:Sapphire laser only, b) photogenerating with the Ti:Sapphire laser under continous background illumination.

ensuring carrier generation in the QW remained independent of bias.

Figure 4.11a shows the apparatus used for this experiment. The Ti:Sapphire laser was modulated to allow the successive dark and light IV measurements to be taken. The QW photocurrent was then deduced from the difference between the light and dark IV. Holding the bias constant for the dark and laser measurements, serves to decouple the laser induced photocurrent from the recombination processes. When $V < V_{oc}$, the source measure unit (SMU) serves to sink all the necessary photocurrent to maintain a particular bias and when $V > V_{oc}$[3] the SMU serves to source additional current, feeding the recombination processes to maintain the bias. The dynamic resolution of the SMU allowed photocurrents to be measured that were two orders of magnitude smaller than the dark-current. Measurements were taken at laser powers ranging from 0.02-20mW, controlled by placing neutral density (ND) filters in the path of the laser beam.

The results for QT458 are shown in figure 4.12. The linearity of the photocurrent lines indicate consistent carrier escape across the bias range at all measured intensities. Indeed, the carrier escape seems to be unaffected until the dark-IV becomes over an order of magnitude greater than the QW signal. The intersection between the PC curves and the dark-IV marks the V_{oc} point. The curvature at biases in excess of 1V was found to be caused by the SMU autorange function. Additional measurements, whereby the SMU was

[3] A condition that will never be reached under normal solar cell operation.

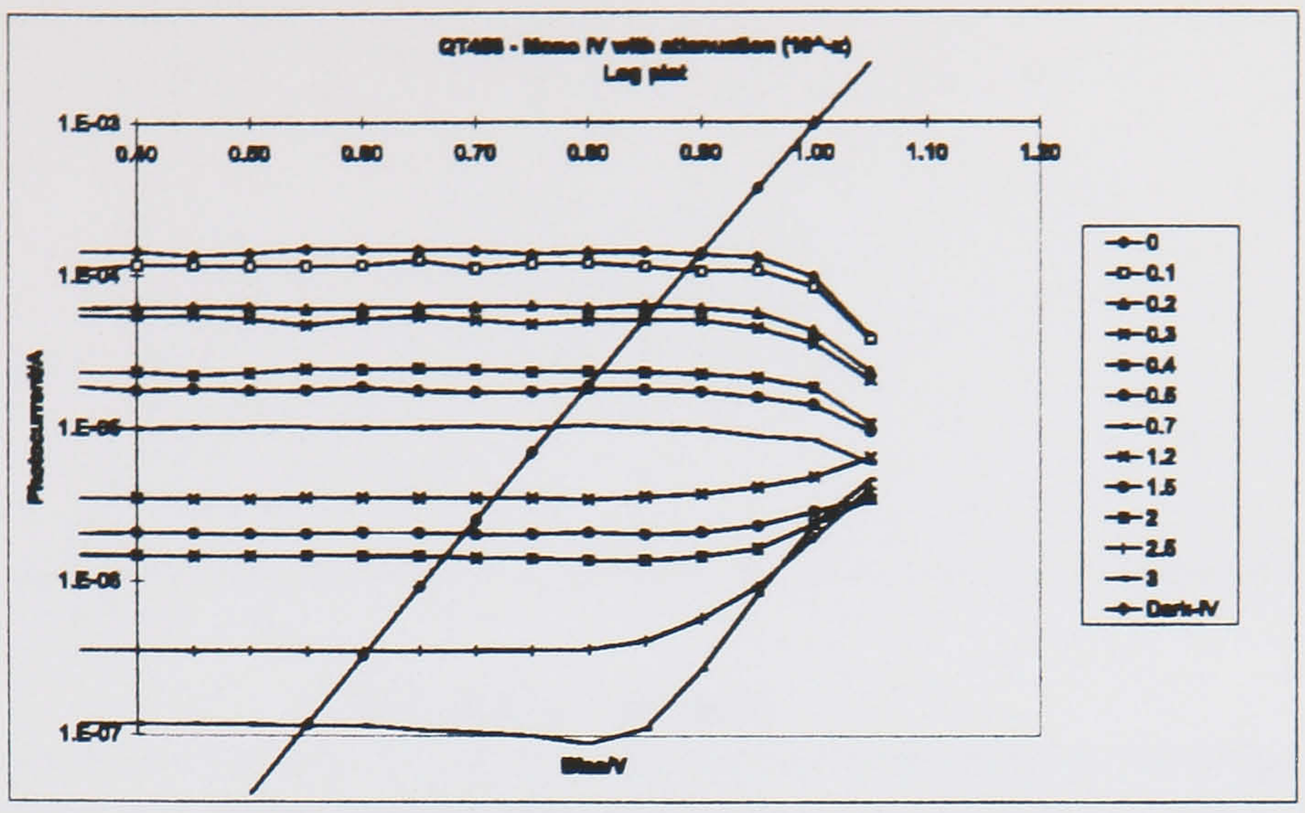

Figure 4.12: Monochromatic IV curves for QT458 taken with different strengths of ND filter. A typical dark-IV curve is also shown.

forced onto a single range, showed flat behaviour until the dark-current noise dominated the measurement.

Slightly more elaborate measurements were performed upon the the shifted-well samples; RM1368, RM1369 and RM1370. The same experimental technique was used to measure the QW photocurrent, but the effect of background illumination was also investigated; the modified apparatus is shown in figure 4.11b. For the background illuminated curves, a 3000K tungsten fibre-optic illuminator was arranged to give a comparable short-circuit current as under AM 1.5 illumination. For this measurement successive light-IV curves were taken; 3000K illumination + laser then 3000K illumination only. Also the J_{sc} expected from the QW absorption under AM1.5 illumination was calculated[4] and is indicated by the AM1.5 line.

The results for the shifted well samples are shown in figures 4.13, 4.14 and 4.15. The same device and processing difficulties described in section 4.5.2 apply, yet the low currents ensured that the series resistance was not too problematic. In every case the QW photocurrent remained unchanged across the bias range and all observable fluctuations are attributed to the SMU auto-range and laser instability. The noise floor for the background illuminated curves was several orders of magnitude greater than the non-illuminated curves, the dominant noise source being output fluctuations from the 3000K lamp.

While the accuracy of the experiment is not high (20% error due to measurement and laser instabilities), it is significant that neither the dark, or background illuminated samples show any evidence for a bias dependent photocurrent. Therefore the importance of

[4] $|q| \int_{QWlevels} F(\lambda)QE(\lambda)d\lambda$, where F is the AM1.5 photon flux, QE the quantum efficiency and q the electronic charge

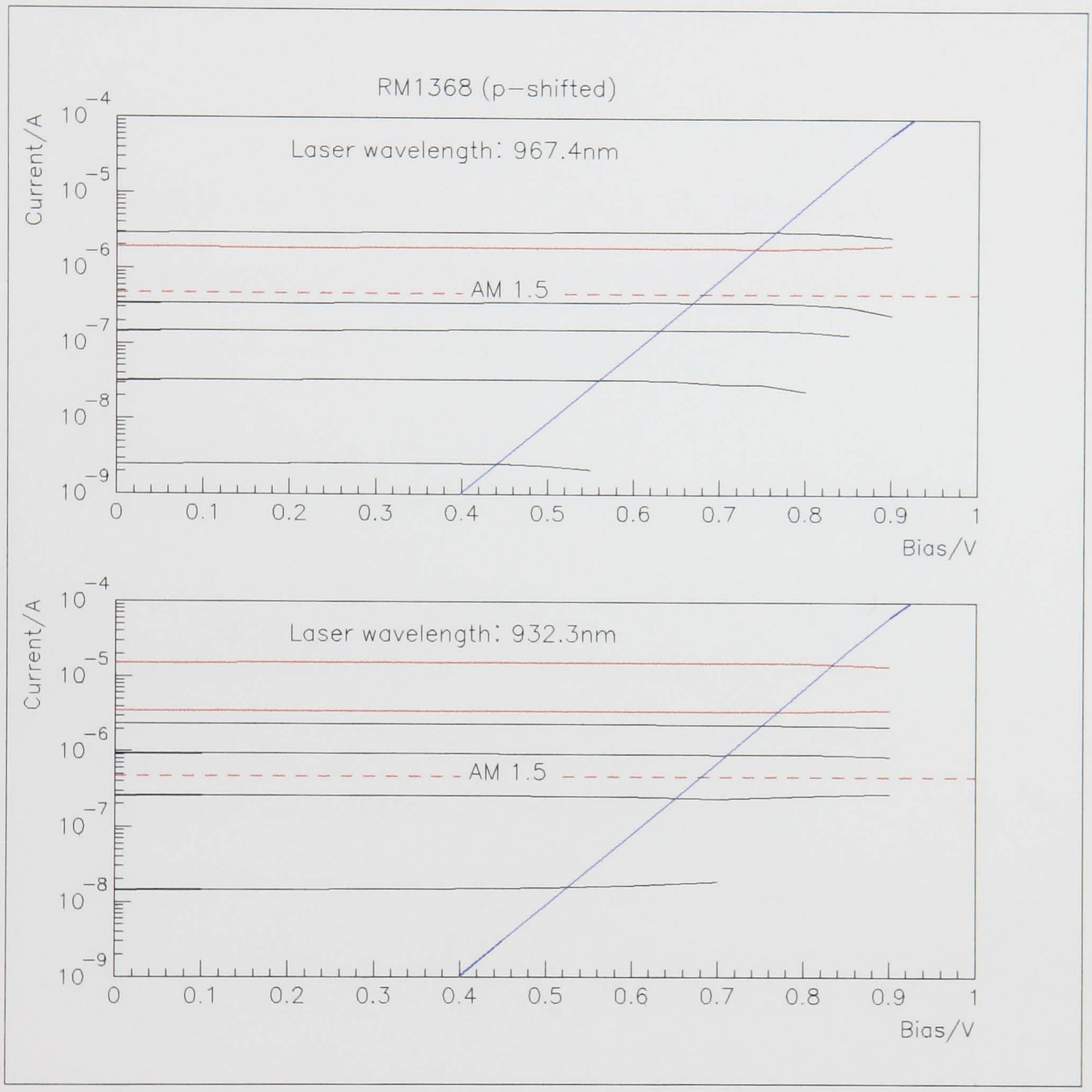

Figure 4.13: Monochromatic IV curves for RM1368 taken at different laser intensities. The red curves indicate data taken with 3000K background illumination and the blue curve indicates the dark-IV profile. The AM 1.5 line shows the approximate level of QW photocurrent under AM 1.5 illumination

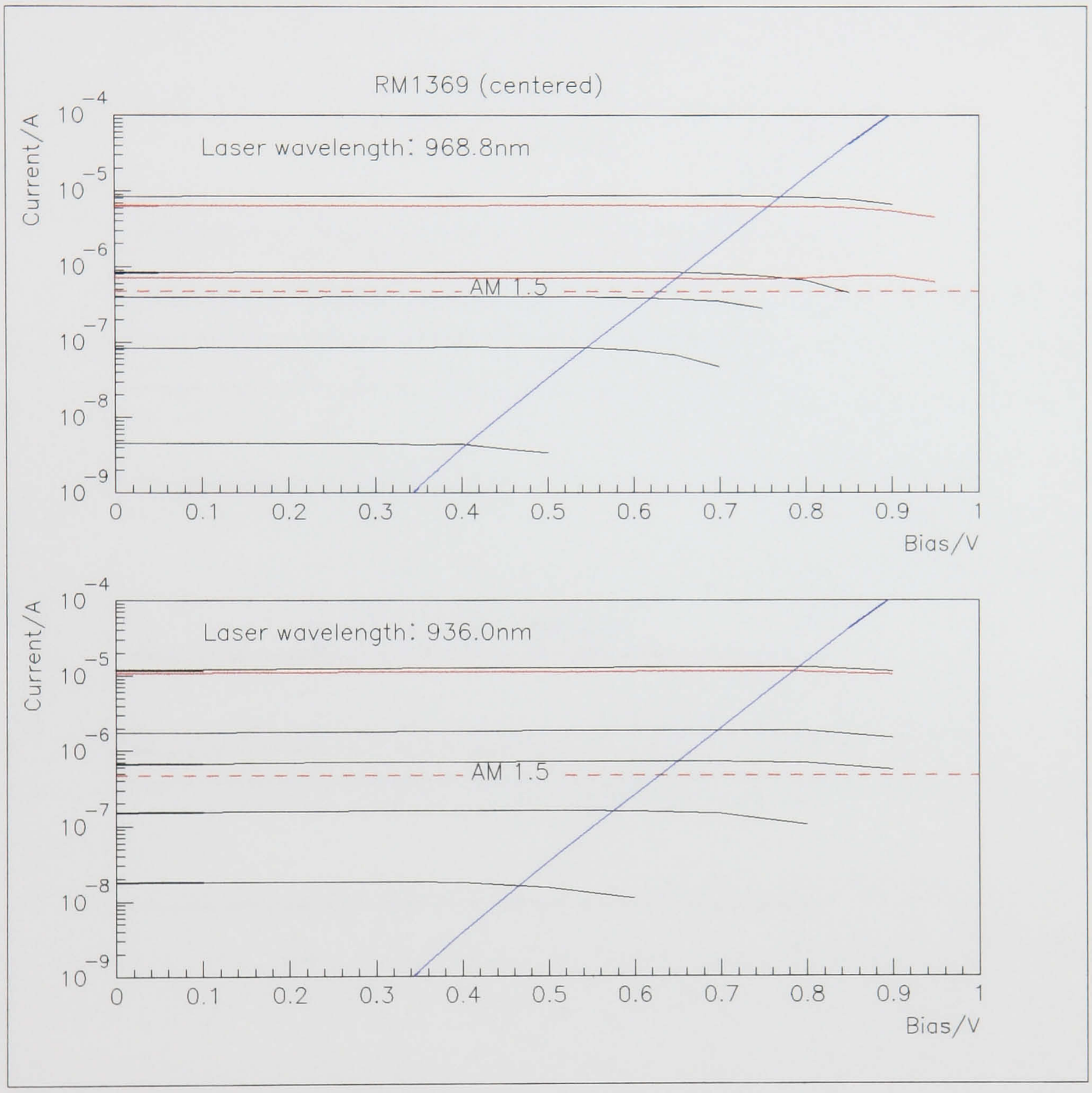

Figure 4.14: Monochromatic IV curves for RM1368 taken at different laser intensities. The red curves indicate data taken with 3000K background illumination and the blue curve indicates the dark-IV profile. The AM 1.5 line shows the approximate level of QW photocurrent under AM 1.5 illumination

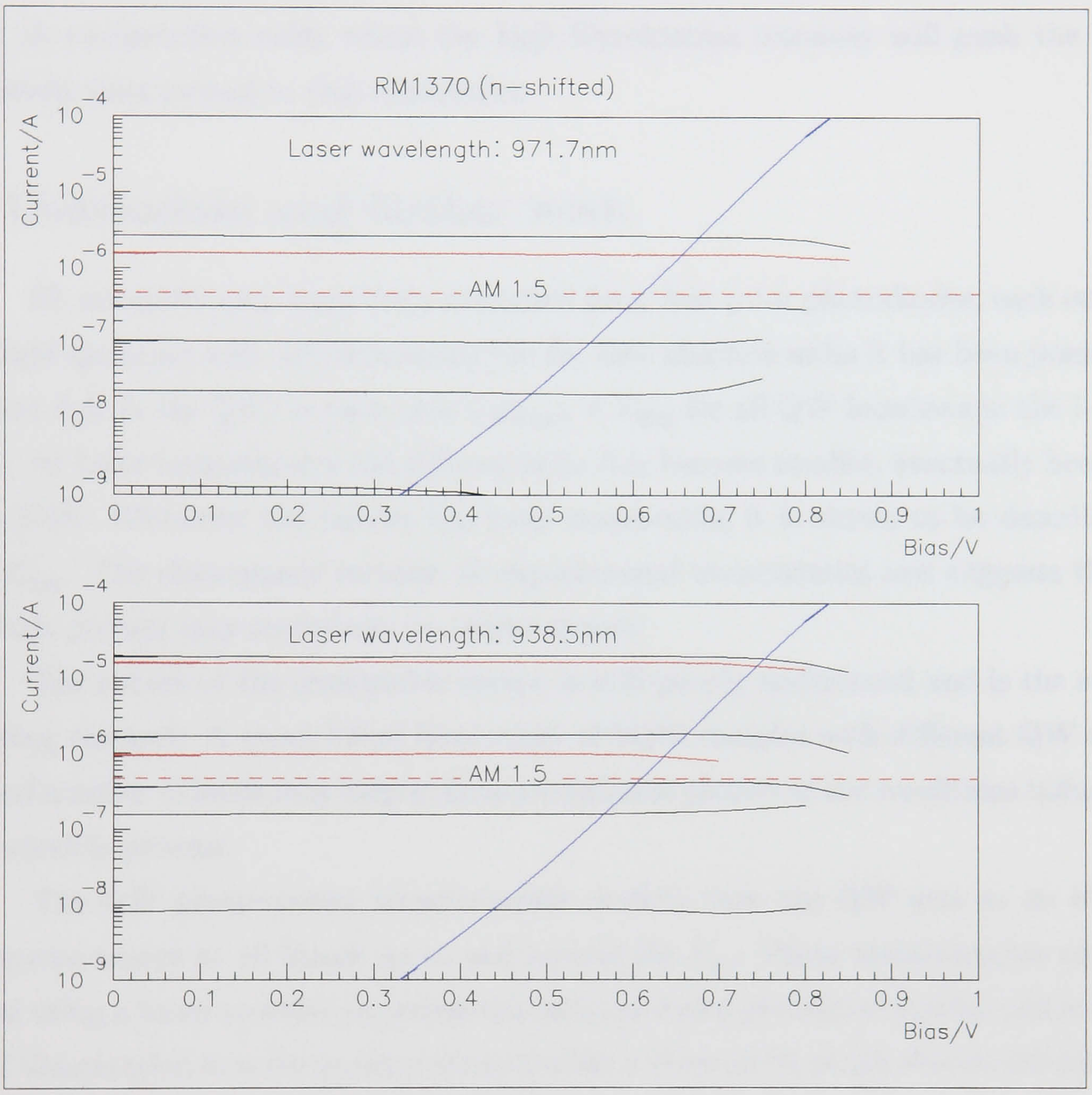

Figure 4.15: Monochromatic IV curves for RM1368 taken at different laser intensities. The red curves indicate data taken with 3000K background illumination and the blue curve indicates the dark-IV profile. The AM 1.5 line shows the approximate level of QW photocurrent under AM 1.5 illumination

this measurement lies in establishing that the same QW photocurrent conditions hold at 0V as at V_{oc} (and beyond), confirming that superposition holds for these SQW cells. Further, the measurement has been performed under the same conditions as the EL measurements described earlier. QW photocurrents corresponding to 1 sun illumination, are extracted as efficiently under high field conditions (i.e. $V = 0$) as at greatly reduced field (i.e. $V = V_{oc}$). The question over a lower-limit to the electric field remains unresolved and may hold some bearing on concentrator cells; where the high illumination intensity will push the V_{oc} to higher levels than probed in this experiment.

4.8 Conclusions and further work

EL measurements have been presented from four p-i-n photodiodes, each containing a single quantum well. By calibrating the EL into absolute units it has been possible to determine $\Delta\phi_f$ in the QW. In each case $\Delta\phi_{f(qw)} < V_{app}$ for all QW locations in the i-region at 300K. At lower temperatures the differences in $\Delta\phi_f$ become smaller, eventually becoming zero at 200K. Whenever the barrier has been measurable, it is shown to be described by $\Delta\phi_f = V_{app}$. The discrepancy exceeds all experimental uncertainties and suggests that an irreversible process may contribute to carrier escape.

The nature of the irreversible escape is still poorly understood and is the subject of on going research. A quasi-Fermi level study of SQW samples with different QW energy levels and number of levels may help to form a consistent picture of the conditions influencing the irreversible process.

The QW photocurrent measurements confirm that the QW acts as an efficient photocurrent source at all biases up to and beyond the V_{oc}. These measurements could be repeated using a more sensitive experimental setup and also performed at solar concentrator levels of illumination in order to determine whether a lower-limit to the electric field is likely to be encountered under solar power conversion.

In conclusion, the quasi-Fermi levels measured experimentally from QW diodes are not consistent with the assumptions made under 2-band equilibrium theories discussed in section 4.1. The behaviour is better described by the multi-band models, offering the possibilities of enhanced efficiency over single band-gap cells.

Chapter 5

Light trapping

Light trapping allows the optical path length of an incident ray to be greatly extended thus increasing its chances of absorption by the solar cell material. Silicon cells owe much of their performance to light-trapping techniques that ensure that the light makes several passes through the cell when the cell absorption is low. The silicon cell problem is very similar to that of the multi-quantum well cell, where strong absorption takes place at short wavelengths, but the longer wavelengths would benefit greatly from light trapping.

The first part of this chapter will discuss some techniques routinely used in silicon solar cells and discuss their application to MQW cells. The subsequent section will describe some results achieved with planar mirrors and finally the effects of radiative photon reabsorption or photon recycling will be explored.

5.1 Light trapping techniques

The diagram shown in figure 5.1 shows four types of light-trapping structure, listed in order of complexity. In each case the cells are assumed to be optically thin, that is only a small fraction of the incident light is absorbed by the cell.

1. The simplest form of light trapping solar cell is a planar cell with a back surface reflector. Light will perform a series of passes under this geometry, but a well designed solar cell will possess a good AR coating on the top surface, meaning that light is coupled very well both in and out of the cell. As a result, the largest number of passes (or trapping factor) achievable under these circumstances will be 2.

2. A textured front surface assists by coupling the incident light obliquely into the cell, thereby increasing the single-pass path-length. However, it does not greatly assist

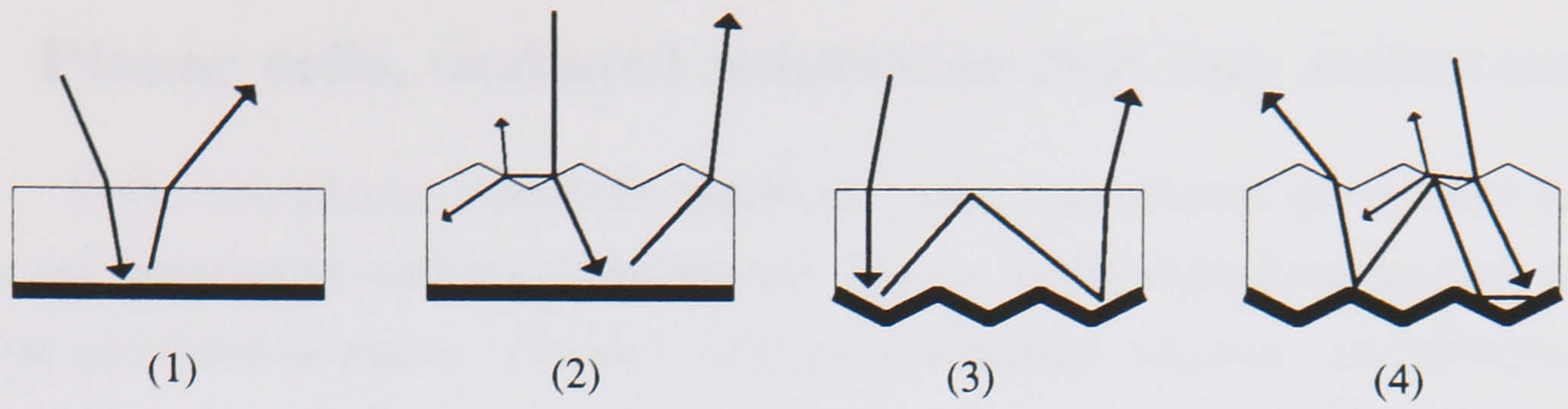

Figure 5.1: Four types of light trapping structure. In each case the rear has a mirror deposited upon it.

in actually trapping the light as the back reflected ray possess the same angular properties as the incident ray. The best trapping factor in this case is still ≈ 2.

3. A textured rear surface does allow for substantial light trapping as the incident rays have their direction randomized and only a small cone of light, within the critical angle can actually escape. Trapping factors of $4n^2$ may be achieved, where n is the refractive index [81].

4. A textured front and rear surface offers the best combination of optimal light coupling into the cell and light trapping within the cell. Again, trapping factors in excess of two may be achieved.

Achieving a back surface reflector is a straightforward process, simply depositing a reflective coating onto the rear surface of the cell. However, surface texturing as performed in cells 2-4 requires anisotropic etching. High efficiency silicon solar cells employ technique 4 to achieve light trapping, exploiting a wet-chemical etch on the [111] surface. Under suitable conditions, random pyramids and inverted pyramids may be formed. Considerable literature exists on the formation of surface pyramids and in the case of crystalline silicon, the technology is mature [82]. However, pyramid structures are not necessarily the most efficient form of surface texture on account of symmetrical reflections. A 'quiltwork' pattern of V-grooves has been proposed as a means of surmounting this problem [83]

In the case of GaAs, there is no convenient etch which can spontaneously produce pyramids on [001] surfaces. Instead lithographic techniques have been used together with anisotropic etches to obtain V-grooved surfaces. The following section describes some results obtained on planar surfaces, while section 5.3 discusses some results from V-grooved wafers.

5.2 Planar cells, undoped substrates and rear reflectors

Cells with planar geometries represent a rare coincidence, where light trapping theory and experiment meet with relative ease. From a mathematical perspective, the light trapping processes in planar cells yield analytical solutions, whereas computationally intensive ray-tracing calculations are often required for non-planar geometries. Experimental reflectivity and transmission measurements are straightforward for normal incidence, providing a good basis for comparison with mathematical models. This section describes the development of a planar geometry model, allowing for perfectly planar cavities as well as cavities with a diffuse reflection at the rear surface.

Experimentally, one measures the surface reflectivity and the transmission through a wafer or the quantum efficiency from a device. These quantities are assigned R, T and QE in the computer model.

The reflectivity parameters (illustrated in figure 5.2) are the front surface reflectivity r_f and some estimate for the rear surface reflectivity. In this model the rear surface reflectivity is separated into two components, r_b which is the direct normal incidence reflection and r_d which is a diffuse component of the reflectivity. Indeed, it is possible to define the diffuse and direct reflectivity as the integral of a scattering function $F(\Delta)$, where Δ is the deviation from the reflection angle. Figure 5.3 shows two possible reflectivity scattering functions.

For an ideal, planar reflector the distribution function $F(\Delta)$ is given by a Dirac-delta function $\delta(\Delta)$. For a random rear surface reflector, the function broadens into the diffuse curve shown.

So, for a reflectivity distribution $F(\Delta)$, the reflection parameter r_b and r_d can be written as:

$$r_b = \int_{-\theta_c}^{\theta_c} F(\Delta)d\Delta \tag{5.1}$$

$$r_d = \int_{\theta_c}^{\pi/2} F(\Delta)d\Delta + \int_{-\pi/2}^{-\theta_c} F(\Delta)d\Delta \tag{5.2}$$

As yet it has not been possible to measure reflectivity scattering functions, but this approach may be useful should experimental data become available.

The model also requires a measure of the absorption within the cavity, this is expressed as a single-pass absorption defined by:

$$a = e^{-\alpha L} \tag{5.3}$$

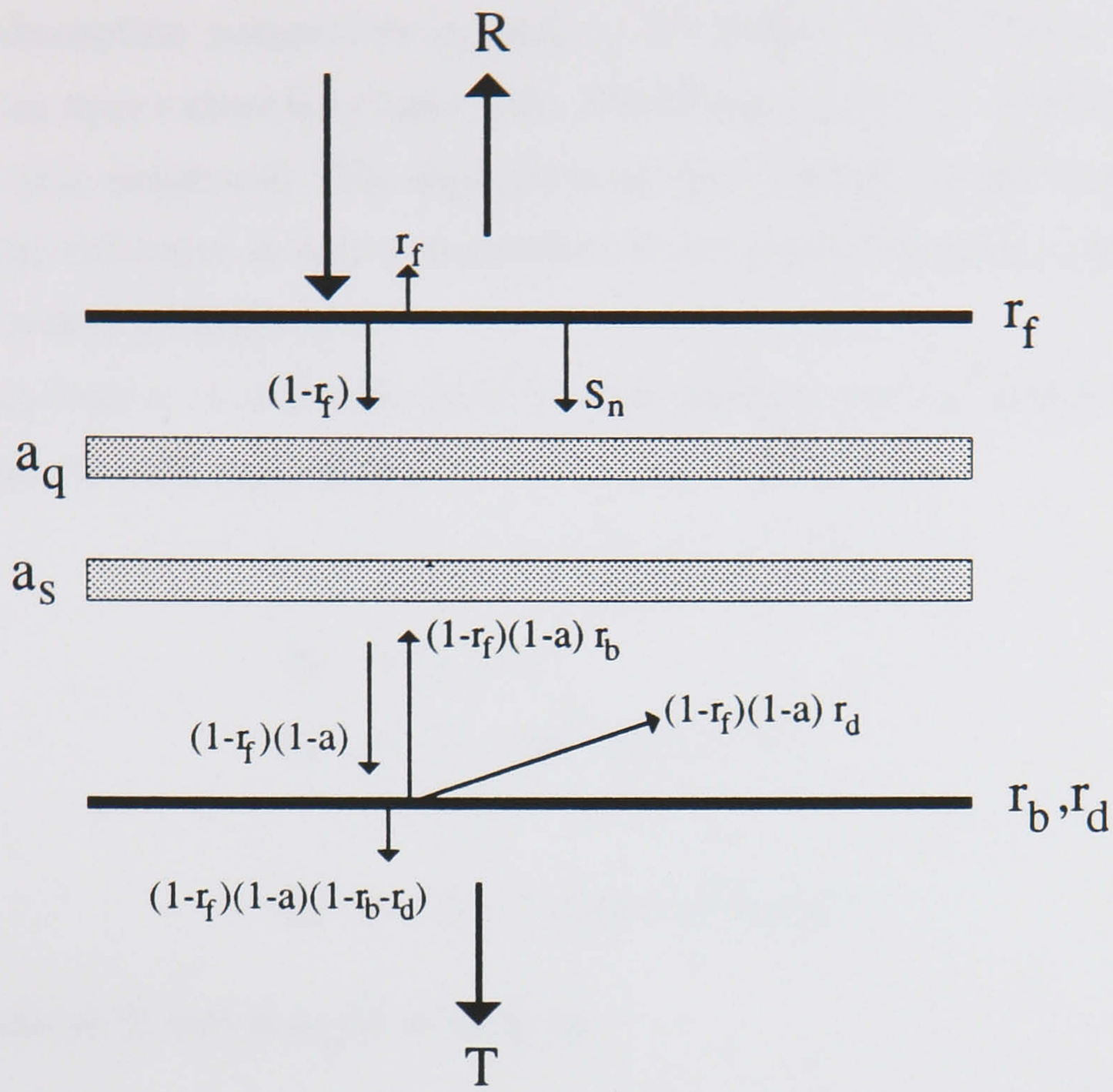

Figure 5.2: Diagram to show the general geometry and terms used in the normal incidence model.

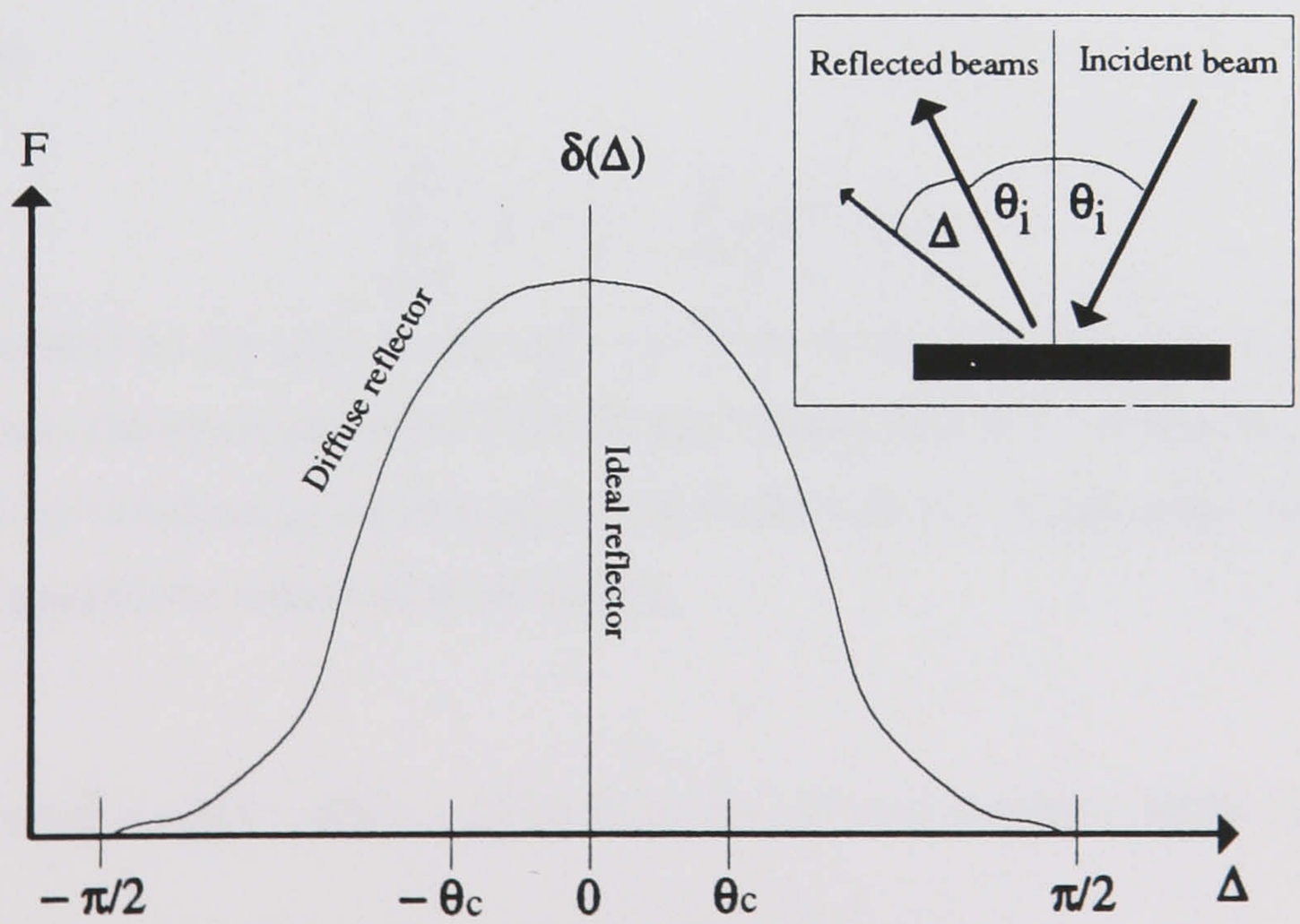

Figure 5.3: Two possible reflectivity scattering functions and the definition of Δ (inset).

where α is the absorption coefficient and L is the absorbing length of the layer.

Two absorption parameters a_s and a_q are defined such that $a = a_s + a_q$. a_q corresponds to an upper absorbing layer, (the MQW region) and a_s corresponds to a lower absorbing layer (the substrate). The separation is only relevant for the quantum efficiency calculation as the reflection R and transmission T are purely external quantities and only depend on the overall absorption a.

It is convenient to define an inner-surface incident ray S_n, where n is the number of passes through the cell, such that:

$$\begin{aligned} S_0 &= 1 - r_f \\ S_1 &= (1-a)^2 r_b r_f (1 - r_f) \\ &\ldots \\ S_n &= (1 - r_f)((1-a)^2 r_b r_f)^n \end{aligned}$$

This allows T and R to be written as:

$$T = (1-a)(1 - r_b - r_d) \sum_{n=0}^{\infty} S_n \tag{5.4}$$

$$R = r_f + (1-a)^2 r_b (1 - r_f) \sum_{n=0}^{\infty} S_n \tag{5.5}$$

where,

$$\sum_{n=0}^{\infty} S_n = \frac{1 - r_f}{1 - r_b r_f (1-a)^2} \tag{5.6}$$

It is useful to be able to extract the true surface reflectivity r_f and single pass absorption a from the external reflectivity R and transmission T measurements. By assuming $r_d = 0$ and by combining equations 5.4, 5.5 and 5.6 the single pass absorption can be expressed as a quartic in terms of T,R and r_b;

$$-r_b^2 T(1-a)^4 + (r_b^2 - r_b)(1-R)(1-a)^3 + 2Tr_b(1-a)^2 + (1-r_b)(1-R)(1-a) - T = 0 \tag{5.7}$$

and the front surface reflectivity can be written as:

$$r_f = \frac{(1-a)(1-r_b) - T}{(1-a)(1-r_b) - Tr_b(1-a)^2} \tag{5.8}$$

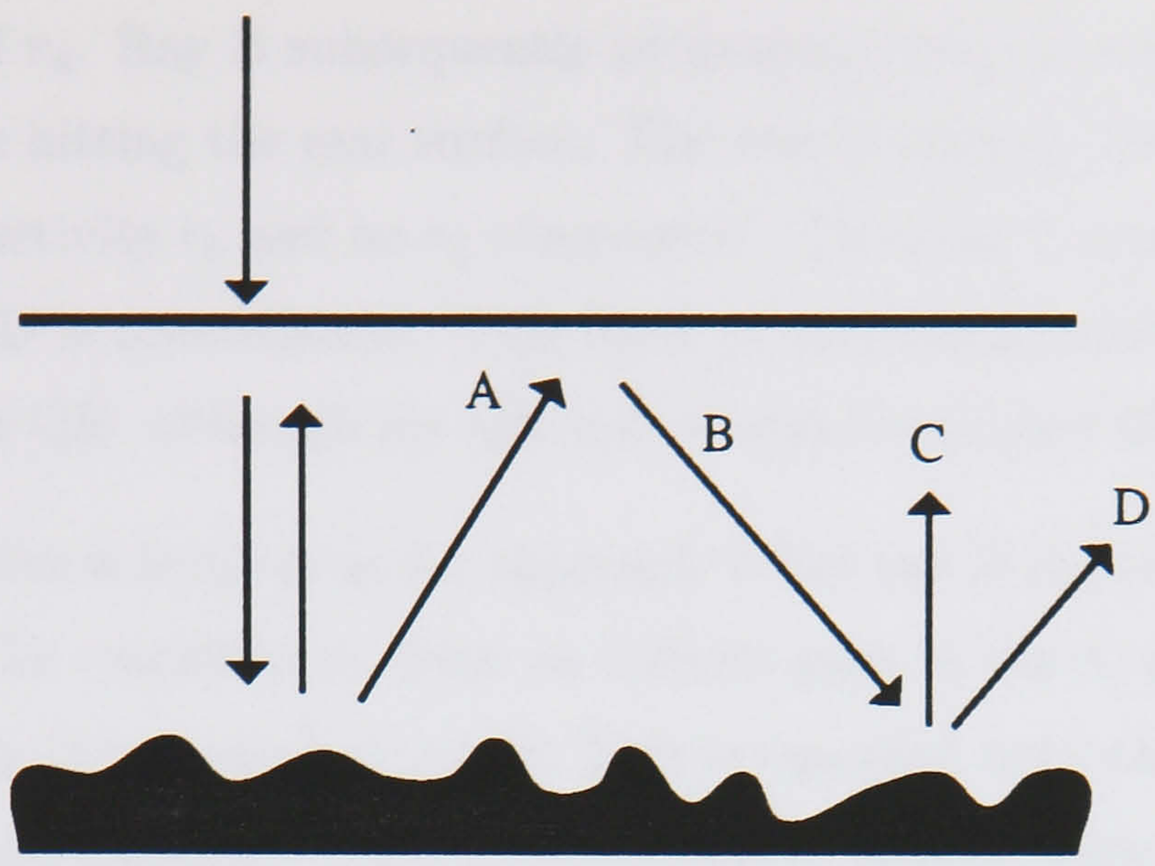

Figure 5.4: Optical paths for the diffuse reflected light

Equation 5.7 can be solved numerically and by virtue of equation 5.8 it is possible to obtain values for a and r_f from a single measurement of R and T.

In the case of a free standing substrate, the rear-surface reflectivity is simply GaAs-air. In this case the reflectivity can be calculated simply from the refractive index using Fresnel coefficients.

The quantum efficiency can also be calculated from the normal incidence model. One must assume ideal transport within the device, so that all photons absorbed in the a_q layer appear as electrons at the device terminals. In addition it is necessary to make certain assumptions for the absorption of the diffuse light.

The diagram in shown in figure 5.4 shows the incident ray, propagating normal to the surface. Inside the cell, the normal incidence component will perform multiple passes and the QW absorption due to this *normal* component can easily be accommodated using the S_n formulation above. However it is less clear what will happen to the diffuse reflectivity; represented by path A. Three possible approaches are discussed below.

1. The simplest approach is to assume that all the diffuse reflection is absorbed in the QW layer, with no further contributions to the reflectivity or transmission. This gives an upper limit to the quantum efficiency and a lower limit to the transmission and reflectivity. The quantum efficiency is given by:

$$QE = (a_q + a_q r_b(1-a) + r_d(1-a_s)(1-a)) \sum_{n=0}^{\infty} S_n \tag{5.9}$$

2. The next simplest approach assumes that ray A is attenuated by the substrate and QW layer and then undergoes a 100% reflection at the upper surface; on account of

the definition of r_d. Ray B subsequently propagates back through the QW layer and substrate before hitting the rear surface. The rear surface is then treated as a planar cavity with reflectivity r_b and no r_d component. Thus ray C makes a series of infinite passes and ray D is non-existent. This leads to additional contributions to R and T as well as to the QE, although the QE will always be smaller than that of (1).

3. The most complex scheme is as for approach 2 but ray B splits into beams C and D with $r_d \neq 0$. The contribution from an infinite pass of ray C is added to R, T and QE and then ray D is treated as ray A. This is repeated until the magnitude of ray B becomes less than 0.0001%. This leads to slightly greater contributions to R, T and QE than approach 2, as the r_d parameter is not neglected after the first pass. Note that this approach assumes that the scattering function $F(\Delta)$ is independent of the angle of incidence (θ_i in figure 5.3).

5.2.1 Doped and undoped substrates

A simple method of reducing absorption losses in a solar cell is to replace the doped substrate with a semi-insulating undoped substrate. A doped substrate will exhibit significant free carrier absorption, below the band-gap [84]. An undoped substrate will have a greatly reduced free carrier concentration and hence exhibits a much lower absorption.

Studies have been performed on the role of free carrier absorption in the quantum well solar cell [84], and showed that a doped substrate possessed around 30% absorption per pass.

After the completion of the aforementioned study, two substrates one doped and one undoped were available for measurement. Both transmission and reflectivity measurements were performed by the methods described in section 3.3.3 and the data is shown in figure 5.5.

Using the normal incidence model, it was possible to deduce values for the surface reflectivity and single pass absorption. The graph shown in figure 5.6 shows the results from these calculations.

The data provides a good test for the normal incidence model. At short wavelengths, above the GaAs band-gap, the substrate absorption is strong and the surface reflectivity closely follows the measured reflectivity. However, below the band-gap where the absorption is weaker, the measured reflectivity is noticeably higher than the calculated surface reflectivity; indicating the light is beginning to make multiple passes through the substrate. The single pass absorption calculation provides further evidence for multiple

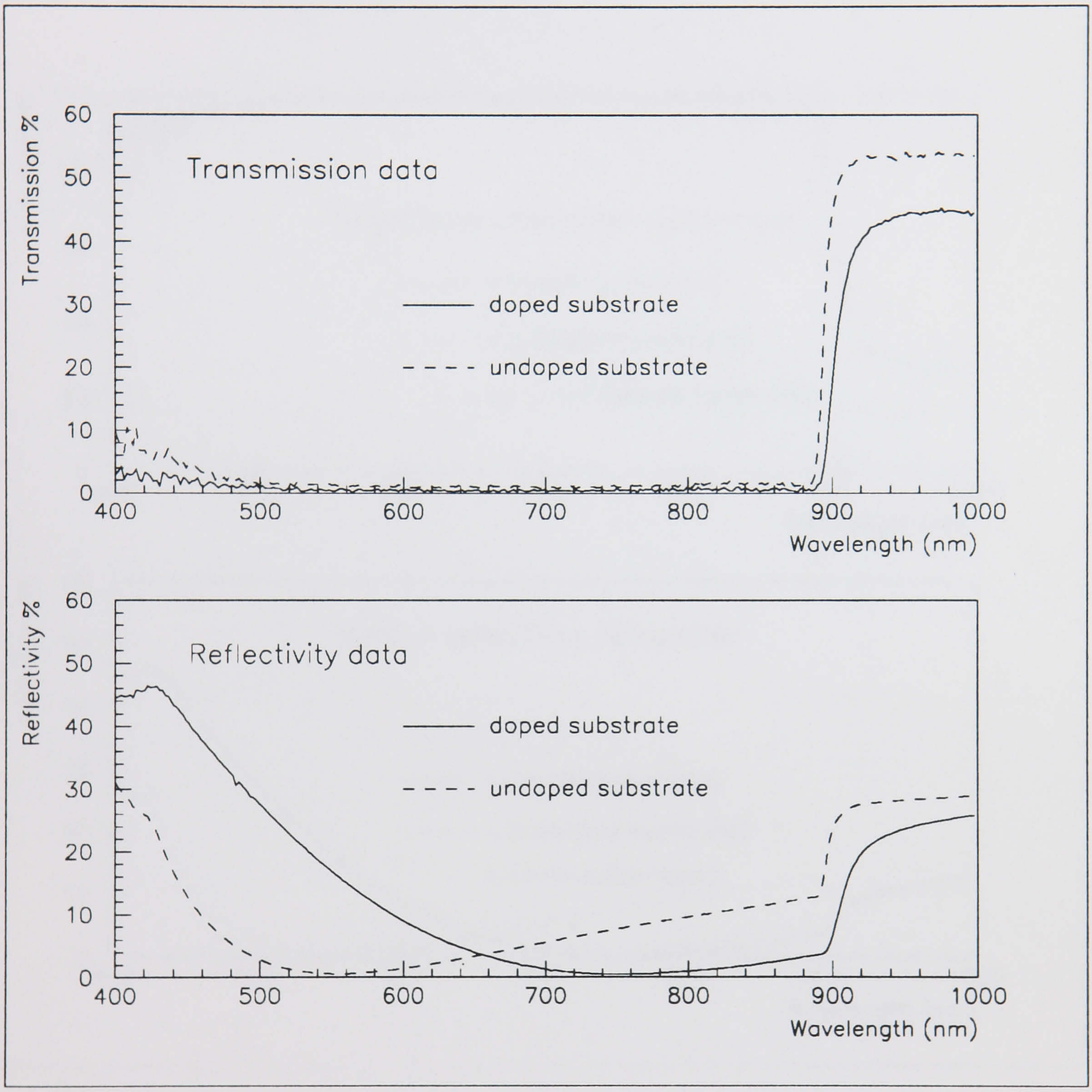

Figure 5.5: Measured transmission and reflectivity data for doped and undoped substrates

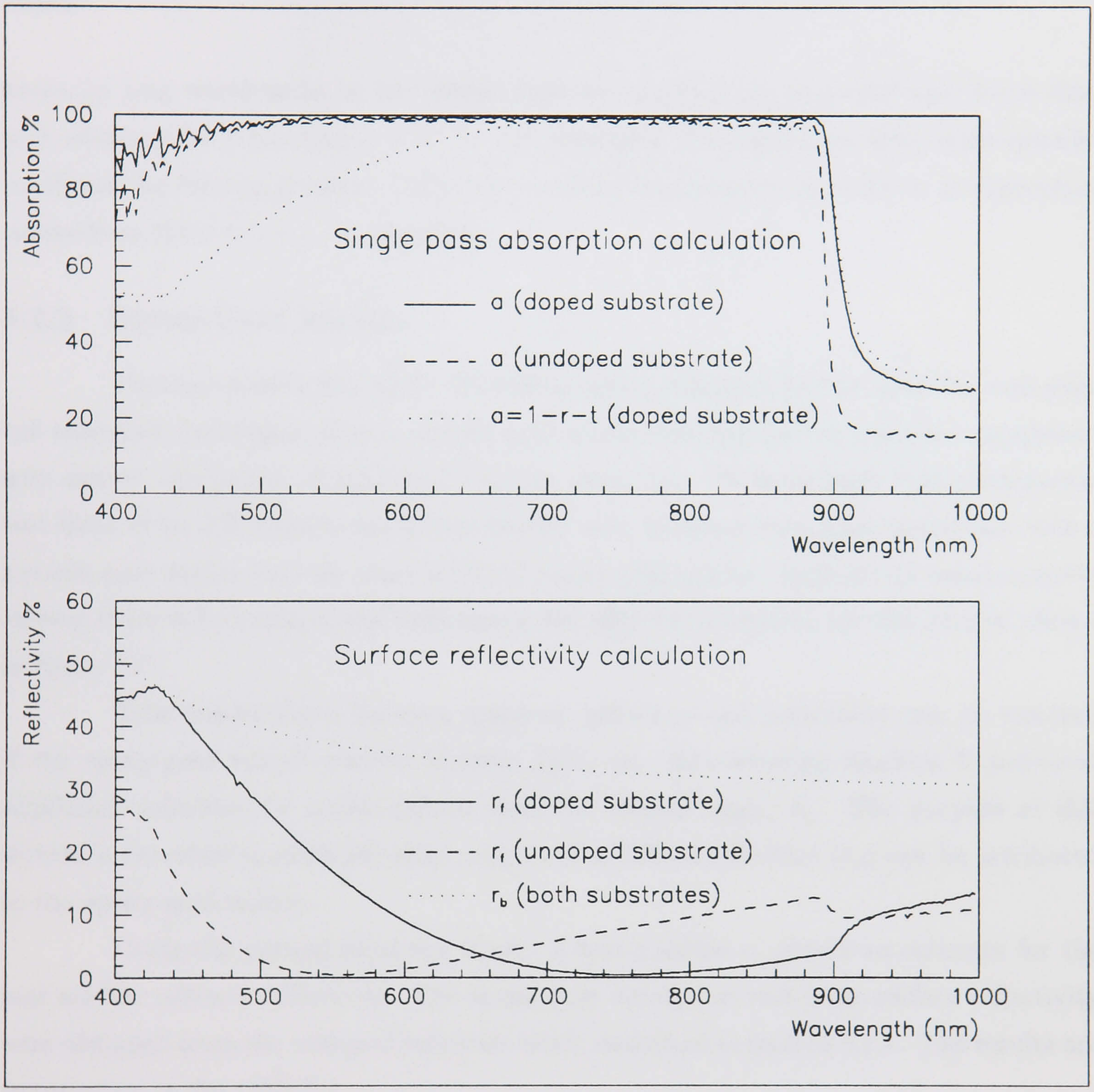

Figure 5.6: Calculated values for r_f and a from the doped and undoped substrate data shown in figure 5.5

	R	r_f	a	λ	r_b
Au mirror	69.3%	12%	15%	$1\mu m$	95%
Epoxy mirror	24.2%	12%	15%	$1\mu m$	30%

Table 5.1: Values for r_f, calculated using the normal incidence model with the parameters shown.

passes at long wavelengths as the infinite pass model yields values persistently lower than that obtained by evaluating $a = 1 - r - t$. Similarly the single-pass absorption remains unaffected by the rising surface reflectivity at short wavelengths; in contrast to absorption values from the $a = 1 - r - t$ expression.

5.2.2 Epoxy-Gold mirrors

Previous studies had noted that the quantum efficiency for the quantum well solar cell remained unchanged when a smooth gold mirror was replaced by a slightly roughened gold mirror; consisting of gold loaded epoxy resin [84]. To investigate this phenomena, two slices of an AR coated, undoped substrate were mounted onto glass slides, one with a smooth gold mirror and the other with the epoxy-gold mirror. Reflectivity measurements showed there to be a substantial difference in the reflectivity between the two devices, shown in figure 5.7.

This contradiction between quantum efficiency and reflectivity can be resolved if the epoxy-gold mirror scatters incident light, i.e. its scattering function F processes significant reflection at angles greater than the critical angle, θ_c. The purpose of this section is therefore to establish what magnitude of diffuse reflection (r_d) can be attributed to the epoxy-gold mirror.

Using the normal incidence model, it was possible to obtain an estimate for the rear surface (direct) reflectivity. The single pass absorption and front surface reflectivity were obtained from the undoped substrate work, described in section 5.2.1. The results are summarised in the table 5.1.

These parameters could then be applied to another set of measurements, performed on the QT957 series of samples allowing the single pass quantum well absorption to be determined together with the diffuse reflectivity r_d for an epoxy mirror. This was achieved by processing QT957C [1] such that some devices had an epoxy-gold on the rear-surface whilst others had a black paint on the rear-surface. The devices were top-contacted to

[1] 10 MQW sample; 78Å$GaAs/In_{0.15}Ga_{0.85}As$ quantum wells

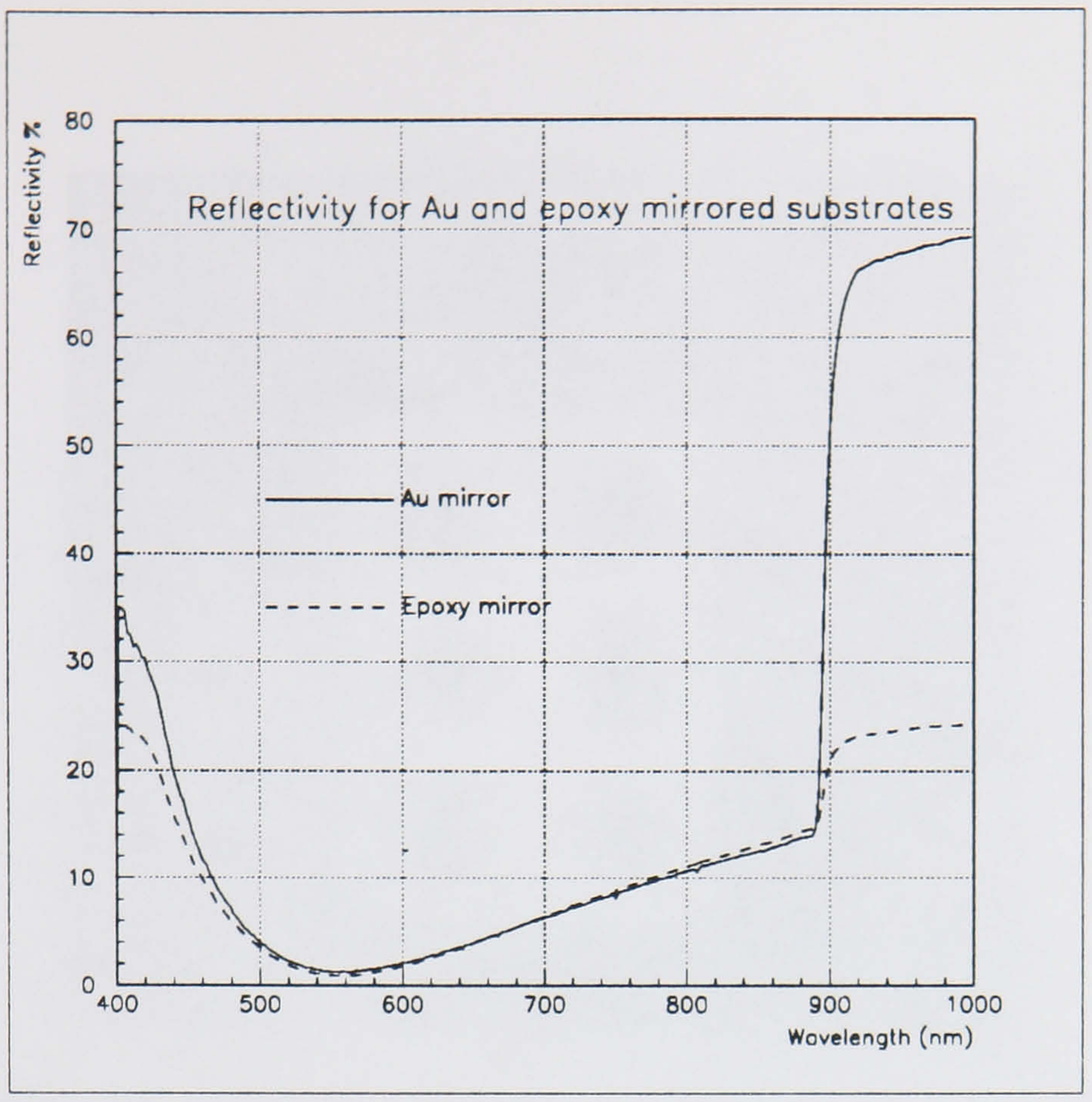

Figure 5.7: Reflectivity for an AR coated undoped substrate with a smooth gold mirror and a gold-epoxy mirror.

allow for insulating rear- surfaces and were also grown on an undoped substrate in-order to minimize substrate losses. Figure 5.8 illustrates the pin-out of the device and the extent of the black paint/gold epoxy.

The quantum efficiency for this device is shown in 5.9 and shows a distinct increase in quantum efficiency for the devices with an epoxy mirror over the devices with a black rear-surface. These results are summarised for $\lambda = 950nm$ below:

Pin 1	Pin 2	Pin 4	Pin 7	Pin 9	Pin 11
7%	7%	9%	7%	10%	10%

For the devices with black paint covering the rear surface, the rear-surface reflectivity can be assumed to be similar to GaAs-Air, so $r_b = 30\%$. Assuming $r_f = 12\%$ for a typical AR-coated front surface, $r_d = 0$ for a planar rear-surface and $a_s = 15\%$ for an undoped substrate, then the normal incidence model shows the single pass QW absorption to be $a_q = 7\%$ at $\lambda \approx 950nm$. Hence one may establish a rule of thumb that the GaAs/InGaAs quantum well solar cell absorption is about 0.7% per level per well.

Using this data, it is possible to establish three values for the diffuse reflectivity r_d, stemming from approaches 1-3 in section 5.2. The following data was obtained for the epoxy (QE=10%) devices with $r_b = 30\%$, $r_f = 12\%$ $a_s = 15\%$ and $a_q = 7\%$.

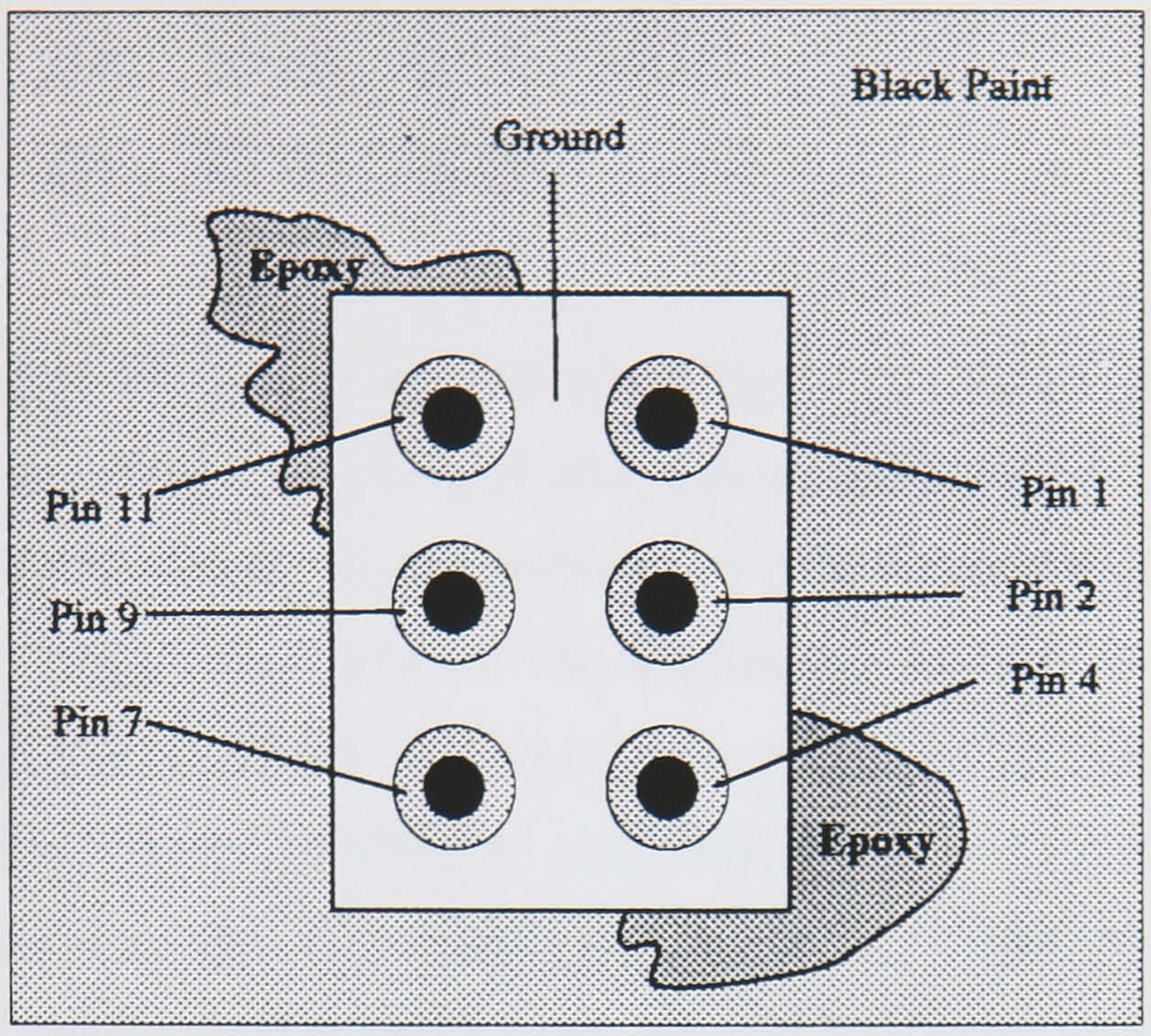

Figure 5.8: Diagram to show the extent of the gold-epoxy mirror and the black paint

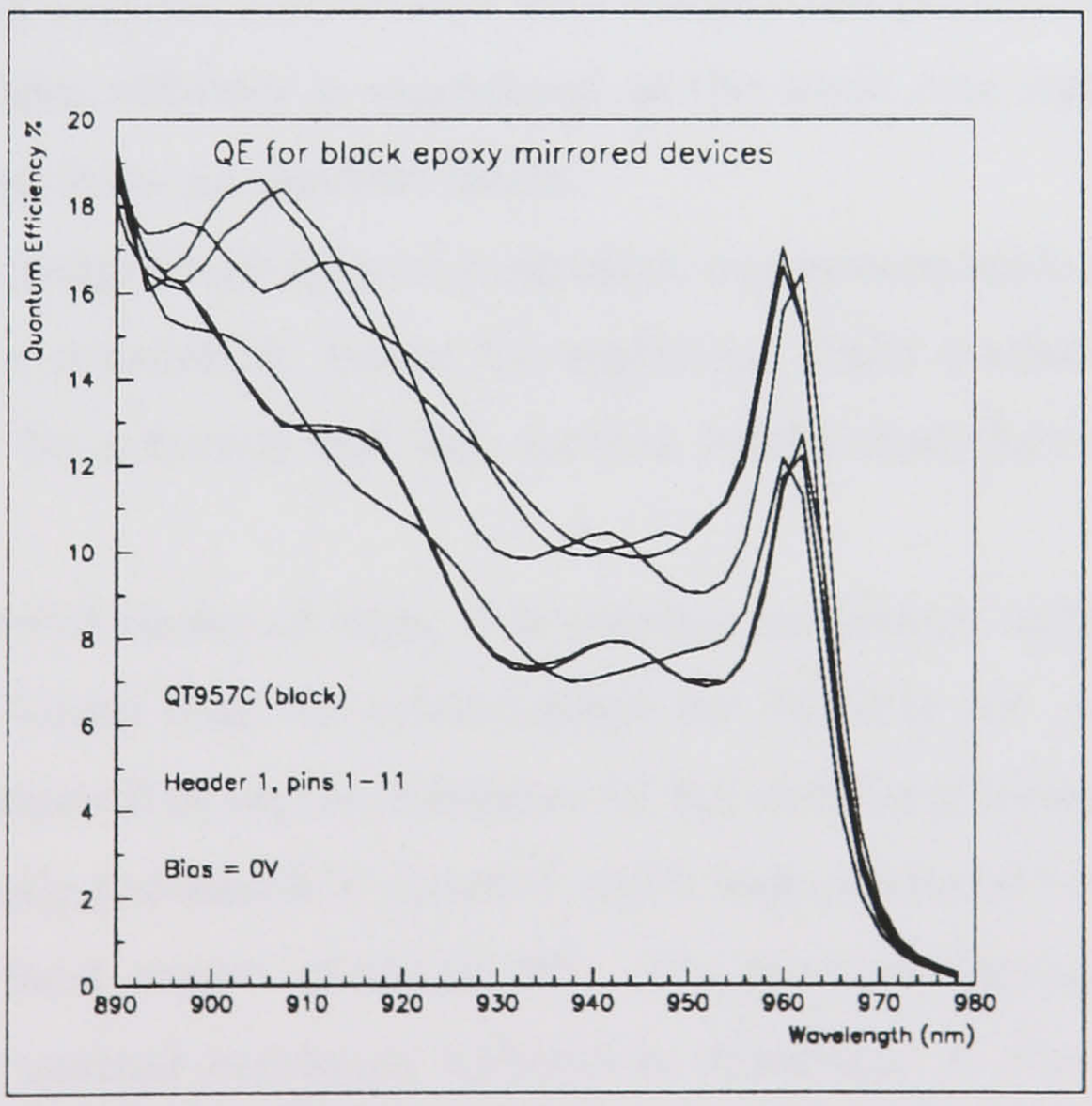

Figure 5.9: Quantum efficiency for QT957C, processed with black paint.

Approach	r_d	T	R	QE
1	3.8%	46.5%	26.5%	10.0%
2	25%	39.2%	28.7%	10.0%
3	25%	37.4%	29.1%	10.4%

The gold epoxy offers a cheap and straightforward means of achieving a modest degree of light-trapping, equivalent to that of a planar gold mirror. The model indicates the diffuse rear-surface reflectivity for the gold-epoxy mirror lies between $3.8\% < r_d < 25\%$. Therefore, while the direct reflectivity of the gold-epoxy mirror is low, it is the diffuse component that brings the quantum efficiency level with that of the planar gold mirrored sample. However, if this 'diffuse' gold-epoxy mirror can only achieve the same photocurrent as a planar mirror, it is desirable to consider a more efficient light-trapping structure. The following section will briefly review work done by Markus Hepp and Ruth Woodward on the use of patterned substrates for light-trapping.

5.3 Achieving textured GaAs surfaces

Successful light trapping requires the rear surface to scatter the light in such a way that the resulting angular distribution falls outside the critical angle and is internally reflected. A Lambertian reflector is considered as the ideal rear surface, completely randomising the reflection from an incident beam.

The surface morphology may be controlled on a micron scale using standard lithography and provides a convenient means for texturing GaAs surfaces. In particular, V-grooved features can be achieved and this section briefly describes work performed with some MQW cells.

Through careful choice of etch, it is possible to achieve arbitrary facet angles for a particular feature. Given that the critical angle for GaAs is 16°, a desirable facet angle will be around 20°, depending on the tolerance of the etching process [84].

A continuously patterned V-grooved wafer was produced by Dr. Geoff Hill[2] with a pitch of 2μm and facet angles of about 50°. The characterisation of these wafers was performed using the normal incidence techniques described in the previous section and formed the basis of several MSc projects.

Reflectivity measurements on the patterned substrate indicated that the normal

[2]EPSRC III-V facility, University of Sheffield

or direct component of the reflectivity was reduced with increased surface texturing. Upon overgrowth and surface planarisation, a 3% loss in transmission was observed hinting some form of light trapping due to a thin textured AlAs layer buried within the device [54]. Recent measurements on processed devices have shown an increase in QW photocurrent of $(14 \pm 0.9)\%$ [55].

Future work on surface texturing must now deal with strengthening the reflectivity of the textured AlAs layer. Conceptually this could be most easily achieved if the substrate were removed, exposing the texture to a much higher mismatch of refractive indices. The next section deals with cavity cells and details some of the additional advantages that thin cells with no substrate may possess.

5.4 Photon recycling and cavity cells

While light trapping is concerned with increasing the absorption of a solar cell, photon recycling affects the radiative recombination in a cell. To date, photon recycling has remained a theoretical fancy, with little direct experimental evidence to support it. This section will review some of the existing literature and then describe some MQW samples in which photon recycling may be apparent.

Conceptually, photon recycling is simple; a photon is released by some radiative process and is subsequently reabsorbed elsewhere in the device. The extent of photon recycling is determined by the geometry of the device and requires radiatively dominated material.

Consider the structures in figure 5.10; in radiatively dominated material, the electrical current is determined by the photon loss from the device.

1. An ideal radiator in free space; draws a current I, allowing photons to emerge over a 4π solid angle. Under such circumstances if all photons could be collected and measured, the measured EL would equal the injected current ($EL = I$); i.e. a one to one correspondence between carrier injection and photon emission, in the radiative limit. There is no photon recycling in this situation.

2. An ideal radiator surrounded by a perfect reflector; no photons are lost from this cavity, so any external EL measurement would always indicate $EL = 0$. The current drawn is also zero, as in the radiative limit, photons represent the only loss for carriers to escape. This represents the most extreme instance of photon recycling.

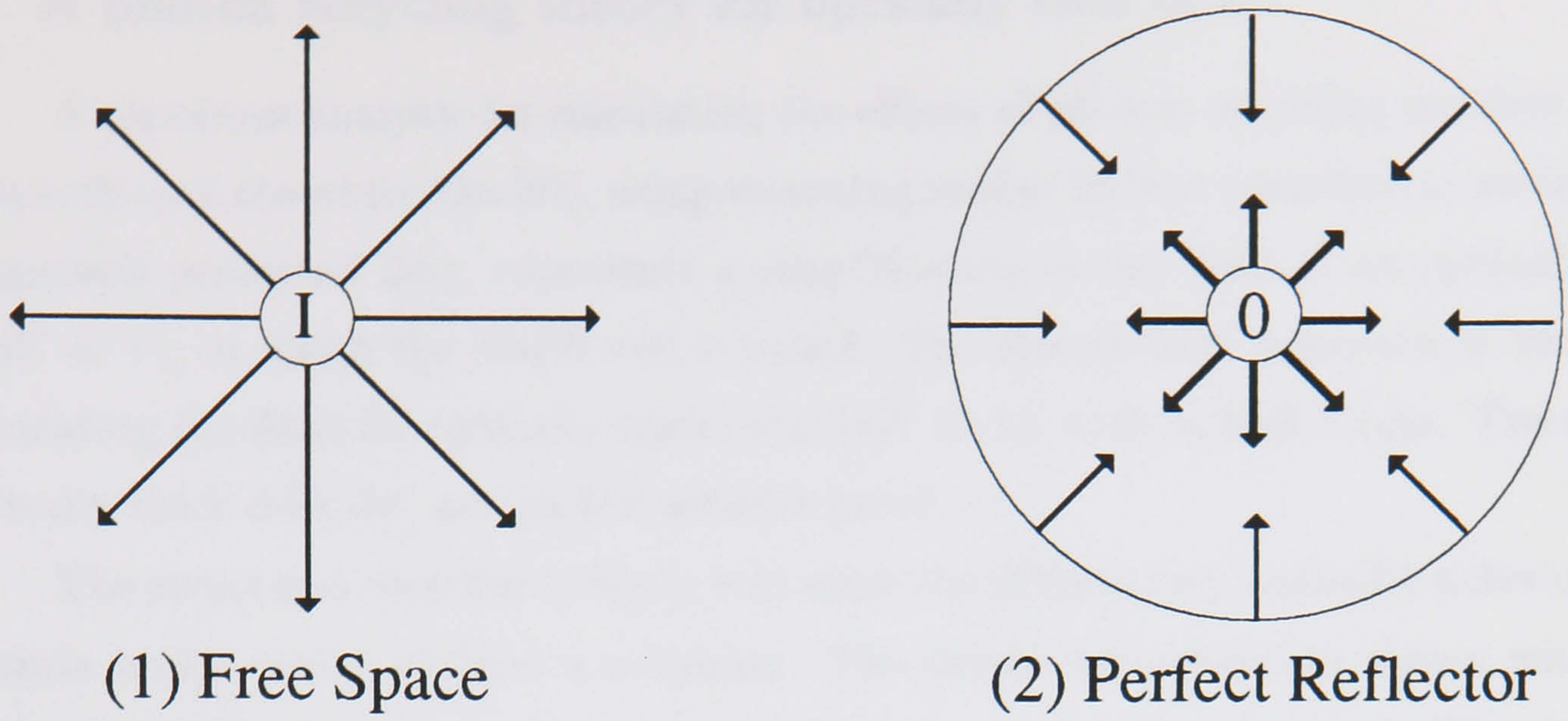

Figure 5.10: Two geometries representing the limits; 1) radiation into free space with no photon recycling and 2) radiation into a mirrored cavity with total photon recycling

While the two structures shown in figure 5.10 illustrate the two limiting cases, the situation for a real solar cell lies somewhere between the two. The cell geometry can be arranged to restrict losses and studies to date are mainly concerned with planar geometries, typically a cell with a substrate and a mirrored cavity cell with no substrate as depicted in figure 5.11.

An important condition for photon recycling is that radiative recombination is dominant over other recombination processes. The extent to which this is necessary is unclear; while extended PL decay times have been observed for cavity samples and attributed to photon recycling [85, 86, 87]. Similarly, increased LED external quantum efficiencies have been observed upon substrate removal [88]. However, attempts to transfer such effects to photovoltaic devices have yet to demonstrate convincing electrical cell characteristics.

Relevant theoretical work includes a device analysis of potential advantages for photon recycling in GaAs solar cells. The simulations show that an absolute 2% gain in efficiency may be possible over the existing record holding 24% efficient GaAs cells [89, 90, 91].

Early attempts at producing highly efficient cavity cells showed some encouraging attributes. First it was shown that good quality GaAs diodes could be maintained through the substrate removal process [92] and the thin cell remounted on Si [93] and glass [94] substrates. While none reported any photon recycling effects, the work was motivated by the financial prospect of reusable GaAs substrates and high-power density cells [95]. Processing techniques have now been developed to allow entire films to be removed, crack-free, from 2 inch wafers [96].

5.4.1 A photon recycling theory for optically thin cells

A rigourous analysis for calculating the effects of photon recycling involves calculating specific cell absorbtivities [97], using reasoning similar to that described in section 4.4. The approach presented here, represents a simplification in the limit of an optically thin cell ($\alpha W \ll 1$), to which the MQW cell is suited. The absorbtivity approach is necessary for calculating the limit for optically thick cells ($\alpha W \gg 1$), such as bulk GaAs. The results for optically thick cells [98] are quoted without proof.

The structures depicted in figure 5.11 show the different ray paths for a device with a substrate and a device without a substrate. The device structures are shown with rays 1-4 indicating different paths available for spontaneous emission at point A. The emission diagrams show the direction of radiative emission (or loss) within the cell. It is assumed that the substrate is a photon sink and photons propagating into it are lost. Rays that escape are within the critical angle (θ_c) cone and may be detected externally as EL.

The current of the cell is determined by the emission surface of each cell. The surface area of a sphere of radius r which is cut by a cone of semi-angle θ, can be calculated considering an annular ring on the spherical surface of width $rd\theta$ and radius $r\sin(\theta)$. From figure 5.11c, the elemental area dA is given by:

$$dA = 2\pi r^2 \sin\theta d\theta \tag{5.10}$$

Therefore the cone and sphere surface areas S_{el} and S_{total} are given by :

$$S_{el} = \int_0^{\theta_c} 2\pi r^2 \sin\theta d\theta = 2\pi r^2(1-\cos\theta_c) \tag{5.11}$$

$$S_{total} = \int_0^{\frac{\pi}{2}} 2\pi r^2 \sin\theta d\theta = 4\pi r^2 \tag{5.12}$$

For structure I, the device with a substrate, the external EL, EL_{sub} is given by a fraction of the current I_{sub}:

$$EL_{sub} = \frac{S_{el}}{S_{total}} I_{sub} \tag{5.13}$$

which by substituting from equations 5.11 and 5.12 gives:

$$EL_{sub} = \frac{1}{2}(1-\cos\theta_c) I_{sub} \tag{5.14}$$

For structure II, the cavity device and mirror, the external EL is given by the forwards (EL_{fwd}) and backwards (EL_{back}) propagating emission, within the critical angle cone θ_c. Ray 1 emerges from the top of the cell and in the limit of an optically thin cell,

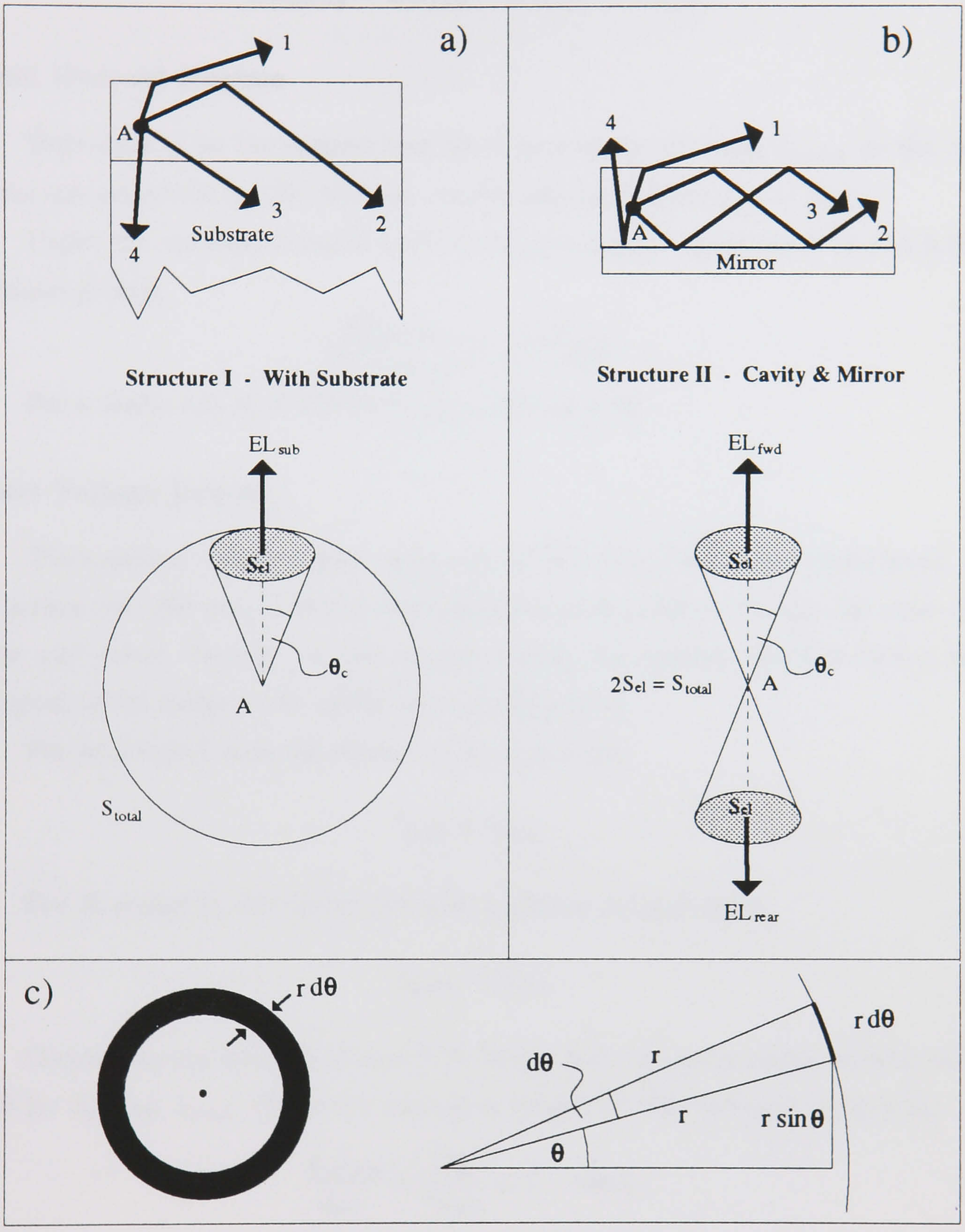

Figure 5.11: a) Ray diagram and emission geometry for a planar cell with substrate. b) Ray diagram and emission geometry for a planar cavity cell with rear mirror. c) Geometry used to calculate the emission cone surface area.

ray 4 is reflected and also emerges from the top surface. Rays 2 and 3 are trapped, so the external cavity EL EL_{cav} is written as:

$$EL_{cavity} = EL_{fwd} + EL_{back} = I_{cavity} \tag{5.15}$$

Constant Current Regime

Defining I_{sub} as the current that flows into structure I and I_{cavity} as the current that flows into structure II, the constant current regime requires $I_{sub} = I_{cavity}$

Under the constant current condition $I_{sub} = I_{cavity}$, equations 5.14 and 5.15 may be combined giving:

$$\frac{EL_{cavity}}{EL_{substrate}} = \frac{2}{1 - \cos\theta_c} \tag{5.16}$$

For a GaAs cell, $\theta_c \approx 16°$ so $EL_{cavity}/EL_{sub} \approx 50$.

Constant Voltage Regime

The constant voltage regime implies equal splitting of the quasi-Fermi levels, which in turn means that the rate of radiative recombination at point A remains the same for the substrate and cavity devices. In the radiative limit, the current which is drawn will be proportional to the surface area of the photon loss sphere.

For structure I with the substrate, we may write:

$$I_{sub} \propto S_{total} \tag{5.17}$$

For structure II, the cavity cell with a mirror, we may write:

$$I_{cavity} \propto 2S_{el} \tag{5.18}$$

Combining equations 5.17 and 5.18 above with the geometrical expressions 5.11 and 5.12 for S_{el} and S_{total}, the cavity current is related to the substrate current by:

$$\frac{I_{cavity}}{I_{sub}} = \frac{2S_{el}}{S_{total}} = 1 - \cos\theta_c \tag{5.19}$$

in agreement with reference [97].

For a GaAs cell, $\theta_c \approx 16°$ so $I_{cavity}/I_{sub} \approx 0.04$.

The EL relationship is deduced by combining equation 5.19 with equations 5.15 and 5.14, yielding;

$$\frac{EL_{cavity}}{EL_{sub}} = 2 \tag{5.20}$$

Summary of photon recycling expressions

As mentioned previously, the derivations above represent a simplified and intuitive means of understanding the current voltage and EL behaviour of optically thin cells. The results for optically thick cells are quoted here for interest and also for brief discussion of some published results in section 5.4.4. Derivations for optically thick cells are beyond the scope of this thesis.

$$\text{Constant Current} \quad \begin{cases} \dfrac{EL_{cavity}}{EL_{sub}} = \dfrac{2}{1 - cos\theta_c} & \text{when } \alpha W \ll 1 \\[2ex] \dfrac{EL_{cavity}}{EL_{sub}} = n^2 + 1 & \text{when } \alpha W \gg 1 \end{cases}$$

$$\text{Constant Voltage} \quad \begin{cases} \dfrac{EL_{cavity}}{EL_{sub}} = 2 & \text{when } \alpha W \ll 1 \\[2ex] \dfrac{EL_{cavity}}{EL_{sub}} = \dfrac{n^2+1}{n^2} \approx 1 & \text{when } \alpha W \gg 1 \end{cases}$$

Table 5.2: Summary of photon recycling expressions in the constant current and constant voltage regimes. Optically thin cells correspond to $\alpha W \ll 1$ while optically thick cells correspond to $\alpha W \gg 1$

The EL expressions listed in table 5.2 are extremely important clues when searching for the photon recycling signature. In real material where non-radiative recombination affects samples, it is often unclear whether changes in a dark-IV characteristic are due to changes in non-radiative recombination or a photon recycling process. The EL expressions provide a means of lifting the ambiguity.

The remainder of this chapter will deal with MQW data whose dark-IV profile suggests a photon recycling process, but is later shown to contradict the EL analysis. For comparison, some published data from Purdue University is also analysed in this manner.

5.4.2 Samples for investigating photon recycling

A series of samples were grown by John Roberts using MOVPE to investigate the effects of substrate removal on an MQW diode. Full growth details may be found in the appendix, but the samples and characterisation are summarised in table 5.3. These samples have already been discussed briefly earlier in section 5.2.2, where differences in QE for samples grown on doped and undoped substrates allowed the single pass absorption to

Sample	Description	In_xGaAs Well Width/Å	x	Etch-stop	Wafer
QT957A	10 MQW	82 ± 4	0.15 ± 0.005	No	n^+
QT957B	10 MQW	82 ± 4	0.15 ± 0.005	Yes	n^+
QT957C	10 MQW	78 ± 3	0.15 ± 0.005	Yes	UD
QT957D	GaAs control	-	-	Yes	UD

Table 5.3: QT957 sample series: brief description and characterisation data

be determined. Some of the samples were grown with an AlGaAs etch stop layer, described in chapter 3, allowing the substrate to be removed. The cavity samples were processed in three different 'flavours', similar to the samples described in section 5.2.2. One was simply mounted 'as etched' (A) with no special rear surface treatment, another had black paint applied to the rear surface (B) and the third had a gold mirror evaporated onto the rear surface (C).

Extensive characterisation and analysis was performed on these cells. The next couple of sections describe results obtained from the cells with substrates intact, and after substrate removal where appropriate.

QT957 series; Quantum Efficiency with substrate

The graph in figure 5.12 shows quantum efficiency curves for the QT957 series. Reflectivity curves were measured, for all three AR coated devices and the AR response found to be similar, allowing a meaningful comparison of QE profiles.

The GaAs control cell, QT957D, shows usual saturated quantum efficiency from 500 to 850nm and is typical of p-i-n GaAs controls. QT957A represents the traditional strained 10 MQW cell and its QE is consistent with other samples of similar specification. QT957B shows an impaired spectral response to that of QT957A, consistent with lower diffusion lengths. The QW exciton is also considerably broader for QT957B, suggesting inferior MQW quality. The most likely explanation for the degradation in QT957B, is due to poor surface quality during growth. QT957C shows good QW excitons and a remarkably high quantum efficiency. The increased QE above 900nm is due to the relatively low substrate absorption, leading to a greater rear-surface reflection. The short wavelength QE for QT957C is comparable to the GaAs control (QT957D) and indicates excellent growth quality, especially in the p-region which dominates the short-wavelength response.

The origin for the exceptional material quality for QT957C remains somewhat speculative. The growth notes [99] remark that surface morphology is good with some

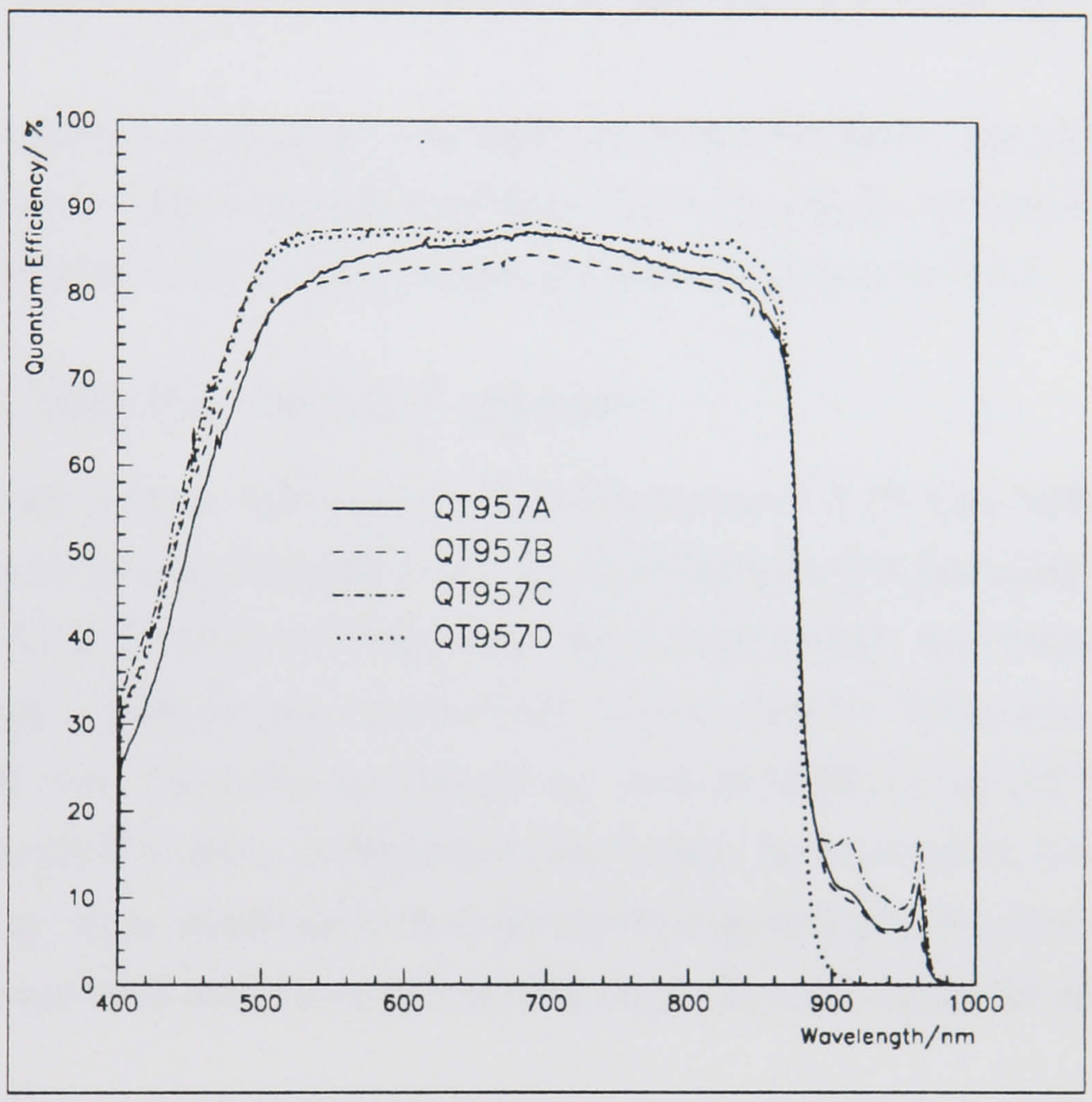

Figure 5.12: Quantum efficiency curves for the QT957 series of samples when processed with substrate. The insert represents an enlargement of the MQW region.

striations noted for QT957A and QT957B, grown on doped substrates. However the surface morphology for QT957C and QT957D grown on undoped substrates is reported as excellent. Such evidence would suggest that MOVPE growth on undoped substrates is superior. The thermal conductivity of undoped substrates is lower than doped substrates, so it is possible that thermal differences are responsible. It is also conceivable that the undoped substrates are higher quality than doped substrates, although the surface defect density is quoted to be the same for both types of substrate. To draw conclusions from such an effect, it would be necessary to grow a large number of test structures under carefully controlled conditions. With only one sample, it must be conceded as a potentially interesting result which warrants further study.

Should growth on undoped substrates prove to be superior, the optical advantages of reduced free carrier absorption reported in section 5.2.1 may be combined in a monolithic interconnected module (MIM) arrangement, as discussed in section 3.2.2.

QT957 series: Dark Currents with substrate

The dark current behaviour is depicted in figure 5.13 and indicates a slightly different pattern to the quantum efficiency. As expected from the reasoning in section 2.1.1, the GaAs control (QT957D) exhibited the lowest dark-current and remained typical of a bulk GaAs cell. QT957A also showed very typical dark-IV behaviour for a strained, unrelaxed MQW cell. The increased dark-IV for samples QT957B and QT957C is likely to be due to an increased number of impurity traps existing in the i-region, introduced via the AlGaAs etch-stop. It is significant that while superior growth may be claimed for QT957C over QT957B, consistent with the quantum efficiency, the same cannot be said for QT957A.

QT957 series: Mono-IV with substrate

The mono-IV behaviour shown in figure 5.14 shows a slight degradation for QT957B over the other samples. The differences in the forward bias fall-off are determined by the dark current and offer no additional information over the dark-IV plots. It is significant that though the dark-IV for QT957C is still worse than that of QT957A, the mono-IV behaviour is comparable for the two samples.

It is evident from all characterisation data, that a problem exists with QT957B. It shows poor QW quality, high carrier recombination rates and inferior carrier collection.

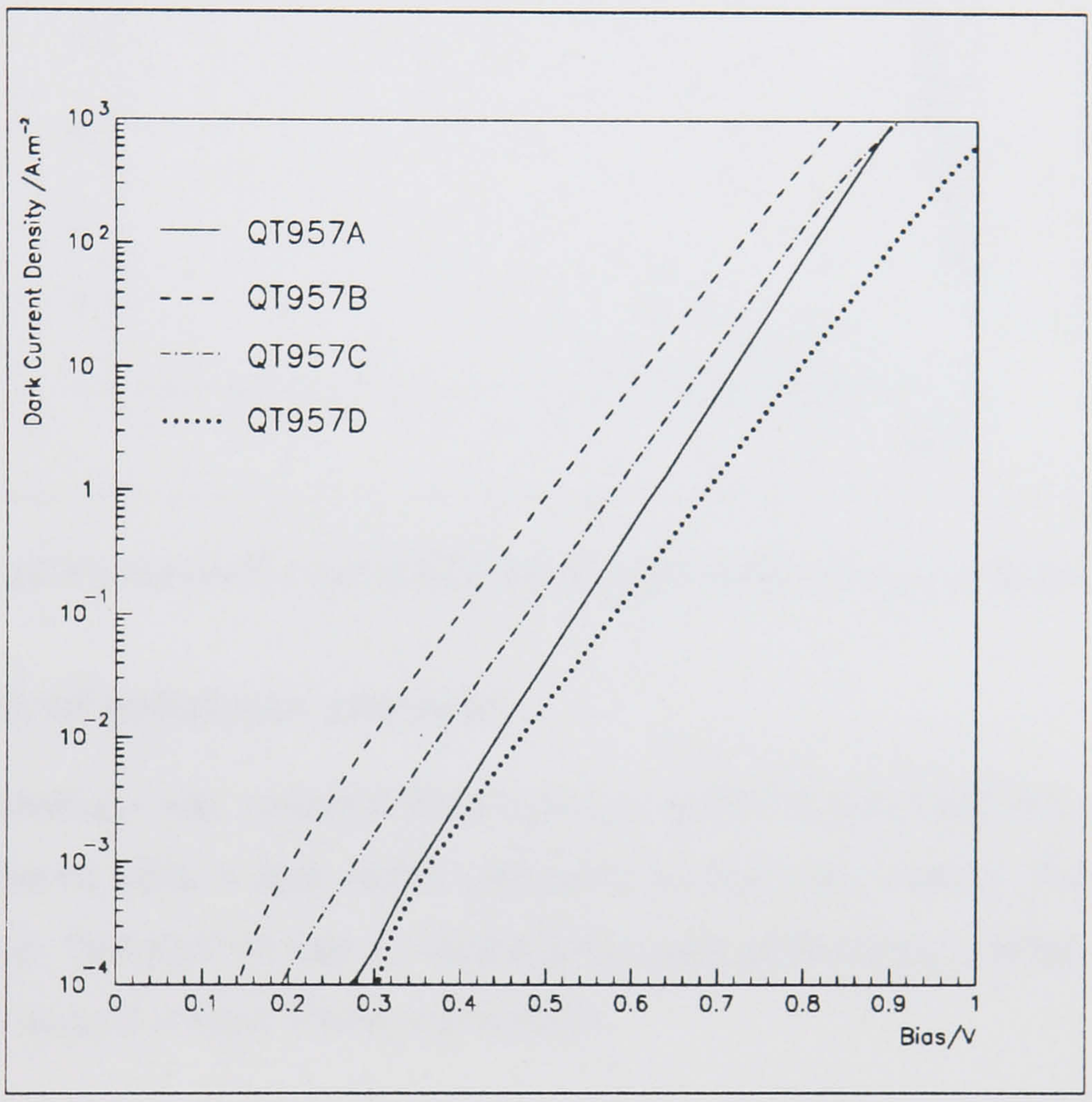

Figure 5.13: Dark current curves for the QT957 series of samples when processed with substrate.

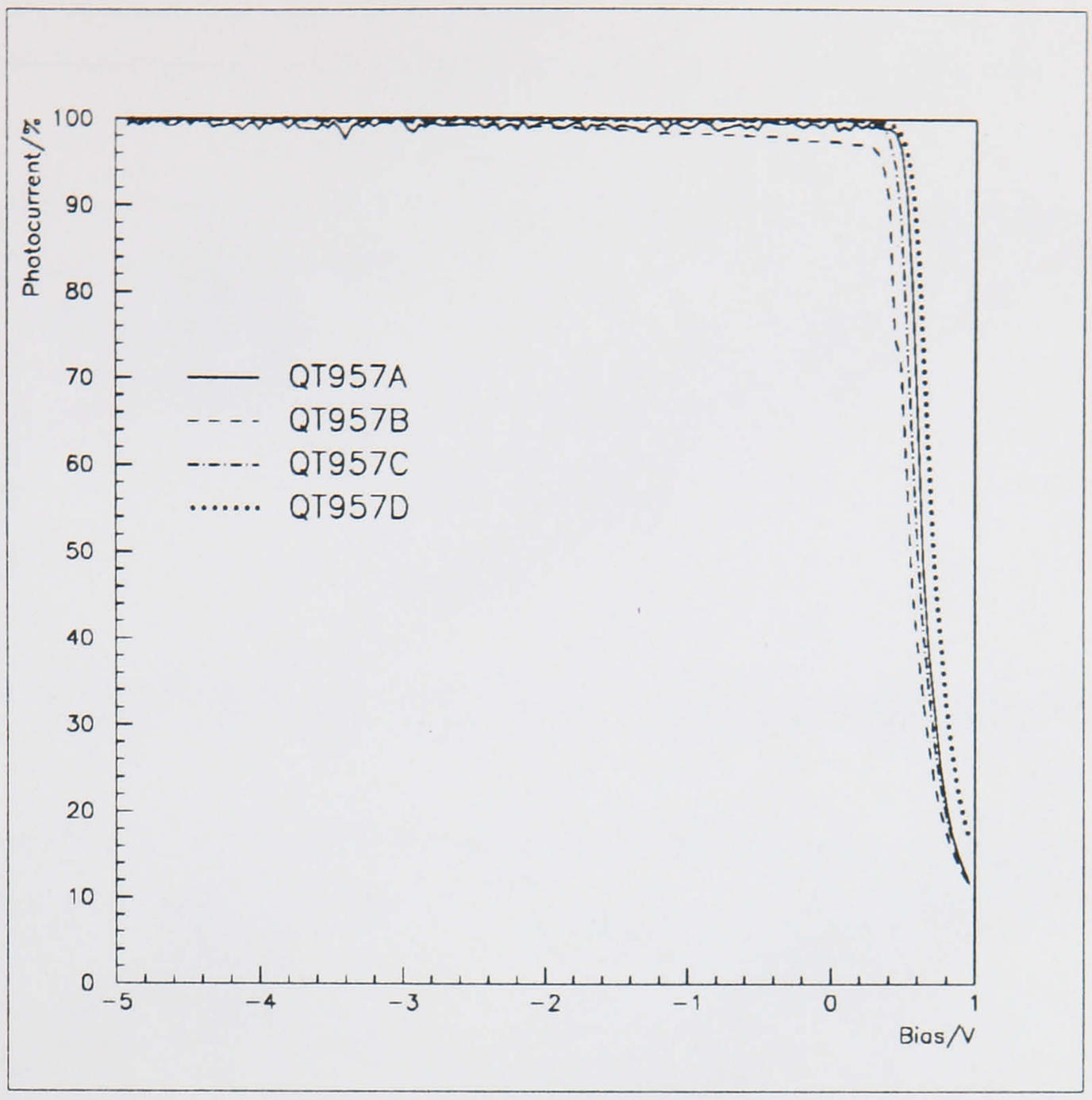

Figure 5.14: Mono IV curves for the QT957 series of samples when processed with substrate.

5.4.3 Effects of substrate removal

The substrate was removed from samples QT957B and QT957C. Problems were initially encountered with a high series resistance to the rear contact, but this was later solved for sample 'flavours' B and C (black paint and gold-mirror) using a large indium contact on the exposed n-type GaAs top surface.

Cavity dark-IV

The electrical properties of the cavity cells were remarkable. The dark-IV curves shown in figure 5.15 indicate considerable variation in dark-IV behaviour. The dark-IV is greatly reduced ($cavity/substrate = 0.05$) for QT957B while a more modest reduction is observed for QT957C. The processing 'flavour' A (i.e. QT957BA and QT957CA) serve to illustrates the dark-IV behaviour of the cell before processing with the large indium dot. All three flavours showed very similar behaviour to A before processing with the indium dot, however the dark-IV level for QT957CB rose after processing with the indium dot and maintained a high level of series resistance.

While the dark-IV results for QT957B and QT957C (excepting QT957CB) are

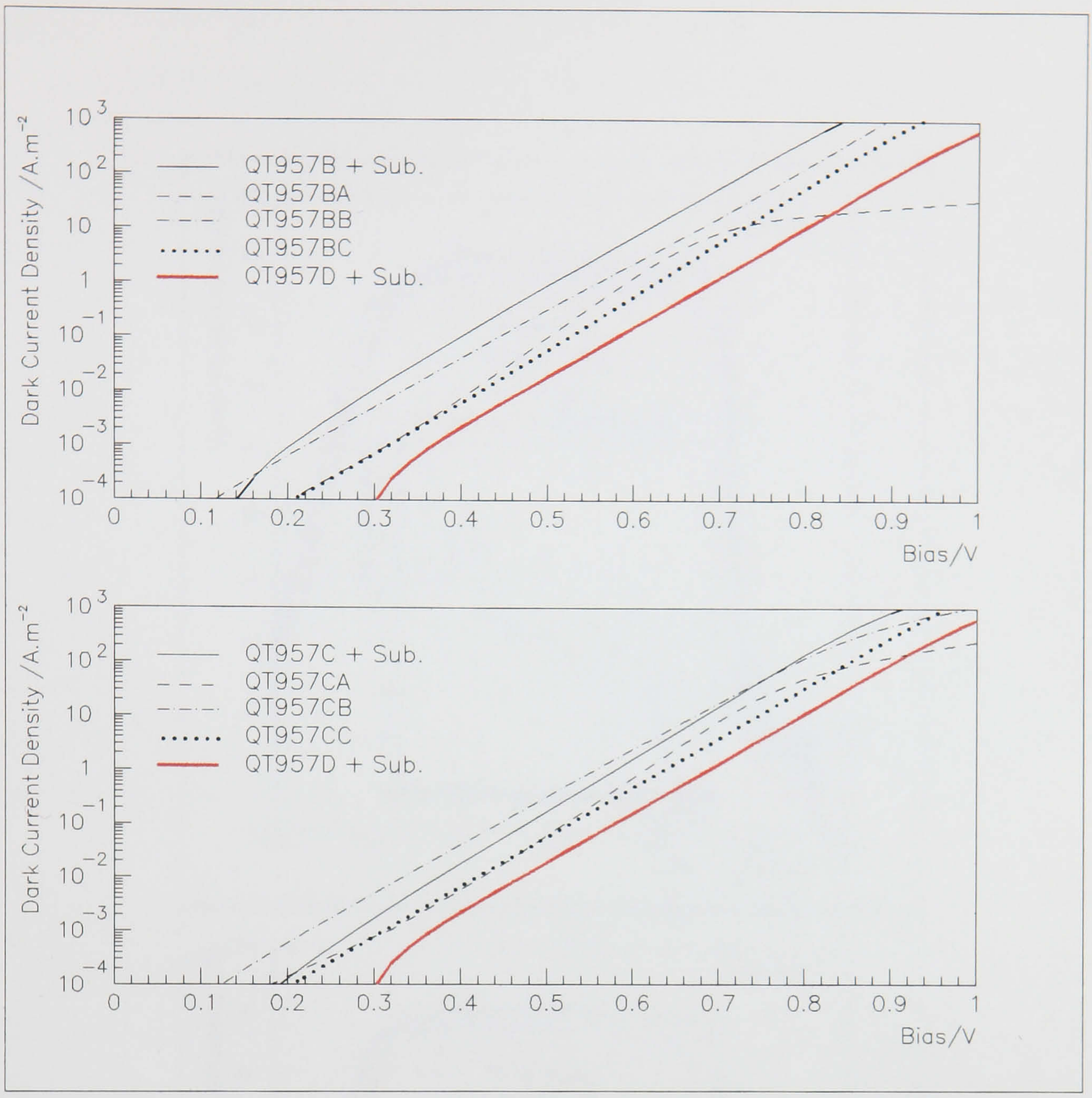

Figure 5.15: Dark current curves for QT957B and QT957C with and without substrate.

consistent with a photon recycling process, the curves possess ideality factors of 2 indicating non-radiatively dominated material. While it is conceivable that some form of recycling process may be taking place, the effects will be mixed with non-radiative processes.

Cavity Quantum Efficiency

The quantum efficiency depicted in figure 5.16 shows evidence of cavity effects, in particular strong Fabry-Perot oscillations for the mirrored cavity sample at long wavelengths. In particular the e1-hh1 exciton is suppressed by the cavity and is discussed later in this section. It is also interesting to note that the oscillations persist at bulk wavelengths, where the GaAs absorption is not entirely saturated.

While some enhancement of long wavelength (800-880nm) QE is expected for the cavity cell, the cavity effects are not expected to affect the short wavelength QE, which is

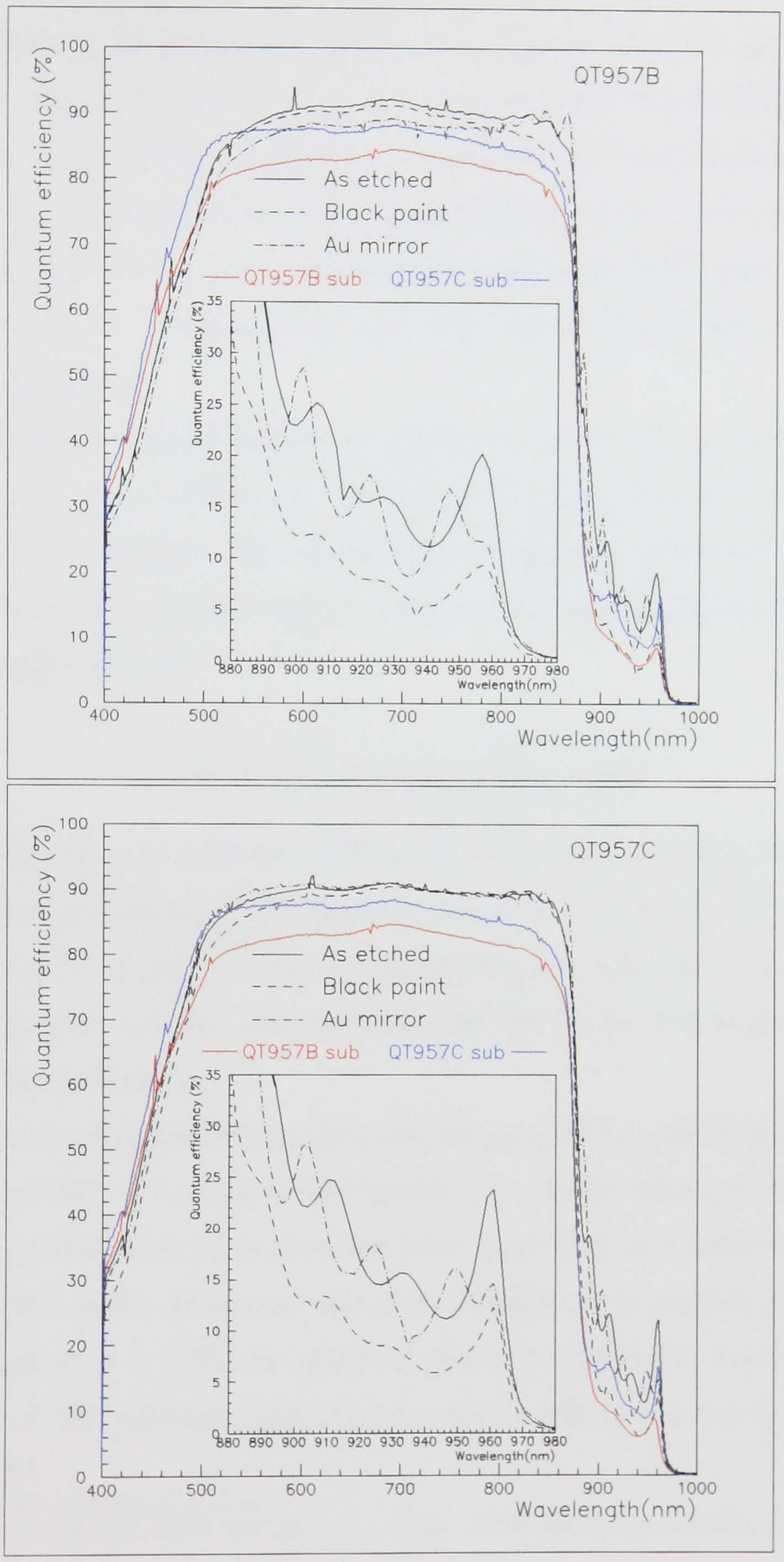

Figure 5.16: Cavity quantum efficiency for QT957B and QT957C

dominated by the p-region. However, QT957B shows an overall increase in QE across all wavelengths.

An optical cavity computer model was written, based on a successful AlGaAs model [56]. The p, i and n layer widths for QT957B were obtained from edge-SEM measurements[3] and found to be somewhat larger than specified on the growth sheet. Using these parameters, a fit to the QE minima was obtained and the electric field intensity in cavity deduced. The chart shown in figure 5.17 indicates the field intensity distribution in the cell, showing cavity minima at half the QWs together with the fit to the QE minima. While the cavity minima serve to lower the absorbtivity of the QW, they will also lower the emissivity. As the radiative recombination is peaked around the e1-hh1 exciton, the overall emission may be suppressed.

To investigate this point further a calculation of the EL spectrum, expected from the quantum efficiency was performed. In the limit of an optically thin cell, to which the QW wavelengths correspond, the absorbtivity a may be approximated to the quantum efficiency, such that $a \propto QE$. From chapter 4 and specifically equations 4.2 and 4.3, the EL behaviour may be expressed as:

$$EL(V) \propto \int_0^\infty a(E) \frac{E^2}{e^{(E-V)/kT} - 1} dE \tag{5.21}$$

The calculation is in arbitrary units, but serves as a relative comparison between the cavity and substrate samples. The spectra calculated from the QE curves for QT957 are shown in figure 5.18 together with the integrated EL intensity. The important value from this analysis is that the EL, derived from the QE, is 1.7 times greater in the cavity sample than with the substrate.

In radiatively dominated material, the EL_{cavity}/EL_{sub} ratio is 2 in the regimes of constant voltage and $\alpha W \ll 1$, as quoted in table 5.2 . In the absence of any other effects, suppression of the e1-hh1 exciton as observed here, may lead to a reduction in cavity dark-IV by a factor $1.7/2 = 0.85$. However, this is not sufficient to explain the large reduction in dark-IV by a factor of ~ 0.05, as observed from the QT957B *cavity/substrate* ratio. Thus modification of the emission spectrum by cavity effects cannot by itself explain the reduction in dark-IV.

[3]Dr. Geoff Hill of the EPSRC III-V Facility, University of Sheffield is gratefully acknowledged for these measurements

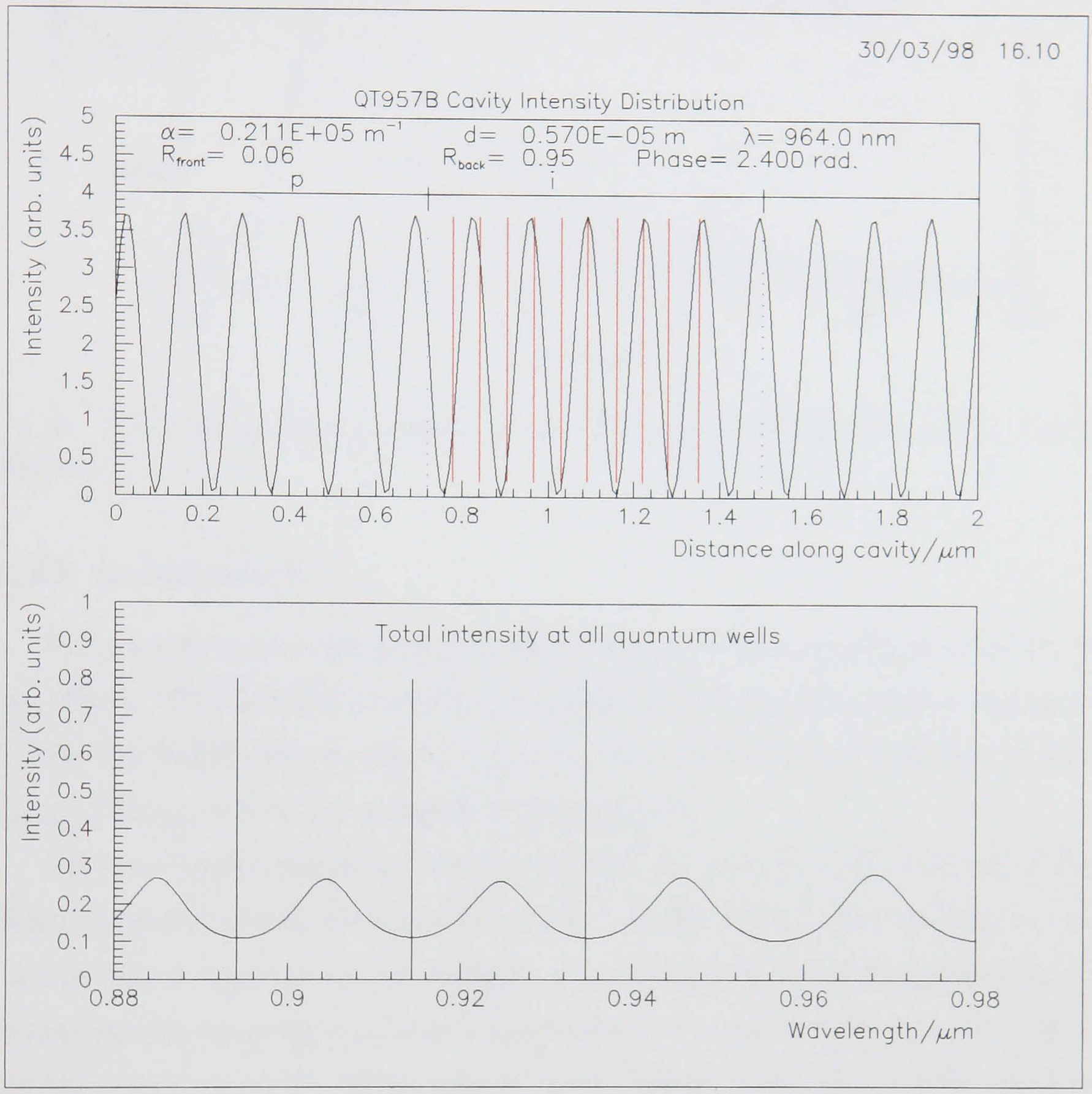

Figure 5.17: Possible Fabry-Perot behaviour for QT957B. The upper graph shows the optical intensity as a function of distance along the cavity, the vertical lines from $0.8\mu m$-$1.4\mu m$ indicating the position of the QWs, the dotted lines indicating the extent of the p, i and n region. The lower graph shows the fit to the cavity minima, obtained by varying the phase at the rear (semiconductor/gold mirror) surface. The vertical lines indicate the cavity minima observed in the QE data (see figure 5.16.

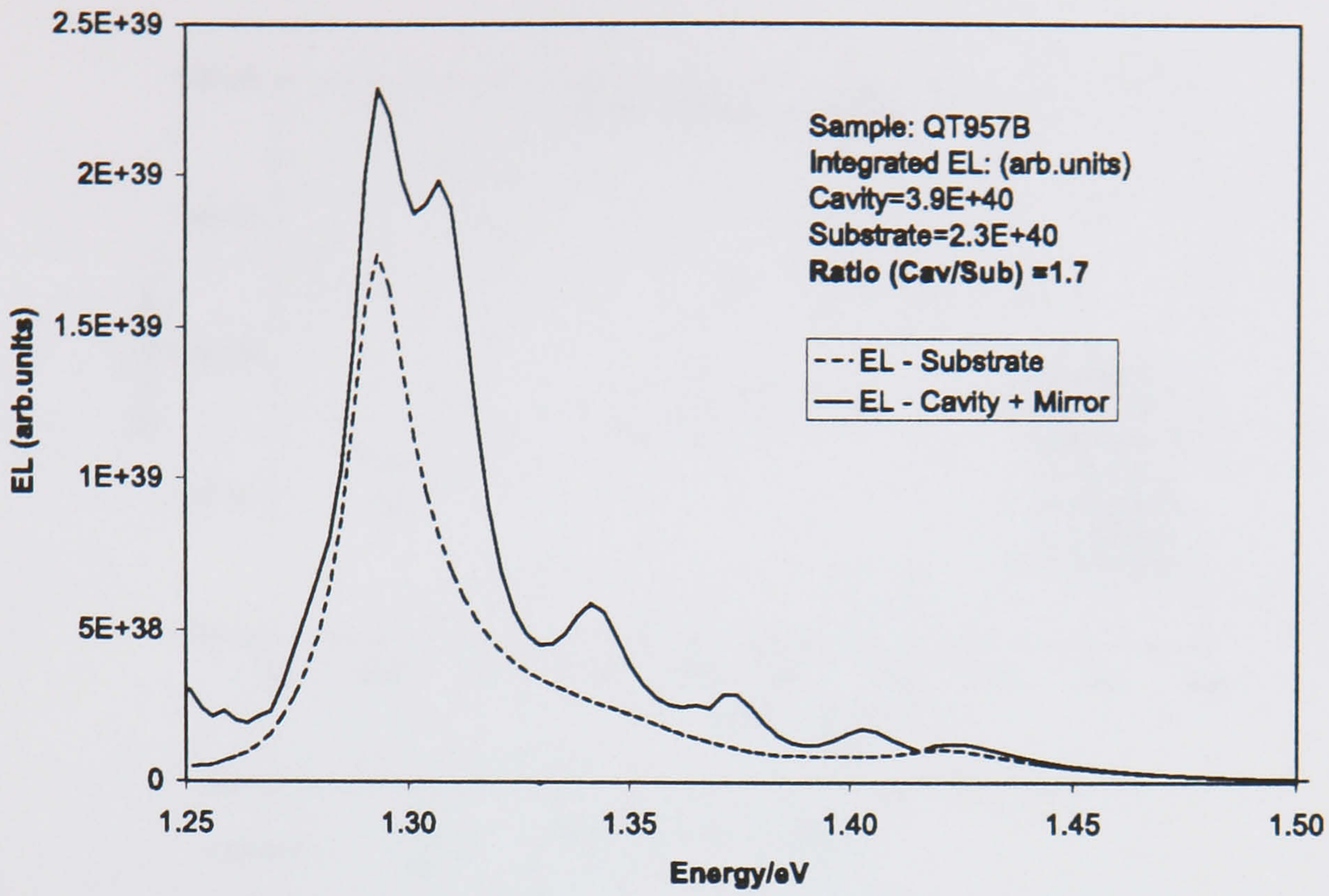

Figure 5.18: Theoretical EL calculation from QE data; QT957B with cavity+mirror and with substrate.

Cavity EL measurement

EL measurements represent a powerful means of discriminating between photon-recycling effects. The behaviour which is expected for photon recycling is summarised in table 5.2 and for MQW cells we expect $EL_{cavity}/EL_{sub} \approx 50$ in the constant current regime and $EL_{cavity}/EL_{sub} \approx 2$ in the constant voltage regime.

All the EL measurements were performed at room temperature using the same experimental apparatus described in section 4.2.1. In the absence of a calibration measurement, it was important that all the samples were located at the same position in front of the collimating lens allowing a relative comparison to be made. This was achieved using a reference laser spot, to which the sample could be aligned by maximising the photocurrent. Once aligned, the laser was turned off and EL measurements taken.

In order to verify the reproducibility of the measurement, four MQW samples were measured with a substrate. QT957B and QT957C were chosen as controls for the cavity samples and two additional substrate samples, QT957A and a nominally identical sample QT459B were measured. In each case two devices were measured for each sample.

The cavity samples proved considerably harder to measure. Samples QT957BA, QT957CA and QT957CB were excluded from the measurement, on account of series resistance evident from figure 5.15. Of the remaining cavity samples, there were a number of defective devices on each header and many of those remaining had bond-wires crossing

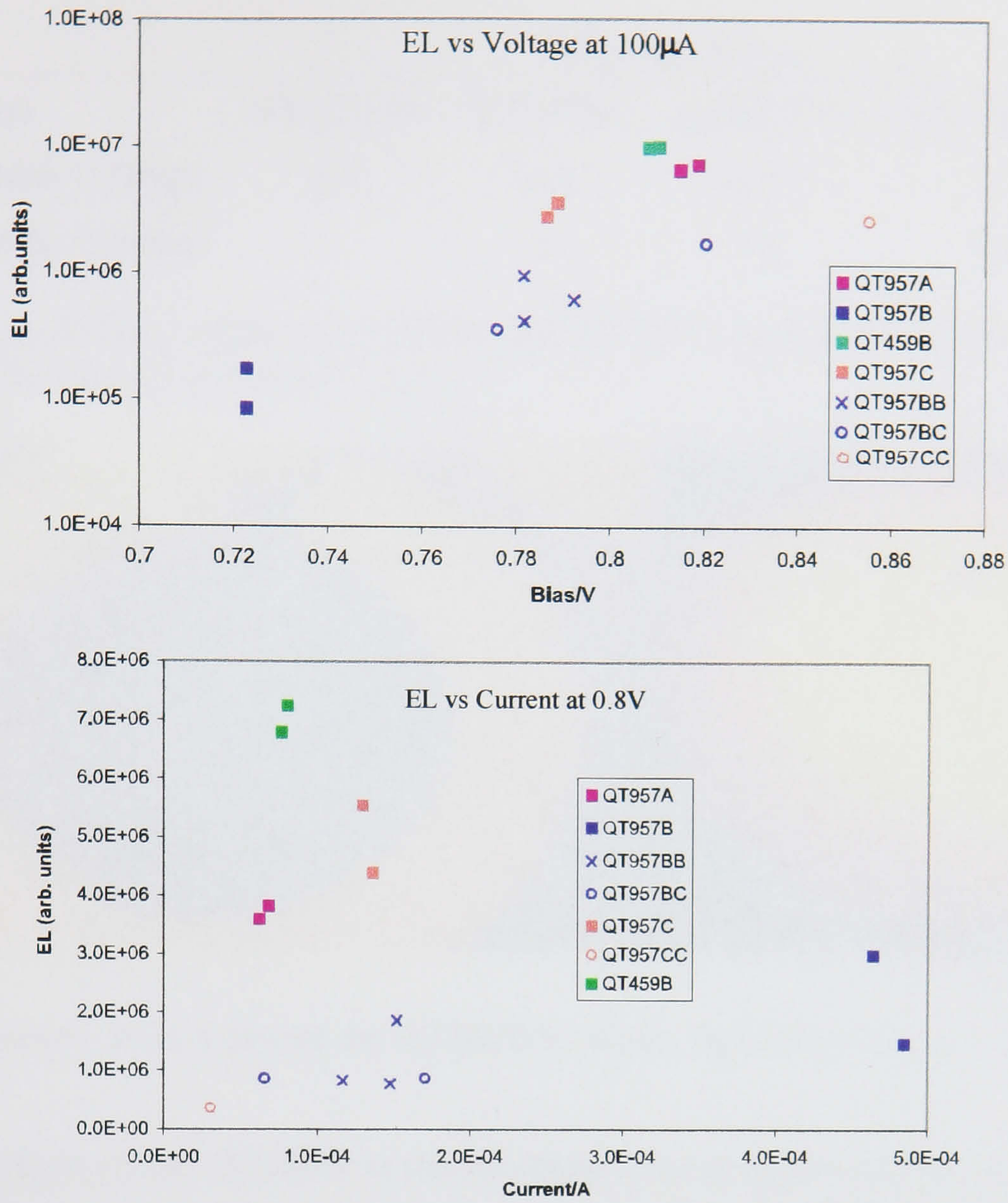

Figure 5.19: Integrated EL data for the constant current and constant voltage regimes. Note sample names with substrate are QTxxxx and cavity samples are followed by the suffix B='black paint' and c='gold mirror'.

the optical window. This restricted the number of devices available for the EL experiment, giving up to two data points for each sample and processing 'flavour'. Further, the cavity + gold mirror samples had become unstuck from the header and were floating in free space suspended only by the bond-wires. Under such circumstances it is surprising that the devices worked at all, but it was consequently difficult to ensure that these devices were normal to the optical axis, defined by the collimating lenses.

The EL data for the constant voltage and constant current regimes is shown in figure 5.19. The control samples show reasonably consistent results, QT459B and QT957A being particularly reproducible. However the cavity cells do not show the same degree of reproducibility and give conflicting behaviour.

The ratios for cavity and substrate EL are summarised in table 5.4. The values were obtained by averaging all the QT957B and QT957C data points plotted on the EL

	EL_{cavity}/EL_{sub}			
Regime	QT957BB	QT957BC	QT957CC	Rad. Theory
Constant Voltage	0.4	0.4	0.07	2
Constant Current	4	8	0.8	52

Table 5.4: EL_{cavity}/EL_{sub} ratios for QT957B and QT957C, together with the value expected from the radiative theory of section 5.4.1.

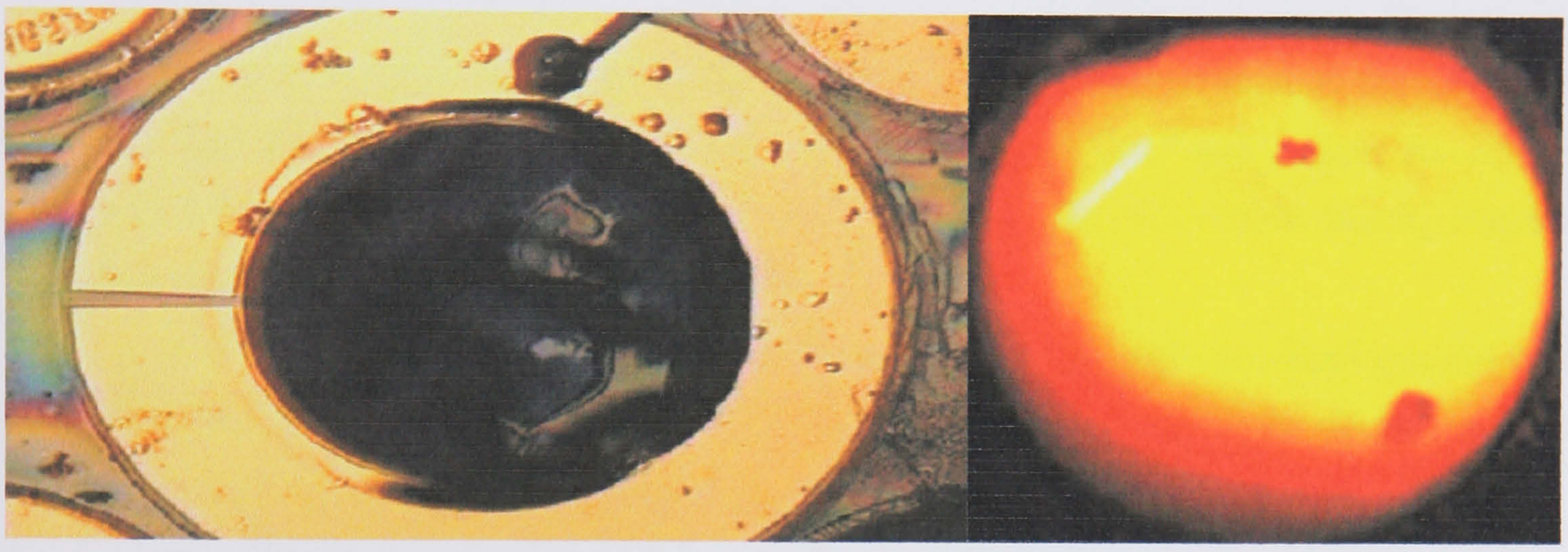

Figure 5.20: Images from a device on QT957BB, white light illumination and spatial EL.

charts shown in figure 5.19. QT957B in the constant current regime is the only sample which shows any semblance to the theoretical expressions of table 5.2. Indeed, while experimental doubts have already been raised over the validity of the cavity+mirror data, QT957C shows conflicting results from all the samples.

With inconclusive EL spectral data it was decided to investigate the spatial variation of the EL across the $550\mu m$ optical diode window. This was performed using a Renishaw Ramascope, operated in imaging mode as a spatially sensitive EL detector[4]. For the sake of brevity, only a small fraction of the EL images obtained are reported in this thesis.

Spatial variation in EL intensity was observed across many of the samples and is the primary reason for the inconsistencies in figure 5.19. For example figure 5.20 shows a white light image of QT957BB together with its EL image, indicating optically significant surface defects. Inhomogeneities were observed for the QT957B device with the lower EL, but QT957A remained consistent between pins. More worryingly, a white light image of QT957CB indicated that back paint had contaminated the surface of the sample, calling the black paint processing technique into question.

[4]Dr. Steve Webb is gratefully acknowledged for assistance with these measurements, together with the South Bank University for allowing time on their Renishaw Raman system

5.4.4 MQW photon recycling - alternative explanations

The experimental data supporting photon recycling is questionable. The primary evidence is the dramatic reduction in dark-IV upon substrate removal, which in radiatively dominated material would strongly favour photon recycling. However, the dark-IV curves are not radiatively dominated and the observation of a larger reduction for a poorer sample (QT957B) suggest caution should be exercised before attributing the effects to photon recycling.

Structural changes might be expected from the delicate nature of the cavity cell. However, any such defects would serve to raise the dark-IV and not reduce it. Further, EBIC microscopy performed by Max Mazzer indicated that the dislocation density remained unchanged upon the removal of the substrate.

The quantum efficiency measurements are consistent with standard optical cavity behaviour and possible effects due to Fabry-Perot oscillations have been shown to be too small to give rise to the large differences in dark-IV.

The EL measurements were disappointing in that the optical quality of the devices was not sufficiently consistent to afford meaningful comparison. However, none of the values extracted from the EL experiment resemble the magnitude of those expected from the photon recycling theory.

A comparable experimental investigation of cavity GaAs diodes performed at Purdue University [100] indicates some evidence for photon recycling. The raw experimental results indicate a factor of 2.5 increase in cavity EL over the substrate EL under constant current and slightly different dark-IV shapes. After considerable data fitting, to remove shunt resistances and non-radiative contributions, a factor of $\frac{1}{3}$ in the radiative (n=1) component is extracted for the cavity over the substrate sample. Although no mention is made of the experimental and fitting errors, the authors of this paper attribute these results to photon recycling.

If the GaAs diode study really is an observation of photon recycling, then it becomes highly unlikely that the dramatic dark-IV differences observed in MQW diodes are the result of photon recycling. While the theory for the GaAs diodes corresponds more to the optically thick cell ($\alpha W \gg 1$), there should be a correspondence in magnitude between the reduction in dark-IV and increase in EL. Unlike the GaAs study, there is only a weak correspondence and some aspects, such as the constant voltage behaviour, are completely contradictory.

A remaining explanation for this behaviour is some form of perturbation in the

electric fields and consequently the quasi-Fermi levels, introduced by moving the rear contact closer to the depletion region. Such a pacifying effect would help explain the strange coincidence that two samples of differing quality converge on the same dark-IV characteristic; evident from figure 5.15 where both cavity cells drop to the same level as the control cell QT957D.

The only means for determining whether the MQW samples reported here are displaying a photon recycling phenomena, is to investigate some more samples. Of particular interest, a pair of 10 MQW samples (one possessing an etch-stop) have been grown by MBE[5]. Characterisation to date, shows both samples possess similarly good optical and electrical characteristics. Although the substrate has yet to be removed, the purity of these two samples seems to be consistent, which will aid any interpretation of cavity cell data. In the longer term a series of samples could be grown with different n-region thicknesses, in order to investigate the effect of the proximity of the rear surface. Further efforts at contacting to the n-region could be attempted, possibly from the rear-surface rather than using the top-surface In dot.

5.5 Light-trapping conclusions

Achieving light trapping in GaAs/InGaAs MQW cells is of paramount importance if the QW photocurrent is to be maximised. A theoretical framework for analysing samples using normal incidence measurements has been described and applied to determine the diffuse reflectivity from a 'rough' gold-epoxy mirror. The theoretical framework has already allowed samples with textured substrates to be characterised and will aid development of an efficient light trapping structure in the future.

The benefits of a cavity cell structure have been discussed, particularly with reference to the possibility of photon recycling in MQW cells. While in principle it should be possible to achieve *cavity/substrate* dark-current reductions by a factor of $\frac{1}{40}$, in practice experimental confirmation has proved elusive. Although QT957B shows such a reduction in dark current, the EL data contradicts photon recycling theory and it is highly questionable whether photon recycling effects could ever dominate in non-radiatively dominated (n=2) material. Further work on samples with differing n-region widths and n-type contacts is required to establish the cause of the reduction in cavity dark-IV.

[5]RM1365, RM1366 grown by Bob Grey, Univ. Sheffield, U.K.

Chapter 6

Strain Balance Techniques

The survey of GaAs/InGaAs strained p-i-n structures reported in chapter 2 discussed the issues concerning the effect of strain on the dark current. Misfit dislocations in the active, field bearing region dominate the dark-IV behaviour, ensuring that strained GaAs/InGaAs p-i-n structures are unable to surpass GaAs in terms of power conversion efficiency.

Strain balance techniques offer a means of controlling the build-up of strain energy in a structure. A strain balanced system is one in which the composition of the device has been specifically chosen such that strained layers are compensated by the adjacent material which possesses exactly the opposite strain. Thus it is possible to grow locally strained layers which are unstrained with respect to a chosen substrate. The modulated structure may be repeated, without relaxation, until the desired thickness is grown.

Considering the structure depicted in figure 6.1, two lattice mismatched materials 1 and 2 are grown on a lattice mismatched substrate. The strain-balance condition is met when the average lattice parameter $\langle a \rangle$ across the modulated region defined by equation 6.1 equates the substrate lattice parameter. Similarly the average strain $\langle f \rangle$ between the MQW stack and neighbouring layers defined by equation 6.2 becomes zero when the structure is strain balanced.

$$\langle a \rangle = \frac{t_1 a_1 + t_2 a_2}{t_1 + t_2} = a_{substrate} \tag{6.1}$$

$$\langle f \rangle = \frac{\langle a \rangle - a_{substrate}}{a_{substrate}} \tag{6.2}$$

In this chapter two such systems are discussed. Section 6.1 describes the GaAs/InGaAs system, relying on a 5% InGaAs virtual substrate and section 6.2 details a GaAs/InGaAs/GaAsP

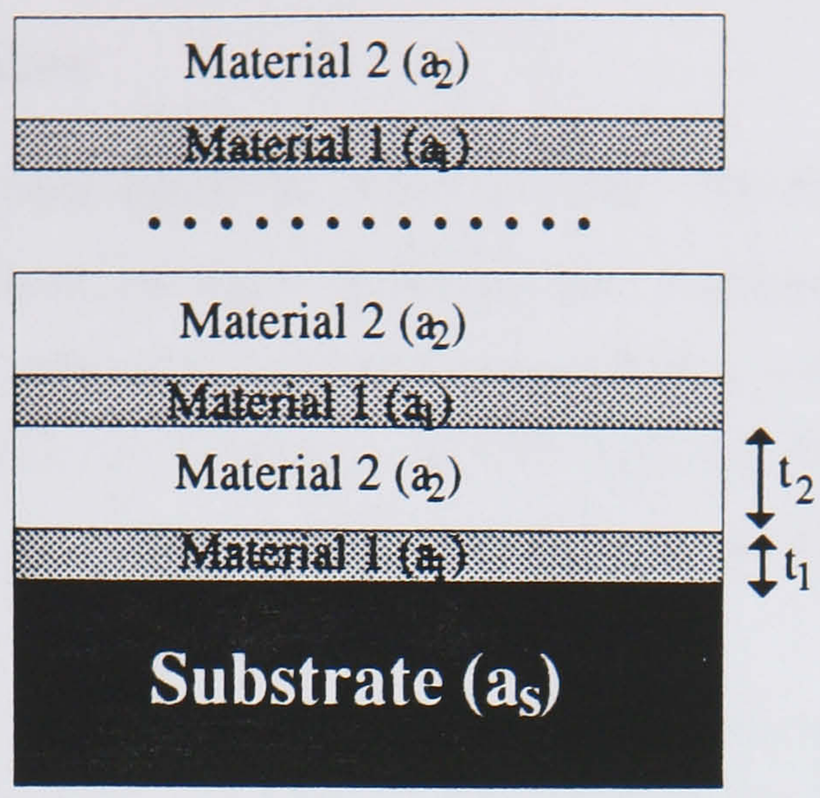

Figure 6.1: A modulated structure composed of materials 1 and 2, grown on an arbitrary substrate of lattice parameter a_s

system grown directly on a GaAs substrate.

6.1 GaAs/InGaAs Strain-Balance

In the GaAs/InGaAs material system, it is necessary to compensate the strain due to the InGaAs QWs with GaAs barriers of suitable thickness. The GaAs barriers, InGaAs well thickness and composition must be specifically chosen to ensure the average lattice constant $\langle a \rangle$ is equal to the substrate. Due to the linearity between the InGaAs lattice parameter and InGaAs composition, the average indium composition across the i-region may be written as,

$$\langle x \rangle = \frac{t_{qw} x_{qw}}{t_{qw} + t_b} \tag{6.3}$$

where t_{qw} is the QW width, t_b is the GaAs barrier width and x_{qw} is the QW indium fraction.

As a consequence, the average indium fraction must always be lower than the QW indium fraction and a substrate must be chosen so to match the average indium fraction. In the study reported here, the average indium composition was chosen to be $In_{0.05}Ga_{0.95}As$ requiring a corresponding substrate.

Whilst there is no intrinsic difficulty in manufacturing $In_{0.05}Ga_{0.95}As$ substrates, they do not exist in large quantities and are prohibitively expensive. It is more appropriate to grow on a GaAs substrate (0.4% lattice mismatch) and form a virtual substrate onto which the strain-balanced layers can be grown.

6.1.1 Virtual Substrates

Conceptually a virtual substrate serves to alter the lattice parameter of a growth surface by depositing lattice-mismatched material and allowing strain relaxation to take place. Naturally the strain relaxation involves generating a large quantity of misfit dislocations, but if one can confine the dislocations to a region in which there are few minority carriers then, as discussed in section 1.2.2, the recombination rate will be low and the dislocations rendered inert.

Indeed, growth on foreign substrates is of general interest to the photovoltaic community. Ge is a desirable substrate for photovoltaic devices as it is considerably stronger than GaAs. Ge substrates may be made thinner and therefore lighter and are less expensive than GaAs. Importantly Ge is almost lattice matched to GaAs (0.1% lattice mismatch) and 24.3% (AM1.5) efficient GaAs/Ge tandem cells have been demonstrated on Ge substrates [101]. From an economic perspective, III-V growth on Si substrates is extremely advantageous; there being a factor of 8 between the GaAs and Si substrate cost [102]. Whilst, the large lattice mismatch (4%) between Si and GaAs poses considerable difficulties, effective techniques have been developed allowing good quality overgrowth producing 20% efficient cells [103]. More recently, attempts to add a third junction to the InGaP/GaAs tandem cell [33, 34] has lead to work growing 15-30% bulk InGaAs cells on Ge substrates [26]. Progress in this area is promising, with cells showing high V_{oc} and low defect densities ($5 \times 10^5 cm^{-2}$).

A virtual substrate is achieved by growing a strained buffer layer, which once the critical thickness is exceeded and relaxation has taken place, possesses the desired lattice parameter. However, the strained layer will not relax entirely to its equilibrium (unstrained) lattice parameter. The residual strain in a post-relaxation epilayer decays exponentially to a non-zero asymtote [104]. The degree of residual strain in a layer varies upon growth conditions and upon any compositional grading in the epilayer [105].

The minimum thickness required for a strained layer is given by a Matthews-Blakeslee estimate of 500Å for $In_{0.05}Ga_{0.95}As$. If the misfit dislocations are to be isolated from the active region, then the relaxed epilayer should be grown at least of the order of a carrier diffusion length.

In practice there are considerable complications ensuring that the strain relaxation takes place in a well behaved manner. A variety of empirical techniques exist for achieving good material quality [105] on relaxed substrates. Two conceptually straightforward techniques were adopted, one was simply growing a $2\mu m$ $In_{0.05}GaAs$ buffer region onto the

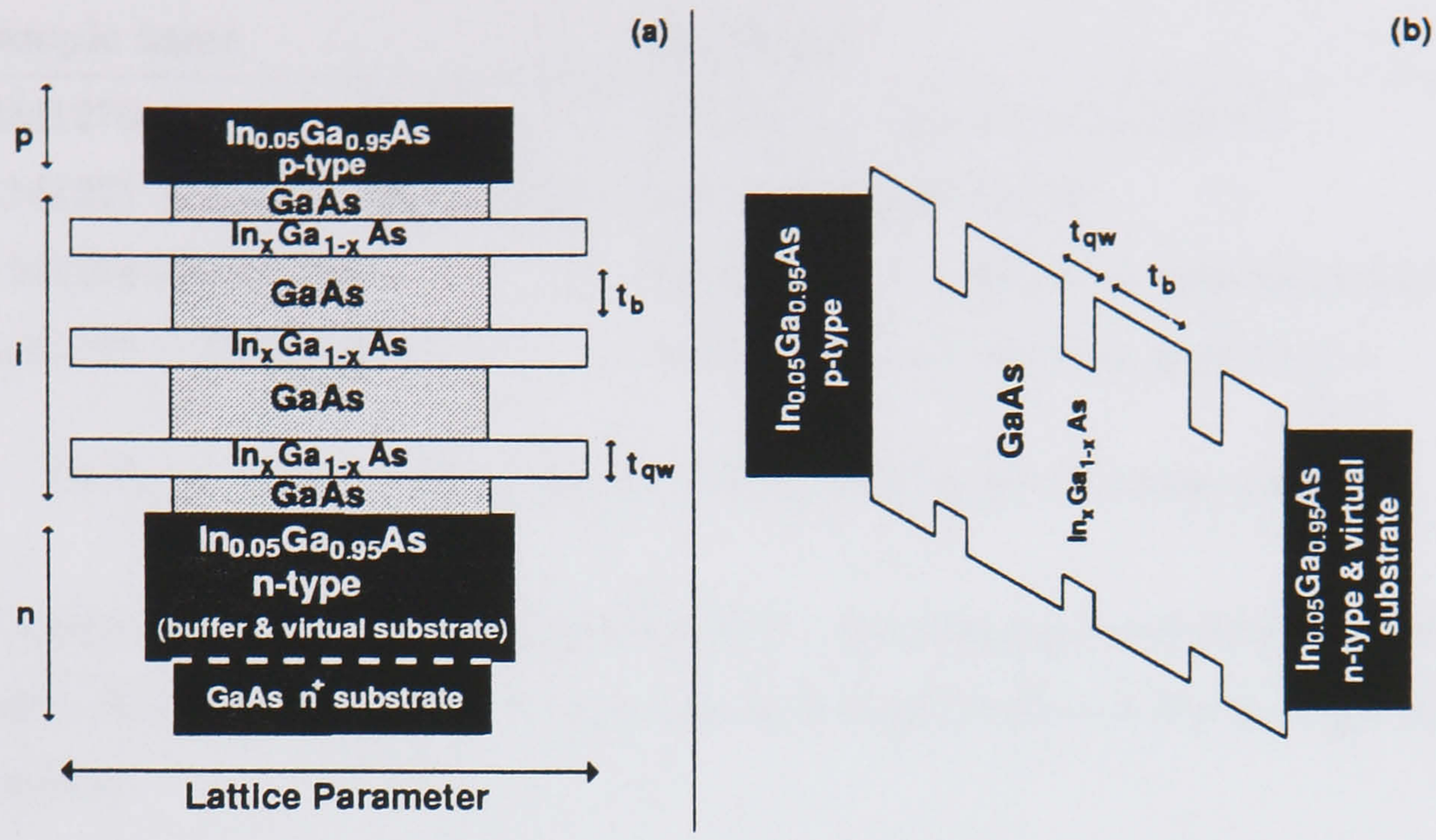

Figure 6.2: Schematic diagram and band-structure for the GaAs/InGaAs strain balanced cell, with $In_{0.05}GaAs$ virtual substrate.

GaAs substrate and the other involved growing a 250nm $In_{0.1}Ga_{0.9}As$ layer followed by the $2\mu m$ $In_{0.05}Ga_{0.95}As$ buffer region. The thin $In_{0.1}Ga_{0.9}As$ layer was designed to relax the layer beyond that required, encouraging the residual strain to asymptote to $In_{0.05}Ga_{0.95}As$ after $2\mu m$ growth [106].

6.1.2 Growth specification

The devices were based around the schematic structure shown in figure 6.2 and grown on n+ doped GaAs substrates. The virtual substrate was formed by allowing the $In_{0.05}GaAs$ n-type layer to relax through the generation of misfit dislocations. MBE growth was performed by Bob Grey[1] and an MOVPE sample (Lecce 001) by Adriana Passaseo[2]. Full layer descriptions may be found in the appendix C.4, but briefly RM1271 was a strain balanced cell containing a 23 period MQW p-i-n structure, with 300Å GaAs barriers, 80Å $In_{0.24}Ga_{0.76}As$ QWs and $In_{0.05}Ga_{0.95}As$ p and n regions. RM1276 was identical to RM1271 except that it possessed a $In_{0.1}Ga_{0.9}As$ strain relaxation layer between the n-type GaAs and $In_{0.05}GaAs$ layers. RM1277 was identical to RM1271 except that it had an AlGaAs/AlAs etch stop. RM1270 was a bulk $In_{0.05}Ga_{0.95}As$ p-i-n control cell. A second series of cells were grown as repeats of RM1271, RM1276 and RM1277. Table 6.1 summarises the samples and their names.

All the samples, except Lecce 001, were subsequently processed into 1mm mesas

[1]EPSRC III-V Facility, University of Sheffield, U.K.
[2]PASTIS-CNRSM, Brindisi, Italy

Sample name	Description
RM1270	bulk $In_{0.05}Ga_{0.95}As$ p-i-n control
RM1271 / RM1386 /Lecce 001	Strain-balanced MQW
RM1276 / RM1391	Strain-balanced MQW + relaxation layer
RM1277 / RM1389/90	Strain-balanced MQW + etch stop

Table 6.1: Sample summary for GaAs/InGaAs strain-balance series.

allowing the dark-current and quantum efficiency to be measured as described in section 3.3. Sample Lecce 001 proved impossible to process as a mesa diode on account of problems with the ring-contact.

6.1.3 Experimental results

The results obtained from the strain balance samples were extremely varied, requiring extensive characterisation of the wafers. This section starts by discussing the large variation in dark current, then the optical characterisation and methods for determining the barrier width. Electron beam induced current (EBIC) microscopy was performed by Max Mazzer, yielding valuable information about dislocation types and densities.

Dark Current

The graphs in figure 6.3 show a comparison of dark IV curves for the two strain balance samples with respect to the RM1270 control. The striking feature of these samples are that there is an extremely large variation between each cell and indeed between the two series.

The samples were all grown in the same MBE chamber and it is unlikely that variations in impurity levels would introduce such large differences in recombination. The strain balance condition places a tight tolerance upon the growth parameters, so it is likely that variation in recombination is due to strain induced dislocations, arising from fluctuations in layer thicknesses and indium composition. The role of dislocations and their effect on the dark-IV has already been discussed in section 2.1 there being a linear relationship between the dark-IV density and active dislocation density [43].

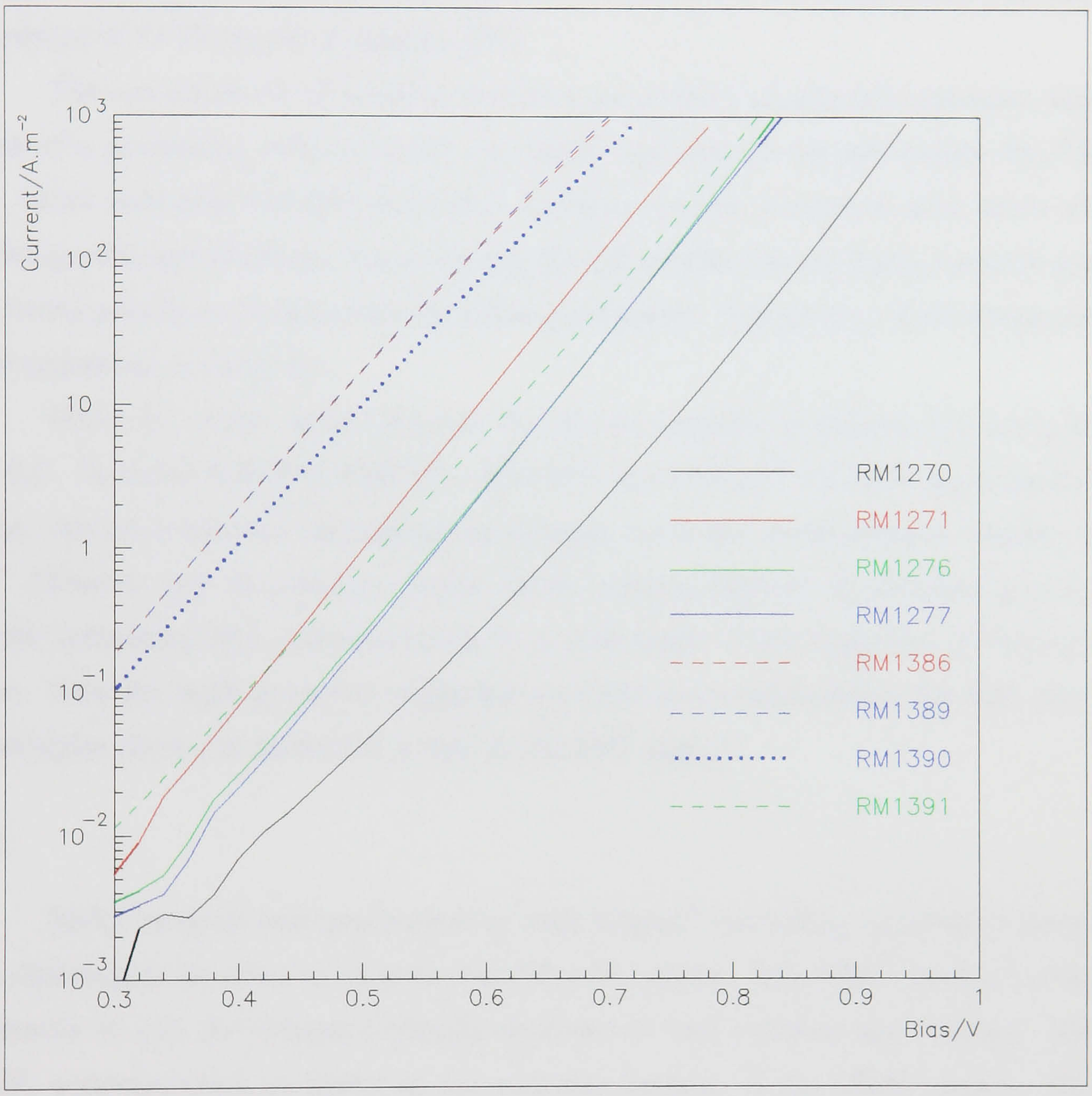

Figure 6.3: Dark IV curves for both series of strain-balance samples. (Nominally identical structures are grouped by line colour)

Quantum Efficiency & Mono-IV

The graphs shown in figure 6.4 show the quantum efficiencies for the two series of samples. The first series show that the samples have reasonable transport qualities, although the data has been corrected for a misleading AR coating. Modeling the quantum efficiency for RM1270, RM1276 and RM1277 showed that the dimensions and composition were consistent with the growth parameters. RM1271 was consistent with an indium composition of 17.5% in the quantum well.

The second series of samples exhibit a poor short wavelength response, mainly on account of a processing error whereby the GaAs cap was not etched before the AR deposition. More seriously, the QW transition energies are not consistent with those expected from the growth specification. By modeling the QE profile, the excitonic features suggested a well width greatly in excess of the specified parameters. A summary of all characterisation data is presented in table 6.4.

Mono-IV curves were obtained for all the samples at 600nm and are plotted in figure 6.5. Samples RM1270, RM1271, RM1276 and RM1277 all show good mono-IV behaviour, the photocurrent remaining unchanged until the measurement breaks down at +0.5V. However the remaining samples show varying degrees of photogenerated carrier loss with increasing bias, corresponding to a narrowing of the depletion width across the i-region. This incomplete carrier collection provides some explanation for why the QE for these samples shown in figure 6.4 is low in the QW region.

EBIC

EBIC analysis was performed by Max Mazzer[3] providing qualitative information on the dislocation densities at various depths in the device. The EBIC images are collected in appendix E and the images typically obtained at two accelerating voltages, 10kV and 30-40kV, corresponding to layers at the top and bottom of the MQW region. From the images, it is clear that the misfit dislocation density (dark-lines) is much greater at the lower MQW interface than at the upper. Indeed, RM1271 possesses very few dislocations at the upper interface but a substantial quantity at the lower interface. The presence of misfit dislocations provides further evidence that the MQW is strained with respect to the surrounding p and n layers. Importantly, RM1276 and RM1277 show a significant threading dislocation density (dark dots) which most likely stem from the strain relaxation in the buffer region. The EBIC analysis places the threading dislocation density at 10^6

[3]CNR-IME, Lecce, Italy

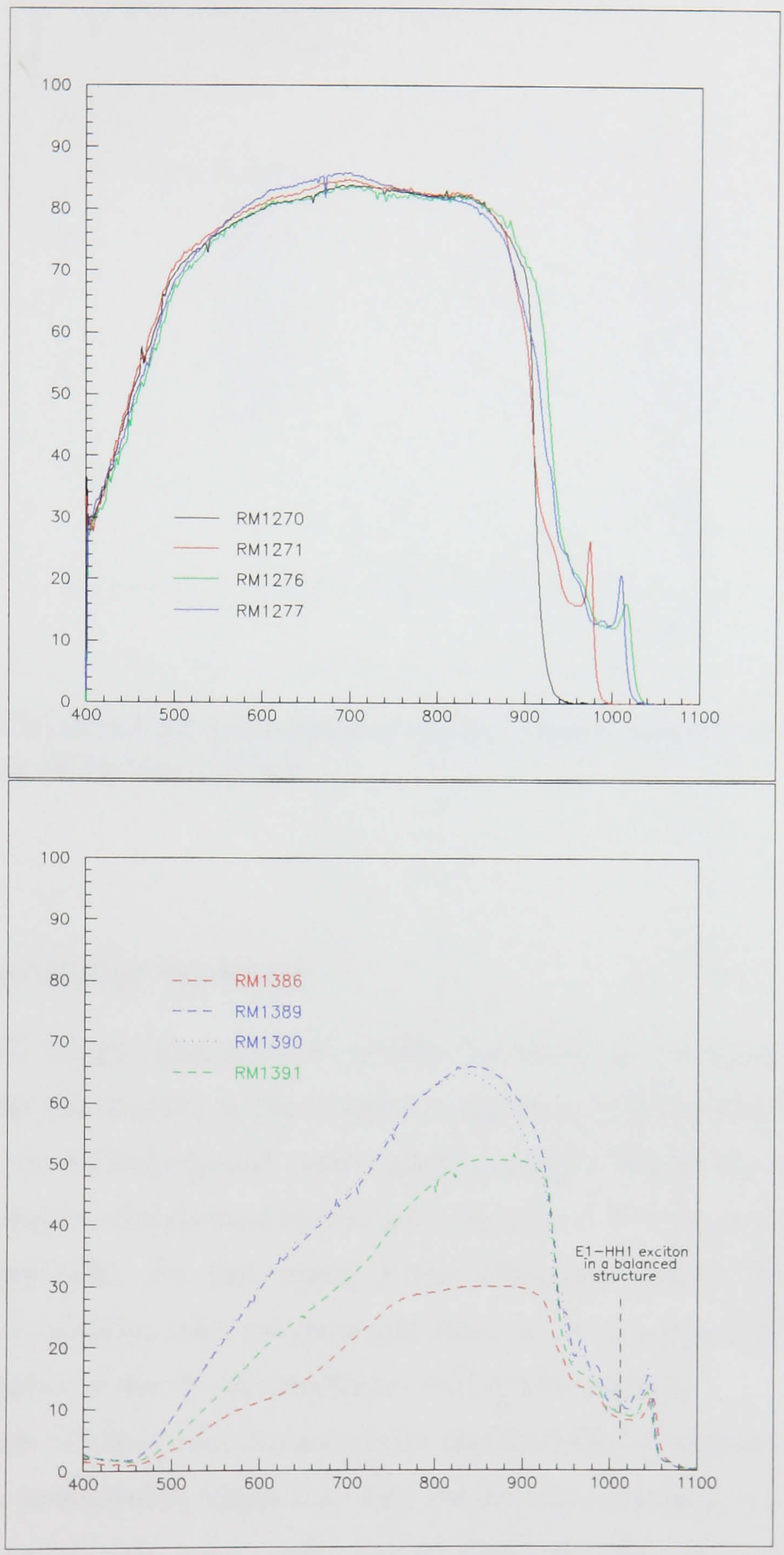

Figure 6.4: External quantum efficiency for samples RM1270, RM1271, RM1276 and RM1277 in the upper graph, and samples RM1386, RM1389, RM1390 and RM1391 in the lower graph.

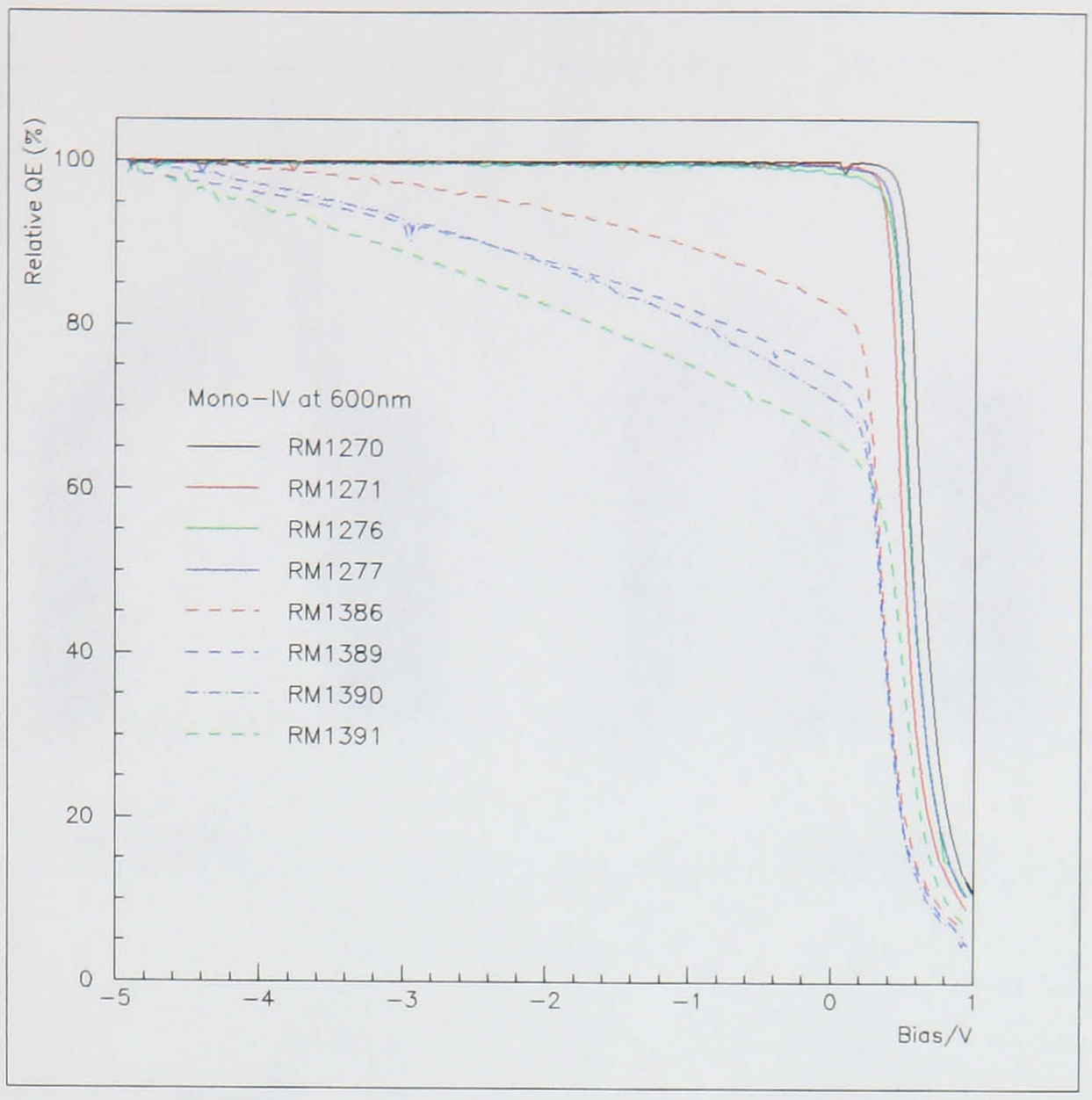

Figure 6.5: Mono-IV curves for both series of strain-balance samples. (Nominally identical structures are grouped by line colour)

dislocations/cm^2.

Determining the barrier thickness

The EBIC images and dark-IV profiles for many of the samples indicate a that strain relaxation has taken place in the i-region, suggesting that the dimensions or composition of the i-region do not correspond to the balanced values. While the quantum well width and composition may be determined by optical methods, it is impossible to determine the barrier thickness optically. For this reason X-ray diffraction (XRD) was performed on all the strain balanced samples, with transmission electron microscopy (TEM) measurements providing confirmation of the X-ray results for two of the samples.

The details of the X-ray measurement are described in chapter 3.3.6 and the experimental data is presented in figure 6.6. The results are presented in table 6.3

TEM measurements were performed by Giancarlo Salviati and Laura Lazzarini[4] on RM1276 and RM1277, providing confirmation of the layer thicknesses and some further information regarding the strain relaxation. The image shown in figure 6.7 shows a cross-section of RM1277. A large quantity of dislocations have been formed at the Al-

[4]CNR-MASPEC, Parma, Italy

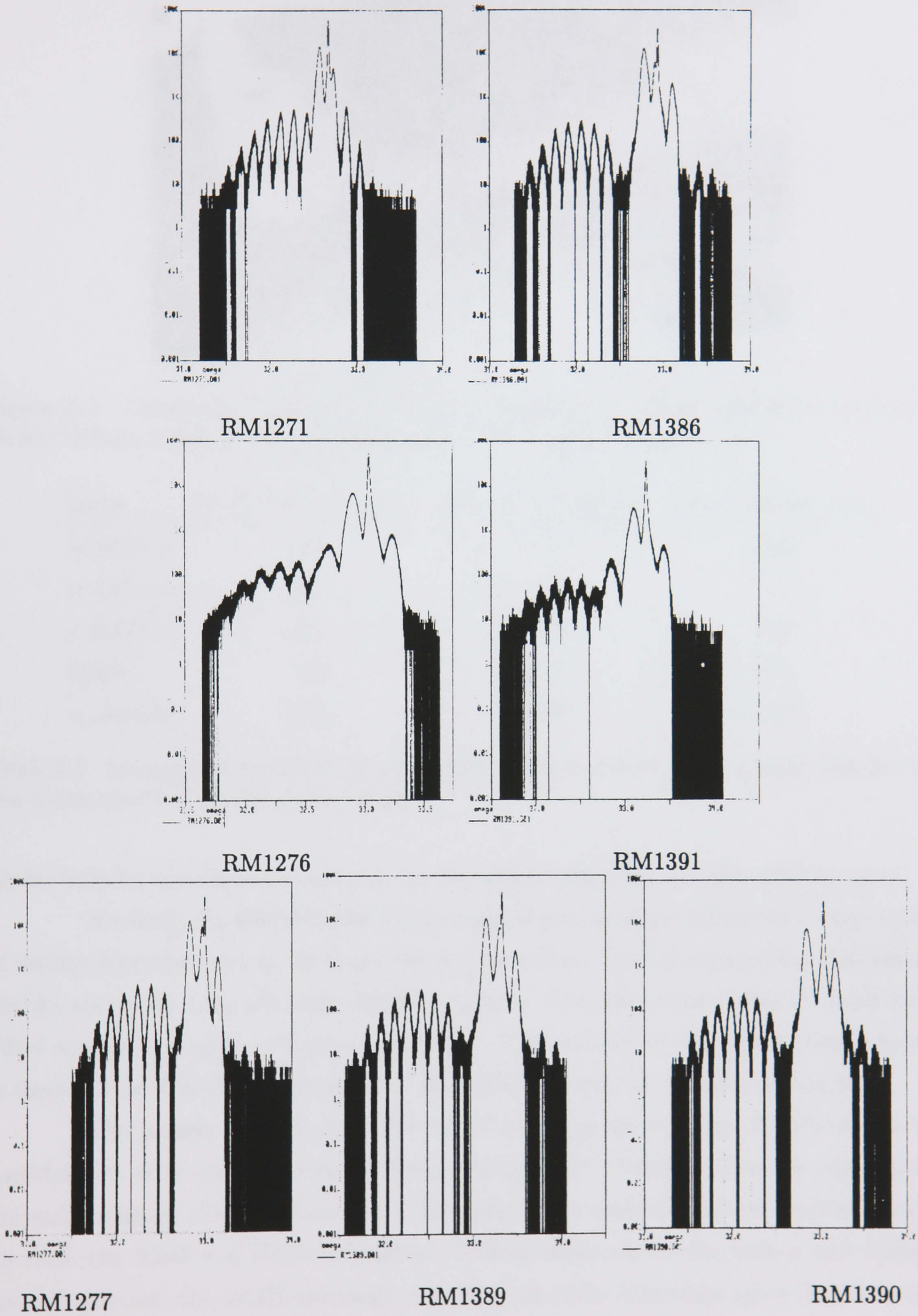

Figure 6.6: XRD rocking curves for samples grouped by type.

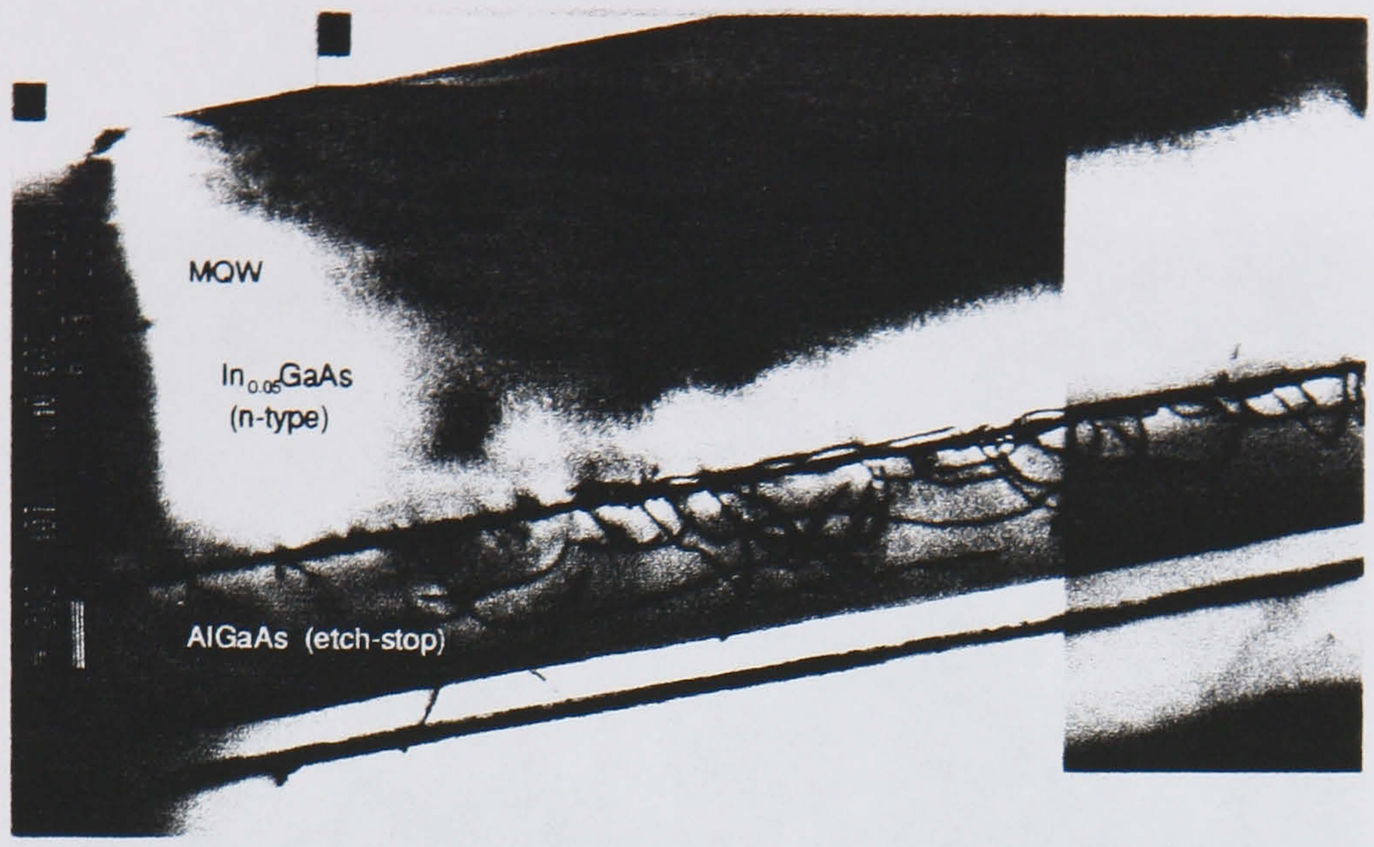

Figure 6.7: Composite TEM image of RM1277, showing strain relaxation between InGaAs/AlGaAs layers and the MQW region in the top left hand corner

Layer	RM1276 TEM(nm)	RM1277 TEM(nm)	Growth sheet (nm)
p InGaAs	185	195	220
p AlGaAs	41	44	43
p InGaAs	420	470	520
MQW	755	806	874
n InGaAs	1725	1720	2030

Table 6.2: Dimensions for RM1276 and RM1277 derived from TEM images together with the width specified on the growth sheet

GaAs/InGaAs and some dislocations can be seen propagating into the AlGaAs layer.

Similarly, for RM1276 the TEM image shown in figure 6.8 shows a large number of dislocations clustered at the GaAs/InGaAs interface. Notably a threading dislocation is visible, stemming from the lower MQW interface. The dislocation detection limit for the TEM images is roughly 10^5 dislocations/cm^2. The observation of a threading dislocation in figure 6.8 by TEM is consistent with the EBIC estimate of 10^6 dislocations/cm^2.

The images indicate that the cell dimensions are between 10-20% below their specification, with the exception of The p-AlGaAs layer. Table 6.2 lists the dimensions of the various layers obtained from the TEM images and table 6.3 lists the barrier thickness for both the TEM and XRD techniques. Whilst variations in the bulk p and n regions are unimportant, the MQW thickness is critical and both techniques agree that the barrier thicknesses are smaller than the specified 300Å.

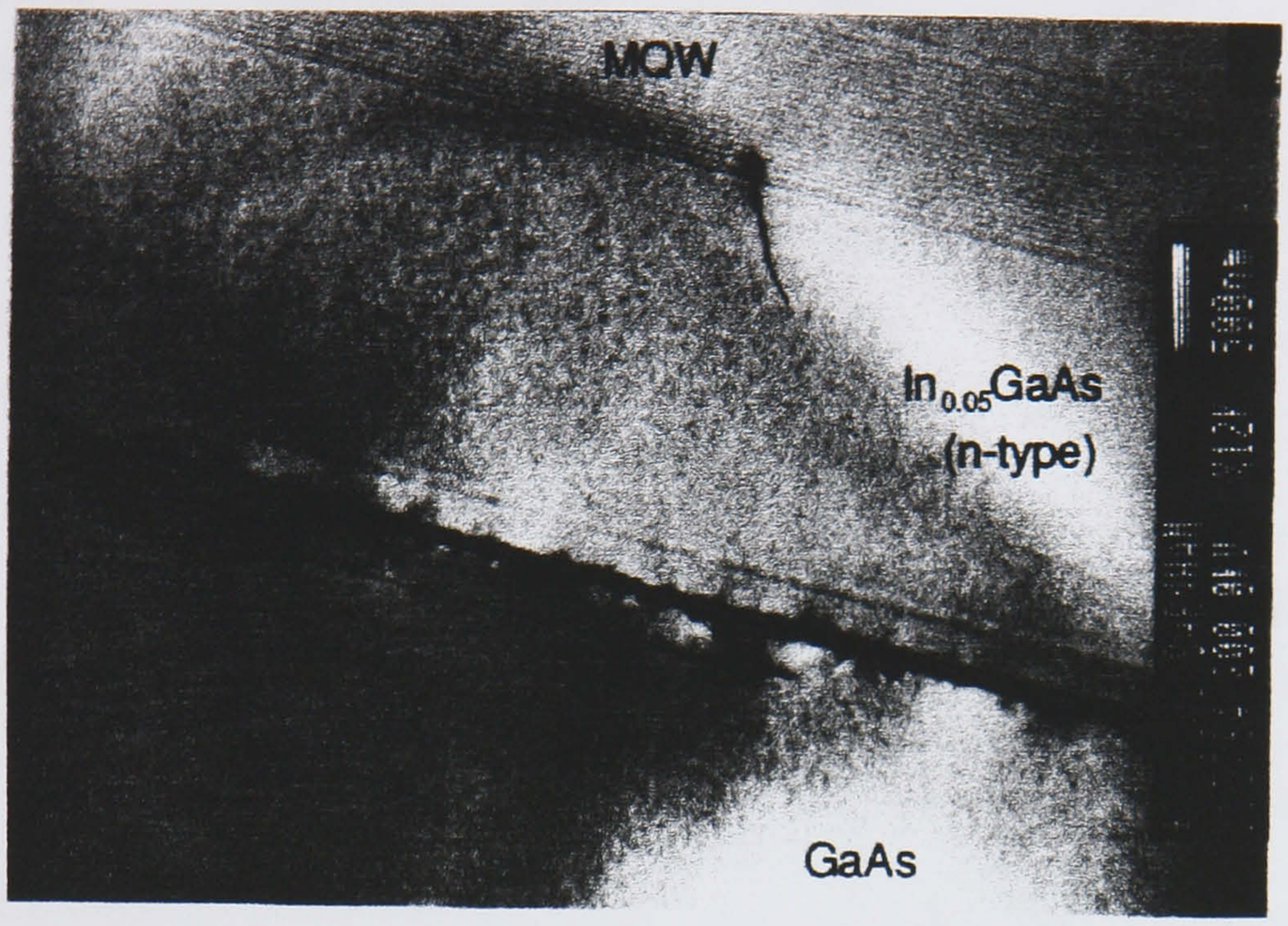

Figure 6.8: TEM image of RM1276, showing strain relaxation between GaAs/InGaAs layers and the MQW region in the top right hand corner. A threading dislocation is noted at the the lower MQW interface.

Sample	XRD Barrier/Å	TEM Barrier/Å
RM1271	268	-
RM1276	257	248
RM1277	267	270
RM1386	225	-
RM1389	210	-
RM1390	220	-
RM1391	205	-

Table 6.3: Barrier dimensions obtained from XRD and TEM measurements. The nominal barrier width was 300Å

Sample	x ± 0.005	$t_{qw} \pm 5/$Å	$t_b \pm 10/$Å	$t_{mqw} \pm 2/$nm	$\langle x \rangle \pm 0.01$	$\langle f \rangle /\%$
Balanced	0.240	80	300	874	0.050	0
RM1271	0.175	80	268	800	0.04	-0.07 ± 0.03
RM1276	0.240	80	257	775	0.06	0.05 ± 0.03
RM1277	0.240	80	267	798	0.06	0.04 ± 0.02
RM1386	0.240	130	225	817	0.09	0.27 ± 0.10
RM1389	0.230	140	210	805	0.09	0.30 ± 0.10
RM1390	0.230	140	220	828	0.09	0.28 ± 0.10
RM1391	0.230	140	205	794	0.09	0.31 ± 0.10

Table 6.4: Summary of QW indium fraction x, QW thickness t_{qw}, XRD barrier thickness t_b and extracted values for MQW thickness t_{mqw}, average indium fraction $\langle x \rangle$, average strain $\langle f \rangle$. The parameters for a hypothetical 'balanced' cell are also shown

6.1.4 Discussion of the results

The optical and structural characterisation is summarised in table 6.4 together with extracted values for the MQW width, average i-region indium content and an estimate for the average strain between the MQW stack and surrounding p and n layers. The estimate for the average strain assumes that the $In_{0.05}GaAs$ layers are fully relaxed, which as discussed in section 6.1.1 is not entirely accurate. Indeed, any departure from the $In_{0.05}GaAs$ composition will change the average strain value. None of the characterisation performed in this study was able to determine the buffer layer indium fraction to a high degree of accuracy. The bulk band-edge shown in the QE plots is consistent with $x = 4.8 \pm 0.8$. The XRD analysis was unable to improve upon this on account of the difficulties modeling structures with a relaxation layer. To account for this, the error quoted for the average strain reflects the error in determining the barrier width, QW parameters and buffer layer composition.

Figure 6.9 compares the average strain modulus $|\langle f \rangle|$ of table 6.4 with the dark-IV profiles of figure 6.3 at 0.5V. A clear trend is evident, that the dark-IV level increases as the average strain increases. However, RM1391 represents a marked departure from this behaviour, it being the most strained yet having a much lower rate of recombination than cells of similar strain; RM1390 for example.

A possible explanation stems from the mono-IV dependance shown in figure 6.5. RM1391 shows the largest loss in carrier collection of any of the samples, indicating that the i-region is never fully depleted under forward bias. The EBIC images shown in figure E.2

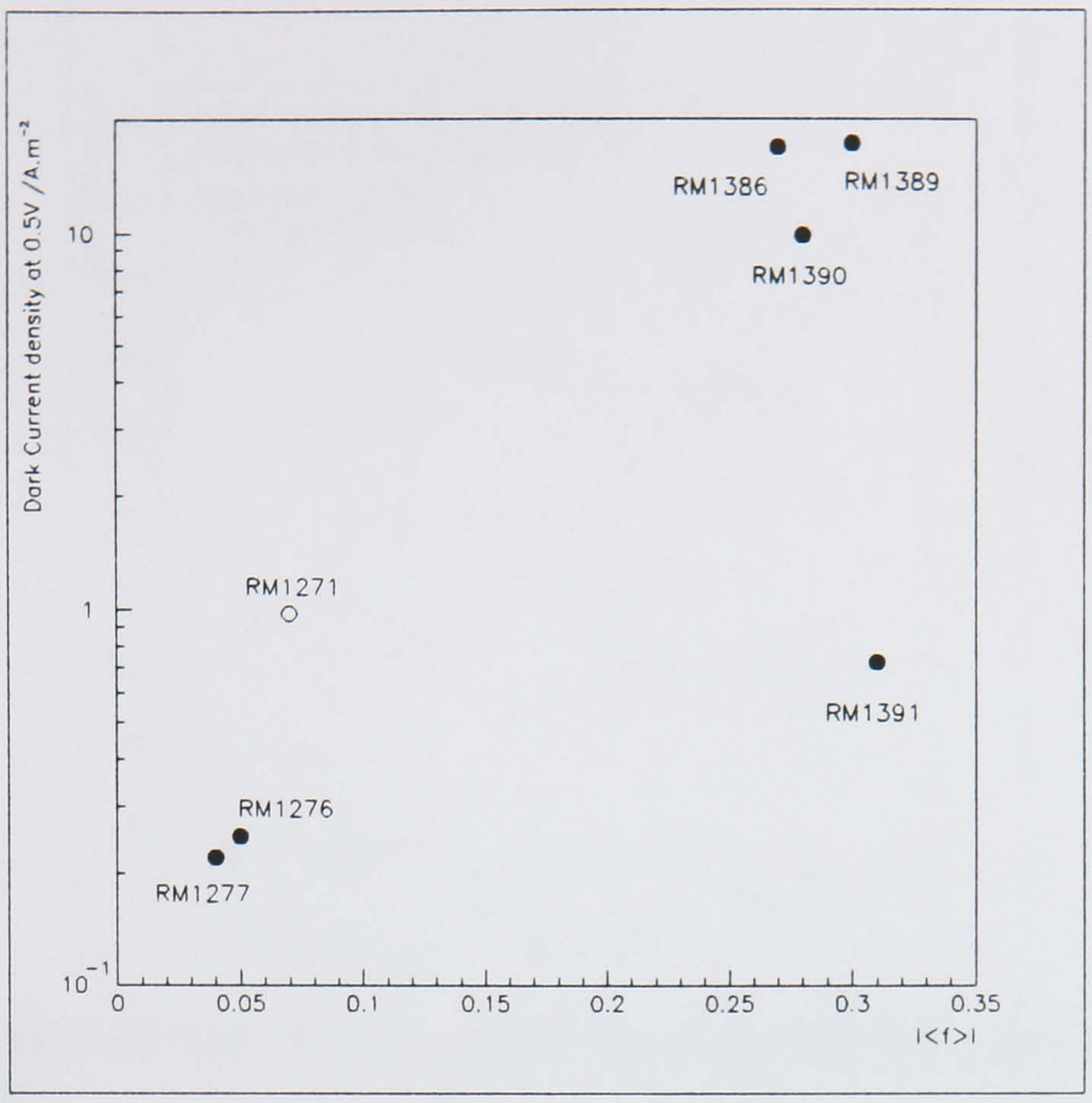

Figure 6.9: Plot showing the general trend between dark-current density at 0.5V and average strain. The modulus of the average strain is plotted, so compressively strained samples are shown by filled circles and tensile samples shown by open circles.

indicate arrays of misfit dislocations, which will be forming at the strained layer interfaces, i.e. at the top and bottom of the MQW stack. If the loss of depletion extends significantly beyond any of the misfit dislocation arrays, the associated traps will become filled and electrically passive. Under these circumstances, the non-radiative recombination rate could be lower than for a sample with comparable but fully depleted trap density.

The similarity between the RM1276 and RM1277 dark-IV curves is also worthy of comment and for this purpose a Matthews-Blakeslee model was invoked as described in the next section.

Matthews-Blakeslee Model

The Matthews Blakeslee model was applied to the GaAs/InGaAs strain balance system to provide some indication of the growth tolerance required to successfully grow of strain balanced cells.

The strain balance system is treated as two bulk layers of particular In fraction. This requires that the lower layer, or substrate be fully relaxed and have a lattice parameter according to its composition (x_s). Similarly the MQW stack is described by an average In fraction(x_e).

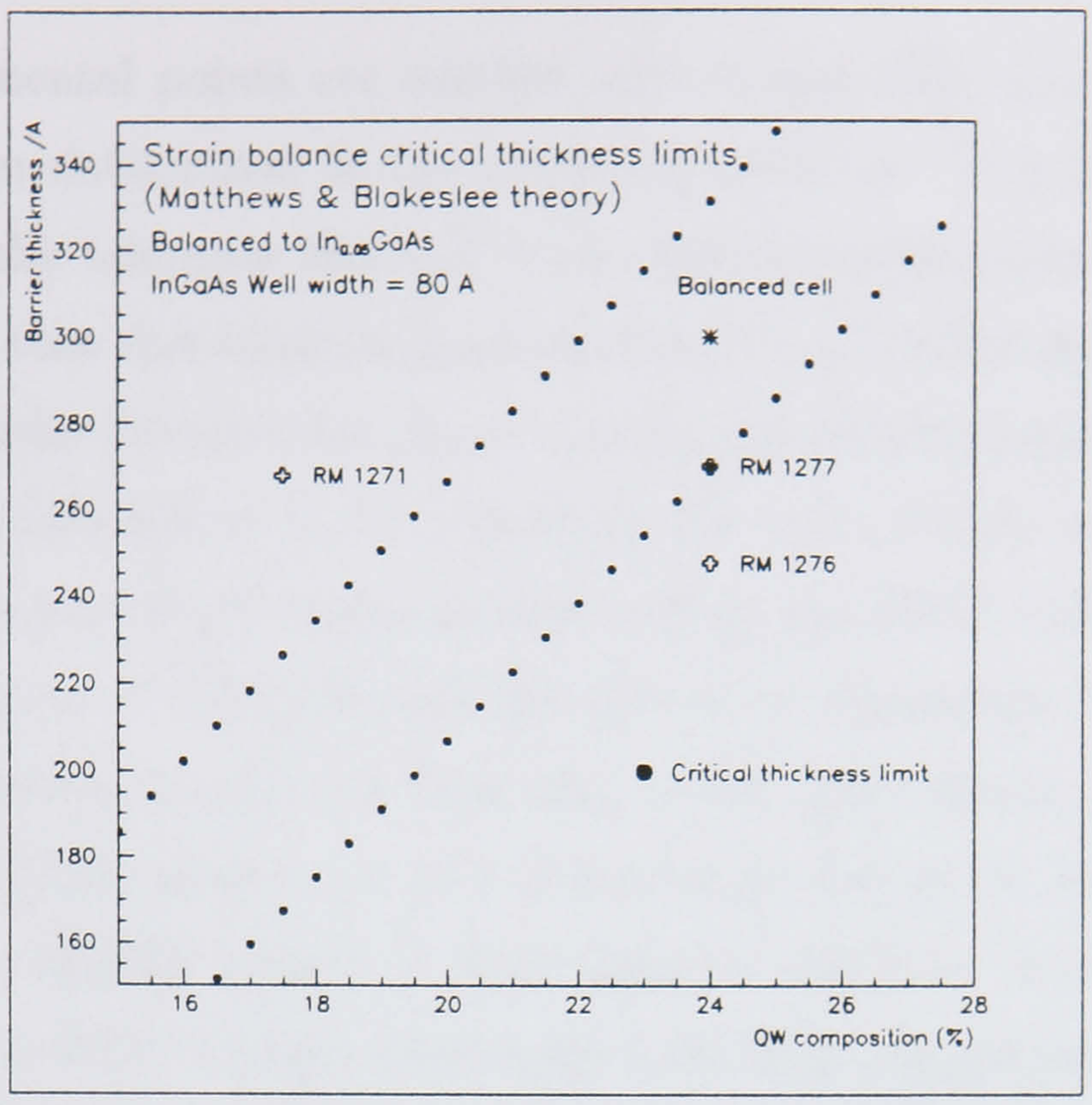

Figure 6.10: Critical thickness limits for variations of a strain-balanced cell (balanced with $t_b = 30$, $x_w = 24\%$)

Further, the definition of strain presented in the previous section describes the situation when an epitaxial layer is deposited on a substrate possessing a smaller lattice constant. In the strain balance scenario, it is necessary to compute critical thicknesses for epitaxial layers with lattice constants larger or smaller than their substrate. The Matthews-Blakeslee model has no solution for negative (or zero) strain, so it is necessary to reverse the substrate and epitaxial layers in order to always ensure a positive strain.

This analysis yields symmetrical critical thicknesses for compressive and tensile strain. This follows from the assumption of linear elasticity in the Matthews-Blakeslee modeling and is not wholly accurate. The potential experienced by a pair of atoms will naturally be greater in compression than tension. Thus a material strained in compression will possess a smaller critical thickness than one strained in tension. This effect is expected to cause deviations in critical thickness of up to a factor of 2 from the Matthews-Blakeslee approach at large values of misfit [107].

The graph shown in figure 6.10 depicts the critical thickness limits for a strain balance cell with fixed indium composition (5% p and n, 80Å QW) but with variable QW indium fraction and barrier thicknesses. The structure is that of the RM127x series such that a balanced cell possesses a barrier thickness of 300Å and 24% QW indium fraction. Thus any deviation in the (x,y) space from (24,300) results in strain between the MQW region and 5% InGaAs p and n regions.

The experimental points are marked with + symbols, their composition and dimensions having been determined in the preceding sections. It is clear that none of the samples conform to the tolerance implied by the Matthews-Blakeslee model, but it is important to remember that this analysis considers the critical thickness for which a threading dislocation is turned into the interface plane to form a misfit dislocation. On this basis, one would expect misfit dislocations to be formed at the lower MQW interface, relieving the strain accumulated in the MQW region as observed by the EBIC measurements.

In the instance of RM1276 and RM1277 it is reasonable to assert that not all the threading dislocations have been bent into misfit dislocations, indeed a substantial number of threading dislocations are still observed at the upper interface. However in RM1271 the strain is slightly greater, but of opposite sign (i.e. tensile strain as opposed to compressive). The EBIC images show extremely clean upper layers, yet lower layers are dominated by misfit dislocations. It is unclear as to why this sample possesses so few threading dislocations, unless they are all bent into misfit dislocations lower down in the structure. However, it may be concluded that the dark-IV behaviour of RM1276 and RM1277 are dominated by threading dislocation density while RM1271 is dominated by misfit dislocation density.

6.1.5 5% InGaAs Conclusions

So far the results for the 5% InGaAs cells have been unable to demonstrate any advantageous properties for solar conversion. However, a sample identical to RM1271 was grown by MOVPE at the University of Lecce called Lecce 001. Full characterisation of this sample could not be performed on account of unsolved difficulties, processing the wafer into test mesa diodes. However a transmission measurement was performed on the wafer identifying the 5% InGaAs band edge and e1-hh1 exciton. EBIC microscopy was also performed on the unprocessed sample and is presented in appendix E, figure E.3, together with a comparable image of RM1391. It is clear that the Lecce 001 wafer is of better quality than RM1391 and indeed any of the previous strain-balanced samples. The level of dislocations are comparable to the 'lower-plateau' strained samples reported in chapter 2.

There is a great deal of further work that may be performed in this area for improving the material quality of these relaxed buffer layer devices. For example, the 20% GaAs on Si cell employed a series of strained layer superlattice (SLS) regions to reduce the threading dislocation density from $1 \times 10^8 \mathrm{cm}^{-2}$ to $1 \times 10^6 \mathrm{cm}^{-2}$. The SLS technique may not be suitable for reducing the dislocation density below $1 \times 10^6 \mathrm{cm}^{-2}$, but it is interesting to

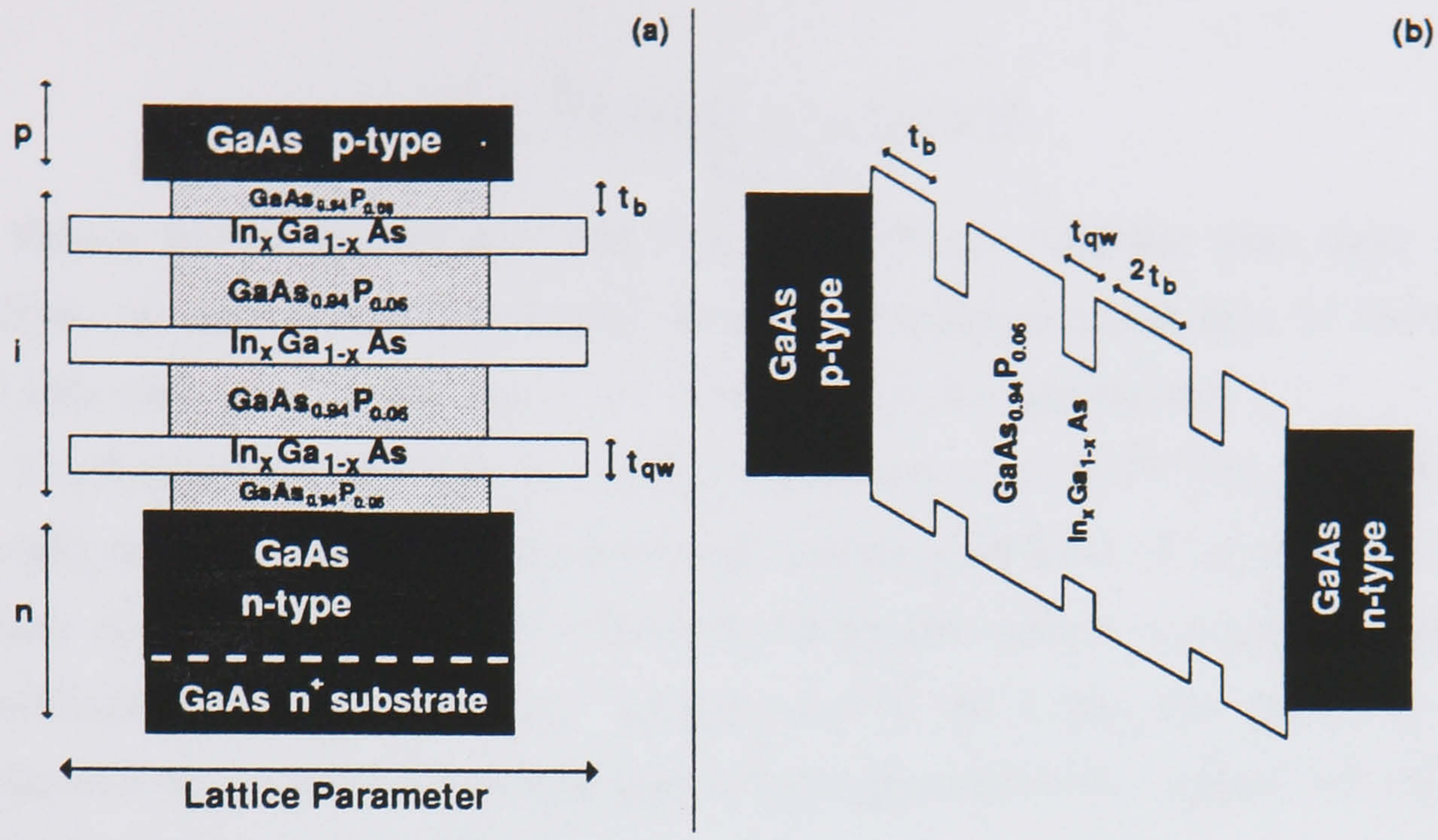

Figure 6.11: Schematic diagram of the GaAsP/InGaAs strain-balance structure and 3-period band structure.

note that a dislocation density of $1 \times 10^5 cm^{-2}$ or below is required for high-efficiency power conversion [103]. A recent study on strain relaxation in non-linear composition graded MBE grown buffer layers [108], has achieved a threading dislocation density $< 7 \times 10^3 cm^{-2}$ with a layer graded to $In_{0.35}Ga_{0.65}As$. This dislocation density is three orders of magnitude lower than the levels observed with the RM series of samples reported in this chapter, giving hope that the threading dislocation problem may be surmounted in the future.

6.2 GaAsP/InGaAs Strain-Balance

The need for a virtual substrate may be eliminated if a barrier material can be found whose lattice constant is smaller than that of GaAs. Figure 2.1 in chapter 2 indicates that alloys of GaAsP, possess a smaller lattice constant than GaAs and a slightly larger band-gap. Thus the compressive strain in the InGaAs QWs may be matched by tensile strain in GaAsP barriers

The strain-balance structure is depicted schematically in Fig 6.11 together with the associated band diagram. The i-region was designed as a 20 period cyclic half-barrier/quantum well/half-barrier structure; each half-barrier composed of GaAsP alloy, providing half the strain compensation for the InGaAs quantum well. The dimensions were chosen to ensure the average lattice parameter across the i-region $\langle a \rangle$ was equal to GaAs. Thus, if t_b is the half-barrier thickness, t_{qw} is the well thickness, a_{GaAsP} and a_{InGaAs} are the respective well and barrier lattice constants; we define:

$$\langle a \rangle = \frac{2t_b a_{GaAsP} + t_{qw} a_{InGaAs}}{2t_b + t_{qw}} \tag{6.4}$$

Values for the barrier and well widths are chosen together with their respective compositions, to ensure that the average lattice parameter equates that of the substrate, GaAs. In this way, the average strain $\langle f \rangle$ of equation 6.2 is minimised.

The first GaAsP/InGaAs device (QT1184) grown by MOVPE by Dr. John Roberts[5] was originally designed as a laser structure and incorporated thick AlGaAs waveguide structures. These structures were located outside the depletion region, but greatly impaired the short wavelength quantum efficiency. Another device (QT1227) was grown in the usual MQW solar cell configuration together with a homogeneous GaAs control cell (QT1228) of nominally identical doping profile.

Secondary neutrals mass spectrometry (SNMS)[6] was used to characterise the barrier alloy composition, yielding $GaAs_{0.939}P_{0.061}$. An X-ray diffraction (XRD) rocking curve was taken and modelled using the phosphorous composition obtained from the SNMS. An excellent fit was obtained and is shown in figure 6.12, indicating a quantum well composition of $In_{0.17}Ga_{0.83}As$, well width of $t_{qw} = 75$Å and GaAsP barrier width of $t_b = 215$Å. Equations 6.4 and 6.2 yield an average strain $\langle f \rangle = 6 \times 10^{-5}$, a negligible quantity for a layer 1μm thick. The device and its control were both processed as 1mm mesa photodiodes.

6.2.1 GaAsP/InGaAs Dark-IV

The forward bias dark-currents are presented in figure 6.13. The GaAs control cell provides a baseline for comparison, it being representative of other homogeneous GaAs cells processed as 1mm mesa diodes. For the first time, the strain-balance QW cell shows little increase in the carrier recombination rate over the GaAs control. Data is presented for a 23 QW relaxed cell (QT510B), where the i-region has exceeded the critical thickness and for a 10 QW strained cell (QT459B). The strained 10 QW cell marks the lowest dark current achieved using strained layer techniques, yet possessing only half the QW absorption profile of the 20 QW strain-balance cell. Further, the relaxed 23 QW cell has an absorption profile equivalent to the strain-balance cell, but at the expense of an increase of dark current in excess of two orders of magnitude.

The EBIC microscopy was performed by Max Mazzer on the GaAsP/InGaAs devices and indicates extremely good material quality, with no detectable dislocations in

[5]EPSRC III-V Facility, University of Sheffield, U.K.

[6]SNMS measurements were performed on the behalf of John Roberts at the MATS Surface Analysis laboratory, Warrington, U.K.

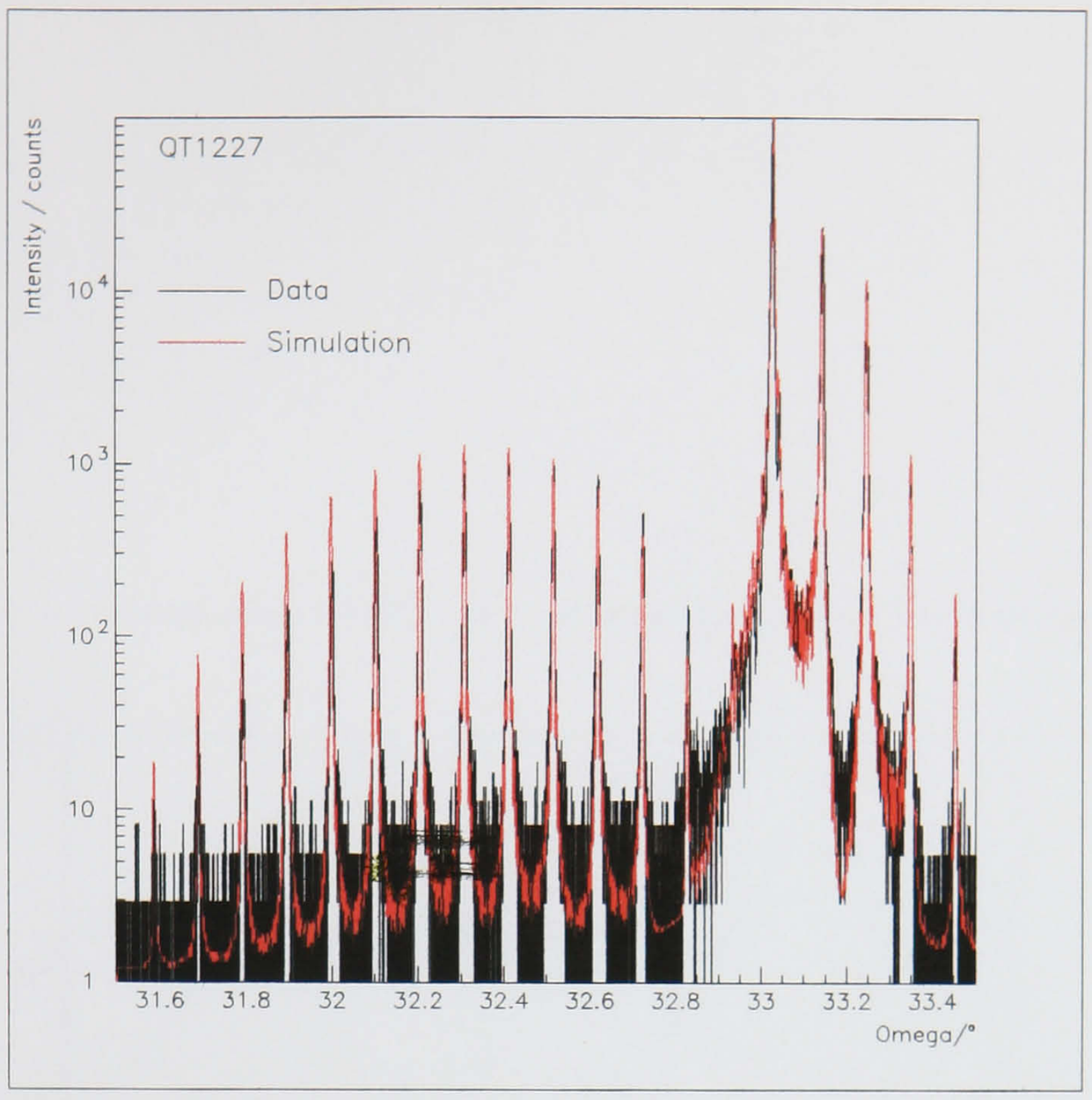

Figure 6.12: XRD rocking curve showing the measured data and the simulation with $GaAs_{0.939}P_{0.061}$ barrier half-width $t_b = 215$Å and 75Å wide $In_{0.17}Ga_{0.83}As$ quantum wells.

the MQW region. A typical EBIC image is shown in appendix E, figure E.4 and may be compared to the 'typical' images obtained for the 5% InGaAs strain-balance cells in figure E.3. It is likely that the improvement in dark-IV between the GaAsP/InGaAs strain-balanced cell and the strained 10 QW cell is due both to an improvement in material quality and the higher band-gap of the GaAsP barrier material. Indeed, the effect of the barrier band-gap has already been demonstrated in AlGaAs/GaAs cells [65].

6.2.2 GaAsP/InGaAs Quantum Efficiency

The external quantum efficiency depicted in figure 6.14 was measured under short-circuit conditions. At wavelengths in excess of the GaAs band-gap, the QW layers extend the cell absorption to 960nm whilst maintaining a short wavelength spectral response comparable to the GaAs control. The GaAsP barriers are responsible for the small drop in quantum efficiency at their absorption edge (835nm). The impaired spectral response at short wavelength in the strain-balanced cell may indicate a slightly shorter electron diffusion length in the emitter p-region due to the minority electrons having to surmount the GaAsP barriers in the i-region. Whilst the former poses few problems regarding the overall solar cell performance, some optimisation may be possible regarding the GaAsP alloy composition to

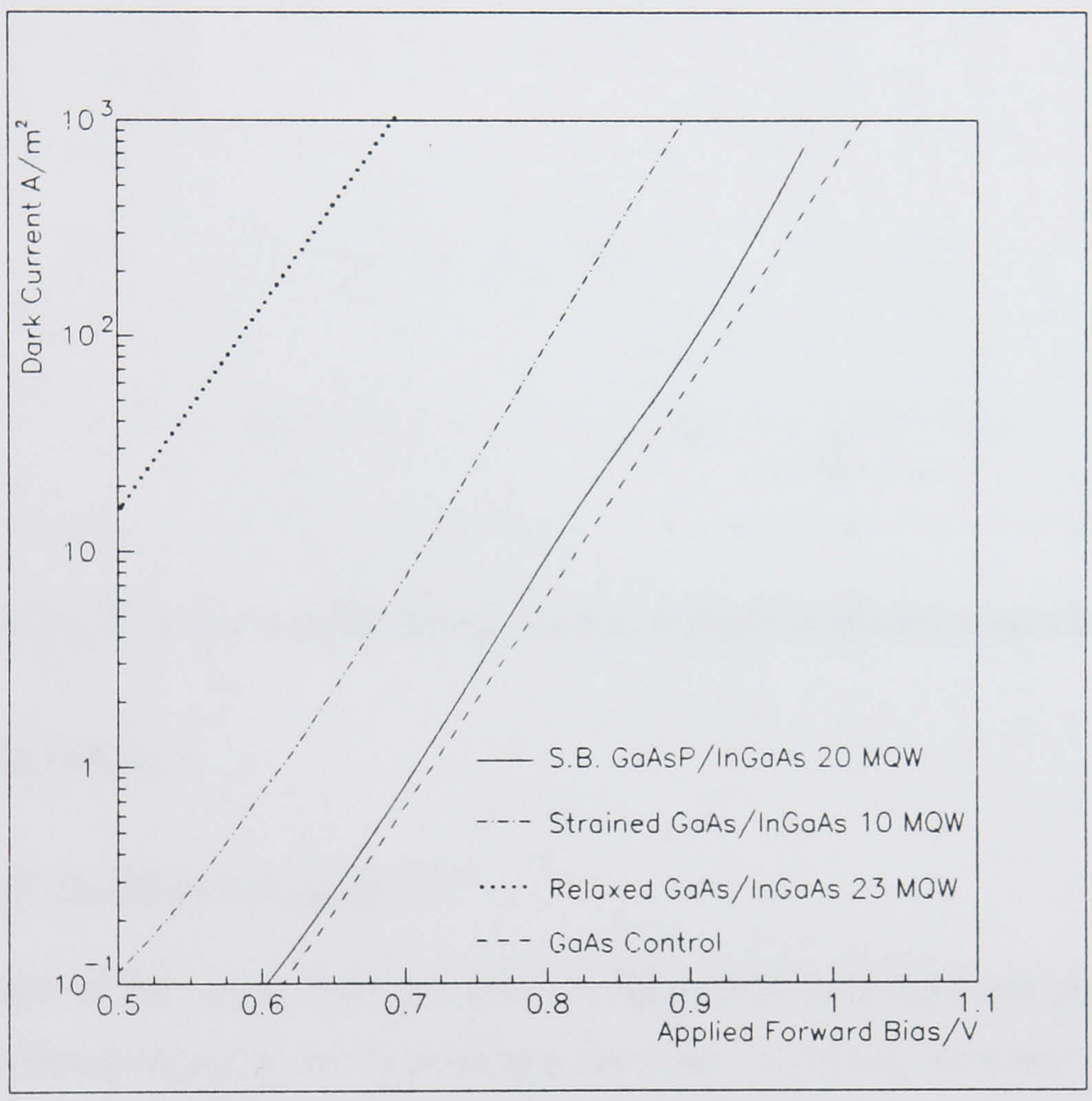

Figure 6.13: Dark IV curves for GaAsP/InGaAs strain-balance MQW cell (QT1227), a relaxed GaAs/InGaAs MQW cell (QT510B), a strained GaAs/InGaAs MQW cell (QT459B) and a GaAs control (QT1228)

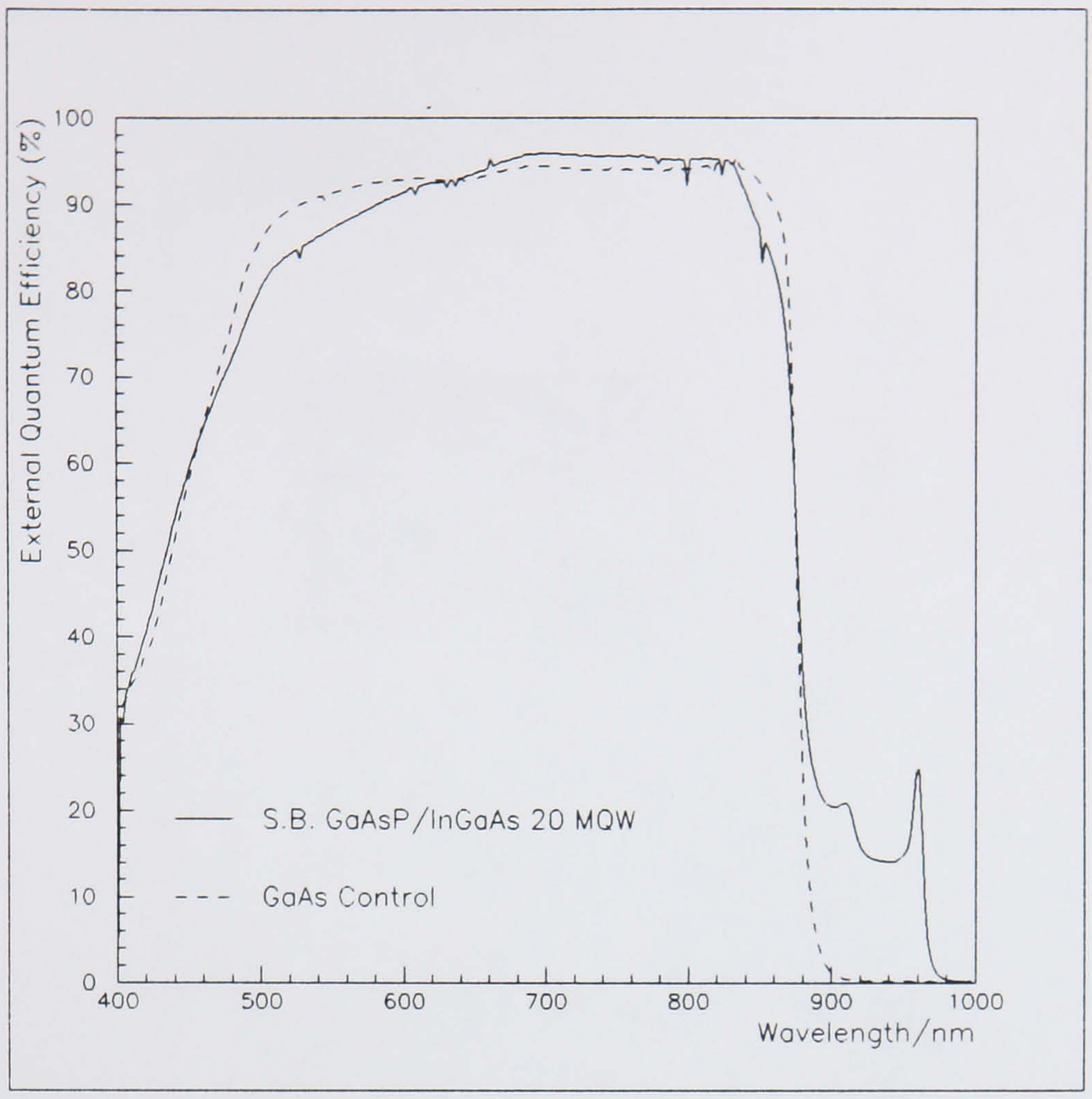

Figure 6.14: External Quantum Efficiency for the GaAsP/InGaAs strain-balanced sample

address the latter effect.

6.2.3 GaAsP/InGaAs Light-IV

The light-IV for these cells is shown in figure 6.15 and has been measured under a 3000K tungsten filament lamp, set to generate the same I_{sc} in a calibrated cell under 3000K illumination as achieved under standard AM1.5 conditions. The 3000K illumination spectrum favours the strain-balance cell absorption profile, so the modest increase in efficiency observed over the GaAs control is to be expected; the 70% shading loss associated with the 1mm mesa test diodes accounting for the low overall efficiency. More importantly, the strain-balanced cell exhibits a larger operating current I_{op} than the GaAs control, whilst maintaining the same operating voltage V_{op}, confirming that the extended QW quantum efficiency exists up to and beyond the operating point.

From the experimental data, it is possible to infer a solar cell power conversion efficiency given the following assumptions: the quantum efficiency at I_{sc} remains largely unchanged at the operating point and the dark current density curve is representative of a large area cell. The former is reasonable on account of the light-IV result presented above

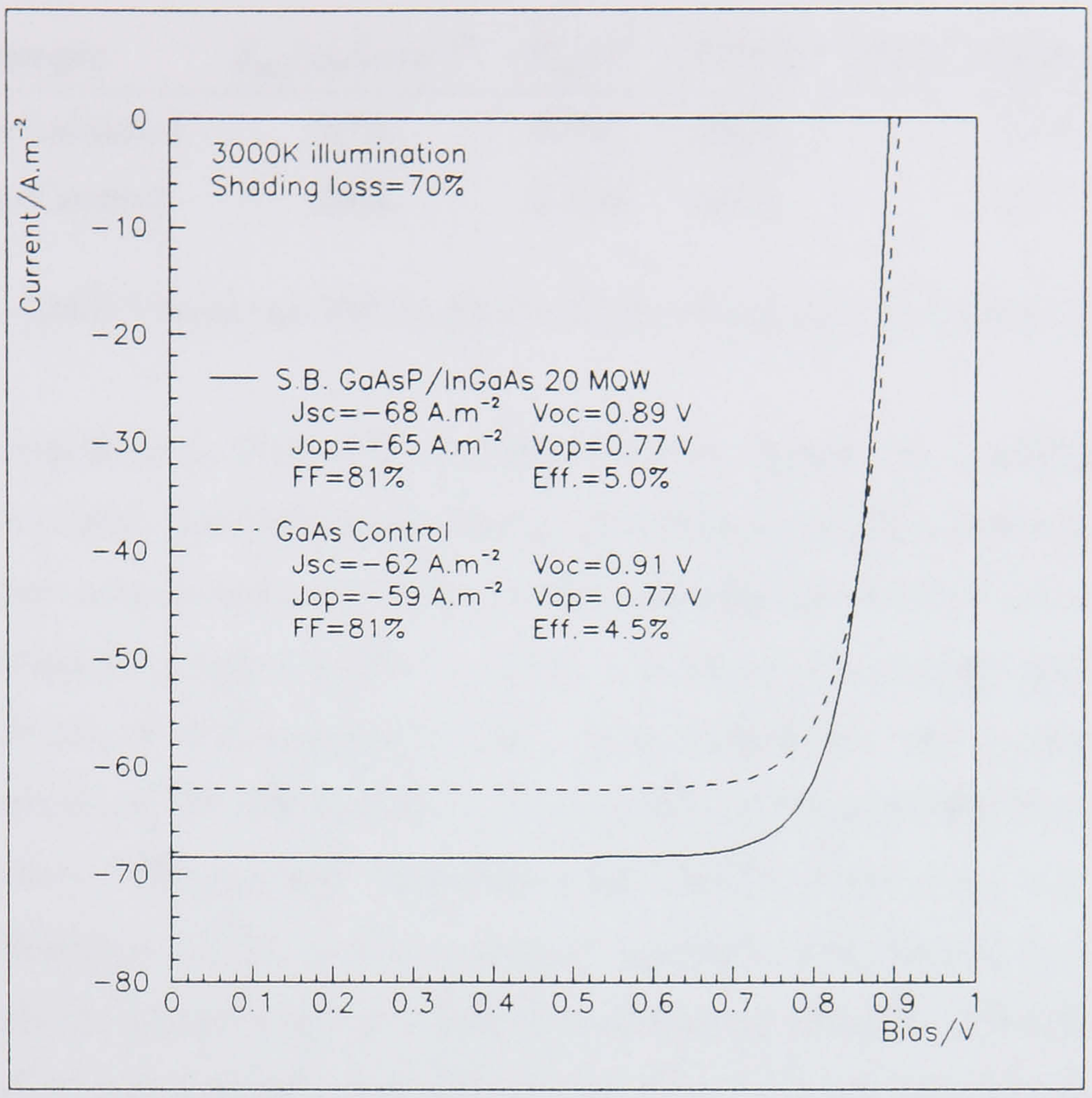

Figure 6.15: 3000K Light-IV for GaAsP/InGaAs strain-balanced sample and GaAs control.

Sample	$J_{sc}/mA.cm^{-2}$	V_{oc}/V	$FF(\%)$	AM1.5 Efficiency (%)
Strain-balanced	25.8	0.943	82.1	20.0
GaAs Control	25.4	0.964	82.3	20.2

Table 6.5: AM 1.5 Projected Efficiency for Strain-Balanced and GaAs Control cells

and the latter should provide a pessimistic estimate, on account of edge effects associated with the 1mm mesas. Under these assumptions and an additional 5% shading loss, the experimental data presented above yields the projected efficiencies quoted in tables 6.5 and 6.6 under AM 1.5 and AM0 illumination respectively. Within errors, the two cells have comparable efficiency, marking the first time that a GaAs/InGaAs based QWSC has achieved comparable efficiency to its homogeneous GaAs control.

6.2.4 Optimisation of GaAsP/InGaAs cell

The GaAsP/InGaAs strain-balanced cell offers plenty of scope for optimisation. Most simply, the QW absorption can be enhanced by light trapping techniques and the overall efficiency raised using a multi-layer AR-coating.

Sample	$J_{sc}/mA.cm^{-2}$	V_{oc}/V	$FF(\%)$	AM0 Efficiency (%)
Strain-balanced	30.8	0.953	82.0	17.6
GaAs Control	30.2	0.975	82.0	17.7

Table 6.6: AM 0 Projected Efficiency for Strain-Balanced and GaAs Control cells

The composition of the device offers another degree for optimisation. Using an analysis similar to that described in section 2.1.2, it was possible to compute J_{sc} curves as a function of indium and phosphorus fractions. The calculation assumed a good AR coating, a maximum permissable i-region width of $1.2\mu m$ and varied the barrier thickness to balance the indium fraction of 80Å quantum wells. The calculation was repeated for $GaAsP_x$ barrier compositions of 6%, 8% and 10%. Some additional approximations had to be made for this calculation. The material parameters for GaAsP alloys were not implemented in the quantum efficiency model, so the quantum efficiency was treated as a GaAs/InGaAs cell. This introduces a small error in the QW confinement energies; the error for $GaAsP_{0.06}$ being equivalent to a systematic -1% shift on the InGaAs composition axis.

Estimating a cell conversion efficiency is complicated through the inevitable variation in dark-IV with In fraction and GaAsP barrier composition. The QW depth is known to influence the dark-IV for lattice matched systems [32], where the defect density is no longer dominates recombination and it is reasonable to assume similar behaviour in this strain-balanced system. The extent to which the wider GaAsP band-gap influences the dark-IV is unknown. For these reasons, efficiency estimates will be very approximate. Assuming the dark-IV is pinned at the level of QT1227, then the maximum efficiencies corresponding to the maxima of figure 6.16 will be 19.3% and 21.9% for AM0 and AM1.5 respectively.

It is also necessary to ensure that the well and barrier strain and thicknesses do not exceed a critical thickness. The curve shown in figure 6.17 indicates how a Matthews-Blakleslee estimate for the critical thickness of $GaAsP_x$ grown on GaAs varies with x; the phosphorus composition. The symbols indicate $GaAsP_x$ total barrier thicknesses required to balance $In_{0.1}GaAs$, $In_{0.2}GaAs$ and $In_{0.25}GaAs$ 80Å quantum wells. The plus-sign (+) located at (6%,452Å) corresponds to the existing strain balance cell, which is known to be virtually free of strain related defects. Surface roughening has been observed from TEM measurements for 80Å $In_{0.25}GaAs$ quantum wells, balanced in a $GaAsP_{0.06}$ structure [51]. The correspondence between the critical thickness curve and quality of devices grown with richer phosphorous contents has yet to be investigated. However, the one data point for which surface roughening is observed, gives some indication to the accuracy of the Matthews-

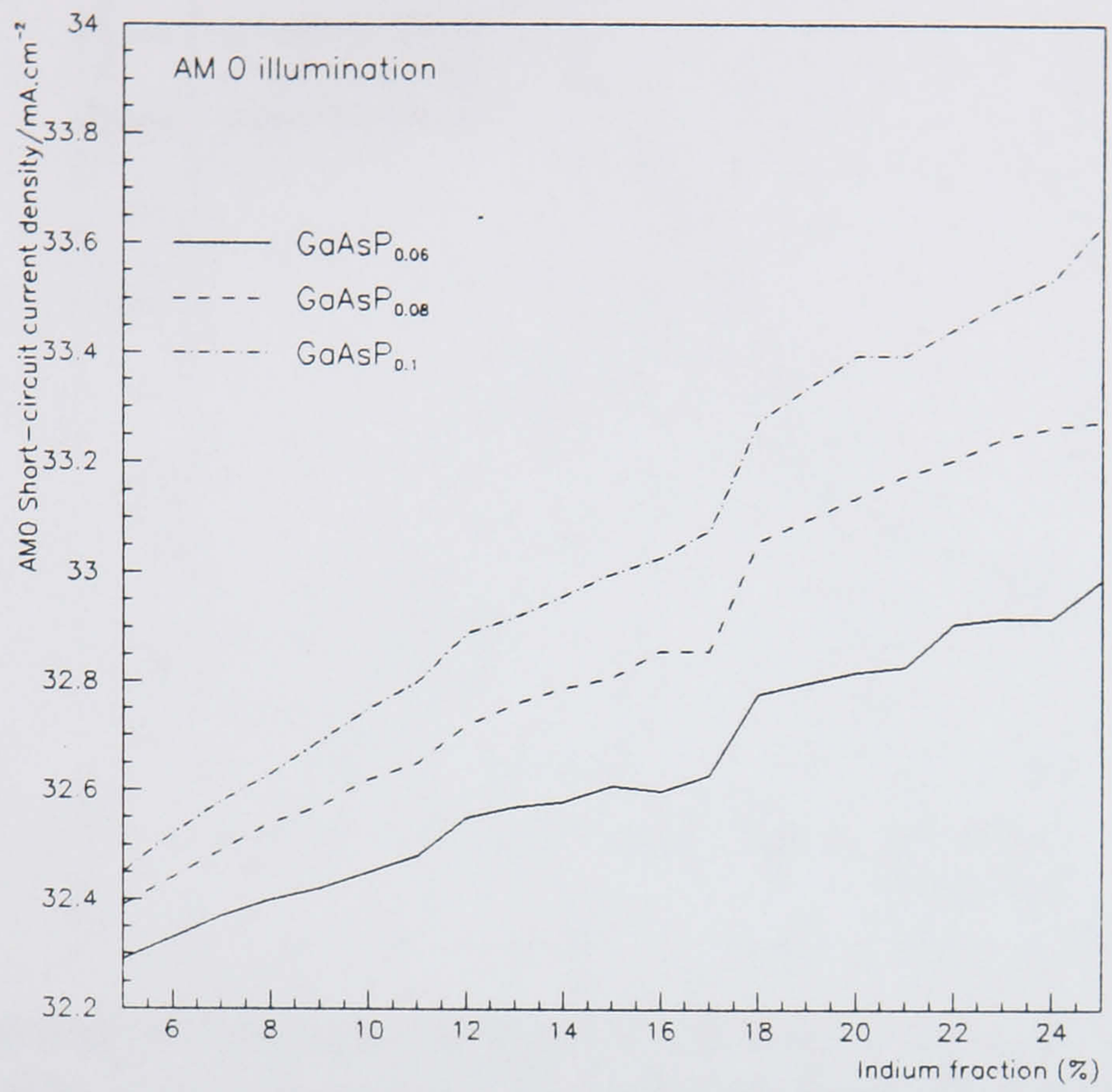

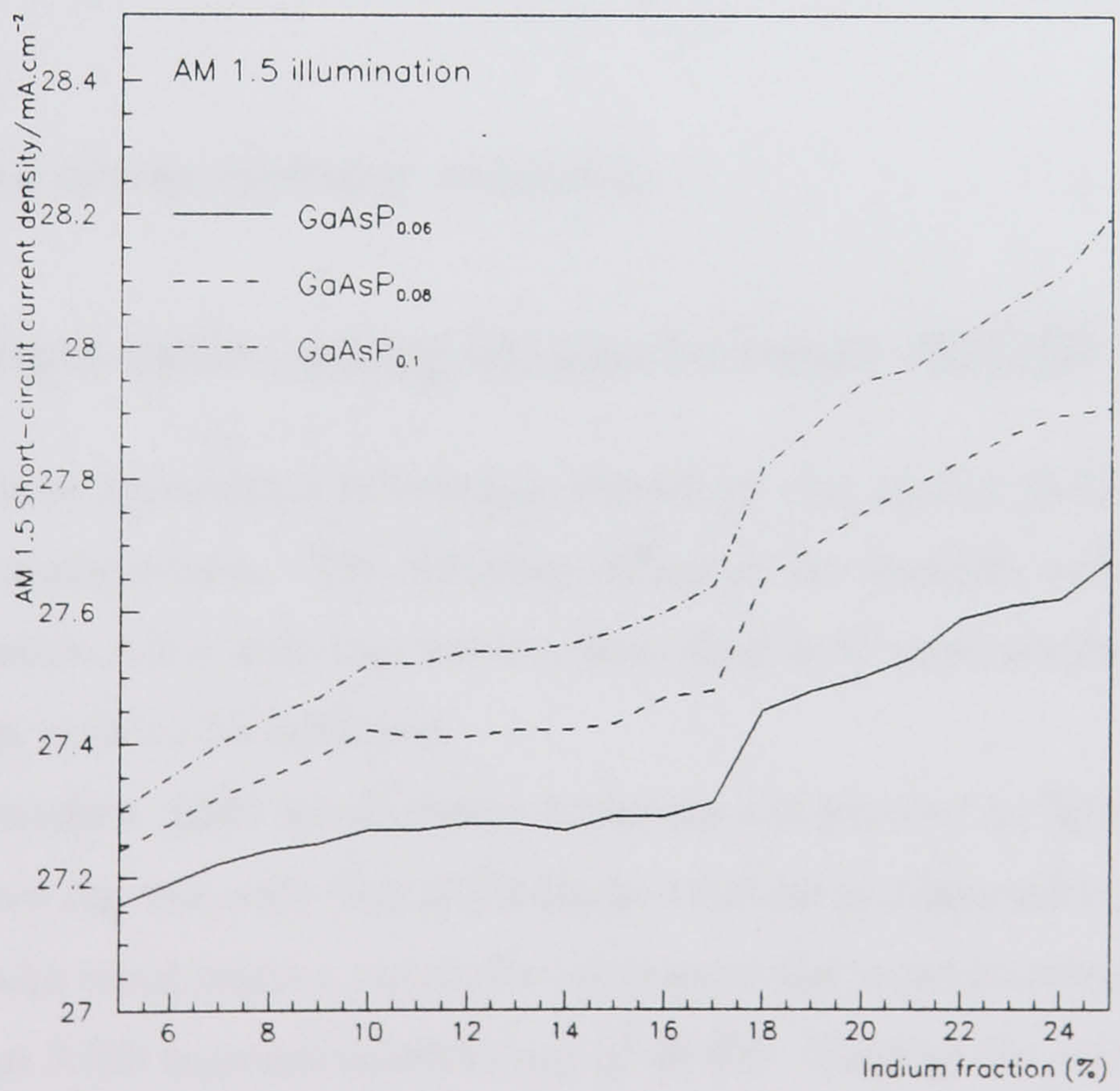

Figure 6.16: Projected AM0 and AM1.5 short-circuit current density curves showing the effect of indium and phosphorous composition on the GaAsP/InGaAs strain balanced cell.

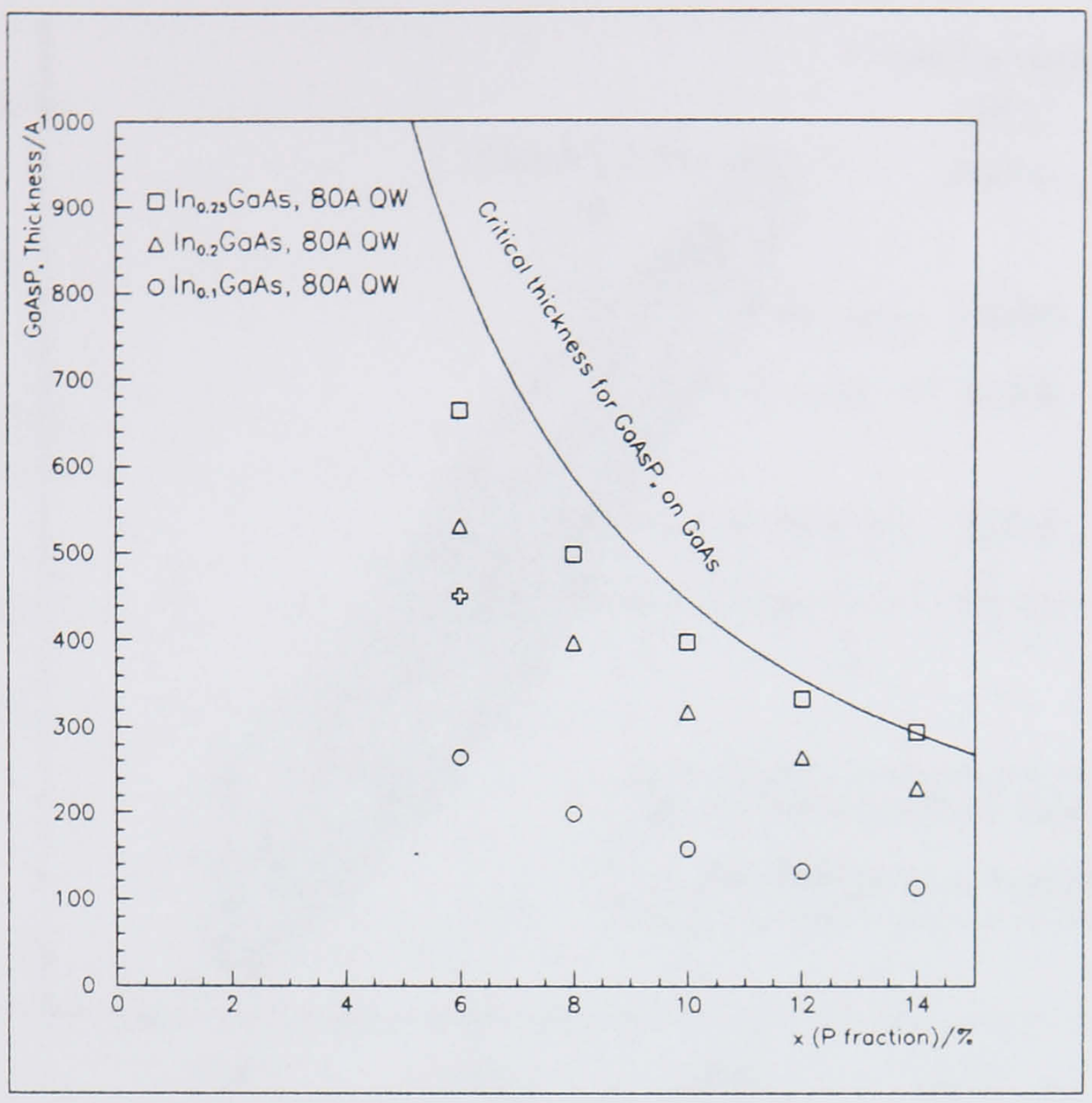

Figure 6.17: Matthews-Blakslee calculation for the critical thickness of GaAsP on GaAs as a function of phosphorous composition. The symbols indicate $GaAsP_x$ total barrier thickness required to balance an 80Å QW composed of $In_{0.1}GaAs$ (circles), $In_{0.2}GaAs$ (triangles) and $In_{0.25}GaAs$ (squares). The existing $GaAsP_{0.06}/InGaAs_{0.17}$ sample is indicated by a plus (+).

Blakeslee critical barrier thickness calculation.

6.3 Tandem cells using strain-balance MQW cells

The most immediate advantage offered by the GaAsP/InGaAs cell is in a monolithic tandem configuration. The limiting efficiency for tandem cells has already been introduced in section 1.2.5 and this section describes how strain-balance MQWs may allow optimal tandem cells to be achieved.

The tandem AM0 isoefficiency contours are plotted in figure 6.18, together with the dashed curve for the *bulk* GaInP/InGaAs tandem configuration, plotted in light blue. The InGaP/GaAs combination currently represents the most successful monolithic tandem cell [24], with an AM0 conversion efficiency of 26.9%. Placing the cell onto the contour map shown in figure 6.18 shows that the band-gap combination of 1.88eV for InGaP and 1.44eV for GaAs is far from optimal. It is clear that bulk material combinations cannot gain access to the optimum tandem efficiency. This is due to insufficient energy spacing between an InGaAs alloy and its lattice-matched InGaP counterpart, shown in figure 2.1. Ideally, a

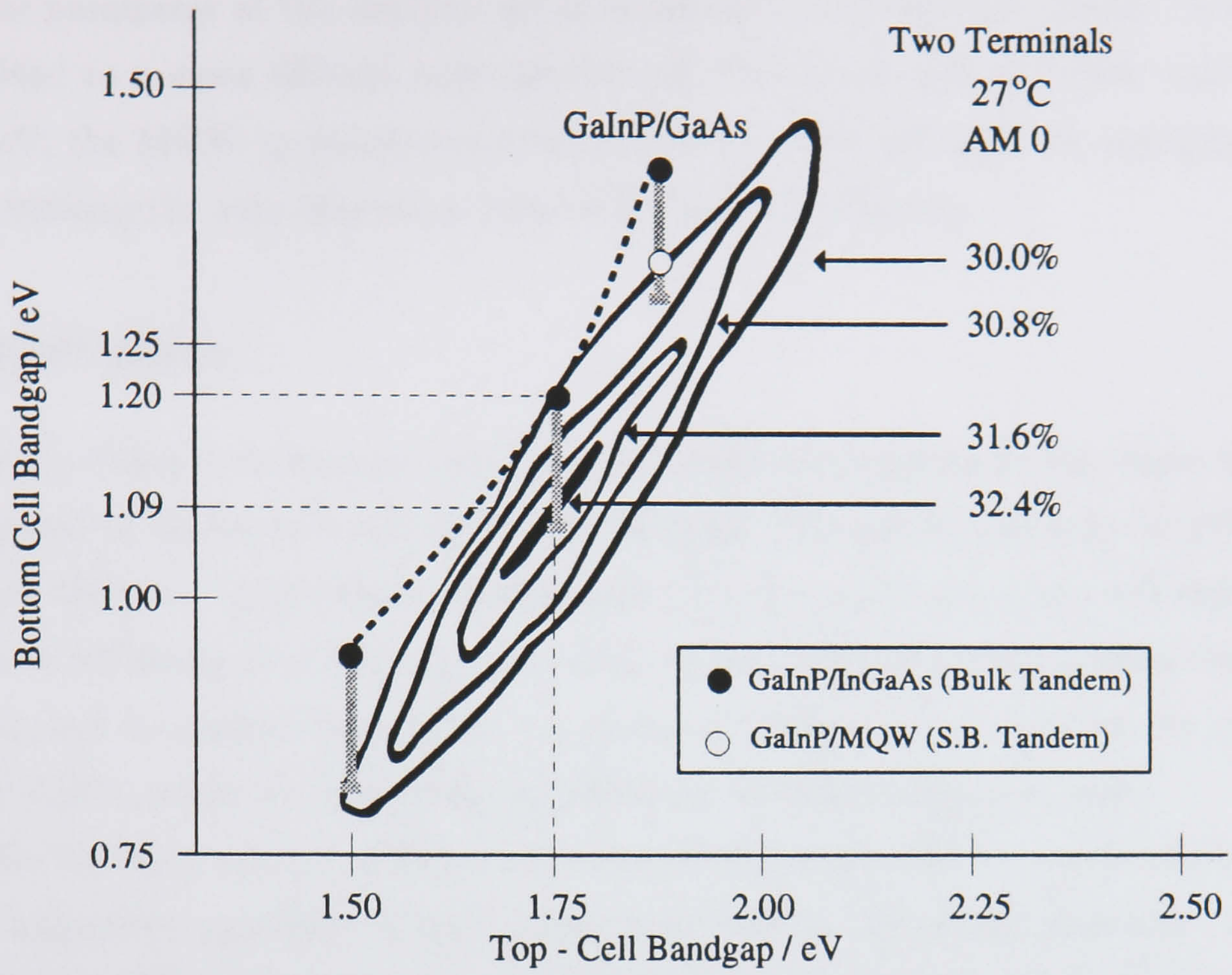

Figure 6.18: AM0 tandem isoefficiency contours (after ref [3]). The dashed curve indicates the monolithic tandem efficiencies accessible using lattice bulk GaInP/InGaAs based tandems. The grey bars indicate the efficiencies available by replacing the lower cell by a strain-balanced MQW cell.

wider InGaP-GaAs band-gap separation would allow for a cell better matched to the AM0 spectrum.

Irrespective of arguments over the fundamental efficiency advantage of quantum wells, MQW strain-balance techniques offer a means of reducing the absorption edge by around 0.13eV, while maintaining a particular lattice constant. The green bars on figure 6.18 indicate the scope for lowering the lower cell band-gap by replacing the GaAs cell with a strain-balanced InGaAs based MQW, while remaining lattice matched to a GaInP top cell. In effect, the strain-balanced MQW allows the InGaAs alloy curve of figure 2.1 to be moved down to lower band-gaps.

For example, the red point on figure 6.18 indicates the location of a hypothetical InGaP/MQW cell, where the MQW is the GaAsP/InGaAs cell reported above. In principle this cell could possess an AM0 efficiency of 30% [27]. From a manufacturing viewpoint, it is worth noting that no additional MOVPE sources are required to move from growing InGaP/GaAs to the proposed InGaP/MQW.

The virtual substrate approach (5% InGaAs) offers further flexibility, allowing the

entire lattice parameter of the tandem cell to be moved along the blue dashed line. While this could lead to a more efficient bulk tandem cell with a top cell at 1.75eV and a lower cell at 1.2 eV, the MQW approach can accommodate a lower cell with an absorption edge at 1.08eV, striking the very maximum monolithic tandem efficiency.

6.4 Conclusion

Strain-balance techniques have been successfully exploited to overcome the limitations imposed by strain with strained MQW designs. The GaAsP/InGaAs MQW strain-balanced cell offers an unprecedented performance for the multi-quantum well cell design, comparable in efficiency to a homogeneous GaAs control cell. The possibilities for further optimisation and immediate integration into existing tandem cell structures are clear and represent a viable means for enhancing the efficiency of existing tandem cells.

The virtual substrate cells require substantially more work, in particular ensuring that strain relaxation proceeds without excessive threading dislocation densities. The success of achieving 20% GaAs cells grown on Si substrates indicates that such control should be possible. Once achieved, an optimised AM0 monolithic tandem cell may be considered with hitherto inaccessible band-gap combinations.

Chapter 7

Summary and further work

The quantum well solar cell concept has been applied to GaAs/InGaAs based materials and its potential for enhancing the efficiency of a bulk GaAs cell explored. Chapter 2 discussed the limits of a strained GaAs/InGaAs MQW cell. The high dark-current associated with a high density of misfit dislocations ensured that a strained MQW cell could never attain the same efficiency as a GaAs control cell.

The theoretical grounds for an enhanced MQW conversion efficiency were discussed in chapter 4. The assumptions underlying a critical theory, claiming no efficiency enhancement for radiatively efficient devices, were examined and shown not to apply to real QW devices. Further, the QW photocurrent was shown to extend up to and beyond the V_{oc}.

Chapter 5 described aspects of light trapping in GaAs/InGaAs MQW cells. The normal incidence model was described and has subsequently allowed potentially useful light trapping structures to be characterised. The possibility of photon recycling in MQW cells is discussed in the radiative limit and compared with a series of cavity MQW cells. While some of the dark-IV characteristics of these cavity cells remains consistent with a photon-recycling process, there are contradictions in the EL behaviour suggesting other effects.

The need to reduce the cell dark-current was addressed in chapter 6. The strain-balance concept was shown to lower the dark-IV while maintaining the QW absorption. Two material systems were investigated: GaAs/InGaAs grown on a $In_{0.05}Ga_{0.95}As$ virtual substrate and GaAsP/InGaAs grown on a GaAs substrate. While the principle was established with the GaAs/InGaAs design, the device efficiency was not high on account of a high level of threading dislocations stemming from the virtual substrate. The GaAsP/InGaAs did not suffer from this problem as it could be grown directly on a GaAs substrate and for the first time, showed a comparable efficiency to a GaAs control cell.

There is much scope for further work. Primarily the high J_{sc} of the GaAsP/InGaAs strain balanced cell can be used to enhance the efficiency of existing GaInP/GaAs tandem cells by replacing the GaAs cell with a GaAsP/InGaAs strain-balanced MQW. In the longer term, it would be desirable to establish an effective means of reducing the dislocation density of the virtual substrate GaAs/InGaAs strain-balanced cell. A GaInP/(GaAs/InGaAs MQW) tandem cell grown on a virtual substrate, holds the greatest potential for achieving a fully optimised tandem cell.

The development of efficient light trapping structures should be pursued, in order to maximise the QW photocurrent. A Monte-Carlo ray-tracing model would allow non-normal incident rays to be treated properly and may help to optimise the structure for maximum light trapping efficiency. The search for photon recyling in MQW cells could continue, especially by growing cells with the rear contact placed at different thicknesses. The advantageous material quality of the strain-balanced GaAsP/InGaAs MQW cells could be incorporated into a cavity cell, so to raise the overall radiative efficiency and increase the likelihood of photon recycling taking place.

Finally, there is much work to be done on the fundamental limits to MQW solar cells. The suppressed quasi-Fermi levels observed in chapter 4 remain an empirical observation and the mechanisms governing the suppression are unclear. A series of cells with differing energy levels may help identify which of the QW properties play a role in the quasi-Fermi level suppression. Once this is understood, then an optimum material configuration, not necessarily III-V, could be conceived which maximises the MQW advantage for solar power conversion.

Appendix A

Record Cell Efficiencies

The following tables list the solar cell performance for existing record holding, or nearly record holding cells. Four categories of crystalline III-V solar cell are reported in this appendix; single-junction and tandem cells for both air mass 1.5 global (AM 1.5) and air mass 0 (AM 0). Broader solar efficiency tables covering other material combinations and multicrystalline cells are published elsewhere [15, 109]. The efficiencies are quoted without error, $\pm$ 0.5% can be assumed unless otherwise specified.

Classification	AM 1.5 Eff. (%)	$V_{oc}(V)$	$J_{sc}(ma.cm^{-2})$	FF (%)	Description	Date
GaAs	25.7	1.039	28.5	86.8	GaInP window[17]	1990
GaAs (Ge substrate)	24.3	1.035	27.6	85.3	AlGaAs window [110]	1990
GaAs (Si substrate)	20.0	-	-	-	AlGaAs window[103]	1991
InP	21.9	0.878	29.3	85.4	Spire [111]	1990
Si	24.4	0.696	42.0	83.6	PERL cell [112]	1998

Classification	AM 0 Eff. (%)	$V_{oc}(V)$	$J_{sc}(ma.cm^{-2})$	FF (%)	Description	Date
GaAs p-n	21.7	1.03	33.1	86.7	25°C, AlGaAs window [1]	1990
GaAs n-p	21.0	1.01	33.8	83	25°C, AlGaAs window [113]	1986
GaAs (Si substrate)	18.3	0.940	33.2	79.1	28°C, AlGaAs window[103]	1991

Table A.1: Single junction AM 1.5 and AM 0 cell efficiencies

Classification	AM 1.5 Eff. (%)	$V_{oc}(V)$	$J_{sc}(ma.cm^{-2})$	FF (%)	Description	Date
InGaP/GaAs	30.28	2.488	14.22	85.6	InGaP tunnel [24]	1997
InGaP/GaAs	29.5	2.385	14.0	88.5	GaAs tunnel [23]	1994
GaAs/$CuInSe_2$	25.8	-	-	-	± 1.3% [114]	1990
GaAs/Ge	24.3	1.219	26.4	75.7	AlGaAs window [101]	1988

Classification	AM 0 Eff. (%)	$V_{oc}(V)$	$J_{sc}(ma.cm^{-2})$	FF (%)	Description	Date
InGaP/GaAs	26.9	2.451	16.85	88.1	28°C, InGaP tunnel [24]	1997
InGaP/GaAs	25.7	2.398	16.4	88.2	GaAs tunnel [23]	1994
GaAs/Ge	21.68	1.225	30.83	78.7	25°C, AlGaAs window[101]	1988

Table A.2: Multi-junction AM 1.5 and AM 0 cell efficiencies

Appendix B

Background Doping

Under considerable forward bias, or high background doping the field may be lost across some of the i region in a p-i-n diode. This can be detected via the mono-IV measurement described in section 3.3.4 and places an upper limit upon the useful width of the i-region for solar cell applications, discussed in section 2.1.2

Once the applied bias or background doping becomes sufficiently high, the field distribution will be typically as shown in figure B.1. In this example a homogenous p-type background doping is assumed.

Poisson's equation is expressed in equation B.1.

$$\frac{d^2V}{dx^2} = \frac{-d\epsilon}{dx} = \frac{-\rho_s}{\epsilon_s} \tag{B.1}$$

Considering the p-doped contribution, under the boundary condition that $\epsilon(x) = 0$ when $x = x_i$ then the p-side electric field (ϵ_π)is given by:

$$\epsilon_\pi(x) = \frac{-qN_\pi}{\epsilon_s}(x + x_i) \tag{B.2}$$

Similarly for the n-side, under the boundary condition $\epsilon(x) = 0$ when $x = x_n$:

$$\epsilon_n(x) = \frac{qN_D}{\epsilon_s}(x - x_n) \tag{B.3}$$

The potential dropped across the junction is therefore given by:

$$\begin{aligned} V &= -\int_{-x_i}^{x_n} \epsilon(x)dx = -\int_{-x_i}^{0} \epsilon_\pi(x) - \int_{0}^{x_n} \epsilon_\pi(x) \\ &= \frac{q}{2\epsilon_s}(N_\pi x_i^2 + N_D x_n^2) \end{aligned}$$

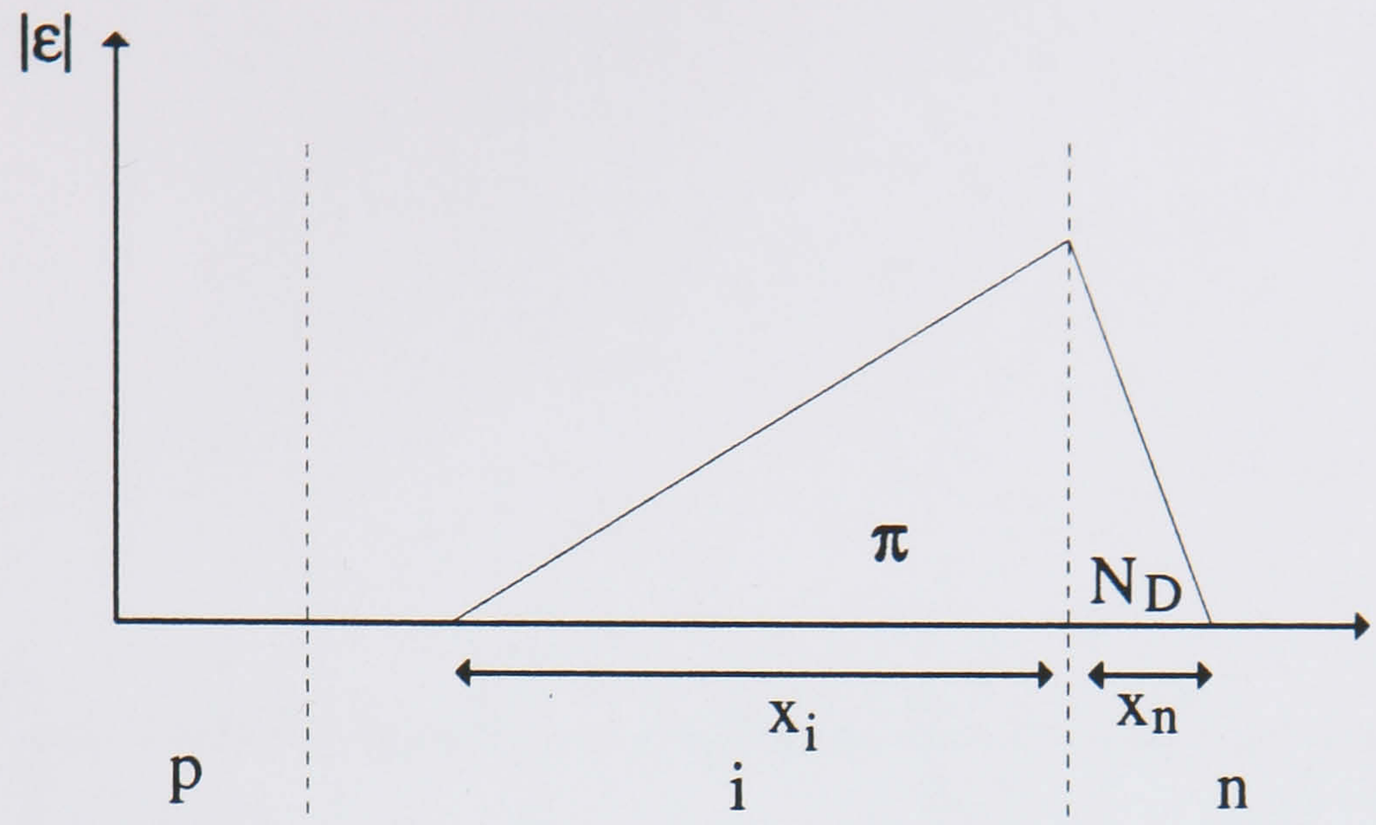

Figure B.1: Electric field distribution across p,i and n regions for a cell with p-type background doping

Charge conservation demands that $x_i N_\pi = x_n N_D$, so the above may be expressed as:

$$V = \frac{q x_i^2}{2\epsilon_s}(N_\pi + \frac{N_\pi^2}{N_D}) \tag{B.4}$$

Defining the forward applied bias (V_{app}) and built-in voltage (V_{bi}) as positive quantities, such that $V_{app} = V_{bi}$ under flat band conditions, the potential dropped across the junction may also be expressed by:

$$V = V_{app} - V_{bi} \tag{B.5}$$

Combining equations B.4 and B.5 gives a quadratic in N_π,

$$N_\pi^2 + N_D N_\pi + (V_{app} - V_{bi})\frac{2\epsilon_s N_D}{q x_i^2} = 0 \tag{B.6}$$

The limiting width of the depletion region may be calculated for InGaAs/GaAs diodes with a specific background purity level by solving equation B.6. The graph shown in figure B.2 indicates the limiting purity level vs maximum i-region width, assuming a homogenous impurity distribution and $V_{bi} = 1.1V$ for GaAs/InGaAs diodes [45].

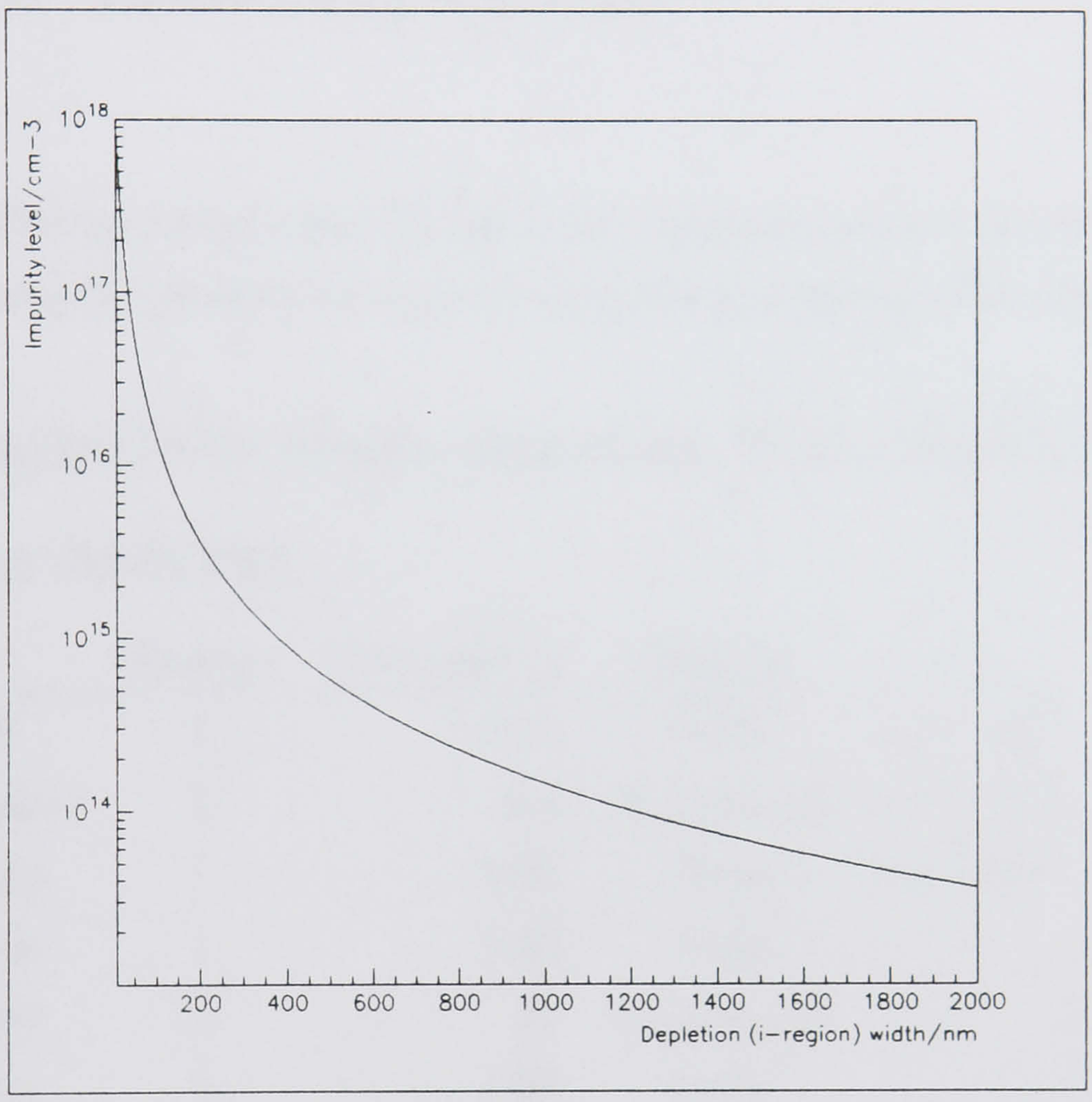

Figure B.2: InGaAs/GaAs MQW limiting purity level required to maintain the indicated depleted i-region width. Calculation assumes $V_{bi} = 1.1V$, $V_{app} = 1.0V$ and $N_D = 1 \times 10^{18}/cm^3$

Appendix C

Sample Descriptions

The following sample descriptions in this appendix are the growth specifications for the sample, plus the grower's estimate of the carrier concentration for the doped regions.

C.1 GaAs/InGaAs Single Quantum Well (SQW) Samples

C.1.1 QT458 (MOVPE)

Layer	Repeats	Thickness(Å)	Material	Conc.
p cap	1	2200	GaAs	1.4×10^{19}
p window	1	430	$Al_{0.8}Ga_{0.2}As$	1.0×10^{18}
p region	1	5000	GaAs	2.0×10^{18}
i region	1	1560	GaAs	
i region	1	80	$In_{0.2}Ga_{0.8}As$	
i region	1	1560	GaAs	
n region	1	20000	GaAs	1.3×10^{17}
n buffer	1	3000	GaAs	2×10^{18}
Substrate		GaAs(100)	(n+)	

C.1.2 RM1368 (MBE)

Layer	Repeats	Thickness(Å)	Material	Dopant	Conc.
p cap	1	2200	GaAs	Be	1.4×10^{19}
p window	1	430	$Al_{0.8}Ga_{0.2}As$	Be	1.0×10^{18}
p region	1	5000	GaAs	Be	2.0×10^{18}
i region	1	800	GaAs		
i region	1	110	$In_{0.16}Ga_{0.8}As$		
i region	1	2400	GaAs		
n region	1	20000	GaAs	Si	1.3×10^{17}
n buffer	1	3000	GaAs	Si	2.1×10^{18}
Substrate		GaAs(100)		(n+)	

C.1.3 RM1369 (MBE)

Layer	Repeats	Thickness(Å)	Material	Dopant	Conc.
p cap	1	2200	GaAs	Be	1.4×10^{19}
p window	1	430	$Al_{0.8}Ga_{0.2}As$	Be	1.0×10^{18}
p region	1	5000	GaAs	Be	2.0×10^{18}
i region	1	1600	GaAs		
i region	1	110	$In_{0.16}Ga_{0.8}As$		
i region	1	1600	GaAs		
n region	1	20000	GaAs	Si	1.3×10^{17}
n buffer	1	3000	GaAs	Si	2.1×10^{18}
Substrate		GaAs(100)		(n+)	

C.1.4 RM1370 (MBE)

Layer	Repeats	Thickness(Å)	Material	Dopant	Conc.
p cap	1	2200	GaAs	Be	1.4×10^{19}
p window	1	430	$Al_{0.8}Ga_{0.2}As$	Be	1.0×10^{18}
p region	1	5000	GaAs	Be	2.0×10^{18}
i region	1	2400	GaAs		
i region	1	110	$In_{0.16}Ga_{0.8}As$		
i region	1	800	GaAs		
n region	1	20000	GaAs	Si	1.3×10^{17}
n buffer	1	3000	GaAs	Si	2.1×10^{18}
Substrate		GaAs(100)		(n+)	

C.2 AlGaAs/GaAs Single Quantum Well (SQW) Samples

C.2.1 NU972 (MBE)

Layer	Repeats	Thickness(Å)	Material	Conc.
p cap	1	169	GaAs	2.0×10^{18}
p region	1	1500	$Al_{0.33}Ga_{0.67}As$	1.33×10^{18}
i region	1	1500	$Al_{0.33}Ga_{0.67}As$	
i region	1	144	GaAs	
i region	1	1500	$Al_{0.33}Ga_{0.67}As$	
i region	20	8.5	GaAs	
n region	20	17	GaAs	2.0×10^{18}
n region	1	4100	$Al_{0.33}Ga_{0.67}As$	1.33×10^{18}
n buffer	1	5100	GaAs	2.0×10^{18}
Substrate		GaAs(100)	(n+)	

C.2.2 QT902B (MOVPE)

Layer	Repeats	Thickness(Å)	Material	Dopant	Conc.
p cap	1	200	GaAs	C	
p region	1	1500	$Al_{0.31}Ga_{0.69}As$	C	8.0×10^{17}
i region	1	728	$Al_{0.31}Ga_{0.69}As$		
i region	1	90	GaAs		
i region	1	2272	$Al_{0.31}Ga_{0.69}As$		
n region	1	6000	$Al_{0.31}Ga_{0.69}As$	Si	
n buffer	1	1000	GaAs	Si	5.0×10^{17}
Substrate		GaAs(100)		(n+)	

C.3 GaAs/InGaAs MQW Samples

C.3.1 QT957A (MOVPE)

Layer	Repeats	Thickness(Å)	Material	Dopant	Conc.
p cap	1	2200	GaAs	Zn	1.0×10^{19}
p window	1	430	$Al_{0.8}Ga_{0.2}As$	C	2.0×10^{18}
p region	1	5000	GaAs	Zn	1.0×10^{18}
i region	10	500	GaAs		
i region	10	80	$In_{0.2}Ga_{0.8}As$		
i region	1	300	GaAs		
n region	1	20000	GaAs	Si	1.3×10^{17}
n buffer	1	3000	GaAs	Si	1.0×10^{18}
Substrate		GaAs(100)		(n+)	

C.3.2 QT957B (MOVPE)

Layer	Repeats	Thickness(Å)	Material	Dopant	Conc.
p cap	1	2200	GaAs	Zn	1.0×10^{19}
p window	1	430	$Al_{0.8}Ga_{0.2}As$	C	2.0×10^{18}
p region	1	5000	GaAs	Zn	2.6×10^{18}
i region	10	500	GaAs		
i region	10	80	$In_{0.2}Ga_{0.8}As$		
i region	1	300	GaAs		
n region	1	20000	GaAs	Si	1.5×10^{17}
n etch stop	1	15000	$Al_{0.3}Ga_{0.7}As$	Si	1.0×10^{18}
n etch stop	1	500	$AlAs$	Si	$2.0\times^{18}$
n buffer	1	3000	GaAs	Si	1.0×10^{18}
Substrate		GaAs(100)		(n+)	

C.3.3 QT957C (MOVPE)

Layer	Repeats	Thickness(Å)	Material	Dopant	Conc.
p cap	1	2200	GaAs	Zn	1.0×10^{19}
p window	1	430	$Al_{0.8}Ga_{0.2}As$	C	2.0×10^{18}
p region	1	5000	GaAs	Zn	2.6×10^{18}
i region	10	500	GaAs		
i region	10	80	$In_{0.2}Ga_{0.8}As$		
i region	1	300	GaAs		
n region	1	20000	GaAs	Si	1.5×10^{17}
n etch stop	1	15000	$Al_{0.3}Ga_{0.7}As$	Si	1.0×10^{18}
UD etch stop	1	500	$AlAs$		
UD buffer	1	3000	GaAs		
Substrate		GaAs(100)		(UD)	

C.3.4 QT957D control (MOVPE)

Layer	Repeats	Thickness(Å)	Material	Dopant	Conc.
p cap	1	2200	GaAs	Zn	1.0×10^{19}
p window	1	430	$Al_{0.8}Ga_{0.2}As$	C	2.0×10^{18}
p region	1	5000	GaAs	Zn	2.6×10^{18}
i region	1	6100	GaAs		
n region	1	20000	GaAs	Si	1.5×10^{17}
n etch stop	1	15000	$Al_{0.3}Ga_{0.7}As$	Si	1.0×10^{18}
UD etch stop	1	500	$AlAs$		
UD buffer	1	3000	GaAs		
Substrate		GaAs(100)		(UD)	

C.4 GaAs/InGaAs Strain Balance Samples

C.4.1 RM1271 & RM1386

Layer	Repeats	Thickness(Å)	Material	Dopant	Conc.
p cap	1	2200	$In_{0.05}Ga_{0.95}As$	Be	1.5×10^{19}
p window	1	430	$Al_{0.8}Ga_{0.2}As$	Be	1.0×10^{18}
p region	1	5000	$In_{0.05}Ga_{0.95}As$	Be	2.0×10^{18}
i region	1	200	$In_{0.05}Ga_{0.95}As$		
i region	23	300	$GaAs$		
i region	23	80	$In_{0.24}Ga_{0.76}As$		
i region	1	200	$In_{0.05}Ga_{0.95}As$		
n region	1	20000	$In_{0.05}Ga_{0.95}As$	Si	1.3×10^{17}
n buffer	1	3000	$GaAs$	Si	2.1×10^{18}
Substrate			$GaAs(100)$	(n+)	

C.4.2 RM1276 & RM1391

Layer	Repeats	Thickness(Å)	Material	Dopant	Conc.
p cap	1	2200	$In_{0.05}Ga_{0.95}As$	Be	1.5×10^{19}
p window	1	430	$Al_{0.8}Ga_{0.2}As$	Be	1.0×10^{18}
p region	1	5000	$In_{0.05}Ga_{0.95}As$	Be	2.0×10^{18}
i region	1	200	$In_{0.05}Ga_{0.95}As$		
i region	23	300	$GaAs$		
i region	23	80	$In_{0.24}Ga_{0.76}As$		
i region	1	200	$In_{0.05}Ga_{0.95}As$		
n region	1	20000	$In_{0.05}Ga_{0.95}As$	Si	1.3×10^{17}
n relax	1	2500	$In_{0.1}Ga_{0.9}As$	Si	4.0×10^{18}
n buffer	1	3000	$GaAs$	Si	2.1×10^{18}
Substrate			$GaAs(100)$	(n+)	

C.4.3 RM1277 & RM1389 & RM1390

Layer	Repeats	Thickness(Å)	Material	Dopant	Conc.
p cap	1	2200	$In_{0.05}Ga_{0.95}As$	Be	1.5×10^{19}
p window	1	430	$Al_{0.8}Ga_{0.2}As$	Be	1.0×10^{18}
p region	1	5000	$In_{0.05}Ga_{0.95}As$	Be	2.0×10^{18}
i region	1	200	$In_{0.05}Ga_{0.95}As$		
i region	23	300	$GaAs$		
i region	23	80	$In_{0.24}Ga_{0.76}As$		
i region	1	200	$In_{0.05}Ga_{0.95}As$		
n region	1	20000	$In_{0.05}Ga_{0.95}As$	Si	1.3×10^{17}
n etch stop	1	15000	$Al_{0.3}Ga_{0.7}As$	Si	1.5×10^{18}
n etch stop	1	1000	$AlAs$	Si	$4.5\times^{18}$
n buffer	1	3000	$GaAs$	Si	2.1×10^{18}
Substrate			$GaAs(100)$	(n+)	

C.5 GaAsP/InGaAs Strain-Balance Samples

C.5.1 QT1227 (MOVPE)

Layer	Repeats	Thickness(Å)	Material	Dopant	Conc.
p cap	1	2200	GaAs	Zn	1.0×10^{19}
p window	1	430	$Al_{0.8}Ga_{0.2}As$	C	1.0×10^{18}
p region	1	5000	GaAs	Zn	2.0×10^{18}
i region	1	100	GaAs		
i region	20	227	$GaAs_{0.094}P_{0.06}$		
i region	20	80	$In_{0.2}Ga_{0.8}As$		
i region	20	227	$GaAs_{0.094}P_{0.06}$		
i region	1	100	GaAs		
n region	1	20000	GaAs	Si	1.5×10^{17}
n buffer	1	3000	GaAs	Si	1.5×10^{18}
Substrate		GaAs(100)		(n+)	

C.5.2 QT1228 control (MOVPE)

Layer	Repeats	Thickness(Å)	Material	Dopant	Conc.
p cap	1	2200	GaAs	Zn	1.0×10^{19}
p window	1	430	$Al_{0.8}Ga_{0.2}As$	C	1.0×10^{18}
p region	1	5000	GaAs	Zn	2.0×10^{18}
i region	1	10680	GaAs		
n region	1	20000	GaAs	Si	1.5×10^{17}
n buffer	1	3000	GaAs	Si	1.5×10^{18}
Substrate		GaAs(100)		(n+)	

Appendix D

Matthews-Blakeslee formalism

D.0.3 Strain balance calculation

The notation for the following analysis stems from the INSPEC data review on InGaAs [115].

The parameters are linearly interpolated from the available GaAs and InAs values. This may not be necessary, as the differences are small and the $In_xGa_{1-x}As$ alloys in this study are dominated by GaAs.

Lattice constant/Å	a_x=6.0583-0.4050(1-x)
Elastic constants/$dynes.cm^{-2}$	$C_{11} = (11.88 - 3.55x) \times 10^{11}$
	$C_{12} = (5.38 - 0.85x) \times 10^{11}$
	$C_{44} = (5.94 - 1.98x) \times 10^{11}$
Strain	$f = \frac{a_{InGaAs} - a_{GaAs}}{a_{InGaAs}}$
Young's Modulus	$Y = C_{11} + C_{12} - \frac{2C_{12}^2}{C_{11}}$
Poisson ratio	$\nu = \frac{C_{12}}{C_{12}+C_{11}}$
Burgers magnitude	$b = \frac{\sqrt{2}}{2} a_{InGaAs}$

Allowing the critical thickness hc to be written as,

$$hc = \frac{D(1 - \nu \cos^2\theta)(ln(hc/b) + 1)}{Yf} \tag{D.1}$$

With parameters,

$$\begin{aligned} G &= C_{44} - \frac{1}{3}(2C_{44} + C_{12} - C_{11}) \\ D &= \frac{bG_{GaAs}G_{InGaAs}}{\pi(G_{GaAs} + G_{InGaAs})(1 - \nu)} \end{aligned}$$

When solved numerically, the equations reproduce the critical thickness curve for 60 degree dislocations shown in figure D.0.3.

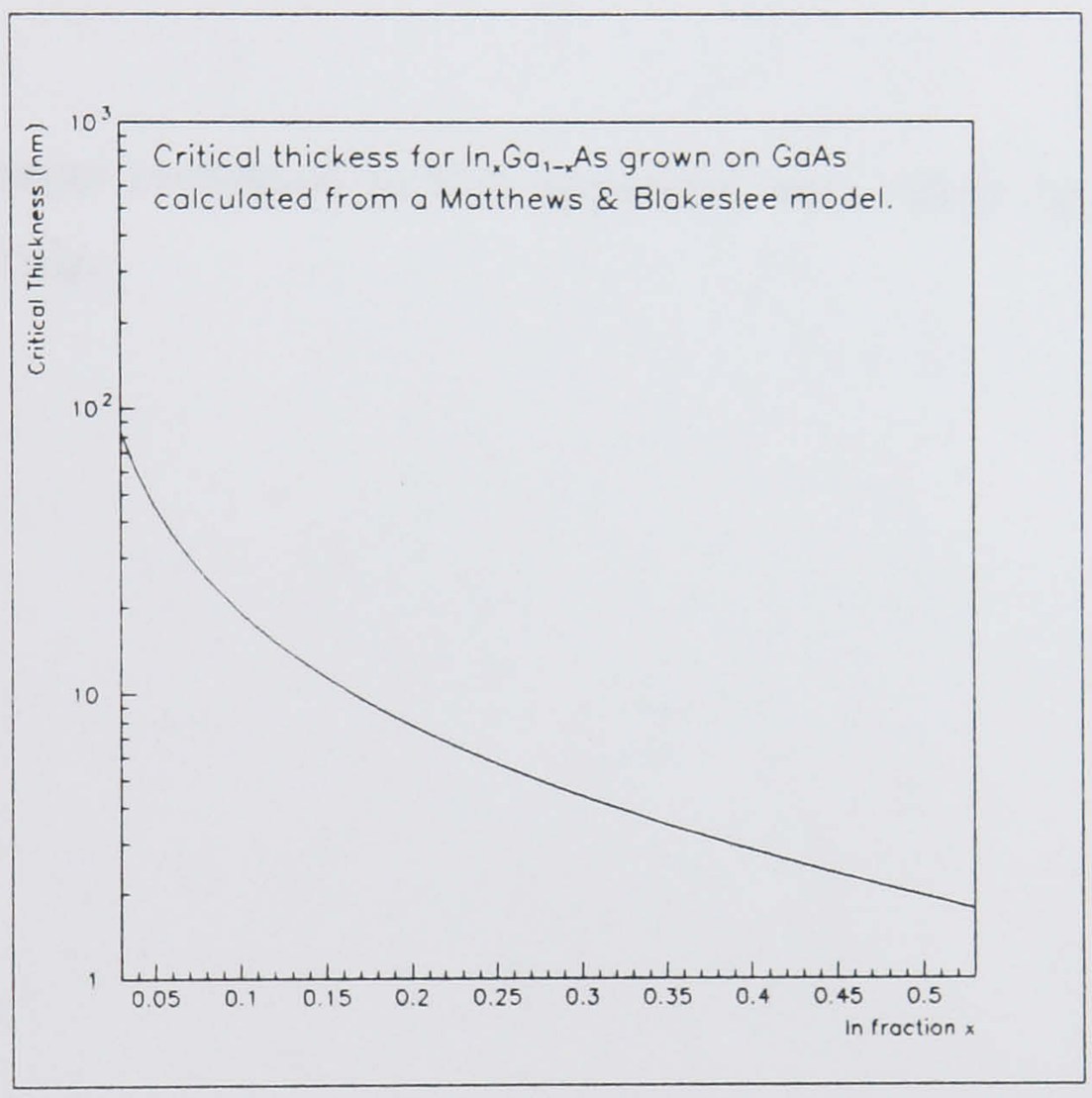

Figure D.1: Critical thicknesses for defect introduction for $In_xGa_{1-x}As$ on GaAs

Appendix E

EBIC Images

All the images presented in this appendix were taken by Max Mazzer based at CNR-IME, Lecce, Italy.

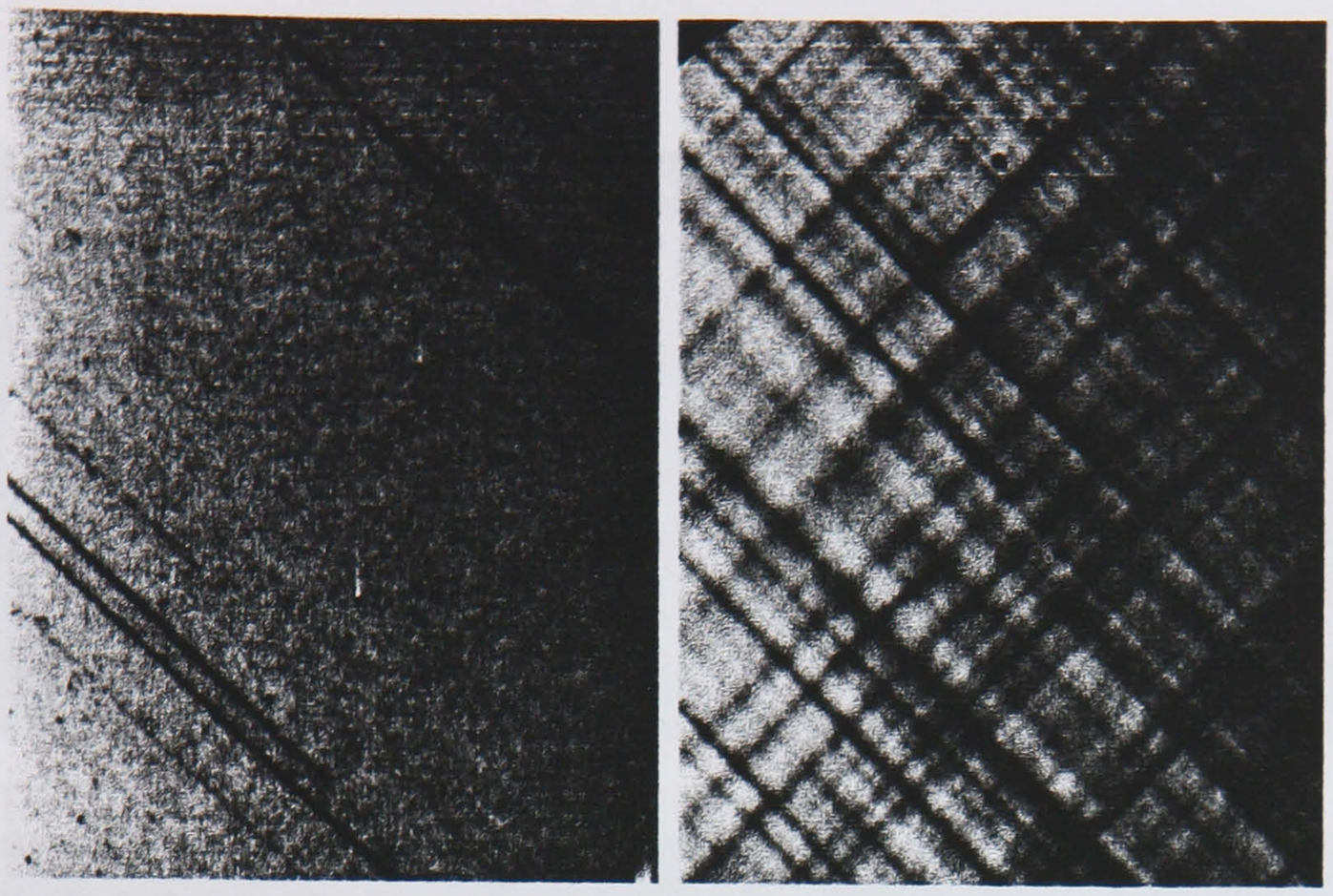

RM1271, 10kV and 40kV, mag=260

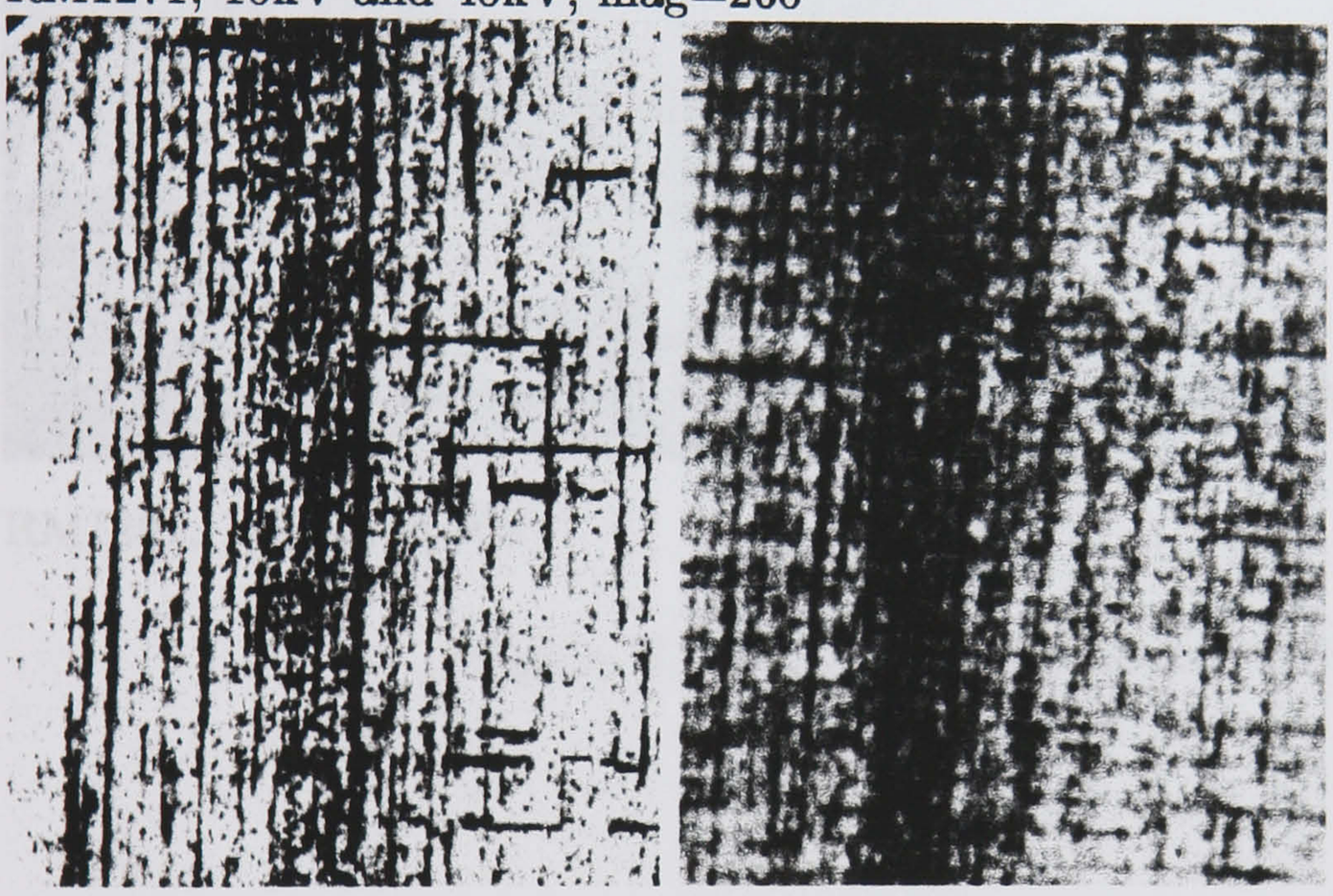

RM1276, 10kV and 30kV, mag=260

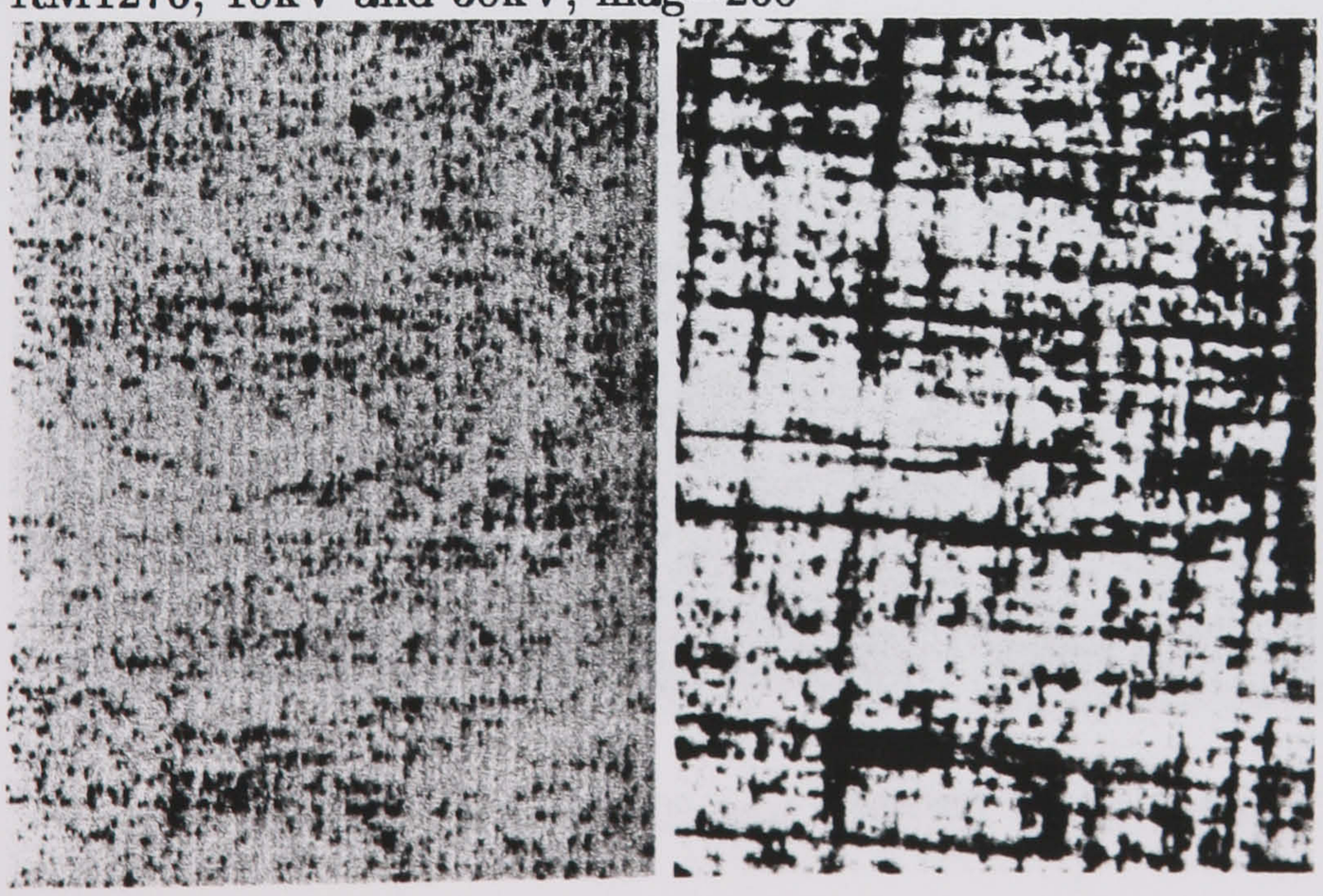

RM1277, 10kV and 30kV, mag=267

Figure E.1: RM1271, RM1276 and RM1277 EBIC Images

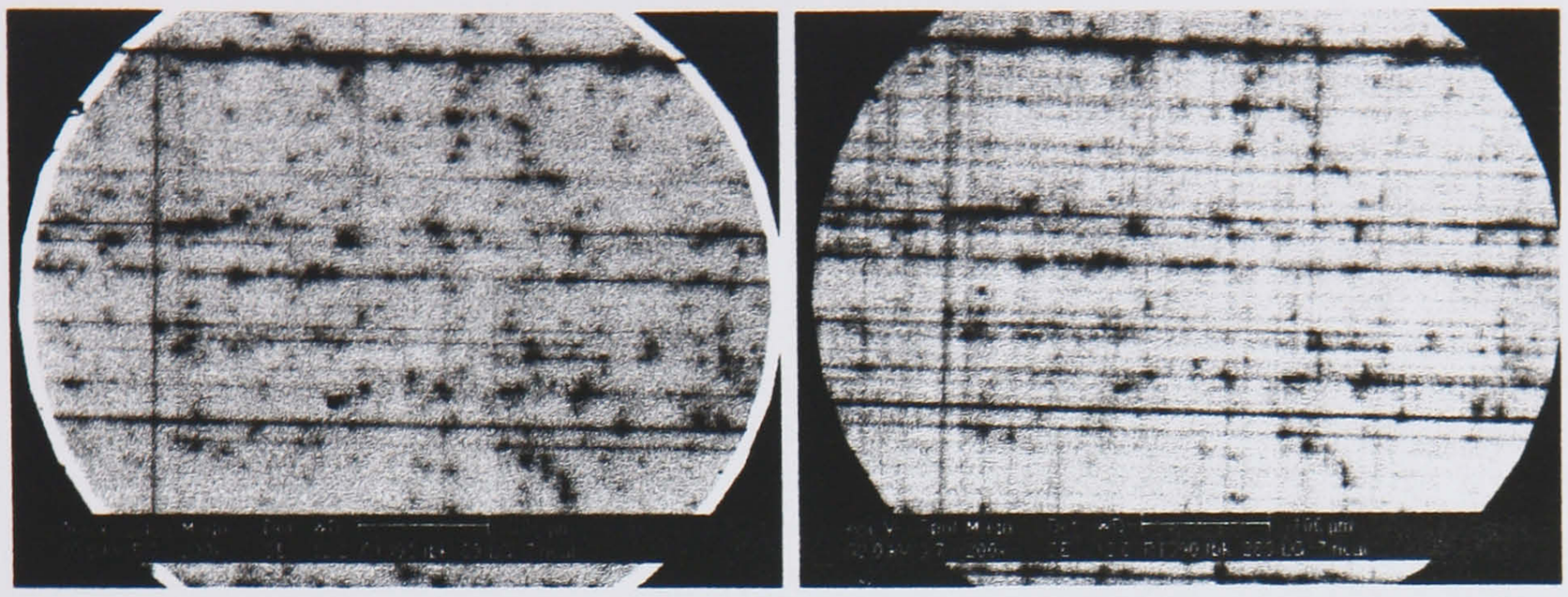

RM1390, 10kV and 30kV.

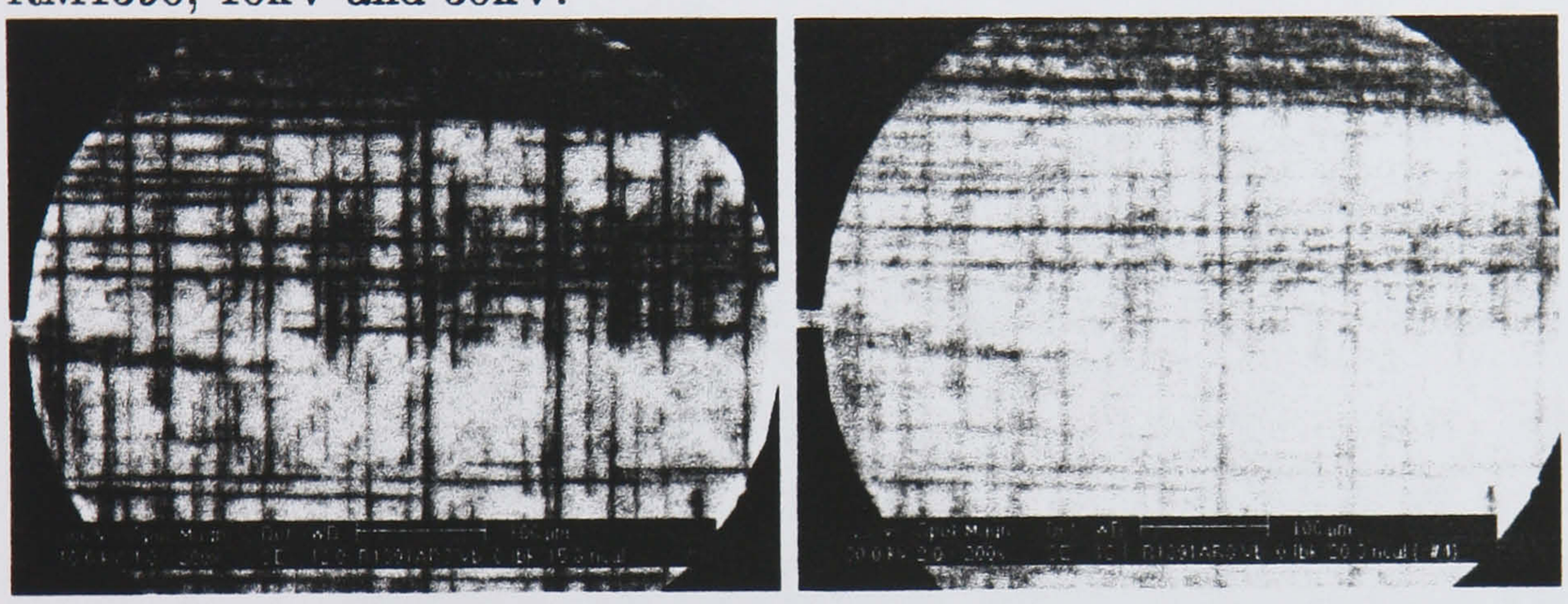

RM1391, 10kV and 30kV.

Figure E.2: RM1390 and RM1391 EBIC Images

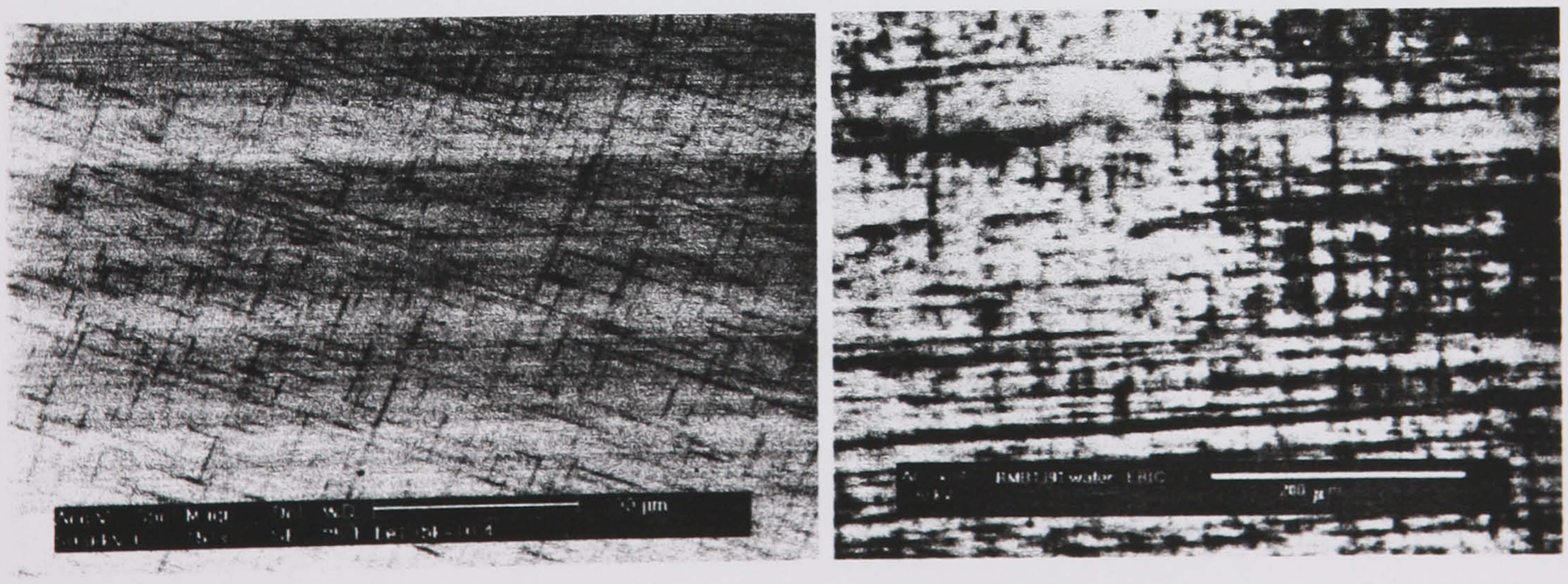

Figure E.3: Lecce001 and RM1391 EBIC Images, both taken at 30kV

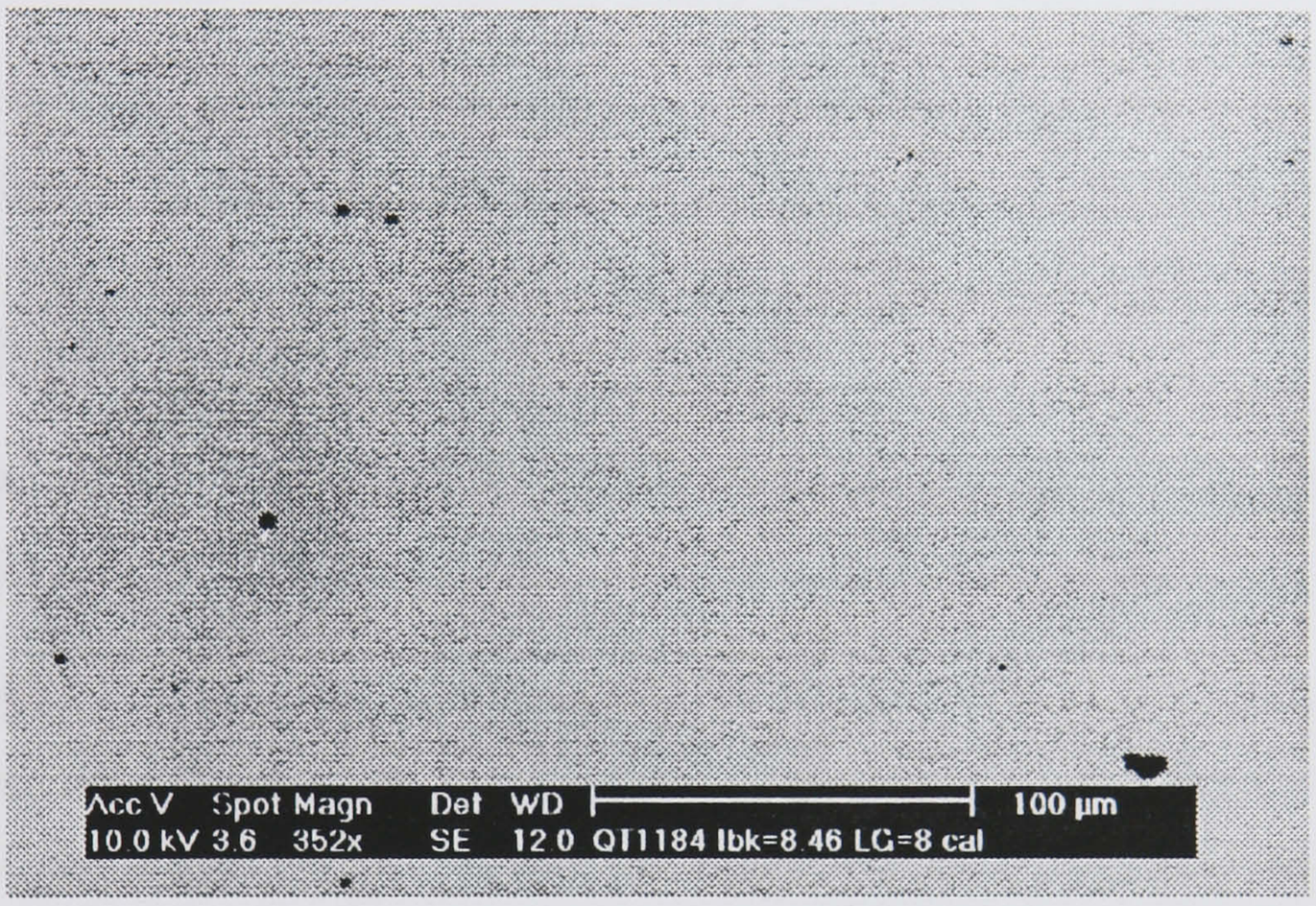

Figure E.4: EBIC image for QT1184, taken at 10kV indicating excellent growth quality

Bibliography

[1] S.P. Tobin, S.M. Vernon, S.J. Wojtczuk, C. Bajgar, M.M. Sanfacon, and T.M. Dixon. Advances in high-efficiency GaAs solar cells. In *Proc. 21st IEEE PV specialists conf.*, pages 158–162, USA, 1990. IEEE.

[2] S.P. Tobin, S.M. Vernon, C. Bajgar, S.J. Woktczuk, M.R. Melloch, A. Keshavarzi, T.B. Stellwag, S. Venkatensan, M.S. Lundstrom, and K.A. Emery. Assessment of MOCVD and MBE grown GaAs for high-efficiency solar cell applications. *IEEE Trans. Electron Devices*, 37(2):469–477, 1990.

[3] J.C.C. Fan, B.Y. Tsaur, and B.J. Palm. Optimal design of high-efficiency tandem cells. In *Proc. 16th PV Specialists Conference, San Diego*, page 692. IEEE, 1982.

[4] A. V. Drigo, A. Aydinli, A. Carnera, F. Genova, C. Rigo, C. Ferrari, P. Franzosi, and G. Salviati. On the mechansims of strain release in molecular-beam-epitaxy -grown InGaAs/GaAs single hetrostructures. *J.Appl.Phys*, 66:1975–1983, 1989.

[5] ASTM. *Standard Solar Constant and Air Mass Zero Solar Spectral Irradiance Tables E490-73a*, 1999.

[6] ASTM. *Standard Tables for References Solar Spectral Irradiance at Air Mass 1.5: Direct Normal and Hemispherical for a 37° Tilted surface G159-98*, 1998.

[7] Godfrey Boyle, editor. *Renewable energy: power for a sustainable future.* Oxford University Press, 1996.

[8] S.M. Sze. *Physics of Semiconductor Devices.* John Wiley and Sons, 2nd edition, 1981.

[9] M.A. Green. *Solar Cells: Operating Principles, Technology and System Applications.* Prentice-Hall, London, 1982.

[10] L.D. Partain. *Solar Cells and their applications.* John Wiley and Sons, 1995.

[11] R.H. Bube. *Photovoltaic Materials.* Imperial College Press, 1998.

[12] P.T. Landsberg. *Recombination in semiconductors.* Cambridge University Press, 1991.

[13] C.T. Sah, R.N. Noyce, and W. Shockley. *Proc. instn. Radio. Eng.*, 45:1228, 1957.

[14] S.R. Kurtz. Private Communication.

[15] M.A. Green, K. Emery, K. Bücher, D.L. King, and S. Igari. Solar cell efficiency tables. *Prog. Photovoltics Research and Applications*, 7(4):321–326, 1999. Also http://www.pv.unsw.edu.au/eff/.

[16] J.M. Olson, R.K. Ahrenkiel, D.J. Dunlavy, B. Keyes, and A.E. Kibbler. Ultralow recombination velocity at $Ga_{0.5}In_{0.5}P$/GaAs heterointerfaces. *Appl.Phys.Lett*, 55(12):1208–1210, 1989.

[17] S.R. Kurtz, J.M. Olson, and A. Kibbler. High efficiency GaAs solar cells using GaInP window layers. In *Proc. 21st IEEE PV specialists conf.*, pages 138–140, USA, 1990. IEEE.

[18] P.D. DeMoulin, S.P. Tobin, M.S. Lundstrom, M.S. Carpenter, and M.R. Melloch. Influence of perimeter recombination on high-efficiency GaAs p/n heterointerface solar cells. *IEEE Electron Device Lett.*, 9(8):368–370, 1988.

[19] S.A. Ringel and A. Rohatgi. The effects of trap-induced lifetime variations on the design and performance of high-efficiency GaAs solar cells. *IEEE Trans. Electron Devices*, 38(11):2402–2409, 1991.

[20] G.L. Araújo and A. Martí. Generalized detailed balance theory to calculate the maximum efficiency of solar cells. In *Proc. 11th European Photovoltaic Solar Energy Conference*, page 142. Harwood Academic Publications, 1992.

[21] U. Bach, D. Lupo, P. Comte, J.E. Moser, F. Weissörtel, J. Salbeck, H. Spreitzer, and M. Grätzel. Solid-state dye-sensitized mesoporous TiO_2 solar cells with high photon-to-electron conversion efficiencies. *Nature*, 395:583–585, 1998.

[22] J. S. Ward, M. W. Wanlass, K. A. Emery, and T. J. Coutts. GaInAsP solar cells with the ideal band gap for terrestrial concentrator applications. In *Proc. 23th IEEE PV specialists conf.*, USA, 1993. IEEE.

[23] K.A. Bertness, S.R. Kurtz, D.J. Friedman, A.E. Kibbler, C. Kramer, and J.M. Olson. 29.5-percent-efficient GaInP/GaAs tandem solar-cells. *Applied Physics Letters*, 65:989–991, 1994.

[24] T. Takamoto, E. Ikeda, H. Kurita, and M. Ohmori. Over 30% efficient InGaP/GaAs tandem solar cells. *Appl.Phys.Lett*, 70(3):381–383, 1997.

[25] D.J. Friedman, J.F. Geisz, S.R. Kurtz, and J.M. Olson. 1-ev solar cells with GaInNAs active layer. *J. Crystal Growth*, 195:409–415, 1998.

[26] R.W. Hoffman, N.S. Fatemi, M.A. Stan, P. Jenkins, and V.G. Weizer. High efficiency InGaAs on GaAs devices for monolithic multi-junction solar cell applications. In *Proc. 2nd World Conf. and Exhibition on Photovoltaic Solar Energy Conversion*, pages 3604–3608. European Commission, 1998.

[27] A. Freundlich and I. Serdiukova. Multi-quantum well tandem solar cells with efficiencies exceeding 30% AM0. In *Proc. 2nd World Conf. and Exhibition on Photovoltaic Solar Energy Conversion*, page 3707, Ispra, Italy, 1998. European Commission.

[28] K. W. J. Barnham and G. Duggan. A new approach to high-efficiency multi-band-gap solar cells. *J.Appl.Phys*, 67:3490–3493, 1990.

[29] Jenny Nelson. Quantum-well structures for photovoltaic energy conversion. In M.H. Francome and J.L. Vossen, editors, *Physics of Thin Films*, volume 21, pages 311–368. Academic Press, New York, 1995.

[30] Keith Barnham, Ian Ballard, Jenny Barnes, James Connolly, Paul Griffin, Benjamin Kluftinger, Jenny Nelson, Ernest Tsui, and Alexander Zachariou. Quantum well solar cells. *Applied Surface Science*, 113/114:722–733, 1997.

[31] K. W. J. Barnham, B. Braun, J. Nelson, M. Paxman, C. Button, J. S. Roberts, and C. T. Foxon. Short-circuit current and energy efficiency enhancement in a low-dimensional structure photovoltaic device. *Appl.Phys.Lett.*, 59:135–137, 1991.

[32] K. W. J. Barnham, J. Connolly, P. Griffin, G. Haarpaintner, J. Nelson, E. Tsui, A. Zachariou, J. Osborne, C. Button, G. Hill, M. Hopkinson, M. Pate, J. S. Roberts, and T. Foxon. Voltage enhancement in quantum well solar cells. *J.Appl.Phys*, 80(2):1201–1206, 1996.

[33] P.K. Chiang, J.H. Ermer, W.T. Nishikawa, D.D. Krut, D.E. Joslin, J.W. Eldredge, B.T. Cavicchi, and J.M. Olson. Experimental results of GaInP/GaAs/Ge triple junction cell development for space power systems. In *Proc. 25th IEEE PV specialists conf.*, pages 183–186, USA, 1996. IEEE.

[34] October 1999. Press release from Spectrolab.

[35] S. Tanaka, M. Takahashi, A. Moto, T. Tanabe, S. Takagishi, K. Karatani, T. Nakanishi, and M. Nakayama. Optical characterisation of GaInNAs/GaAs quantum well structures. In *25th Int. Symp. Compound Semiconductors*, pages 633–638. IOP Publishing, 1998.

[36] R.L. Williams, M. Dion, F. Chatenoud, and K. Dzurko. Extremely low threshold current strained InGaAs/AlGaAs lasers by molecular-beam epitaxy. *Appl.Phys.Lett.*, 58(17):1816–1818, 1991.

[37] J. Barnes, T. Ali, K. W. J. Barnham, J. Nelson, and E. S. M. Tsui. Gallium Arsenide/Indium Gallium Arsenide Multi-Quantum Well solar cells. In *Proc. 12th European PV solar energy conf.*, pages 1374–1377, Bedford, U.K., 1994. H.S. Stephens & Associates.

[38] F.W. Ragay, J.H. Wolter, A. Martí, and G.L. Araújo. Experimental analysis of GaAs-InGaAs MQW solar cells. In *Proc. 1st World Conference and Exhibition on Photovoltaic Solar Energy Conversion*, page 1754, USA, 1994. IEEE.

[39] W.A. Jesser and J.H. van der Merwe. Prediction of critical misfit and thickness in epitaxy. In F.R.N. Nabarro, editor, *Dislocations in Solids*, volume 8, chapter 41, pages 421–460. North Holland, 1989.

[40] J. W. Matthews and A. E. Blakeslee. Defects in epitaxial multilayers. *J.Crystal Growth*, 27:118–125, 1974.

[41] P. R. Griffin, J. Barnes, K. W. J. Barnham, G. Haarpainter, M. Mazzer, C. Zanotti-Fregonara, E. Grunbaum, C. Olson, C. Rohr, J. P. R. David, J. S. Roberts, R. Grey, and M. A. Pate. Effect of strain relaxation on forward bias dark currents in GaAs/InGaAs multiquantum well p-i-n diodes. *J.Appl.Phys.*, 80:5815–5820, 1996.

[42] Paul Griffin. *Investigation of Quantum Well Solar Cells for Concentrator and Thermophotovoltaic Applications.* PhD thesis, Imperial College, University of London, 1997.

[43] M. Mazzer, E. Grünbaum, K.W.J. Barnham, J. Barnes, P.R. Griffin, D.B. Holt, J.L. Hutchinson, A.G. Norman, J.P.R. David, J.S. Roberts, and R. Grey. Study of misfit dislocations by EBIC, CL and HRTEM in GaAs/InGaAs lattice-strained multi-quantum well p-i-n solar cells. *Materials science and engineering*, B42:43–51, 1996.

[44] M. Paxman, J. Nelson, B. Braun, J. Connolly, K. W. J. Barnham, C. T. Foxon, and J. S. Roberts. Modeling the spectral response of the quantum well solar cell. *J.Appl.Phys*, 74:614–621, 1993.

[45] Jenny Barnes. *An experimental and theoretical study of GaAs/InGaAs quantum well solar cells and carrier escape from quantum wells.* PhD thesis, Imperial College, University of London, 1994.

[46] C. Monier, A. Freundlich, and M.F. Vilela. Oscillator strength of excitons in (In, Ga)As/GaAs quantum wells in the presence of a large electric field. *J.Appl.Phys.*, 85(5):2713–2718, 1999.

[47] M.R. Melloch, S.P. Tobin, T.B. Stellwag, C. Bijgar, A. Keshavarzi, M.S. Lundstrom, and K. Emery. High-efficiency GaAs solar cells grown by molecular-beam epitaxy. *J.Vac.Sci.Technol.B*, 8(2):379–383, 1990.

[48] S.R. Kurtz, J.M. Olson, K.A. Bertness, K. Sinha, B. McMahon, and S. Asher. Hidden but important parameters in $Ga_{0.5}In_{0.5}P$ cell growth. In *Proc. 26th IEEE PV specialists conf.*, pages 37–42, USA, 1996. IEEE.

[49] M. T. Bulsara, V. Yang, A. Thilderkvist, E. A. Fitzgerald, K. Haüsler, and K. Eberl. Graded InGaAs/GaAs 1.3μm wavelength light emitting diode structures grown with molecular beam epitaxy. *J.Appl.Phys.*, 83:592–599, 1998.

[50] J.S. Roberts, J.P.R David, T.E. Sale, and P.L. Tihanyi. High-purity AlGaAs from methyl-based precursors using in-situ gettering of alkoxides. *J. Crystal Growth*, 143(3-4):135–140, 1994.

[51] J.S. Roberts. Growth of GaAsP/InGaAs structures. Presented at the EPSRC III-V users meeting, Sheffield, U.K., July 1999.

[52] J.S. Ward, A. Duda, K. Zweibel, and T.J. Coutts. Large-area, high-intensity PV arrays for systems using dish concentrating optics. In *Proc. 2nd World Conf. and Exhibition on Photovoltaic Solar Energy Conversion.* European Commission, 1998.

[53] Navid S. Fatemi, David M. Wilt, Phillip P. Jenkins, Victor G. Weizer, Richard W. Hoffman, Jr., Christopher S. Murray, David Scheinman, David Brinker, and David Riley. InGaAs monolithic interconnected modules (MIMs). In *Proc. 26th IEEE PV specialists conf.*, pages 799–804, USA, 1997. IEEE.

[54] Markus Hepp. Light trapping in quantum well solar cells grown on patterned substrate. Master's thesis, Imperial College, University of London., 1998.

[55] Ruth Woodward. Light trapping. Master's thesis, Imperial College, University of London., 1999.

[56] James Connolly. *Modelling and Optimising GaAs/AlGaAs MQW solar cells.* PhD thesis, Imperial College, University of London, 1997.

[57] J. Nelson, J. Ballard, K. W. J. Barnham, J. Connolly, J. S. Roberts, and M. Pate. Effect of QW location on quantum well solar cell dark currents. *J.Appl.Phys.*, 86(10):5898–5905, 1999.

[58] J. Barnes, E. S. M. Tsui, K. W. J. Barnham, S. C. McFarlane, C. Button, and J. S. Roberts. Steady state photocurrent and photoluminescence from single quantum wells as a function of temperature and bias. *J.App.Phys*, 81:892–900, 1997.

[59] J. Barnes, J. Nelson, K.W.J. Barnham, J.S. Roberts, M.A. Pate, R. Grey, S.S. Dosanjh, M. Mazzer, and F. Ghiraldo. Characterization of GaAs/InGaAs quantum wells using photocurrent spectroscopy. *J.Appl.Phys*, 79:7775–7779, 1996.

[60] Robert T. Ross and Arthur J. Nozik. Efficiency of hot-carrier solar energy converters. *J.Appl.Phys*, 53:3813–3818, 1982.

[61] Y. Rosenwaks, M. C. Hanna, D. H. Levi, D. M. Szmyd, R. K. Ahrenkiel, and A. J. Nozik. Hot-carrier cooling in GaAs: Quantum wells versus bulk. *Phys.Rev.B*, 48:14675–14678, 1993.

[62] Mark C. Hanna, Zhenghao Lu, and Arthur J. Nozik. Hot carrier solar cells. Presented at Future generation of photovoltaic technologies (1997), Denver, USA.

[63] R. Corkish and M.A. Green. Recombination of carriers in quantum well solar cells. In *Proc. 23rd PV Specialists Conference, New York*, pages 675–689. IEEE, 1993.

[64] G.L. Araújo, A. Martí, F.W. Ragay, and J.H. Wolter. Efficiency of multiple quantum well solar cells. In *Proc. 12th European Photovoltaic Solar Energy Conference*, pages 1481–1484, Bedford, U.K., 1994. H.S. Stephens & Associates.

[65] F.W. Ragay, J.H. Wolter, A. Martí, and G.L. Araújo. Experimental analysis of the efficiency of MQW solar cells. In *12th European Photovoltaic Solar Energy Conference*, pages 1429–1433, Bedford, U.K., 1994. H.S. Stephens & Associates.

[66] A. Luque and A. Martí. Increasing the efficiency of ideal solar cells by photon induced transitions at intermediate levels. *Phys.Rev.Lett.*, 78(26):5014–5017, 1997.

[67] S. Kettermann and J.F. Guillemoles. Limiting efficiency of LDS solar cells. In *Proc. 13th European Photovoltaic Solar Energy Conference*, pages 119–121. Bedford: Stephens, 1995.

[68] J. Nelson, B.G. Kluftinger, E.S.M. Tsui, K.W.J. Barnham, J.S. Roberts, and C. Button. Quasi-fermi level separation in quantum well solar cells. In *Proc. 13th European Photovoltaic Solar Energy Conference*, pages 150–153, Bedford, U.K., 1995. H.S. Stephens & Associates.

[69] P. Würfel. The chemical potential of radiation. *J.Phys.C: Solid State Phys.*, 15:3967–3985, 1982.

[70] Ernest Tsui, Jenny Nelson, Keith Barnham, Chris Button, and John S. Roberts. Determination of the quasi-Fermi-level separation in single-quantum-well p-i-n diodes. *J.Appl.Phys.*, 80(8):4599–4603, 1996.

[71] J. Nelson, M. Paxman, K. W. J. Barnham, J. S. Roberts, and C. Button. Steady state carrier escape from single quantum wells. *IEEE Journal of Quantum Electronics*, 29:1460–1467, 1993.

[72] J. Nelson, J. Barnes, N. Ekins-Daukes, B. Kluftinger, E. Tsui, K. W. J. Barnham, T. Foxon, T. Cheng, and J. S. Roberts. Radiative currents from GaAs/InGaAs and AlGaAs/GaAs quantum well solar cells. In *Proc. 15th European Photovoltaic Solar Energy Conference*, Bedford, U.K., 1997. H.S. Stephens & Associates.

[73] J. Nelson, J. Barnes, N. Ekins-Daukes, B. Kluftinger, E. Tsui, K. W. J. Barnham, T. Foxon, T. Cheng, and J. S. Roberts. Observation of suppressed radiative recombination in single quantum well p-i-n photodiodes. *J.Appl.Phys.*, 82:6240–6246, 1997.

[74] D.E. Aspnes. *Properties of GaAs.* (INSPEC) Institution of Electrical Engineers: London, 2nd edition, 1990.

[75] D.E. Aspnes, S.M. Kelso, R.A. Logan, and R. Bhat. Optical-properties of AlGaAs. *J.Appl.Phys.*, 60(2):754–767, 1986.

[76] J.F. Guillemoles and S. Kettermann. Private Communication, 1997.

[77] B. Kluftinger, J. Barnes, K. Barnham, N. Ekins-Daukes, and J. Nelson. A detailed study of the radiative currents from double quantum well solar cells. In *Proc. 2nd World Conf. and Exhibition on Photovoltaic Solar Energy Conversion*, page 19. European Commission, 1998.

[78] G. Bastard. *Wave mechanics applied to semiconductor heterostructures.* Les Editions de Physique, 1988.

[79] D.A.B. Miller, J.W. Weiner, and D.S. Chemla. *IEEE Journal of Quantum Electronics*, 22:1816, 1986.

[80] M. Whitehead, G. Parry, K. Woodbridge, P.J. Dobson, and G. Duggan. Experimental confirmation of a sum rule for room-temperature electroabsorption in gaas-algaas multiple quantum well structures. *Appl.Phys.Lett.*, 52(5):345–347, 1988.

[81] E. Yablonovitch and G.D. Cody. Intensity enhancement in textured optical sheets for solar cells. *IEEE Trans. Electron Devices*, ED-29:300–305, 1982.

[82] P.R. Campbell and M.A. Green. Light trapping properties of pyramidally textured surfaces. *J.Appl.Phys.*, 62:243–249, 1987.

[83] M.A. Green. Two new efficient crystalline silicon light-trapping textures. *Prog. Photovolt. Res. Appl.*, 7(4):317–320, 1999.

[84] Lars Steinke. Light trapping in MQW solar cells. Master's thesis, Imperial college, University of London, 1996.

[85] R.K. Ahrenkiel, D.J. Dunlavy, B. Keyes, S.M. Vernon, T.M. Dixon, S.P. Tobin, K.L. Miller, and R.E. Hayes. Ultralong minority-lifetime epitaxial GaAs by photon recycling. *Appl.Phys.Lett*, 55(11):1088–1090, 1989.

[86] I. Schnitzer, E. Yablonovitch, C. Caneau, and T.J. Gmitter. Ultrahigh spontaneous emission quantum efficiency, 99.7% internally and 72% externally, from AlGaAs/GaAs/AlGaAs double heterostructures. *Appl.Phys.Lett.*, 62(2):131–133, 1993.

[87] Khaled Zahraman, Jean-Claude Guillaume, Gilles Nataf, Bernard Beaumont, Mathieu Leroux, and Pierre Gibart. High-efficiency $Al_{0.2}Ga_{0.8}As/Si$ stacked tandem solar cells using epitaxial lift-off. *Jpn. J. Appl. Phys.*, 33:5807–5810, 1994.

[88] I. Schnitzer, E. Yablonovitch, C. Caneau, T.J. Gmitter, and A. Scherer. 30% external quantum efficiency from surface textured, thin-film light-emitting diodes. *Appl.Phys.Lett.*, 63(16):2174–2176, 1993.

[89] Greg Lush and Mark Lundstrom. Thin film approaches for high-efficiency iii-v cells. *Solar Cells*, 30:337–344, 1991.

[90] J.E. Parrot, A. Potts, V. Badescu, and P.T. Landsberg. Photon recycling in thin film homo- and heterojunction solar cells. In *Proc. 13th European Photovoltaic Solar Energy Conference*, pages 921–924. Bedford: Stephens, 1995.

[91] J.L. Balenzategui, A. Martí, and G.L. Araújo. Numerical modelling of photon recycling effects in solar cells using PC-1D. In *Proc. 13th European Photovoltaic Solar Energy Conference*, pages 1223–1226. Bedford: Stephens, 1995.

[92] G.B. Lush, M.P. Patkar, M.P. Young, M.R. Melloch, M.S. Lunstrom, S.M. Vernon, L.M. Gagnon, E.D. Geoffroy, and M.M. Sanfacon. Thin-film GaAs solar cells by epitaxial lift-off. In *Proc. 23rd PV Specialists Conf.*, pages 1343–1346. IEEE, 1993.

[93] Franck Omnes, Jean-Claude Guillaume, Gilles Nataf, Gerold Jäger-Waldau, Philippe Vennegues, and Pierre Gibart. High efficiency epitaxial lift-off GaAs solar cells on Pd-coated silicon. In *Proc. 13th European Photovoltaic Solar Energy Conference*, pages 122–125. Bedford: Stephens, 1995.

[94] X.Y. Lee, A.K. Verma, C.Q. Wu, M Goertemiller, E. Yablonovitch, J. Eldredge, and D. Lillington. Thin film GaAs solar cells on glass substrates by epitaxial liftoff. In *Proc. 25th IEEE PV specialists conf.*, pages 53–55, USA, 1996. IEEE.

[95] S. Wojtczuk and K. Reinhardt. High-power density (1040 w/kg) GaAs cells for ultra-light aircraft. In *Proc. 25th PV specialists conf.*, pages 49–52, USA, 1996. IEEE.

[96] P.R. Hageman, G.J. Bauhuis, A. van Geelen, P.C. van Rijsingen, J.J. Schermer, and L.J. Giling. Large area, thin film epitaxial lift off III/V solar cells. In *Proc. 25th IEEE PV specialists conf.*, pages 57–60, USA, 1996. IEEE.

[97] A. Martí, J. L. Balenzategui, and R. F. Reyna. Photon recycling and shockley's diode equation. *J.Appl.Phys.*, 82:4067–4075, 1997.

[98] A. Martí. Private communication.

[99] J.S. Roberts. Private communication.

[100] M.P. Patkar, M.S. Lundstrom, and M.R. Melloch. Characterization of photon recycling in thin crystalline GaAs light emitting diodes. *J.Appl.Phys*, 78:2817–2822, 1995.

[101] S.P. Tobin, S.M. Vernon, C. Bajgar, V.E. Haven, L.M. Geoffroy, and D.R. Lillington. High-efficiency GaAs/Ge monolithic tandem solar cells. *IEEE Electron Device Lett.*, 9:256–258, 1988.

[102] M.A Green. Silicon solar cells. Plenary talk at the Future of PV, Imperial College, U.K., 1997.

[103] M. Yamaguchi. Dislocation density reduction in heteroepitaxial III-V compound films on Si substrates for optical devices. *J.Mater.Res.*, 6(2):376–384, 1991.

[104] E.A. Fitzgerald. *Lattice mismatch and dislocations in InGaAs/GaAs strained heterostructures*, pages 6–14. INSPEC, 1993.

[105] B. Beanland, D.J. Dunstan, and P.J. Goodhew. Plastic relaxation and relaxed buffer layers for semiconductor epitaxy. *Advances in Physics*, 45:87–146, 1996.

[106] R Grey. Private Communication.

[107] L. Dong, J. Schnitker, R.W. Smith, and D.J. Srolovitz. Stress relaxation and misfit dislocation in the growth of misfitting films: A molecular dynamics simulation study. *J.Appl.Phys.*, 83:217–227, 1998.

[108] F. Romanato, E. Napolitani, A. Carnera, A.V. Drigo, L. Lazzarini, G. Salviati, C. Ferrari, A. Bosacchi, and S. Franchi. Strain relaxation in graded composition $In_xGa_{1-x}As$/GaAs buffer layers. *J. Appl. Phys.*, 86(9):4748–4754, 1999.

[109] K. Bücher. Efficiency tables. http://www.ise.fhg.de/kallab/.

[110] Y.C.M. Yeh, C. Chang, F. Ho, and H. Yoo. Large scale, high efficiency GaAs/Ge cell production. In *Proc. 21st IEEE PV specialists conf.*, pages 79–83, USA, 1990. IEEE.

[111] C.J. Keavney, V.E. Haven, and S.M. Vernon. Emitter structures in MOCVD InP solar cells. In *Proc. 21st IEEE PV specialists conf.*, pages 141–144, USA, 1990. IEEE.

[112] J.H. Zhao, A.H. Wang, M.A. Green, and F. Ferrazza. 19.8% efficient honeycomb textured multicrystalline and 24.4% monocrystalline silicon solar cells. *Appl.Phys.Lett*, 73(14):1991–1993, 1998.

[113] J.G. Werthen, G.F. Virshup, C.W. Ford, C.R. Lewis, and H.C. Hamaker. 21% (one sun, air mass zero) 4cm^2 GaAs space solar cells. *Appl.Phys.Lett*, 48(1):74–75, 1986.

[114] R.P. Gale, R.W. McClelland, D.B. Dingle, J.V. Gormley, N.P. Burgess, R.M. Kim, Mickelsen R.A., and B.J. Stanbery. High-efficiency GaAs/CuInSe2 and AlGaAs/CuInSe2 thin-film tandem solar cells. In *Proc. 21st IEEE PV specialists conf.*, pages 53–57, USA, 1990. IEEE.

[115] P. Bhattacharya, editor. *Properties of lattice-matched and strained Indium Gallium Arsenide*. INSPEC, 1993.

BIBL
LONDON
UNIV